Constraining the parameters of deformation recorded in fault-generated pseudotachylytes

Lucy Richenda Campbell

Submitted in accordance with the requirements of the degree of Doctor of Philosophy

The University of Leeds

School of Earth and Environment

September, 2016

The candidate confirms that the work submitted is her own, except where work which has formed part of jointly authored publications has been included. The contribution of the candidate and the other authors to this work has been explicitly indicated below. The candidate confirms that appropriate credit has been given within the thesis where reference has been made to the work of others.

Chapter 3 contains research published in the following jointly-authored publication:

Ferré, E. C., Chou, Y.-M., Kuo, R. L., Yeh, E.-C., Leibovitz, N. R., Meado, A. L., Campbell, L. and Geissman, J. W. (2016) Deciphering viscous flow of frictional melts with the mini-AMS method, Journal of Structural Geology, 90, pp. 1526.
doi: http://dx.doi.org/10.1016/j.jsg.2016.07.002.

Section 3.6.2.3 details the results from the Anisotropy of Magnetic Susceptibility analysis carried out by E.C. Ferré on a sample provided by the candidate.

This copy has been supplied on the understanding that it is copyright material and that no quotation from the thesis may be published without proper acknowledgment.

The right of Lucy Richenda Campbell to be identified as the Author of this work has been asserted by her in accordance with the Copyright, Designs and Patents Act 1988.

©2016 The University of Leeds and Lucy Richenda Campbell

Acknowledgements

The support and guidance of Geoff Lloyd and Richard Phillips have been invaluable during the course of this project, and I thank them for giving me the opportunity to carry out this research at Leeds. In addition, many thanks to Rachel Walcott and Bob Holdsworth for their insightful discussions. I am grateful to Stefan Nielsen and Nicola De Paola for their time and expertise in making it possible to use the Rock Mechanics Lab at Durham University, without which part of this work would not have been possible, and to Eric Ferré for seeing the magnetic potential in these rocks. Also to John, for his abounding wisdom, knowledge and discussion, so freely given.

Many thanks to Harri Wyn Williams for his time, supervision and endless patience, both in creating my samples and during the far the more time-consuming effort of teaching me to do my own. Thanks also to Richard Walshaw for training and assistance on the electron microscopes.

To all my friends and colleagues in Earth and Environment, thankyou for all the discussion and support down the years. Thanks particularly to my flatmates, to the structural team for answering and asking questions, for reviews, advice and generally lighting the way, and to the rest of office 8.152 for a large helping of support, humour, distraction and friendship. Thanks to my intrepid field-assistant and of course many thanks also to family and friends at home for their never-ending belief and support through my years of study.

Abstract

Understanding fault zone evolution is crucial to appreciating how deformation mechanisms may change in time and space. This is of particular importance when considering seismic slip, with its potential for human hazard. Histories of fault evolution and reactivation are recorded as overprinted structures in ancient fault zones, now exhumed from seismogenic depths. Recognition of ancient seismicity is aided by the occurrence of pseudotachylyte, a solidified frictional melt generated at seismic slip speeds along faults. Because pseudotachylytes form on similar timescales to the duration of seismic slip, they capture a snapshot of earthquake parameters such as temperature, depth, strength, magnitude and stress drop.

The Outer Hebrides Fault Zone, UK, was repeatedly reactivated during long-lived collision and bears widespread pseudotachylyte. It is used in this thesis as a case study in which to constrain the seismic history. Slip directions on pseudotachylyte faults are identified using field observations supported by microstructural evidence. The depth and temperature of faulting, and the coseismic temperature rise, are studied using the composition and microstructures in the pseudotachylyte veins, whilst experimentally produced melts further understanding of the control of lithology on coseismic fault strength. Finally, the static strength and the dynamic weakening are derived from further field observations.

Seismicity occurred at $\geq$ 10 km, somewhat deeper than has been previously thought, and was initially scattered diffusely round the fault zone on small, strong faults. Magnitudes are recorded up to M_W 6.3 and static stress drops from 1.5-8.8 MPa. The lithology hosting the fault is shown to control the coseismic strength of the pseudotachylyte-bearing fault both through the melt composition and through the development of fault roughness. Overall, results show that seismicity in the Outer Hebrides occurred throughout a long convergence history because fault weakening, slip localisation and fluid influx were heterogeneously distributed around the fault zone.

Contents

1 Seismogenic fault zones and pseudotachylyte: Introduction, rationale and aims **1**

1.1 Introduction . . . 1

1.2 Theoretical background to pseudotachylyte generation . . . 3

1.2.1 Fault structure and seismogenesis . . . 3

1.2.2 Pseudotachylytes as frictional melts . . . 6

1.3 Aims and objectives . . . 10

1.3.1 Aims of the thesis . . . 10

1.3.2 Outline of the thesis . . . 11

2 Geological context of pseudotachylyte in the Outer Hebrides Fault Zone **13**

2.1 Introduction . . . 13

2.2 Initiation and evolution of the Outer Hebrides Fault Zone . . . 14

2.2.1 Time constraints on faulting activity . . . 14

2.2.2 Kinematic constraints on the OHFZ . . . 16

2.2.3 Displacement along the OHFZ . . . 19

2.2.4 Fault rocks in the OHFZ . . . 21

2.2.5 Depth and temperature of OHFZ activity . . . 23

2.3 Pseudotachylyte occurrence . . . 25

2.3.1 Spatial distribution and association with faults . . . 26

2.3.2 Pseudotachylyte mineralogy and microstructure . . . 28

2.3.3 Age of pseudotachylyte formation . . . 30

2.4 Regional tectonic history . . . 33
2.4.1 Regional and offshore structures . . . 35
2.5 Nature of the host rock lithologies . . . 36
2.6 Summary . . . 41

3 Characterisation of pseudotachylyte orientations and the kinematics of seismic slip in the Outer Hebrides Fault Zone 43

3.1 Introduction . . . 43
3.2 Pseudotachylyte occurrence and geometry . . . 45
3.3 Vein orientations . . . 48
3.3.1 Variation along strike . . . 49
3.3.2 Variation between fault zone and country rock . . . 49
3.3.3 Selected localities . . . 50
3.3.4 Initial interpretation of pseudotachylyte fault orientations of the OHFZ 54
3.4 Host rock controls on pseudotachylyte faulting . . . 55
3.4.1 Foliation . . . 55
3.4.2 Riedel shear systems . . . 57
3.4.3 Initial interpretation of host rock controls on fault orientation . . . 59
3.5 En echelon pseudotachylyte arrays . . . 61
3.5.1 Approach and methodology . . . 62
3.5.2 Orientations of local and regional stresses . . . 67
3.5.3 Rotation of stress fields . . . 67
3.5.4 Initial interpretation of en echelon pseudotachylyte injection veins . . . 68
3.6 Field kinematic indicators . . . 69
3.6.1 Pseudotachylyte injection veins . . . 69
3.6.2 Other kinematic indicators . . . 77
3.6.3 Initial interpretation of kinematic indicators . . . 84
3.7 Discussion . . . 85
3.7.1 Orientation of pseudotachylyte veins in the OHFZ . . . 85
3.7.2 Spatial variation in pseudotachylyte vein orientations . . . 86

3.7.3 Controls on pseudotachylyte orientation . . . 87
3.7.4 Slip direction . . . 88
3.7.5 Orientation of remote stress and strain fields . . . 93
3.7.6 Tectonic context of slip phases . . . 94
3.8 Chapter conclusions . . . 96

4 Characterisation of the depth and temperature of pseudotachylyte generation in the Outer Hebrides Fault Zone 99

4.1 Introduction . . . 99
4.2 Methodology . . . 100
4.2.1 Sample preparation and microscopy . . . 100
4.2.2 Quantitative compositional analysis . . . 101
4.2.3 Thermobarometry . . . 102
4.2.4 Clast analysis . . . 106
4.3 Results . . . 108
4.3.1 Characteristic microstructures of pseudotachylyte veins . . . 108
4.3.2 Crystalline textures and undercooling . . . 116
4.3.3 Clasts as markers of temperature and deformation processes . . . 123
4.3.4 Composition of OHFZ pseudotachylytes . . . 129
4.3.5 Thermobarometry . . . 140
4.3.6 Initial interpretation of thermobarometry . . . 141
4.4 Discussion . . . 144
4.4.1 Temperature and pressure conditions of pseudotachylyte generation . . . 144
4.4.2 Evaluation of thermal and cataclasic processes . . . 148
4.4.3 Compositional effects . . . 151
4.4.4 Timing of crystallisation . . . 152
4.5 Chapter conclusions . . . 153

5 Experimental investigation of coseismic strength of pseudotachylyte faults in the Outer Hebrides Fault Zone 155

5.1 Introduction . . . 155

5.2 Methods . . . 157
5.2.1 Field sampling . . . 157
5.2.2 Sample characteristics . . . 158
5.2.3 Experimental procedure . . . 159
5.2.4 Analysis of slip zone roughness . . . 161
5.2.5 Compositional Analysis . . . 163
5.2.6 Viscosity modelling . . . 164
5.3 Results . . . 166
5.3.1 Microstructural development . . . 167
5.3.2 Compositional analysis of experimentally produced melts . . . 180
5.3.3 Mechanical results . . . 185
5.4 Discussion . . . 185
5.4.1 Fault zone roughness . . . 186
5.4.2 Melt heterogeneity . . . 189
5.4.3 Clast content . . . 190
5.4.4 Composition of experimental pseudotachylytes . . . 192
5.4.5 Viscosity and shear strength . . . 193
5.4.6 Distribution of pseudotachylyte in the Outer Hebrides Fault Zone . . . 194
5.5 Chapter conclusions . . . 196

6 Coseismic strength of pseudotachylyte bearing faults 199

6.1 Introduction . . . 199
6.2 Methods . . . 200
6.2.1 Data sources and geological context . . . 201
6.2.2 Assignment of rock properties . . . 202
6.2.3 Field data collection . . . 204
6.2.4 Theoretical derivation of average shear stress . . . 206
6.2.5 Analysis of fault strength, earthquake magnitude and seismic stress drops 208
6.3 Results . . . 212
6.3.1 Average dynamic shear stress . . . 212

6.3.2 Yield stress . . . 216
6.3.3 Seismic moment and magnitudes . . . 219
6.3.4 Stress drops . . . 219
6.4 Discussion . . . 221
6.4.1 Critical assessment of approach . . . 221
6.4.2 Spatial averaging and comparison with seismological results . . . 222
6.4.3 Melt related weakening . . . 224
6.4.4 Slip weakening distance . . . 225
6.4.5 Stress drops . . . 228
6.4.6 Yield strength of fault zones . . . 230
6.4.7 Fault zone structure . . . 233
6.5 Chapter conclusions . . . 235

7 Discussion and synthesis 237

7.1 Introduction . . . 237
7.2 Use and applicability of pseudotachylyte to constrain earthquake parameters . 238
7.2.1 Preservation of primary crystallisation . . . 238
7.2.2 Magnitudes and stress drops . . . 240
7.3 Forming a model of seismic slip on the Outer Hebrides Fault Zone . . . 242
7.3.1 Tectonic significance of pseudotachylyte in the Outer Hebrides Fault Zone 242
7.3.2 Evolution of OHFZ seismic activity in time . . . 244
7.3.3 Kinematic evolution of pseudotachylyte faults in the OHFZ . . . 247
7.4 Application to fault zone models . . . 257
7.4.1 Fault zone style of the OHFZ . . . 257
7.4.2 Development of fault zones through time: strain localisation and strength evolution . . . 258
7.4.3 Fault zones within multiple lithologies . . . 263
7.5 The Outer Hebrides Fault Zone and orogenic models . . . 264
7.5.1 The OHFZ as an orogenic fault . . . 264
7.5.2 Collisional history recorded in OHFZ pseudotachylytes . . . 265

8 Conclusions and Further Work **273**

8.1 Conclusions 273

8.2 Future Work 275

8.2.1 Slip direction 275

8.2.2 Thermobarometry 275

8.2.3 Controls on roughness during slip 276

8.2.4 Strength of pseudotachylyte bearing fault zones 277

A Appendix: Characteristics of pseudotachylyte samples used in compositional analysis **279**

List of Figures

1.1 Schematic diagram of fault orientations and associated principal stress directions following the theory of Anderson (1942) 4

1.2 Sibson-Scholz type fault model (Scholz (1988)) for vertical fault 5

2.1 Geological map of onshore and offshore lithostratigraphy in and around Scotland, UK showing positions of major faults 15

2.2 Cross-section from NW-SE through the Western Isles and OHFZ, Minch basins, Moine Thrust Zone and Great Glen Fault 16

2.3 Maps showing locality names referred to in text, pseudotachylyte occurrences, trends of Laxfordian foliation and fault rock occurrences 17

2.4 Typical section through Outer Hebrides Fault Zone 25

2.5 Observations and interpretive model of the OHFZ, the Minch fault and related offshore basin to the east of the Western Isles 31

2.6 Tectonic evolution of Scotland during the major phases of the Caledonian orogen, showing activity on the OHFZ (here termed 'Outer Isles Thrust') in the Scandian retro-wedge. From Streule et al. (2010). 34

2.7 Geological map of the Western Isles, UK. Reproduced from geological map data ©NERC 2015 38

3.1 Field examples of various pseudotachylyte generation vein geometries 46

3.2 Field examples of pseudotachylyte vein geometries 47

3.3 OHFZ orientations of pseudotachylyte veins 50

3.4 Comparison of orientations of pseudotachylyte generation planes and injection veins between the Northern and Southern sections of the OHFZ 51
3.5 Orientations of pseudotachylyte generation planes and injection veins from the footwall and fault zone of the OHFZ 52
3.6 Orientations of pseudotachylyte generation planes and injection veins in selected Western Isles localities 53
3.7 Comparison of pseudotachylyte generation planes and foliation within the mapped OHFZ 56
3.8 Angular relations between pseudotachylyte generation planes and local foliation 57
3.9 Predicted angles for Riedel-type shear plane development using relative angular relations from Flodin and Aydin (2004) and $\phi = 35.37$ (Jaeger 1959). 58
3.10 Comparison of idealised Riedel shear orientations with pseudotachylyte generation planes 60
3.11 Acute angular difference between injection veins and their parent generation plane 61
3.12 Examples of en echelon pseudotachylyte injection vein arrays 63
3.13 Examples of cross cutting pseudotachylyte en echelon arrays and the development of an injection vein into an en echelon array 63
3.14 Model of en echelon fracture formation at tip of parent fracture adapted from Clemente et al. (2007) 64
3.15 Hand specimen of pseudotachylyte vein showing splitting of single injection vein (note lack of offset) into en echelon branches 64
3.16 Schematic model showing opening directions of en echelon array, and rose diagrams of measured opening directions 65
3.17 Direction and angle of rotation of en echelon array from individual segments, by opening trend of array (n=30) 66
3.18 Map of Áird a' Mhuile, South Uist, showing direction of en echelon array opening directions 67
3.19 Model used to explain injection vein inclination and resulting calculations of slip direction 70

3.20 Slip directions calculated from injection vein-fault vein intersections 73
3.21 Map of selected localities in the Western Isles showing slip directions indicated by injection vein angles 74
3.22 Misalignment of slip direction trend from dip slip movement on parent fault . . 75
3.23 Kinematic analysis plots, showing hangingwall slip directions 76
3.24 Focal-mechanisms showing fault dip and earthquake slip direction calculated from application of off-fault tensile crack model to OHFZ pseudotachylytes . . 78
3.25 Field and microstructural evidence for pseudotachylyte fault slip direction . . . 79
3.26 Apparent hangingwall movement directions from pseudotachylyte faults showing offset markers and microstructures 81
3.27 AMS results for sample SU2 84
3.28 Schematic stereonet representation of dominant slip directions across the OHFZ region 89

4.1 Features of pseudotachylyte veins cutting through host rock 110
4.2 Melt derived features of clasts in pseudotachylyte veins 110
4.3 Pseudotachylyte matrix phases 111
4.4 Spherulites in pseudotachylyte veins 111
4.5 Cataclasite - melt relations within pseudotachylyte veins 112
4.6 Relations between pseudotachylyte veins and previous brittle structure 113
4.7 Transect through $\sim$ 2 mm wide fault vein in sample SU2 showing changing clast and crystalline textures across vein 114
4.8 Textures of pseudotachylyte crystallisation and alteration 116
4.9 Deformation of pseudotachylyte spherulites 117
4.10 Analysis of spherulite geometry in pseudotachylyte sample B7 117
4.11 EBSD imaging of pseudotachylyte vein SU2 118
4.12 Plot showing experimental results of Lofgren (1974), displaying the crystal morphologies of plagioclase compositions expected from differing magnitudes of undercooling. 119

4.13 Schematic diagram showing change in Δ T with position in vein (SU2) based on experimental data from Lofgren (1974) 120

4.14 Radiating plagioclase lathes in pseudotachylyte matrix of sample SU4 120

4.15 Branching spray morphology of undercooled plagioclase in pseudotachylyte vein 121

4.16 Frequency of clast sizes in pseudotachylyte samples. Shown on a log-log scale, the distribution for each pseudotachylyte vein is represented as the number of clasts larger than the specified area. Grey lines indicate the typical fractal range although this may vary for individual samples lying outside the main distribution. 124

4.17 Fractal D-values (2D) indicated by Fig. 4.16. Error bars represent $\pm$ 1 standard deviation error for measurements on each sample, totalled for each bin. 125

4.18 Ratio of wear to melt processes (based on the ratio of clasts to melt) in pseudotachylyte samples from different contexts. Error bars represent 1 s.d. for each sample from multiple measurememnts summed per bin. 125

4.19 Plot after O'Hara (2001) showing results for OHFZ pseudotachylyte samples based on measured wear-to-melt ratios. Coloured envelopes outline error of one standard deviation on the $\frac{W}{M}$ ratio. Red box outlines range considered where T_melt = 1230-1350°C. 127

4.20 Examples of pseudotachylyte matrix compositional heterogeneity 131

4.21 Evidence for secondary alteration in pseudotachylyte veins 132

4.22 Ternary diagrams showing composition of plagioclase in host rock and vein phase crystals 135

4.23 Weight percentages of major element oxides in host rock and pseudotachylyte vein amphiboles 136

4.24 TEM brightfield image of crystalline vein phases in sample SU2 139

4.25 Temperatures and pressures from host rock and pseudotachylyte vein amphibole-plagioclase thermometer of Holland and Blundy (1994) and the barometers of Schmidt (1992) and Anderson and Smith (1994) 142

5.1 Field examples of pseudotachylyte development along boundaries between quartzofeldspathic and amphibolitic bodies 156

5.2 Configuration of the Low to High Velocity Rotary Shear Apparatus (LHVRSA) at Durham University, with detail of sample holders and a typical slip velocity profile. 160

5.3 Example of process used to generate roughness analysis 162

5.4 Selected microstructures of experimentally generated pseudotachylytes 168

5.5 Vesicle distribution in experimentally generated pseudotachylytes 169

5.6 Size distribution of clasts in experimental pseudotachylytes with natural pseudotachylyte results included for comparison. Solid lines indicate best fit lines to experimental results, used to gain the fractal dimension D; the extent of best-fit line indicate the fractal range considered to fit the line. 171

5.7 Selection of profiles of slip zone margins in experimental samples 173

5.8 Microstructures indicating preferential melting and pre-existent weak planes as controls on roughness 176

5.9 Power spectral densities for roughness of slip zone profiles highlighted in Fig. 5.7, normalised and presented against wavelength of the asperity. 178

5.10 Major element oxide analyses taken using EDS and EMPA methods. Also shown are the analyses for oligoclase and a relatively Mg-rich hornblende (from Deer et al. (1992)). 181

5.11 Analyses from EDS and EMPA for SiO_2 vs Na_2O + K_2O of experimental pseudotachylytes , overlain on a typical classification of igneous extrusive rocks (Best (2009)). 182

5.12 Relationship of suspension viscosity with temperature for a singe lithology quartzofeldspathic core (R2), the Corodale - quartzofeldspathic mixed core (R5) and metabasic - quartzofeldspathic mixed core (R7) 183

5.13 Mechanical results for many of the experiments run during this study, shown as frictional coefficient (μ) against displacement. 186

5.14 Schematic diagram of fault between quartzofeldspathic and amphibolitic metabasic samples, based on Fig. 5.7, highlighting the differences in asperity and slip zone properties that might be expected to influence wear of the opposing fault wall differently to if the same-lithology was juxtaposed. 189

5.15 Host rock biotites and hornblendes melting in situ, in both natural and experimental samples 191

6.1 Schematic diagram illustrating change of shear stress (black curve) along a fault (averaged per unit area) during a single episode of seismic slip. Terms used in this chapter are defined here. After Niemeijer et al. (2012). 206

6.2 Plot of seismic moment against fault slip area with data from the publications used to estimate the scaling law 210

6.3 Thickness of pseudotachylyte fault veins plotted against the displacement seen across them. Error bars shown represent measurement inaccuracy (± 0.001 m) and true displacement uncertainty (+ 0.1 m). 213

6.4 Average dynamic shear stress, $\bar{\tau}$, plotted against displacement for all datasets on a log-log graph (top) and for individual fault zones on linear axes (lower plots214

6.5 Average dynamic shear stress, $\bar{\tau}$, plotted against displacement for data from the OHFZ collected during this study, delineated by apparent sense of slip. Error bars shown represent measurement inaccuracy (± 0.001 m) and true displacement uncertainty (+ 0.1 m). 215

6.6 Mohrs circles representing constraints on the fault shear strength within the range 5-10 km under different failure conditions 217

6.7 Moment magnitudes, M_W, plotted by location across the OHFZ from data collected during this study 218

6.8 Static stress drops and dynamic stress drops plotted against seismic moment for pseudotachylyte faults form all datasets. Also shown are literature values of seismically derived static stress drops from Abercrombie and Rice (2005) and Baltay et al. (2011) 220

6.9 Four models of stress drop and fracture energy behaviour between large and small earthquakes from Abercrombie and Rice (2005) with model refined by this study 229

7.1 Cooling model for timing of crystallisation of pseudotachylytes 239
7.2 Map of fault strands suggested to have originated as brittle thrusts, including offshore strands after Brewer and Smythe (1986) 248
7.3 Map of seismic slip evolution of the OHFZ, part 1 252
7.4 Map of seismic slip evolution of the OHFZ, part 2: 253
7.5 Model of strength evolution during faulting episodes on the OHFZ 257
7.6 Cumulative frequencies of magnitudes calculated in section 6.3.3 for the OHFZ, the Gole Larghe Fault Zone (GLFZ) and the Otago normal fault 261
7.7 Caledonian plate configuration highlighting location and role of OHFZ, modified after Streule et al. (2010) 266

List of Tables

2.1 Comparison of proposed OHFZ evolution models 20

2.2 Comparison of bulk analyses for OHFZ pseudotachylytes 32

2.3 Outline of tectonothermal history for Western Isles and OHFZ, based on Fettes and Mendum (1987) 39

4.1 Major element analysis of pseudotachylyte vein amphiboles used for thermobarometry, with plagioclase X_An ratio. Analysis EDX9 was obtained using TEM EDS, all others are EMPA 103

4.2 Major oxide analysis of host rock amphiboles used for thermobarometry, with plagioclase X_{An} ratio. 104

5.1 Modal percentages of lithologies sampled for experimental study 158

5.2 Configurations of cores used in experiments 159

5.3 Clast analysis from experimental pseudotachylytes . Errors on clast % are ± 1 s.d. and errors on D-values represent observation uncertainties of $1\mu m^2$. 172

6.1 Geological setting of fault zones used from published studies for analysis of dynamic shear stress 202

6.2 Input parameters for calculation of dynamic shear stress used in chapter 6 . . . 204

6.3 Results of single factor ANOVA tests between $\bar{\tau}$ values for different fault types 215

6.4 Differential and shear stresses needed to fail a 25° fault at 5 km and 10 km depth 216

A.1 Sampling location and fault characteristics (where applicable) of pseudotachylyte samples used for qualitative and quantitative compositional analysis 280

A.2 Microstructural and compositional characteristics of pseudotachylyte samples used for qualitative and quantitative compositional analysis 281

List of Abbreviations

AMS	Anisotropy of magnetic susceptibility
An	Anorthite
BGS	British Geological Survey
BSE	Back Scattered Electron
Bt	Biotite
CPO	Crystal preferred orientation
CPX	Clinopyroxene
EBSD	Electron back scatter diffraction
EDS	Energy dispersive X-ray spectroscopy
EMPA	Electron microprobe analysis
Hbl	Hornblende
K-spar	Potassium feldspar
M_0	Seismic moment
M_W	Moment magnitude
MOIST	Moine and Outer Isles Seismic Traverse
NRM	Natural remanent magnetisation
OHFZ	Outer Hebrides Fault Zone
OPX	Orthopyroxene
Pl/Plag	Plagioclase
PST	Pseudotachylyte
Qtz	Quartz
SHIC	South Harris Igneous Complex
TEM	Transmission electron microscopy
XRD	X-ray diffraction
XRF	X-ray fluorescence

Chapter 1

Seismogenic fault zones and pseudotachylyte: Introduction, rationale and aims

1.1 Introduction

Large continental faults feature in plate boundaries worldwide, accommodating significant proportions of plate movement and acting as a locus for large magnitude, hazardous earthquakes. Due to the differing plate vectors at each boundary, there is significant variation in large scale structure and developmental history between fault zones. At the simplest level, faults may exhibit normal, strike-slip or reverse/thrusting slip senses, depending on the type of plate boundary (e.g. collisional, divergent, transform). However, faults of all slip types are often found within a single fault zone or orogen (e.g. Himalayan orogen, Molnar and Tapponnier (1978), Avouac and Tapponnier (1993); San Andreas fault zone, Lin and Nishikawa (2011)). Over time, the properties of a fault are altered, causing the deformation behaviour of that fault and its neighbours to change. Because faults are planes of weakness compared to the average strength of undamaged crust, a fault zone tends to reactivate when possible under repeated applications of stress, even if this means changes in deformation mechanism and slip sense to do so. A single crustal fault therefore can exhibit a complex, overprinted deformation history.

Understanding the development of a fault zone in space and time is crucial for improving knowledge of where, when and how earthquakes occur, both along a single fault and across a complex fault zone. Studies of active faults employ techniques such as seismology, geodesy and numerical modeling to investigate complex spatial behavior of faults during, immediately subsequent to, and between earthquake slip events (coseismic, post-seismic and interseismic behaviour respectively). These techniques can be applied to active fault zones worldwide, with or without a surface expression, each of which is at a certain stage of its temporal evolution. Understanding the longer term slip history of active, or recently active, faults can be gained through palaeoseismological techniques. However, in order to derive the complete deformation history of a fault, potentially over tens of millions of years (i.e. the average duration of an orogenic event), through to reactivation histories over many hundreds of millions of years, geological techniques are necessary. Exhumed regions may reveal faults eroded down to once-seismogenic depths.

Ancient seismic faulting may be recognised by the presence of specific fault rocks and geometries (Cowan (1999), Rowe et al. (2012), Melosh et al. (2014), Savage et al. (2014), Rowe and Griffith (2015)). The present study considers one of these seismic fault rocks, pseudotachylyte, exposed along a long-lived, reactivated and major crustal fault zone, the Outer Hebrides Fault Zone in north-west Scotland, UK. The study aims to track the development of seismic activity during the evolution of the fault zone, and to constrain the parameters controlling the presence of seismicity and pseudotachylyte production enacted by the faulting environment (e.g. depth/pressure, temperature), by the structure of the fault zone (lithology, orientation, fault style) as well as to investigate seismic source parameters such as magnitude, coseismic fault strength and stress drop that may vary as a result of such environmental variation.

1.2 Theoretical background to pseudotachylyte generation

This section presents an overview of current models and terminology of fault behaviour and the coseismic generation of frictional melts - pseudotachylytes - that will be referred to during the analytical chapters of the thesis.

1.2.1 Fault structure and seismogenesis

1.2.1.1 Fault mechanics

In ideal materials, failure occurs when the applied stress exceeds the strength of the material. Once a heterogeneity, such as a crack, is present, the stress distribution becomes variable, with stress concentrations around the crack tips that may lead to unstable crack propagation and failure at stresses below the ideal strength (Griffith (1924)). Relative displacements between the crack walls are described with three modes: the tensile Mode I, where the crack walls open perpendicular to the crack; Mode II, where the walls shear parallel to the plane of the crack; and Mode III, where the crack walls shear out of the plane of the crack (Scholz (2002)). Throughgoing mode II shear zones at the laboratory scale form from the growth and linkage of Mode I microcracks and other heterogeneities in the rock (Peng and Johnson (1972), Moore and Lockner (1995)).

Brittle faults are discontinuous planes of displacement, idealised as Mode II or Mode III shear cracks. The sense of displacement on a fault can be used to predict the orientations of the three principal stresses (where $\sigma_1 > \sigma_2 > \sigma_3$, and compressive stresses are positive). Based on the theory of Anderson (1942) and assuming Byerlee friction (Byerlee (1978)), faults tend to form at angles $\sim 30^\circ$ to the maximum principle stress (Fig. 1.1).

To form a new fault plane out of intact rock, the shear stress resolved from the applied stress is $\tau = \mu\sigma_n + C_0$, where τ is the shear stress, μ the frictional coefficient, σ_n the normal stress and C_0 the cohesion term. This expression is known as the Mohr-Coulomb criterion (Scholz (2002)). General values for many lithologies if σ_n >200 MPa are $\mu = 0.6$ and $C_0 = 50$

(Byerlee (1978)). Although a fault might form at the expected angle to the principle stresses, in either a normal, strike-slip or reverse slip configuration, the fault may later be able to slip with a different slip sense, dependent on the new orientation of the principal stresses and the strength of the fault plane, which is controlled by the frictional strength alone, as $\tau = \mu\sigma_n$ (assuming no cohesion).

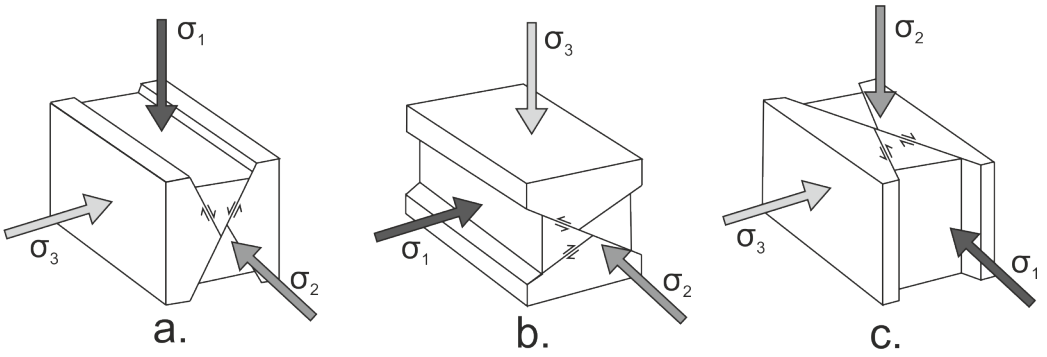

Figure 1.1: Schematic diagram of fault orientations and associated principle stress directions following the theory of Anderson (1942): a. normal faulting; b. reverse (thrust) faulting; c. strike-slip faulting.

1.2.1.2 Fault zone models

Deformation mechanisms vary on fault zones with depth, as generalised by a commonly used fault model (Fig. 1.2) developed predominantly by Sibson (1977a), Sibson (1983), and Scholz (1988). Such models portray the changing strength of the fault with depth, as deformation mechanisms transition from brittle, seismogenic processes through a brittle-ductile transition zone to ductile processes such as diffusion creep (e.g. Tullis and Yund (1991)) and dislocation creep (e.g. Hirth and Tullis (1992)). In quartzofeldspathic rocks, the transition tends to occur over depths of 10-15 km (Sibson (1983)), but depends on the geothermal gradient, water content and lithology, as well as strain rate. However, earthquakes are also known to nucleate below the brittle-ductile transition (e.g. Sibson (1980), Hobbs et al. (1986), White (1996a)). Under changing conditions, the brittle-ductile transition can change depth through time, influencing the deformation style of the fault zone (Imber et al. (2001)).

The structure and strength of fault zones tends to change over time. In laboratory ex-

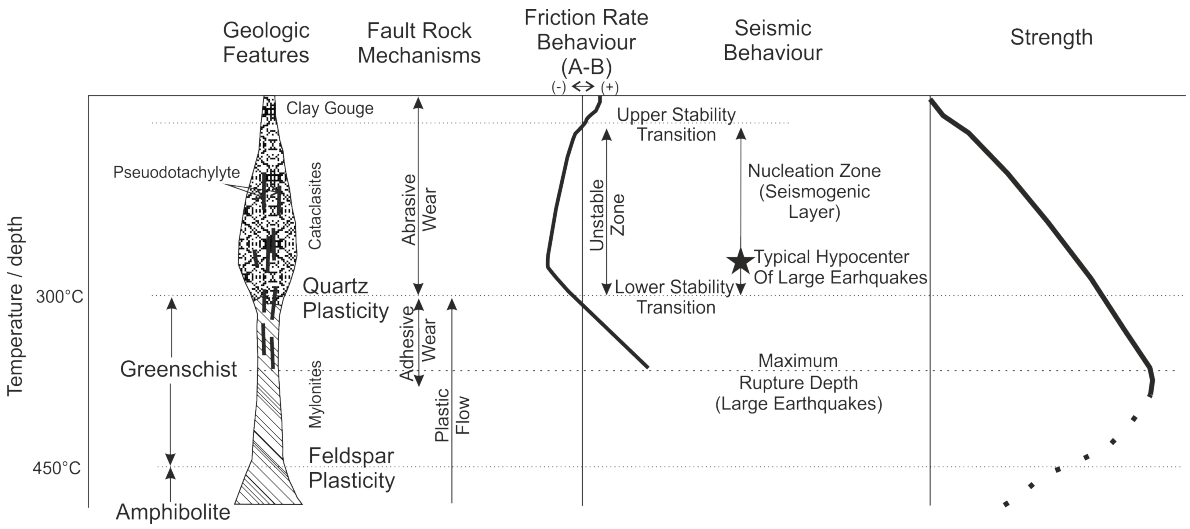

Figure 1.2: Sibson-Scholz type fault model (Scholz (1988)) for vertical fault. The general distributions of geological fault products, deformation mechanisms and seismogenic behavior are shown to vary with depth and temperature. For frictional rate behaviour, negative values are velocity weakening and positive values are velocity strengthening.

periments, the initial increase in stress above the strength of the rock tends to induce small microcracks dispersed across the sample, which under continued stress may join into a through-going fracture (Lockner et al. (1991)). A similar model is envisaged for the development of regional scale fault zones (Sibson (1975)). Fault growth is closely linked with slip localisation. The growth of large faults through processes such as segment linkage (e.g. Gupta et al. (1998)) is facilitated through slip, but in turn allows increased rupture area during subsequent events. Additionally, slip weakening mechanisms (e.g. Holdsworth (2004)) tend to act to localise slip onto dominant faults, which continue to grow as a result. Generally, the growth of faults is thought to be dominated by propagation and increased displacement of the fault during earthquake slip (Cowie and Scholz (1992)). In turn, deformation (including seismicity) tends to localise on the weakest structures, which fail at lower applied stress. The distribution of seismic activity along a fault may indicate varying fault properties such as friction, elastic moduli, pore-fluid pressure or fault orientation which control the heterogeneous distribution of seismic rupture across faults (Bouchon (1997)). Meanwhile, the distribution of earthquakes across the wider fault zone may indicate the trends of localisation onto mature, weaker faults (Perrin et al. (2016)). Fault maturity is defined here in a more general sense relative to the definition of Manighetti et al. (2007) which quantifies the lengths, cumulative displacement

and slip rate of a mature fault. In this work it is used as a non-quantitative term for a large, localised and relatively weak fault thought to be advanced in its development, as is more appropriate for an ancient fault.

1.2.2 Pseudotachylytes as frictional melts

1.2.2.1 Frictional wear, frictional heating and the earthquake energy budget

During slip, sliding of the fault walls against each other leads to processes of mechanical wear (Scholz (1987)). Fault surfaces are rough and contact between the walls is supported on the protruding asperities, which may act to lock the fault unless they can be sheared off to produce wear material (e.g. Wang and Scholz (1994)). The wear products are often preserved along the fault as gouge or cataclasite (Sibson (1977a)) and may give some idea as to the energy used during frictional work (e.g. Chester et al. (2005)). Energy from frictional work is also converted into heat, which serves to raise the temperature locally on the fault plane, as rocks in general are poor conductors of heat and hence little is lost into the fault walls (McKenzie and Brune (1972), Spray (2010)).

At seismic slip rates $>0.1\text{ms}^{-1}$, the increase in temperature may be as much as 800°C with just 0.02 m of displacement (Sibson (1975)), and increases further at larger displacements, slip velocities, normal stresses and frictional coefficients. The lower threshold of seismic slip velocity for frictional melting is derived from the equation defining the necessary temperature change (ΔT) along the fault (Sibson (1975)),

$$\Delta T = \frac{Q}{k}\sqrt{\frac{K.d}{\pi \upsilon}} \tag{1.1}$$

where Q is the heat input, k the thermal conductivity, and K the thermal diffusivity, d is displacement and υ the slip velocity. The heat, Q, is equivalent to the shear resistance and slip velocity as $Q = \tau\upsilon$, where τ is the shear stress (Sibson (1975)). Q can also be considered to equal the total frictional work done by the fault, E_f, assuming adiabatic heating (O'Hara

(2001)). The overall energy budget of an earthquake is defined as (Scholz (2002)),

$$E = E_r + E_f + E_e + E_g \tag{1.2}$$

where E is the total work, E_r is energy radiated as seismic waves, E_e is the work done to propagate the fault tips and E_g the energy used to slip against gravity (Scholz (2002)). Up to 95% of the total energy may be used for the frictional work (Lockner and Okubo (1983), Kanamori et al. (1998)), so that analysis of the temperature increase along faults may reveal a significant portion of the entire earthquake energy budget.

The temperature increase along a fault plane produced by frictional work may be sufficient to melt the immediate wallrock along with any any gouge material, producing a fault rock known as pseudotachylyte. Fault related pseudotachylytes typically appear in the field as dark, 'glassy' or aphanitic veins and are found in exhumed fault zones worldwide, often in crystalline rocks (e.g. Caggianelli et al. (2005), Di Toro and Pennacchioni (2005), Grocott (1981), Allen (2005), Kirkpatrick and Shipton (2009), Swanson (1988), Price et al. (2012), Camacho et al. (1995), Seward and Sibson (1985), but see Viganò et al. (2011)). Pseudotachylyte has also been reported in drillcore from active faults (Otsuki et al. (2003), Janssen et al. (2013)). Nevertheless, because of the apparent ease with which the theoretical conditions needed to produce pseudotachylyte are reached in many earthquakes (Sibson (1975)), there remains some debate as to why pseudotachylytes are not more commonly observed in many more exhumed fault zones (Sibson and Toy (2006), Kirkpatrick et al. (2009)).

1.2.2.2 Definition of tectonic pseudotachylyte

Recognition of pseudotachylyte is dependent on the definition chosen; occasionally used as a field description of glassy fault rocks, which may have a cataclasic or crystal deformation origin even if amorphous (Lin (1996), Pec et al. (2012)), the preferred use here is the genetic definition as a frictional melt (e.g. Maddock (1983)). In this study, confirmation of the melt origin of samples followed the list of microstructural evidence outlined in Magloughlin and

Spray (1992).

Tectonic pseudotachylytes were first recognised as a signature of ancient seismic activity by Sibson (1975) along the Outer Hebrides Fault Zone, although their link to fault processes in this location had initially been recognised by the early survey geologists Jehu and Craig (1923) who termed the dark veins 'flinty crush rock'. Pseudotachylyte is produced not only in a tectonic environment but also may be associated with bolide impact sites and large landslides. In impact settings, pseudotachylyte is generated either by shock melting and fracturing, or by frictional faulting during crater collapse (Reimold (1995)). The best known occurrences of impact pseudotachylytes are Vredefort, South Africa (e.g. Wilshire (1971)), and Sudbury, Canada (e.g. Thompson and Spray (1992)). Additionally, pseudotachylytes are also known to form along the base of large landslides (e.g. Masch et al. (1985), Lin et al. (2001)), a setting which would be expected to be clearly distinguishable in the field from relations between a glide plane and the surficial rocks underneath. In the Outer Hebrides Fault Zone, pseudotachylytes are observed to be related to fault planes, and hence are generally thought to be of tectonic origin (e.g. Sibson (1975), Imber (1998)). However, the large volume of pseudotachylyte exposed has led some to suggest a contribution from bolide impact (Sherlock et al. (2009)).

1.2.2.3 Pseudotachylyte in the field

Pseudotachylyte is generated along fault planes but, as a pressurised melt within moving boundaries, has the ability to flow into space opened in the surrounding rock during coseismic displacement. Injection veins, predominantly tensile cracks leading off the generation plane, are common features (Sibson (1975)), as are pseudotachylyte -filled dilational structures such as jogs and brecciated zones. Previous studies on pseudotachylytes have used field measurements to: develop relationships between the thickness of pseudotachylyte veins and the displacement that generated them (Sibson (1975)); to define rupture directivity and rupture length of a single earthquake (Allen (2005)); to estimate the fictional coefficient, shear stress and width of slip weakening of the fault zone (Di Toro et al. (2005b)); to constrain the depth, stress drop and stress distribution across the fault (Kirkpatrick et al. (2012)); and to inves-

tigate values of the dynamically varying Young's modulus (Griffith et al. (2012)). However, the approaches that can be used on an individual fault zone will depend particularly on the exposure, structures, and preservation of the fault zone.

1.2.2.4 Conditions required for pseudotachylyte generation

The global dataset of pseudotachylyte - bearing faults provides constraints on the conditions required for frictional melting and also seismicity. A review by Sibson and Toy (2006) revealed that pseudotachylytes occur on all fault types (reverse, strike-slip and normal), and at depths typically between 0 - 20 km, although much deeper examples (30 - 80 km) have been found in specific settings such as the Norwegian Western Gneiss Region and Corsica, where seismicity may have been induced by high fluid pressure in deep eclogites (Lund and Austrheim (2003)) and by a low-geotherm subduction setting (Austrheim and Andersen (2004)) respectively. In contrast to the example from the Western Gneiss Region, where the fluid content may be 4% (Andersen and Austrheim (2006)), most settings in which pseudotachylyte is generated appear to be dry, supporting the theoretical argument that fluid-present faults have too low an effective normal stress for a sufficient coseismic increase in fault plane temperature (Sibson (1975)), or that coseismic heating of the fluid might lead to processes such as thermal pressurisation (Lachenbruch (1980)) that weaken the fault before melting can occur. However, recent experimental studies have shown that frictional melts can be produced in fluid-present conditions (Violay et al. (2014)). The applied stress, and strength of the fault, are considered by Sibson (1975) to need to be >100 MPa in order to generate pseudotachylyte, although pseudotachylyte forming in lower strength cataclasite is reported from the Gole Larghe fault zone (Di Toro et al. (2005b)). Slip speeds $>\sim 0.1$ ms^{-1}, the lower limit for unstable seismic slip, are required to produce pseudotachylyte (Sibson (1975), Di Toro et al. (2004)).

1.3 Aims and objectives

Seismic hazard is a considerable risk to life in regions of large, active fault zones. Understanding where earthquakes may occur along fault zones involves constraint of the fault zone conditions under which earthquakes may nucleate and propogate. As a fault zone evolves through time, and is subjected to changing tectonic stress states, the parameters that control seismic behavior change. To be able to track these developments over the timescales of orogens, and beyond, it is necessary to study the seismic record stored in exhumed, ancient fault zones. This thesis investigates the controls on temporal and spatial distribution of seismicity recorded in an exhumed, crustal scale fault with abundant seismically generated fault rocks.

1.3.1 Aims of the thesis

This study aims to investigate the evidence for seismicity preserved in ancient crustal scale fault zones exhumed from seismogenic depths, in order to constrain the conditions that control the source parameters of individual earthquakes, and to understand the seismic evolution of the fault zone through time. The specific fault zone considered is the Outer Hebrides Fault Zone (OHFZ), UK. Specifically, the prinicipal aims are as follows:

1. To constrain the number of distinguishable phases of seismicity recorded in OHFZ pseudotachylytes;

2. To create a model of differing tectonic phases in the OHFZ through changing slip direction and stress fields;

3. To observe which faults in the OHFZ pseudotachylytes occur upon, and hence to analyse the evolution of the fault zone and the accompanying changes in the fault zone environment and the distribution of seismicity;

4. To constrain the depth of seismicity and pseudotachylyte formation via analysis of ambient temperature and pressure;

5. To constrain the temperature of the pseudotachylyte melt, used as a proxy for the coseismic fault temperature, for improved accuracy of onward analysis that requires this as an input parameter;

6. To explore the effect of different fault lithology, and to further understand the behaviour of seismic faults separating two adjacent lithologies;

7. To constrain the strength of seismic, pseudotachylyte bearing faults in the OHFZ, and to calculate likely stress drops and magnitudes of the earthquakes recorded by pseudotachylytes;

8. To explore the changes in seismicity in fault zones characterised by fluctuating strengths and deformation mechanisms through their reactivation history;

9. To compare the fault models defined by observations of pseudotachylyte in the OHFZ to other fault zones worldwide, both ancient and active;

10. To explore the wider tectonic context of pseudotachylyte in the OHFZ in comparison with models of present day collisional orogenic processes.

1.3.2 Outline of the thesis

This thesis is divided into eight chapters, as outlined here:

Chapter one provides the background context to fault mechanics and fault behaviour, relevant to the current understanding of pseudotachylyte formation, including the application of field and laboratory studies, and outlines the aims and structure of the thesis.

Chapter two gives an overview of the geological context of the Outer Hebrides Fault Zone, including the lithologies and structures.

Chapter three presents results from field work and microstructural analysis for the orientation of pseudotachylyte - bearing faults in the Outer Hebrides Fault Zone, exploring the controlling influences on fault orientation, and considers the evidence for determining slip direction on

pseudotachylyte -faults using two models of angular relationships between injection pseudotachylyte and fault pseudotachylyte veins.

Chapter four describes results from compositional and microstructural analysis of pseudotachylytes from the Outer Hebrides Fault Zone, seeking to constrain coseismic melt and ambient temperatures, in addition to pressure and depth during faulting.

Chapter five presents results from high velocity rotary shear experiments, which generate frictional melt, using samples of Outer Hebrides Fault Zone lithologies, and analyses the microstructural and compositional controls on the development of the slip zone geometry and strength of the coseismic fault.

Chapter six includes results for the strength behaviour of pseudotachylyte bearing faults in the Outer Hebrides Fault zone, including pre-seismic strength and coseismic weakening; equivalent observations from other fault zones are also processed for analysis of stress drops and seismic magnitudes.

Chapter seven discusses the evolution of seismic activity on the Outer Hebrides Fault Zone, the environmental parameters of seismogenesis, and how such activity could relate to models of evolving continental collision accommodated by active faults; the application of pseudotachylyte to derive parameters for such models is also considered.

Chapter eight presents the main conclusions of this study, and suggests areas where further work could be undertaken.

Chapter 2

Geological context of pseudotachylyte in the Outer Hebrides Fault Zone

2.1 Introduction

Establishing a solid geological framework is important for placing into context observations of changing fault behaviour, which may occur, for example, due to changes in lithology, fault rock, or vary along different fault structures within the wider fault zone. This chapter reviews what is currently known about the Outer Hebrides Fault Zone (OHFZ) and its slip history, including the timing and depth of slip, the mechanisms of deformation and the fault rocks produced, in order to provide a framework with which to set observations of seismicity through the occurrence of pseudotachylytes. An outline of the wider regional structures and tectonic history is provided, along with a description of the rock types cut by the fault. A final summary outlines the reasons for using the OHFZ as a field area and the information still needed to be gained.

The chapter begins with an outline of the Outer Hebrides Fault Zone, detailing the timing of initiation and reactivation, the kinematic evidence for slip direction and the constraints

on the magnitude of displacement. The various fault rocks present along the OHFZ are then briefly described, along with the constraints they provide on temperature and pressure of fault activity. Pseudotachylyte is covererd in greater detail, outlining the occurrence along the fault, typical field observations and compositional studies, and the results of dating. A brief description of the likely regional tectonic history relevant to the OHFZ is given, before an outline of the wider structures offshore from the Western Isles. Finally, the various lithologies hosting the OHFZ and pseudotachylytes are described.

2.2 Initiation and evolution of the Outer Hebrides Fault Zone

The Outer Hebrides Fault Zone (OHFZ) is exposed onshore within the islands of the Western Isles, or Outer Hebrides, which form a long and narrow archipelago in the northwest of Scotland, UK (Fig. 2.1). The fault zone is exposed for some ∼200 km along strike, which broadly tracks the sweep of the islands from the southwest to the north east. It lies along the eastern edge of the islands, forming a fault zone of varying thickness between 100 m and 15 km, and generally faults dip 20-30° towards the southeast or east-southeast (Smythe et al. (1982)).

2.2.1 Time constraints on faulting activity

The youngest units in the Western Isles cut by the OHFZ are the 1890 Ma South Harris Igneous Complex (Mason and Brewer (2004)) and the ∼1710 Ma Uig Hills granites and pegmatites (van Breemen et al. (1971)), which provide a maximum fault initiation age. In addition, a thermal event reactivating the South Harris Langabhat shear zone may have occurred around 1.1 Ga (Cliff and Rex (1989)), a structure that is cut by the OHFZ. Latest fault movement is limited by Permo-Carboniferous dyking cutting the fault at the southern end in Barra and South Uist, and to the north by the presence of pseudotachylyte veined Lewisian clasts in the conglomerates of the Permo-Triassic Stornoway formation (Fettes et al. (1992)). Initiation of movement is thought by several workers to date to ∼1100 Ma, possibly relating to the Grenvillian tectonothermal event (Table 2.1). Fettes et al. (1992) note that on the mainland,

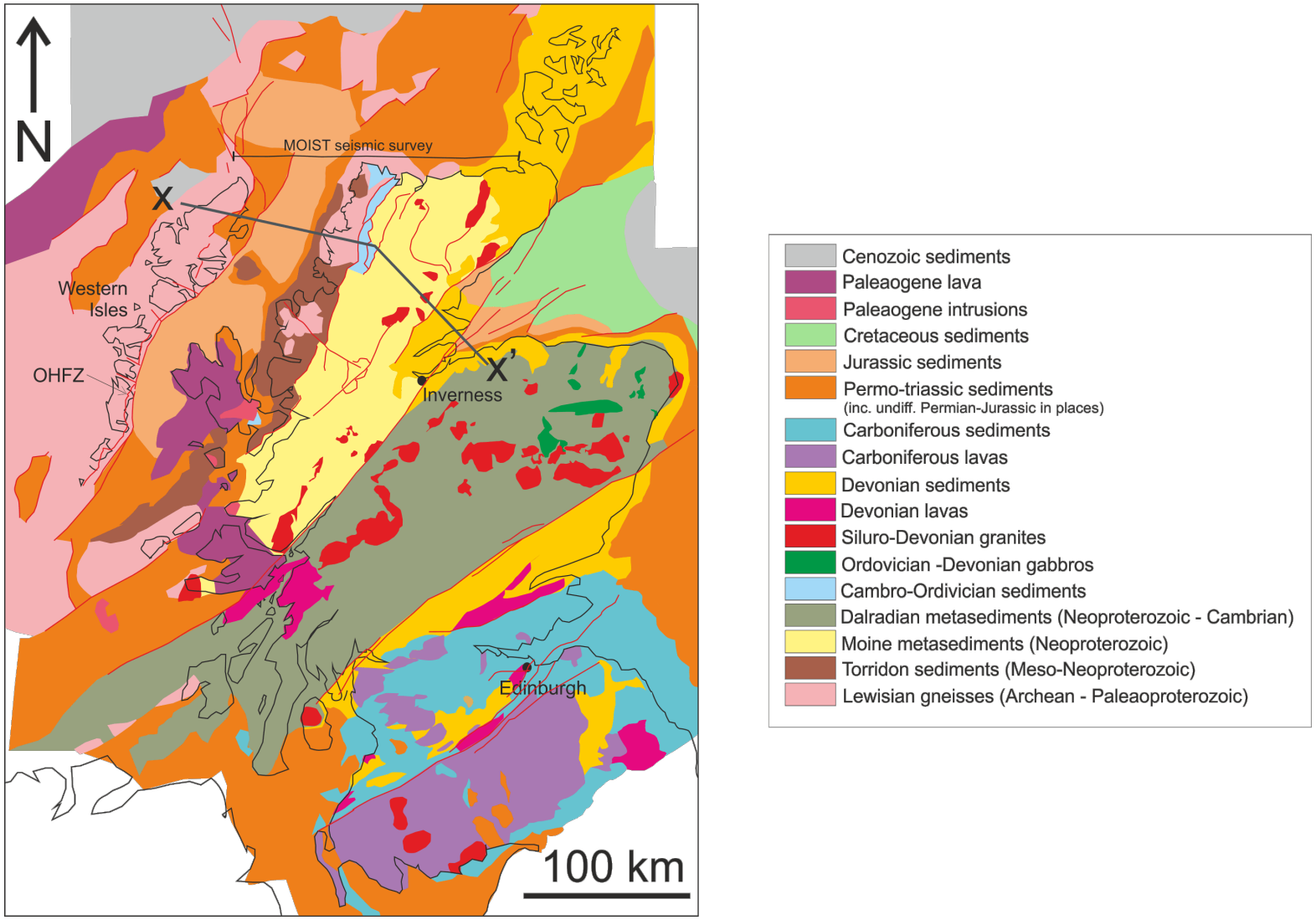

Figure 2.1: Geological map of onshore and offshore lithostratigraphy in and around Scotland, UK showing positions of major faults (in red). The line of cross-section in Fig. 2.2 is marked X-X'. Compiled with data from ©NERC 2015.

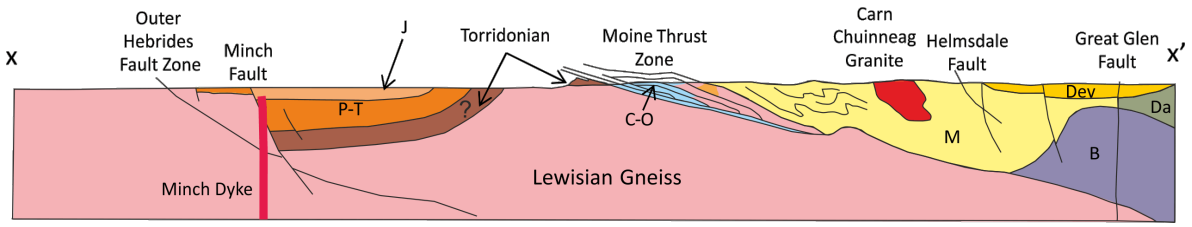

Figure 2.2: Cross-section from NW-SE through the Western Isles and OHFZ, Minch basins, Moine Thrust Zone and Great Glen Fault. Line of section is marked on Fig. 2.1. Unit 'B' is undifferentiated basement. Reproduced from geological map ©NERC 2015.

the Applecross Formation of the sedimentary Torridon Group contains a large volume of both greenschist and amphibolite facies Lewisian Gneisses, indicating uplift of the Lewisian basement from depth to the surface around 994± 48 Ma, from Rb-Sr isochron dating of the underlying Diabeg Formation (Turnbull et al. (1996)). The duration of such uplift is rather unconstrained, with Watson (1977) suggesting uplift concurrent with the deposition of the Torridonian sediments, involving a block bounded by a large fault near to the present day Minch, whilst Fettes et al. (1992) alternatively suggest that uplift could have begun from the Late-Laxfordian onwards, possibly enhanced by early thrusting creating topography around the OHFZ. The interpretation of growth thickening of the Torridon sediments into the base of the OHFZ/Minch Fault on the MOIST seismic line would necessitate the OHFZ to be active around 1.1 Ga (Stewart (2002)) but further evidence for the presence of Torridonian in the Minch is lacking (although is included in Fig. 2.2 from British Geological Survey data). Biotite cooling ages near the South Harris Shear Zones (see Fig. 2.3b) were reset around 1.1 Ga (Cliff and Rex (1989)), suggesting late movement on the shear zone which does not cut the OHFZ. Between these lines of evidence, the OHFZ is therefore thought to have initiated around this time.

2.2.2 Kinematic constraints on the OHFZ

Most workers agree that the OHFZ shows an evolution from ductile thrusting, to brittle thrusting, strike slip and extension (Table 2.1). Alternatively, White and Glasser (1987) interpret a continuous increase in strain and fluid influx through time, beginning with the onset of brecciation, through localised cataclasis and ending with fluid-enhanced ductile phyllonitisation, and suggest a major normal fault zone lies offshore to the east. However, these

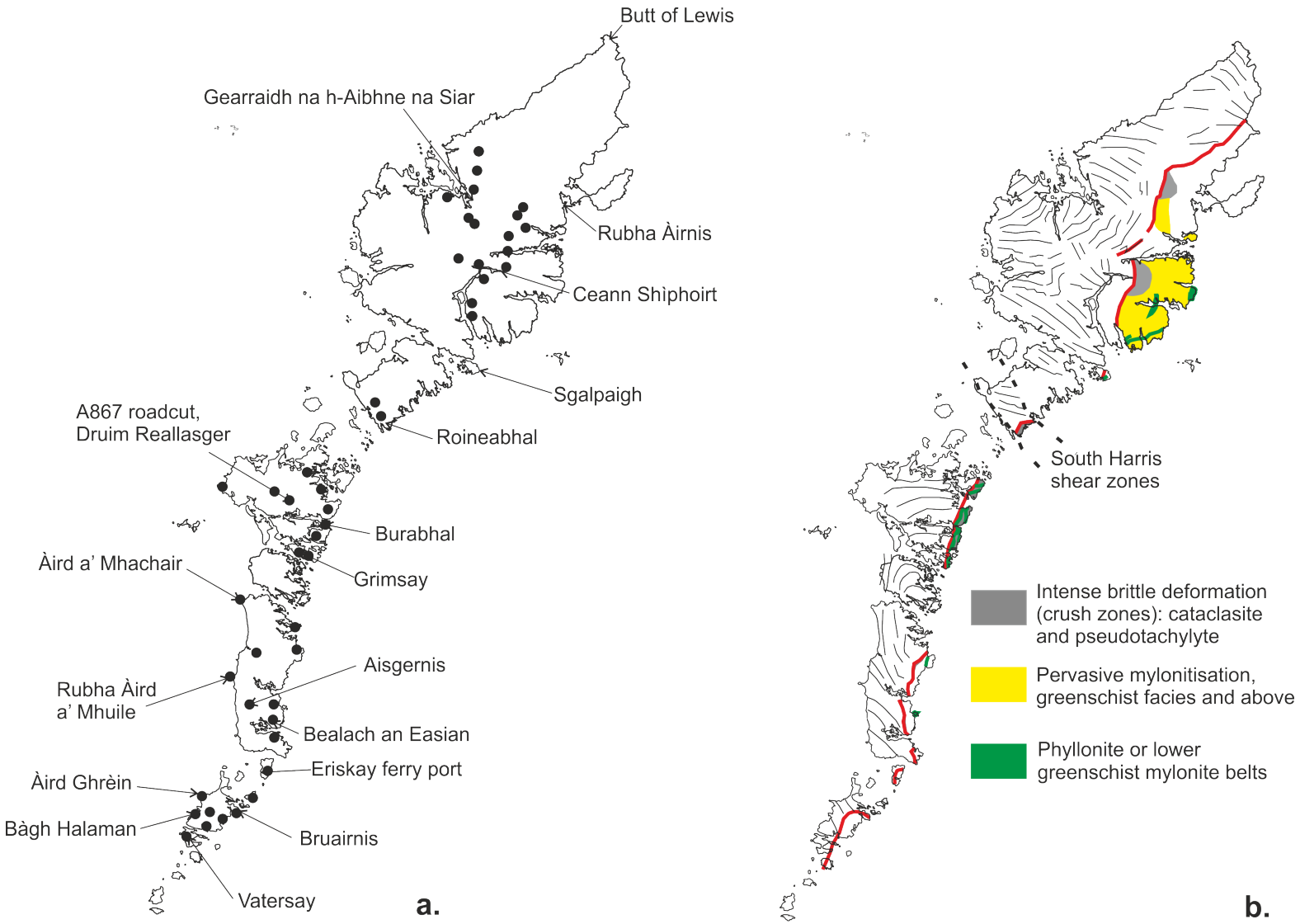

Figure 2.3: a. Map showing locality names referred to in text and locations of pseudotachylyte observations as black circles (from Fettes et al. (1992) and present study); b. Map showing trends of Laxfordian foliation in footwall of OHFZ (from Fettes et al. (1992)) and major fault rock occurrences within the fault zone (from Imber et al. (2001)).

authors themselves admit that this model cannot account for some field evidence, for example the presence of unretrogressed ultracataclasites found in the crush zone. Furthermore, these interpretations are specific to their small study area in the region of Beinn na Tobha in South Uist, and later workers considering larger parts of the fault zone have failed to agree with this model (e.g. Butler (1995), Imber (1998)). However, as seen in Table 2.1, there is a strong and widespread argument for at least one phase of normal movement on the OHFZ. Phyllonite bands, to the west of the basal thrust of the OHFZ, display sinistral strike slip and extensional kinematic indicators and have led many workers to agree on a low-grade, fluid-facilitated, ductile phase of movement probably late in the Caledonian Orogen (see Table 2.1, also Butler et al. (1995), Szulc et al. (2008)). Detachments along with shallowly dipping and, later, steeper dipping normal faults are observed to post-date these extensional shear zones. The latest normal faults observed onshore are the Permo-Triassic basin bounding faults to the Stornoway Formation in Lewis (Steel and Wilson (1975)).

The nature of brittle faulting on the OHFZ, producing pseudotachylyte and cataclasite, is perhaps the most ambiguous, despite often being referred to as the 'main' phase of faulting (Sibson (1975), Kelley et al. (1994)). Previous names including the 'Outer Isles Thrust', and similar variations, reflect the initial belief that brittle faulting predominantly involved reverse movement. At the regional scale, juxtaposition of the granulite facies Corodale gneiss over the footwall amphibolite facies quartzofeldspathic gneiss in South Uist supports the dominance of thrust movement. Thermobarometry on the Corodale Gneiss by Osinski et al. (2001) shows differing metamorphic grades between the hanging wall and footwall, but the authors note that the sampling of a dyke in the footwall gneiss, from the variably altered Younger Basic suite, may not reflect the maximum footwall temperature grade. Evidence has also emerged for localised ductile top-to-the-NW thrusting within the Corodale gneiss in South Uist (Osinski et al. (2001)) and in Barra (MacInnes et al. (2000)), meaning that the Corodale unit may have been moved over the quartzofeldspathic footwall before the transition to brittle movement. White and Williams (1987) suggest that an alternative model where the Corodale Gneiss originated at a similar crustal level to the current footwall is also feasible. Similar juxtapositions of granulite facies and amphibolite facies units exist elsewhere in the Western

Isles, notably in South Harris, brought together by pre-OHFZ movements (see section 3.2). However, field relations show the Corodale to be structurally above the quartzofeldspathic footwall, and separated by a sequence of fault rocks (Sibson (1977b)), so that dip-slip reverse movement seems more reasonable.

At the field outcrop scale, sense of true displacement across individual faults appear difficult to come by due to lack of identifiable markers in the gneiss (Sibson (1975), Nielsen et al. (2010a)). Additionally, the fine-grained nature and complicated network characteristics of ultracataclasites and pseudotachylytes in the 'crush zone' (Fig. 2.3b) makes kinematic analysis of one of the major features of brittle OHFZ movement particularly difficult (Imber (1998)). Kinematic indicators are occasionally observed along the faults - Osinski et al. (2001) observed top-to-the-NNW indicators in cataclasites and top-to-the-WNW movement from slickensides (both from South Uist). Pseudotachylytes have been observed in both contractional and extensional geometries (e.g. White and Glasser (1987), Butler (1995), Imber (1998), MacInnes et al. (2000), Osinski et al. (2001)) throughout the OHFZ. Butler (1995) argues that these extensional features could occur within an overall compressive regime during gravitational-driven and rotational space adjustments accommodating differential block movement. However, all authors agree that neither extensional or contractional movement sense is particularly dominant amongst the pseudotachylytes, even within a single locality.

2.2.3 Displacement along the OHFZ

With a complex reactivation history involving varying movement senses, it is difficult to calculate the overall displacement along the OHFZ for any single tectonic phase. Sibson (1977b) produced an estimate of 10 $\pm$ 5 km for displacement during the ductile thrusting phases based on the geometry of deformed markers, often amphibolitic meta-intrusive bodies. Butler (1995) regards this figure as untrustworthy, since the technique requires several inappropriate assumptions including an initial spherical geometry for often dyke-like features and the use of simple shear where pure shear has been inferred from the field (Butler (1995)). Additionally, the marked heterogeneity along strike makes a single value for displacement potentially

Table 2.1: Comparison of proposed OHFZ evolution models

Author(s)	Butler et al. 1995	Butler et al. 1995	Imber et al. 2001	Imber et al. 2001	MacInnes et al. 2000	White and Glasser 1987	Osinski et al. 2001
Study Area	Northern Section	Southern Section	Northern Section	Southern Section	Barra	South Uist	South Uist
Laxfordian (c. 1700 Ma)							
Post Laxfordian (1700 - 1100 Ma)			Top-to-NW ductile thrusting	Obliterated by SHSZ movement			Top-to-NW ductile thrusting
Grenvillian (c.1100 Ma)	Top-to-NW ductile thrusting (could be earlier)	-	Dextral shear on SHFZ offsets and differentially uplifts OHFZ sections. Later top-to-E extension thickens Torridon Group in Minch.	Dextral shear on SHFZ offsets and differentially uplifts OHFZ sections. Later top-to-E extension thickens Torridon Group in Minch.			
Early Caledonian					To-to-NW ductile thrusting with some sinistral strike slip		
Early/mid Caledonian (c. 450 Ma)	Top-to-NW brittle thrusting	Top-to-NW brittle thrusting	Top-to-NW brittle thrusting	Top-to-NW brittle thrusting	Top-to-NW brittle thrusting	? Brittle development of 'crush melange' (uncertain of timing and movement sense)	Brittle faulting, both compressional and aextensional
Late Caledonian (c. 400 Ma onwards)	Sinistral strike slip	Sinistral strike slip	Sinistral strike slip, top-to-NE	Sinistral strike slip, top-to-NE	Sinistral and dextral strike slip	Extensional dip-slip, widespread cataclasis	
...	Extensional shear zones	Extensional shear zones	Extensional shear zones, top-down-to S or E	Extensional shear zones, top-down-to E or SE	Extensional shear zones, top-down-to-E and SE followed by steeper brittle top-down to-E and SE	Phyllonite development, extensional shear	Top-to-ENE to ESE extension, with phyllonitisation
Late Palaeozoic			Carboniferous onset of brittle extension	Pre-Carboniferous strike slip and extension, top-to-NE and E			
Mesozoic	Brittle extension	Brittle extension	Brittle extension	Dextral strike slip			Top-to-ENE to ESE extension on high angle faults and shallower detachments. Later WNW-ESE faults cut all OHFZ structures.

invalid. However, Butler et al. (1995) notes that in the case of the mylonites in SE Lewis and particularly Sgalpaigh (Scalpay), the ∼600 m thickness of the mylonites oserved would imply several kilometres of movement. Similarly, estimates of brittle thrust displacement are limited by the lack of constraint on later extensional reactivation of the fault and by the lack of markers that correlate between the hanging- and foot -walls. Francis and Sibson (1973) attempted to match a Laxfordian fold hinge across the OHFZ fault trace in Barra, and estimated 4-8 km of offset. However, there is some doubt expressed as to whether these hinges represent the same fold. In South Uist, Coward (1969) looked at the thickness of the ultracataclasite-pseudotachylyte crush zone on the basal fault and estimated 2-3 km of E - W shortening, although there is no reliable relationship between the thickness of such zones and offset. If parts of the Torridon Group are believed to occur in the Minch basins (e.g. Fig. 2.2), post-Grenvillian vertical movement cannot be too large as those sediments would have become subjected to erosion (Butler (1995)).

2.2.4 Fault rocks in the OHFZ

The OHFZ contains a variety of fault rocks, different combinations of which are observed to vary along strike (Fig. 2.3b). In the so-called 'northern section', mylonites of varying grades are dominant, whereas in the 'southern section' ductile fault rocks are generally more localised and cataclasites, ultracataclasites and pseudotachylytes form the bulk of the fault products (Fig. 2.4). Recognition of this regional change led to the differentiation of the northern and southern sections of the OHFZ, which may be either regarded as a transitional change along strike (Sibson (1977b)) or as a discrete change caused by differential uplift across a fault, usually invoking the South Harris Shear Zone (Butler et al. (1995), Imber (1998)). The main fault rocks within the OHFZ are as follows:

Mylonites (top-to-NW): Higher grade mylonites are most extensively developed in south-east Lewis, and are observed to form bands or lenses up to hundreds of metres in thickness (Fettes et al. (1992)). The mapped extent of this mylonite complex is much wider horizontally than in the fault rock complex along strike to the south (Fig. 2.3b), but the amount

of strain varies widely across this area, with anastomosing high strain, highly mylonitised lenses interspersed by low strain regions (Fettes et al. (1992)). The mylonite fabric shows variable angular relationships to the host rock foliation but generally dips moderately to the SE (Fettes et al. (1992)). Mylonite bands at Ceann Shìphoirt (Seaforth Head) contain sheared bands of pseudotachylyte (White (1996a)). Further south, localised mylonites are associated with the later, dominantly brittle structures - for example in South Uist, mylonitised pegmatites become caught up and cataclased within individual fault planes (Osinski et al. (2001)).

Mylonites/phyllonites (strike slip and extensional): Lower grade (greenschist facies) mylonites recording sinistral strike slip and later extension (Butler et al. (1995)) are found predominantly in the eastern exposures of the fault zone (Figs. 2.3b, 2.4). These occur both in the Northern Section (e.g. eastern Sgalpaigh, Butler et al. (1995), Szulc et al. (2008)) and in the Southern Section, for example around Stulaigh and Uisinis - both South Uist (Sibson (1977a), Osinski et al. (2001)) and on the eastern shores of Lì a Tuath and Lì a Deas in North Uist (Sibson (1977a)). Many of these mylonites are referred to as phyllonites (e.g. Fig. 2.4, Sibson (1977a)), although the mica content is variable. Lenses of unaltered gneiss lie within the phyllonite/mylonite belts, between which a gradual strain gradient may be observed (Butler et al. (1995), Osinski et al. (2001)).

Crushed/mashed gneiss: A number of terms appear in the literature relating to brittle deformation in the country rock gneiss. 'Crushed' or 'broken' gneiss is generally applied to intensely brecciated gneisses with or without some cataclasite (Fig. 2.3b), whereas 'Mashed' gneiss was first used by Jehu and Craig (1923) to describe zones of intensely brecciated gneiss shot through with veins of cataclasite, ultracataclasite or pseudotachylyte. The term 'crush zone' has been used by several workers (e.g. Coward (1969), Butler et al. (1995), Imber (1998)) to refer to zones of such fractured rocks (with varying levels of pseudotachylyte) on fault planes of the mapped OHFZ, usually above the basal plane and most extensively observed in North and South Uist (e.g. Fig. 2.4).

Cataclasites/ultracataclasites/pseudotachylytes: Brittle fault rocks overprint ductile my-

lonites where the older deformation phase is present in the fault zone (e.g. Butler (1995), Osinski et al. (2001)). This includes undeformed pseudotachylytes cutting sheared pseudotachylytes in the mylonites of SE Lewis (Butler et al. (1995), White (1996a)).

Fluid influx and regression: Greenschist facies regression occurs particularly along the eastern coast, causing alteration of the fault rocks and preserved gneisses, notably with the growth of epidote and chlorite. This front is restricted to the east of the OHFZ fault base in South Uist, roughly coinciding with the phyllonites on the coast, but advances inland along strike to the north until it includes much of the brittle fault zone in North Uist, including the crush zone (Imber et al. (2002)). In South Harris, retrogressive alteration is seen westwards of the fault zone front, affecting the intensely fractured zones where pseudotachylytes have been observed (Macaudière and Brown (1982)). Fluid influx and formation of the greenschist facies mylonites are associated, with fluid presence inferred to allow ductile deformation at relatively low temperatures. The timing of this fluid flux is therefore likely to be late-Caledonian (Imber et al. (2002)).

2.2.5 Depth and temperature of OHFZ activity

2.2.5.1 Temperature

Thermobarometry has not previously been undertaken directly on non-resheared OHFZ pseudotachylyte, but associated fault rocks have been analysed. The temperature evolution of the OHFZ as a whole has been studied using fluid inclusion studies of syn-tectonic quartz veins in fault rocks from the island of Sgalpaigh (Szulc et al. (2008)). The earliest phase of ductile NW-orientated thrusting reveals a temperature of $500 \pm 30°C$, with the subsequent (presumably late-Caledonian) lower-greenschist assemblage phyllonites at $230 \pm 20°C$. A later extensional detachment is considered by these authors to have operated at $150 \pm 20°C$. This study of Szulc et al. (2008) is in broad agreement with previous estimates. Mylonites from the Pairc district of SE Lewis have given formation temperatures of $535 \pm 50°C$ (Fettes and Mendum (1987)). For the greenschist-facies mylonites, Imber et al. (2002) determine from assemblages

and deformation mechanism constraints a temperature $\sim 350°C$, while another fluid inclusion study from Osinski et al. (2001) on mylonites from Stulaigh in South Uist records $370 \pm 20°C$. The only study relating directly to pseudotachylyte formation is that of White (1996b), whose hornblende-plagioclase geothermometry on SE Lewis mylonites containing deformed, coeval pseudotachylye resulted in temperatures of 500°C and above.

One phase of pseudotachylyte production, now resheared, was synchronous with the higher grade mylonitisation (White (1996a), Sibson (1980)) and therefore formed at around 500°C or higher. Pseudotachylytes deformed in lower grade, later phyllonites (e.g. Rubha Bholuim, South Uist) are constrained to ambient generation temperatures upwards of 230-370°C (Osinski et al. (2001)). Undeformed pseudotachylytes remain relatively unconstrained. However. the fluid-present reactions of the greenschist retrogression front, and the ductile nature of the phyllonite shear zones, may rule out production of pseudotachylyte at this stage or later, so that the minimum temperatures of $370 \pm 20°C$ (Osinski et al. (2001)) would apply.

2.2.5.2 Pressure and Depth

Garnet compositions in the mylonite-pseudotachylyte zones of the Pairc district, SE Lewis, suggest a depth of 13.5 km (Fettes et al. (1992)). This is consistent with this deformation representing brittle-ductile transition zone depths, with alternating seismic faulting and ductile deformation. However, arguments for higher lithostatic pressures from the same area, such as 550 MPa (White (1996a)), are equivalent to greater depths of 18 km, and it is these depths which generate discussions over mechanisms to rupture the ductile middle crust (White (1996a), Sibson (1980)). Pseudotachylytes outside the northern section of the OHFZ are less well constrained as to their depth of formation. Sibson (1975) initially considered the pseudotachylyte to have formed at depths of 4-5 km, and later workers have deemed this feasible based on their own observations (e.g. Macaudière and Brown (1982)), but a more recent review states the likely depth range to 5 - 10 km (Sibson and Toy (2006)). The minimum ambient temperatures (section 2.2.5.1) would suggest depths around 12-15 km, assuming geothermal gradients of 25-30°C km^{-1}.

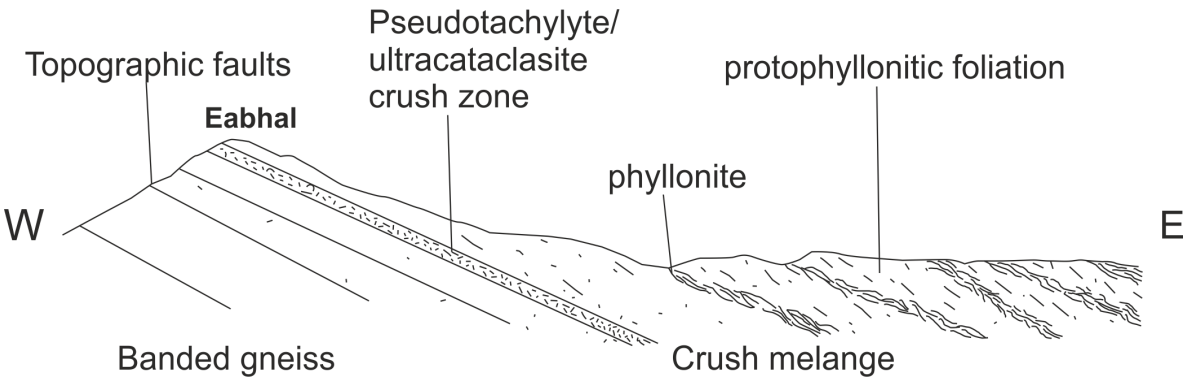

Figure 2.4: Typical section through OHFZ in southern section, showing spatial relationship between topography, fault planes and the pseudotachylyte rich highly fragmented crush zone, as well as the later phyllonite/low grade mylonite development. From Sibson (1977a).

2.3 Pseudotachylyte occurrence

Pseudotachylytes were first described in the Western Isles by Jehu and Craig (1923) who noted the presence of 'flinty crush rock' in Barra. Initial work on attributing pseudotachylytes to ancient seismic slip was developed in Sibson (1975). Through a number of PhD projects (e.g. Watson (1949), Coward (1969), Sibson (1977b), Butler (1995), Imber (1998)) - several of which were used to create the 1:100 000 scale geological maps of the islands (Fettes et al. (1981), reproduced in Fig. 2.7) and subsequent work, it has been established that pseudotachylytes occur on all the major islands of the Western Isles, both within the mapped trace of the OHFZ and in outlying regions (Fig. 2.3a). Maps of OHFZ segments showing pseudotachylyte bearing faults and other fault rock locations within the fault zone, have been produced at up to around 1:20000 by Sibson (1977b), and structural logs taken from similar locations of the fault zone may be found in Imber (1998).

Pseudotachylyte most commonly forms veins discordant to the foliation, which is generally a Laxfordian feature and is overwritten by fault related foliations only locally, most notably in the mylonite zones of Lewis. It may also be observed as networks of veins, sometimes within two parallel bounding fault veins, and also forming the matrix to conglomerates (often also called 'breccias' in the literature, and in this work, although the clasts are often rounded

to some degree). These conglomerates also tend to have planar bounding surfaces, although more irregular geometries have been recorded (Sibson (1975)).

2.3.1 Spatial distribution and association with faults

As the OHFZ lies near to the eastern seaboard of the Western Isles, much of the pseudotachylyte is also found within this region (Fig. 2.3a). Although individual fault planes on the scale of tens of metres can occasionally be observed preserved within the fault zone, particularly in South Uist, pseudotachylyte fault veins tend to be more readily observed along smaller faults of a few metres in length or less. A concentration of pseudotachylyte may be observed within the crush zone sitting above the lowest, westernmost fault of the OHFZ - here it forms a web of veins along with cataclasite and ultracataclasite within a framework of brecciated, fragmented gneiss (Fig. 2.3b). Above this level pseudotachylyte veins tend to be more scattered and discrete (Osinski et al. (2001)). However, a crush zone may be present without bearing significant pseudotachylyte - this is true, for example, on the flanks of Burabhal in North Uist, in contrast to the adjacent hill of Eabhal, $\sim$ 2 km along strike to the south, where abundant pseudotachylyte is once more seen in the crush zone (Butler (1995), see Fig. 2.3a for location).

Outside the OHFZ, pseudotachylyte is still fairly ubiquitous, if less clearly associated with any major tectonic structure (Fig. 2.3a). In Barra, the concentrations of pseudotachylyte exposed along the west coast in localities such as Beinn Tangabhal, Bàgh Halaman and Àird Ghrèin lead some workers to map in a second continuous fault zone parallel to the trace of the OHFZ mapped through central Barra (Sibson (1977b), Fettes et al. (1981), Butler (1995)). Elsewhere, concentrations of pseudotachylyte remain less well associated with large fault structures, for example on Rubha Àird a' Mhuile in South Uist (Fig. 2.3a). Additional scattered observations of pseudotachylyte veins and breccias have been made between the OHFZ and the west coast by several workers (e.g. Sibson (1977b), Piper and Poppleton (1989), Sherlock et al. (2009)). In North Uist, a second fault zone is often mapped through the centre of the island in order to explain a sequence of observations of pseudotachylyte, cataclasite and fragmented gneiss (e.g. Fettes et al. (1981), Fig. 2.3a). In Harris, the OHFZ only briefly cuts

onshore in the southeast, and the fault zone itself is highly regressed. Pseudotachylytes are reported within it (Jehu and Craig (1927), Witty (1975), Heyes (1978)) but appear to be poorly preserved as other workers have failed to find any (Macaudière and Brown (1982)). However, well-preserved pseudotachylyte veins and vein networks are observed in areas of brittle deformation within the anorthosite and the adjacent gabbro on the flanks of Roineabhal to the NE of the OHFZ (Jehu and Craig (1927), Witty (1975), Macaudière and Brown (1982)), where they clearly sit within densely fractured zones and have steep dips parallel to the fractures. Cross-cutting relationships are apparent between a potentially earlier pseudotachylyte phase found on shear fractures and a more voluminous phase forming dilatent structures, although the authors of that study speculate that all pseudotachylyte phases there are of a similar age (Macaudière and Brown (1982)). This study area is useful as, although not lithologically or structurally representative of the typical OHFZ, the pseudotachylytes can be both shown to be the last stage of deformation and to be linked to a set of faults with kinematic markers - in this case, σ_1 is thought to have been predominantly E-W, leading Macaudière and Brown (1982) to conclude a Caledonian tectonic age for these pseudotachylytes .

To the north, in eastern Lewis, pseudotachylyte is once more well-associated with the OHFZ, forming vein networks that cut through the mylonite zones which characterise the fault zone here (Fig. 2.3b). A sheared pseudotachylyte phase has also been observed, most often concordant to the mylonitic foliation, and can be seen in places to be cut by the later, brittle pseudotachylyte phase (e.g. Sibson (1975), White (1996a), Butler (1995)). Pseudotachylytes are most commonly reported towards the base (i.e. towards the western extent) of the fault zone here, and also in the outlying mylonitic lenses (e.g. Sibson (1977b), Butler (1995)). Other occurrences are reported at the Butt of Lewis, the most northerly point of the Western Isles, and across Lewis to the west coast (Fettes et al. (1992)).

Generally it has been noted that, where a lithological change occurs across the fault zone, as with the occurrence of the Corodale Gneiss in the hanging wall in South Uist, the contrast in the volume of pseudotachylyte, and indeed deformation, between the hangingwall and footwall lithologies is particularly strong. In the South Uist example, the crush zone lies almost

entirely within the Corodale Gneiss (Fig. 2.3b) and has been estimated to contain 50-70% volume pseudotachylyte, whilst outwith the crush zone pseudotachylyte veins are still more frequent than in the quartzofeldspatic gneiss in the immediate footwall (Osinski et al. (2001)). This could be due to mafic mineralogies being more susceptible to frictional breakdown and melting (Butler (1995)), but additionally the hanging wall tends to be more intensely deformed along much of the strike of the fault zone (Fig. 2.3b).

2.3.2 Pseudotachylyte mineralogy and microstructure

The colour of the pseudotachylyte in the Western Isles can be variable even within a single locality, usually ranging from a light brown through to black and has been used to differentiate different phases of pseudotachylyte production (e.g. Macaudière and Brown (1982), Sherlock et al. (2009)). Clasts in the pseudotachylyte are observed to consist mainly of plagioclase in the meta-anorthosites of Harris (Macaudière et al. (1985)) and of plagioclase and quartz in the quartzofeldspathic gneisses of much of the rest of the Isles (Maddock (1983)). Rare clasts of titanite, zircon, iron oxides, epidote, hornblende, biotite, garnets and pyroxene may also occur, depending on the make up of the host rock (Macaudière et al. (1985), Maddock (1983)). Melting of the clast margins is observed in both quartz and plagioclase, though seems to be more advanced in the plagioclase (Maddock (1983)). Overall, clasts make up around 20-25% of any pseudotachylyte vein (Maddock (1983), Macaudière et al. (1985)).

Crystals formed in the melt tend not to have a preferred orientation, though these have been reported where flowbanding is present (Macaudière and Brown (1982)). The largest crystals are often plagioclase microlites, displaying a range of forms including tabular, skeletal, acicular, dendritic and spherulitic, and may be interpreted as primary quench crystallisation textures (Maddock (1983), Macaudière et al. (1985)) although others have interpreted spherulitic or radiating textures in particular as devitrification crystallisation from glass (Butler (1995), Imber (1998)). Nucleation of plagioclase, and other crystals, frequently appears to have taken place on the surfaces of clasts, indicating that heterogenous nucleation is favoured (Macaudière and Brown (1982), Maddock (1983)). The reminder of the groundmass has been

found to consist of plagioclase, biotite, quartz, hornblende and ferromagnesian oxides (Maddock (1983), Piper and Poppleton (1989), White (1996a), Sherlock et al. (2009)). Plagioclase crystallising in the vein is reported to have oligoclase to andesine composition, for example ranging from An_{25} - An_{30} (Maddock (1983)) and An_{23} - An_{40} (White (1996a)). Notably, vein crystals of plagioclases show up to 1% FeO, another consequence of rapid crystallisation (Maddock (1983)).

Bulk compositions of Outer Hebrides pseudotachylyte veins are summerised in Table 2.2. These have been shown to strongly reflect their parent rock types (Maddock (1992)). Where a pseudotachylyte vein appears to have formed along a fault picking out a lithological boundary, the composition of both wall components should be incorporated into the melt, but the influence of the more mafic rock tends to be represented most strongly due to the increased presence of the easily melted biotite and amphiboles. Hence pseudotachylytes can show variation in major element-composition even when sampled from the same parent rock, especially if that rock is strongly banded as many are in the Outer Hebrides (Maddock (1992)).

Vesicles are not commonly observed in these pseudotachylytes (Sibson (1975)) but amygdales filled with potassium feldspar, epidote, quartz and titanite have been recognised in some samples by Maddock et al. (1987), who report them to range in size from 20-200 μm and to occasionally be seen elongate parallel to the vein margins. Evidence for alteration comes from assemblages of sericite, epidote and chlorite in the groundmass and sometimes by development of sperulitic textures (Sibson (1975), Imber et al. (1997)). <5 μm garnets have also been found in pseudotachylytes from Lewis and are thought to have recrystallised from the primary assemblage during fluid infiltration (Fettes et al. (1992)). Veins of chlorite or epidote are also commonly observed to cut across pseudotachylyte veins and into the host rock (Imber (1998)).

In the mylonitised pseudotachylytes seen particularly in the northern section of the OHFZ (Butler (1995), Imber (1998)), microstructures such as discordant cutting of foliation and injection veins tend to be seen flattened into the most recent phase of foliation development, so that vein margins becoming diffuse and wavy. Clasts inside the vein show elongation and

the development of dislocation bands and recrystallisation, similar to the mylonitic features of porphyroclasts in the host rock (White (1996a)). Banding in the vein is observed more commonly and strongly than in non-sheared pseudotachylyte and sheath-like folds can be seen (Butler (1995), White (1996a)). In resheared pseudotachylytes, the mineralogy is not observed to change significantly compared to pristine pseudotachylyte veins, with no development of phyllosilicate phases other than <1% biotite plus chlorite from altered amphiboles (White (1996a)). Hence there appears to have been limited fluid involvement in the mylonitisation of these veins.

2.3.3 Age of pseudotachylyte formation

Dating techniques directly applied to the pseudotachylytes use palaeomagnetic and $^{40}Ar/^{39}Ar$ techniques. Piper and Poppleton (1989) found that nine samples from across the Uists and Barra, including localities from both the hanging and footwalls, recorded two remnant magnetisations, one 'mid-Proterozoic' (probably post-Laxfordian) and one Caledonian. These authors note, however, that the spread of data even within the Caledonian group suggest that the pseudotachylytes were generated over extended time periods, long enough to include field reversals. The first use of $^{40}Ar/^{39}Ar$ by Kelley et al. (1994) derived a mean age of 430±6 Ma on a single sample from Grimsay which supports a Caledonian generation age. Further $^{40}Ar/^{39}Ar$ work produced ages of 1900 Ma, 1300-1200 Ma, and 700 Ma (Sherlock et al. (2009)), with the 700 Ma melt sometimes reusing the 1300-1200 Ma faults. These dates are not easily matched with known tectonic ages in the region. 1900 Ma would be associated with the earliest Laxfordian deformation which is otherwise entirely ductile at amphibolite facies, whilst 1300-1200 Ma could be an early Grenvillian faulting event - this period is known to have produced pseudotachylytes around Gairloch on the Scottish mainland although these are more clearly uplift related and dated younger, 980±39 Ma to 1024±30 Ma (Sherlock et al. 2008). An alternative suggestion from Sherlock et al. (2009) is that this date better correlates with the deposition of the Stac Fada formation in the basal Stoer Group of the Torridonian on the mainland. Concretionary lapilli in this fomation have been alternatively interpreted as products from both impact ejecta (Amor et al. (2008)) or volcanic eruption (Sanders and

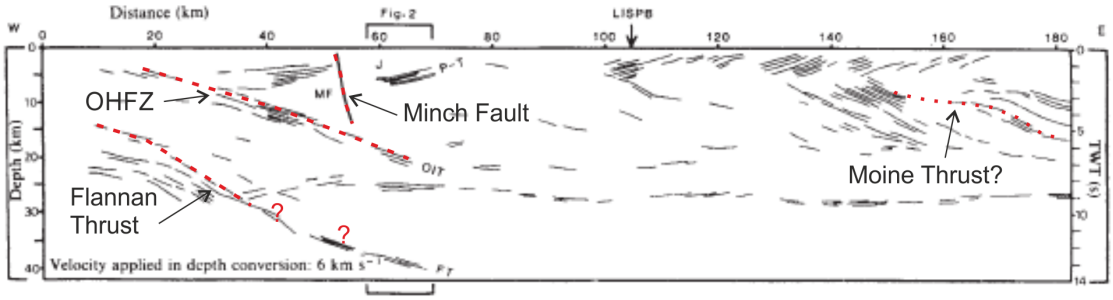

(a) Deep crustal reflection profile taken from the MOIST traverse across the OHFZ (here denoted as OIT - Outer Isles Thrust) and the Minch Basin, from Smythe et al. (1982). Line of profile is shown on Fig. 2.1.

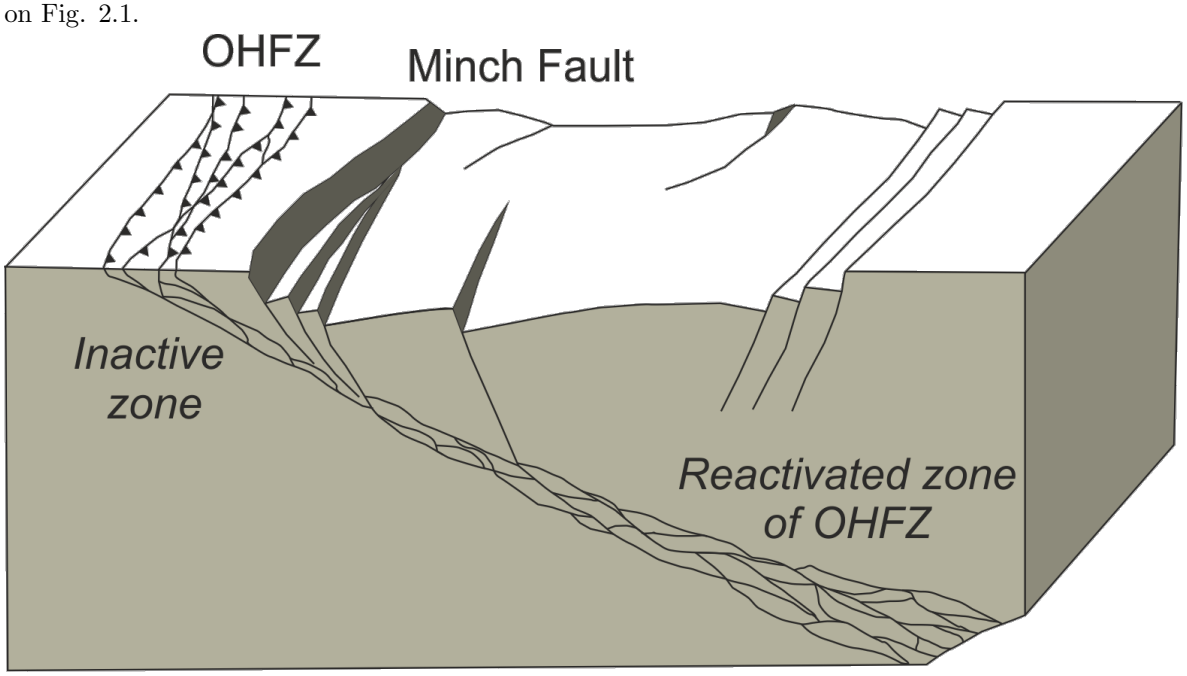

(b) Model of the possible relationship between the Mesozoic Minch normal fault and the OHFZ, involving partial re-activation of the deeper OHFZ. From Stein and Blundell (1990).

Figure 2.5: Observations (a) and interpretive model (b) of the OHFZ and the Minch fault with basin offshore to the east of the Western Isles

Table 2.2: Comparison of bulk analyses for OHFZ pseudotachylytes

Oxides	1	2	3	4	5	6	7	8	9	10	11	12
SiO_2	55.64	57.31	38.11	51.39	67.00	55.40	49.29	48.60	49.35	51.06	49.40	48.20
Al_2O_3	16.00	13.49	13.49	14.56	15.91	19.11	31.15	30.67	25.31	30.88	27.44	26.86
TiO_2	0.63	0.76	2.49	1.41	0.47	0.78	0.10	0.13	0.17	0.32	0.18	0.05
FeO/ Fe_2O_3	7.47	7.00	17.97	14.64	4.26	8.91	0.86	0.99	4.70	0.32	2.76	2.62
MgO	4.57	5.43	10.30	6.70	1.22	6.04	0.42	0.43	4.19	0.21	2.60	3.90
MnO	0.20	NA	0.24	0.25	0.07	0.13	0.03	0.03	0.06	0.00	0.04	0.02
CaO	4.76	2.65	4.63	8.28	3.69	3.17	14.35	15.15	12.11	13.61	12.96	12.53
Na_2O	4.24	2.64	0.31	2.68	5.16	3.26	3.27	3.11	2.83	3.93	3.27	2.80
K_2O	1.69	4.15	4.15	0.78	1.59	3.07	0.13	0.09	0.32	0.05	0.15	0.14
P_2O_5	NA	NA	NA	0.19	0.17	0.13	NA	NA	NA	NA	NA	NA
Total	98.27	96.34	90.67	98.97	100.21	100.00	99.60	99.20	99.36	100.08	98.80	97.12

Analyses sourced as follows: 1-3 and 4-5, microprobe and XRF respectively, both Maddock (1992); 6, XRF, Sibson (1975); 7-12, microprobe, Macaudière et al. (1985).

Johnston (1989)). If impact related, the pseudotachylytes could have been generated by the same event. However, only ambiguous shock microstructures have so far been found in the Western Isles (Sherlock et al. (2009)).

The 700 Ma date is perhaps the most difficult to correlate to regional events as there is little record of this period in the rocks of NW Scotland, although the Moine metasediments in the hangingwall of the Moine Thrust do record an tectonothermal event at this time (Tanner and Evans (2003)), so that the pseudotachylytes could represent a farfield effect (Sherlock et al. (2009)). Considering the Moine metasediments have been displaced by >100 km and that the ∼1000 Ma Torridonian sediments found to the west of the Moine Thrust are undeformed, this interpretation lacks other support at this stage.

2.4 Regional tectonic history

Pseudotachylytes in the OHFZ may be associated with two major collisional episodes - the Grenvillian and Caledonian orogens. The Grenvillian, best exposed in North America as part of the Laurentian continent which the Lewisian complex formed part of, involved widespread collision between 1450 and 1000 Ma (Rino et al. (2008)). The Caledonian orogeny involved collision between the Laurentian continent, represented by the Lewisian complex, and the continents of Baltica and Avalonia, closing the Iapetus ocean. Initially, oceanic subduction, arc accretion and ophiolite obduction are recorded by deformation and metamorphism in Scotland during the Grampian phase (Soper et al. (1999)) before the Scandian phase consisting of terrane accretion and major thrust belt formation through oblique convergence, lasting from ∼ 450 - 430 Ma (Goodenough et al. (2011),Bird et al. (2013)). Later faulting was predominantly strike slip as obliquity of plate motion increased (Dewey and Strachan (2003)). The OHFZ was part of the Laurentian 'foreland' in the retro-wedge of the orogen in NW Scotland (Streule et al. (2010)) and was activated during the Scandian phase as shown in Fig.2.6.

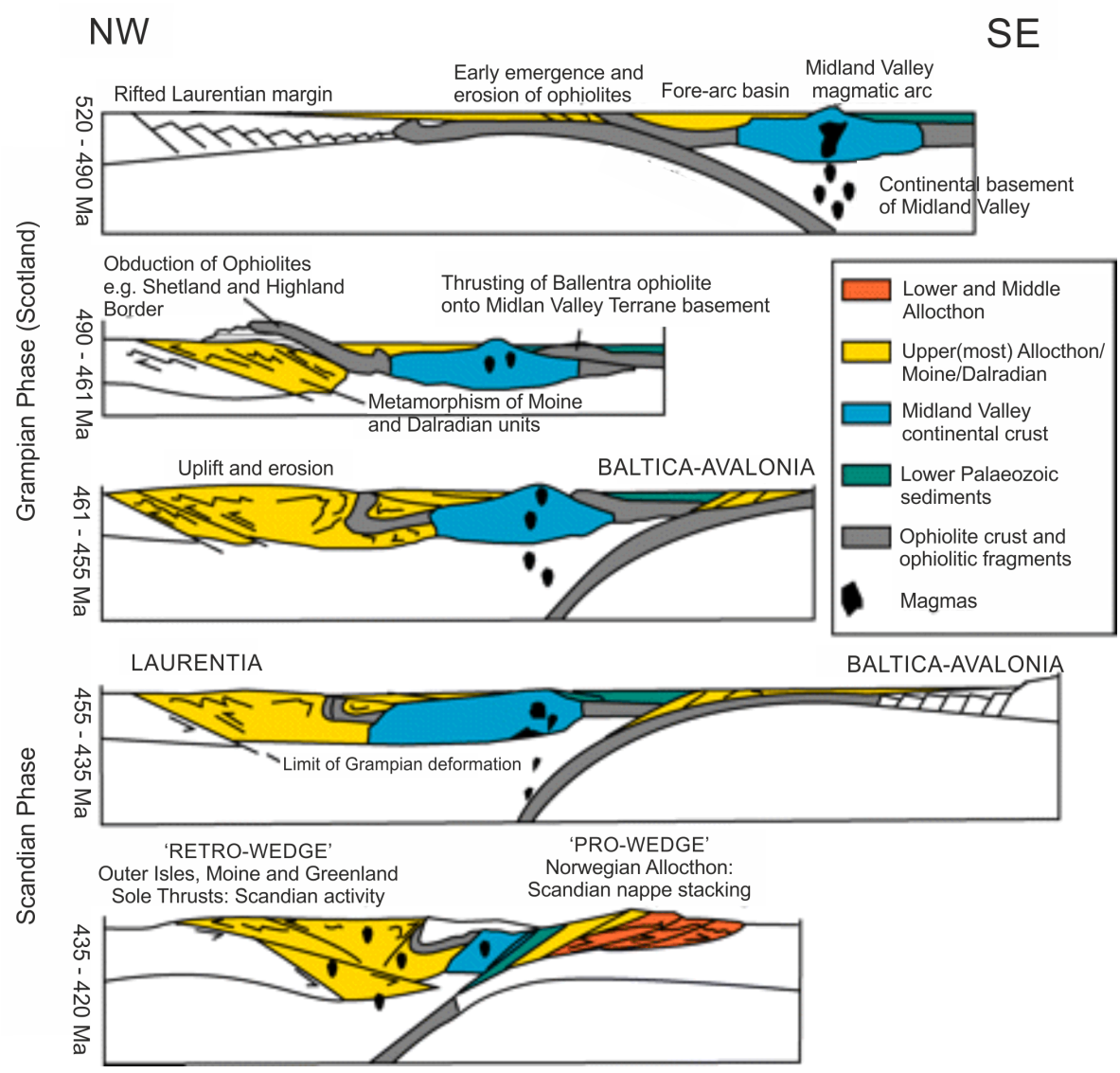

Figure 2.6: Tectonic evolution of Scotland during the major phases of the Caledonian orogen, showing activity on the OHFZ (here termed 'Outer Isles Thrust') in the Scandian retro-wedge. From Streule et al. (2010).

2.4.1 Regional and offshore structures

The Outer Hebrides form the eastern margin of the Hebridean Shelf, which continues westwards up to the shelf break and at the seabed primarily subcrops the Lewisian complex (Fig. 2.1). Basins cut into the faulted Lewisian to the NW and N of the Outer Hebrides contain Permo-Triassic age sediments, predominantly continental redbeds. These basins, the Flannan Trough, North Lewis Basin and West Lewis Basin, are therefore related to same extensional phase as the Sea of Hebrides and North Minch Basins (which collectively form the 'Minch' seaway) and share a similar westerly dipping half-graben geometry with a NE-SW trend (Stoker et al. (1993)). The OHFZ is mapped as a left-stepping jog to the north of the northernmost tip of Lewis, continuing towards the Sula Sgeir High. There is some suggestion that nearby basins (Flannan Trough and North Lewis) may be extensionally reactivating Caledonian reverse faults (Stoker et al. (1993)), which seems feasible given how the extensional Minch Fault seems to reactivate part of the OHFZ in a similar manner (Stein (1988), Figs. 2.5a, 2.5b). The West Lewis Basin is bounded by a series of thrusts which are thought to combine as a transpressional feature (Earle et al. (1989)) attributed to Late Cretaceous and/or Oligocene Alpine inversion (Roberts (1989)).

Several deep seismic reflection profiles have traversed roughly E-W to the north of Lewis, capturing the OHFZ. Initially the 1981 MOIST (Moine and Outer Isles Seismic Traverse) identified the northern offshore strand of the shallowly ($\sim 20°$) dipping OHFZ, the soling of the steeper Minch Fault into the OHFZ and the possibility of extensional reactivation of the OHFZ itself leading to the deposition of sediments into the North Lewis Basin between them (see Fig. 2.5a). The 1984 DRUM line shows the North Lewis Basin bounded by the OHFZ to the NW and the continuation of the Minch Fault to the SE (Smythe et al. (1982)). Building on these results, the 1982 WINCH traverse (Western Isles - North Channel) partially parallels the MOIST line and confirmed many of the initial conclusions there (Brewer et al. (1983)). As well as the North Lewis and Minch basins, half-grabens formed by extensional reactivation of former reverse faults were identified in the northern offshore continuation of the Moine Thrust - hence it seems likely that many similar basins showing the NE-SW trend

show such structural inheritance of Caledonian (or older) features. Stein and Blundell (1990) model this extension as the collapse of a mainly passive hangingwall block above the OHFZ driven by the active extension along parallel faults in the footwall block, west of the OHFZ (Fig. 2.5b). The WINCH profile appears to cut the OHFZ again approximately 100 km SSW of Barra, which remains the southernmost known extent of the OHFZ (Brewer et al. (1983)).

2.5 Nature of the host rock lithologies

The Outer Hebrides archipelago, within which the OHFZ lies, is formed almost entirely of the 'Lewisian Complex' - a suite of Archean to Palaeoproterozoic quartzofeldspathic gneisses with amphibolitised metabasic intrusions and units, and occasional bands of metasediments (Fig. 2.7). Later Palaeozoic rock units consist of OHFZ fault rocks, minor intrusive phases and the Stornoway Formation, a Permo-Triassic unit of continental conglomerates and other alluvial deposits. The OHFZ passes through many of these units (Fig. 2.7), which are detailed below. Pseudotachylytes occur in all the units described, bar the Uig Hills - Harris granites and the younger Stornoway Formation. The mineralogy of the host rock type may be important for assessing whether seismicity is likely to produce pseudotachylytes based on the varying melting temperatures of the minerals present (Spray (2010)).

Archean 'Grey Gneiss' The dominant lithology is a quartzofeldspathic gneiss with a quartz-plagioclase-potassium feldspar-hornblende-biotite composition. It is locally heterogeneous with regards to minerological proportions but is often mapped together as 'undifferentiated gneiss'. Protolith ages range from 3125 $\pm$14 Ma (South Harris, Friend and Kinny (2001)) to 2744$\pm$ 1 Ma (North Harris, Mason and Brewer (2004)). Protoliths for the Grey Gneisses are inferred to be felsic igneous bodies of tonolite-trondhjemite-granodiorite composition, typical of many early-crustal rocks. Metamorphic assemblages of the Grey Gneisses prevalently record Laxfordian amphibolite facies conditions (Fig. 2.3), but some relict areas of granulite assemblages are preserved (Fettes et al. (1992)). A set of basic and ultrabasic-basic layered intrusions known as the Older Basics form lenses and concordant dykes within the

Grey Gneiss and are dated at 2585 Ma (Francis et al. (1971)), and hence broadly share much of the structural and metamorphic history of the host (Table 2.3).

Corodale Gneiss The Corodale Gneiss, with granulite-facies clinopyroxene - orthopyroxene garnet hornblende plagioclase assemblages, is restricted to the hanging wall of the OHFZ in South Uist (Coward (1972)). The dioritic protolith is dated with Sm-Nd and Pb-Pb ages at 2770± 140 Ma and 2900± 100 Ma, which distinguishes this body from the meta-igneous units of South Harris (Whitehouse (1993)). Peak metamorphic P/T conditions are thought to be 880-920°C and 10.3-12.2 kbar (Osinski et al. (2001)), and the granulite grade of metamorphism is therefore higher than the amphibolite-facies quartzofeldspathic gneiss in the footwall below. The pre-faulting relationship of the Corodale gneiss with the quartzofeldspathic gneisses is unclear, as only tectonic contacts now are seen between them (Fettes et al. (1992)).

Younger Basic Intrusions A second set of basic and ultrabasic dyke-like intrusions form a suite termed the Younger Basics. Crystallisation ages are $2049 \pm \frac{78}{100}$ Ma and $2039 \pm \frac{99}{100}$ Ma (Mason et al. (2004)), with metamorphism at 1625 - 1660 Ma (Cliff et al. (1998)) - hence, the Younger Basics postdate the Archean Scourian tectonothermal event, but were deformed and metamorphosed by Palaeoproterozoic Laxfordian tectonism (Table 2.3).

South Harris Igneous Complex (SHIC) and associated metasediments Two metasedimentary belts are mapped in South Harris, containing a mix of pelites, semi-pelites, metacarbonates and various meta-igneous intrusions. The southernmost Leverburgh belt has a maximum age of 2400 Ma (Cliff and Rex (1989)) and is thought to have undergone granulite facies metamorphism during the Laxfordian accretion of, and intrusive activity within, the South Harris Igneous Complex. The Langabhat belt lies between the SHIC and the quartzofeldspathic gneisses to the north, and contains part of the South Harris Shear Zones.

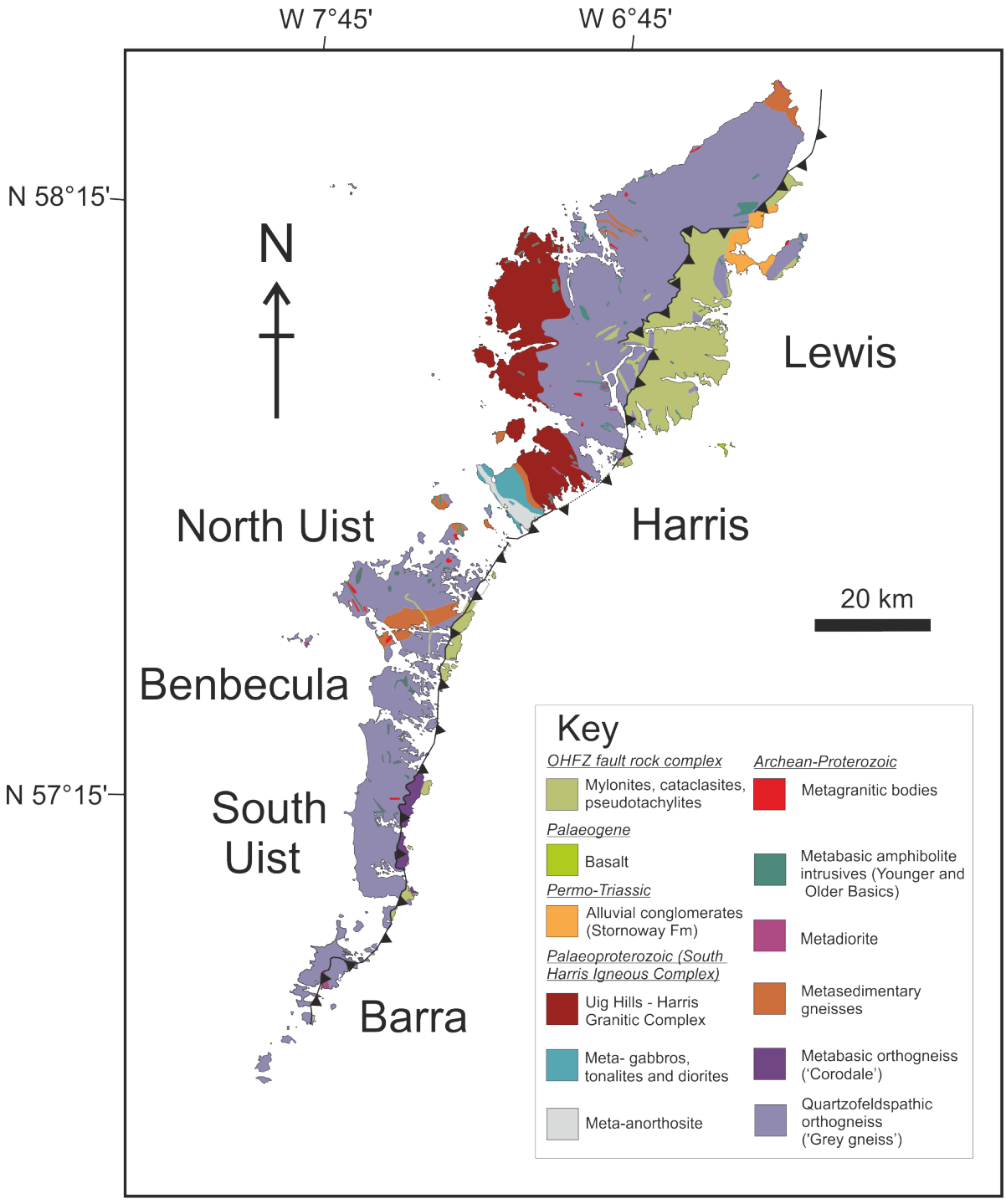

Figure 2.7: Geological map of the Western Isles, UK. Reproduced from geological map data ©NERC 2015

Table 1: Outline of tectonothermal history for Western Isles and OHFZ, based on Fettes and Mendum (1987)

$\sim$ 260 - 145 Ma	**Mesozoic Faulting:** From late Permian, extensional reactivation of deeper OHFZ and formation of Minch (and associated) faults as hangingwall shortcuts. Opening of Minch basins as well as others on Hebrides Shelf and in West-of Orkney regions (Roberts and Holdsworth (1999), Wilson et al. (2010))
430 Ma	**Caledonian:** Activity on Outer Hebrides Fault Zone through variety of kinematic regimes (e.g. Butler (1995), Imber et al. (2002), Szulc et al. (2008))
1100 Ma	**Grenvillian:** Uplift and erosion of Lewisian. Localised heating and recrystallisation to immediate north of Langabhat Shear Zone suggests reactivation (Cliff and Rex (1989). Potential initiation of OHFZ may have followed (Imber et al. (2002))
1680 Ma	**Latest Laxfordian:** Pegmatite intrusions strike E-W (Myers (1971). Localised cataclastic brittle deformation.
1700 Ma	**Later Laxfordian:** Intrusion of the Uig-Hills granite complex. Migmitisation affects South Uist gneisses. Broad folds separated by NW-SE high strain zones dominate the Uists (Myers (1971), van Breemen et al. (1971)). Shear zones in Lewis form NNE-SSW (Coward et al. (1970)).
1890 Ma	**Early Laxfordian:** Widespread folding of Scourian foliation, folding of Younger Basic dykes, creation of weak axial planar foliation locally. Recrystallisation occurs. high strain zones feature tight folding, and shearing occurs along SHIC boundaries (Coward et al. (1970)).
2040 Ma	**Intrusion of SHIC:** diorite and norite intrusions with early development of fabric (Mason et al. (2004)).
2600 Ma	**Intrusion of Younger Basics:** (Francis et al. (1971))
2700 Ma	**Scourian deformation:** High grade deformation and metamorphism accompanying generation of igneous protoliths of Lewisian Gneisses, creating gneissic fabric and compositional banding (Moorbath et al. (1975))

The term 'South Harris Igneous Complex' is used to refer to the igneous units variously intruded into and sheared against the metasedimentary belts, originating from several unrelated generation episodes. These include a 1950 Ma gabbro-anorthosite body and 1890 Ma dioritic and noritic units (Mason et al. (2004)). The gabbro-anorthosite may in fact represent the crystalline basement into which the later units were intruded. The metasediments of the Leverburgh belt have been suggested to correlate with the Loch Maree supracrustal unit on the mainland, which has a maximum age of 2000-2200 Ma (Whitehouse et al. (1997)) and is interpreted as an accretionary complex (Whitehouse et al. (1997)) - the South Harris units are thus thought to be of similar origin (Baba (2002)). Amphibolite-facies retrogression seen along the boundary of SHIC units is associated with later Laxfordian deformation (Fettes et al. (1992)).

Uig Hills-Harris Granite Complex Granite sheeting and altered gneisses form an extensive (420 km^2) outcrop through southwestern Lewis and northwestern and southern Harris. Ages for these rocks have been derived as $1715 \pm \frac{20}{10}$ Ma from U-Pb results (van Breemen et al. (1971)), dating intrusion of the granite into the late-Laxfordian tectonothermal period. The size of the veins or sheets ranges from centimetres to hundreds of metres in width. Cross-cutting relationships of different intrusion phases may be observed, although the composition tends to be consistently quartz - plagioclase - K-spar - biotite (Fettes et al. (1992)). A suite of leucogranite pegmatites typically forms the latest phase.

Permo-Triassic Sediments The Stornoway Formation is the only record left of post-Caledonian bedrock deposition. It consists of a series of alluvial conglomerates with associated sandstones and silt layers and has an apparent thickness of 4 km, although its true thickness is probably less (Steel and Wilson (1975)). Exposure is limited to the northeast of Lewis, around Stornoway. The unit sits unconformabley on the Lewisian, with predominantly gneissic clasts and occasionally showing pseudotachylyte veins indicating that the Lewisian was exposed at the surface at this time. Faulting controls the western boundary of the formation. Six alluvial fan sequences are identified by Steel and Wilson (1975) which are inferred

to represent syn-tectonic fault scarp fans joined by overbank floodplain and braided stream sequences. Jurassic sediments found onshore in the Shiant Islands to the east are largely shales now rather altered by contact metamorphism from Tertiary sills and are analogous to the Jurassic sequence on Skye (Hesselbo et al. (1998)). The Cretaceous is not seen onshore in the Hebrides but is present in places in the Minch basins.

2.6 Summary

The Outer Hebrides Fault Zone records up to 750 million years of episodic reactivation. Within this period, the style of deformation, strength and structure of the fault zone has varied considerably. The OHFZ is additionally a classic locality for the use of pseudotachylyte to identify the location of ancient seismicity after the work of Sibson (1975). Despite this, the conditions of seismicity on the OHFZ remain only loosely constrained. In addition, field evidence such as cross-cutting veins, differing slip senses, reshearing of veins and the simple abundance of pseudotachylyte across the Western Isles points to multiple episodes of seismicity that are also not well recognised. The OHFZ, then, provides a useful study area for the evolution of seismicity on a major crustal fault experiencing changes in temperature, depth and fluid conditions, causing the fault strength to fluctuate through time (Imber et al. (2001)). The abundance of pseudotachylyte allows sampling along several contrasting parts of the fault zone and, as a classic area, improving the constraints on the seismogenic environment will improve further analysis comparing the behaviour of this fault zone with others. It is likely that at least some of the pseudotachylyte producing seismicity took place during the Caledonian orogen - a well studied but complex and long-lived collision - so that further understanding of the role of seismicity as collision progressed can be additionally applied to active collisions worldwide.

Chapter 3

Characterisation of pseudotachylyte orientations and the kinematics of seismic slip in the Outer Hebrides Fault Zone

3.1 Introduction

Pseudotachylyte in the Western Isles is widely distributed around the islands (Fig. 2.3) and may be observed away from the mapped fault zone in relatively high volumes, sometimes mapped as separate fault zones or fault strands (e.g. Sibson (1977b), Fettes et al. (1981), Butler (1995)). Cross-cutting relationships are also observed, although it is not well understood whether these represent seismic activity separated by months or years or rather by different orogenic episodes across hundreds of millions of years (Macaudière and Brown (1982)). This chapter approaches these uncertainties by looking for evidence of change in the orientations of various vein geometries that indicate changing slip direction or stress fields.

The aims of this chapter are therefore to describe the orientations of pseudotachylyte

veins across the field area of the Outer Hebrides Fault Zone (OHFZ); to look for spatial variation along different parts of the OHFZ; to check for regional scale controls on the formation of pseudotachylyte - bearing faults; to analyse movement directions during pseudotachylyte generating slip episodes; and to attempt to constrain the remote stress field(s) during those episodes. Overall, the spatial and temporal variation of pseudotachylyte emplacement is examined, encompassing the distinction of multiple episodes of pseudotachylyte generation and the possibility of generation on fault systems other than the OHFZ. Through these aims, methods for analysis of other pseudotachylyte bearing, poorly constrained fault zones wordwide are also developed and discussed.

To achieve these aims, this chapter:

- Details the orientations of pseudotachylyte generation veins, which represent the orientations of faults, and compares the results along the strike of the fault zone and also at distances perpendicular to it.
- Considers how pre-existing structures, such as foliation and fracture networks, can influence the orientation of faults and cause them to be misaligned relative to the predicted stress field, the orientations of such structures are compared to that of pseudotachylyte bearing faults to evaluate this control.
- These preliminary studies on pseudotachylyte faults show that the orientation of pseudotachylyte faults in the Outer Hebrides Fault Zone (OHFZ) is not controlled by existing structures, nor are they necessarily concordant with the strike of the major structures in the OHFZ. Therefore, further studies on pseudotachylyte injection veins are developed - firstly, en echelon arrays of pseudotachylyte injection vein segments are examined for the orientation of vein opening, after studies on similar geometries in mode I igneous dyking (e.g. Pollard et al. (1982)).
- Secondly, systematic pseudotachylyte injection veining along pseudotachylyte faults are used to indicate the slip direction.
- Field and microstructural observations, where available, are provided to support the

results of the injection-based models.

3.2 Pseudotachylyte occurrence and geometry

Many pseudotachylyte veins are observed in the OHFZ to be approximately planar features and as such can be measured for orientation (also noted by e.g. Sibson (1975), Macaudière and Brown (1982)). These planar pseudotachylytes include fault veins, which are defined here as individual pseudotachylyte veins found along a plane of shear displacement that is assumed to have generated the pseudotachylyte melt (Fig. 3.1), following the terms used in Sibson (1975). Paired shear fractures are also observed to bear pseudotachylyte (e.g. Grocott (1981)) and are formed from bounding planar fault veins connected by secondary internal faulting, along which some displacement or rotation of the rock is commonly observed (Fig. 3.1b). Breccias or 'quasi-conglomerates' (Sibson (1975)), with pseudotachylyte forming the matrix, are often found as tabular bodies (Fig. 3.1c). Internal clasts may be angular to rounded, more often the latter, but here the term breccia is favoured in keeping with much of the literature (e.g. Grocott (1981), Swanson (1988), Bjørnerud and Magloughlin (2004)) and to emphasise the fault-activated formation process, as a subset of the wider fault breccia group. Clasts within these breccias have been significantly rotated. The thickness of the tabular breccias can be as much as two metres (Fig. 3.1d). As with the paired shear zones, there may be noticeable displacement across the upper and lower bounds of the breccia body. These three pseudotachylyte vein geometries (fault veins, paired shear zones and tabular breccias) will be referred to here as a group using the term 'generation planes', as this description emphasises that they are all fault geometries in which pseudotachylyte was generated during seismic slip. Such features do not form in isolation from each other. For example, a simple fault vein may develop along strike into a brecciated system, and there is arguably a progressive spectrum from paired shear zones to brecciated bands forming between overlapping faults (e.g. Sibson (1975), Sibson (1986) but cf. Melosh et al. (2014)) .

An additional group of planar pseudotachylytes known as injection veins are defined as fractures containing pseudotachylyte that has been extruded away from the generating slip

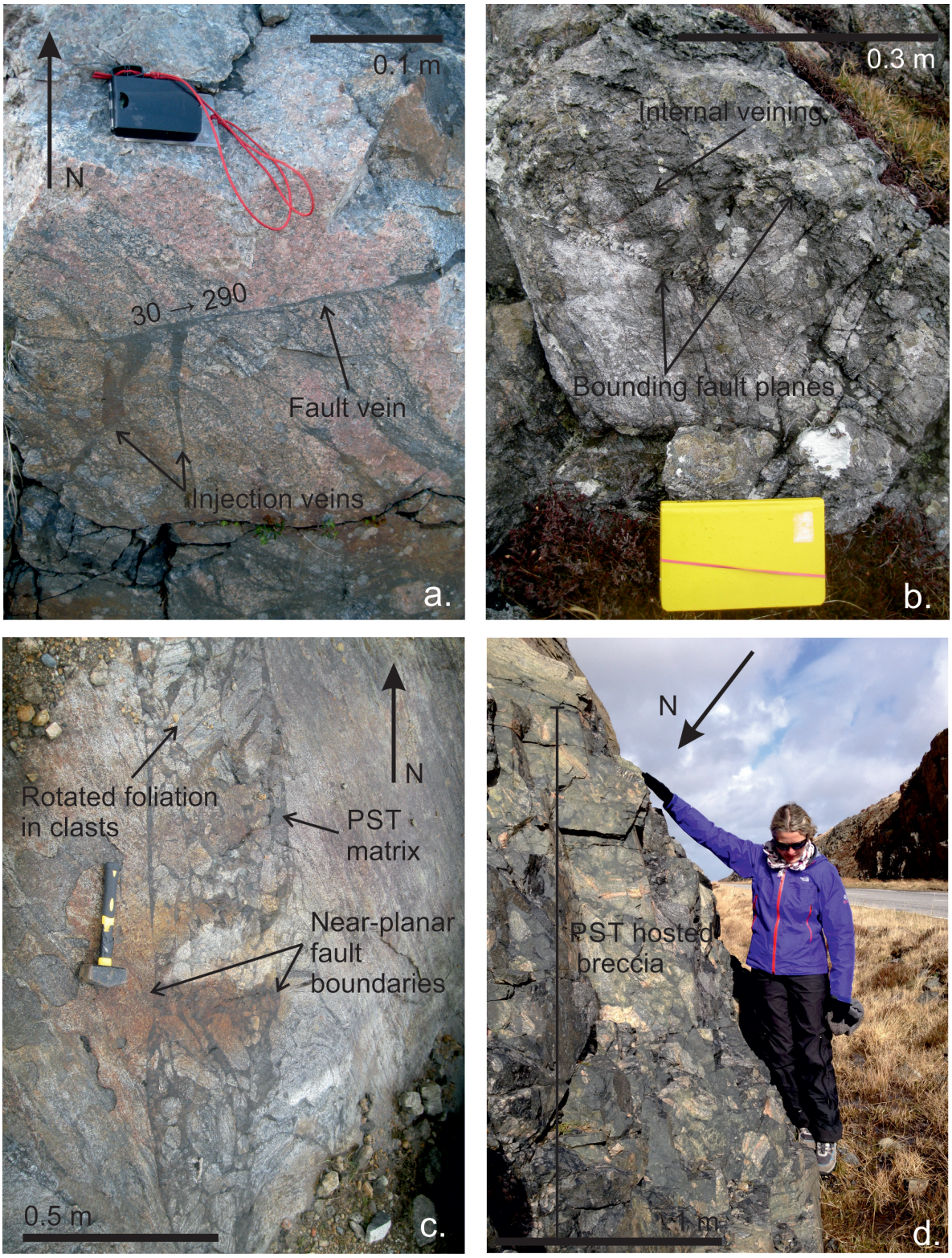

Figure 3.1: Field examples of various pseudotachylyte vein geometries. a. Pseudotachylyte fault vein with injection veins forming into the footwall. Druim Reallasger, North Uist [8613 86662]; b. Pseudotachylyte bearing paired shear zone, Heabhal, Barra [666272 799970]; c. Band of pseudotachylyte breccia, Aisgernis, South Uist [75692 823056]; d.Thick pseudotachylyte breccia, Druim Reallasger, North Uist [86005 866557].

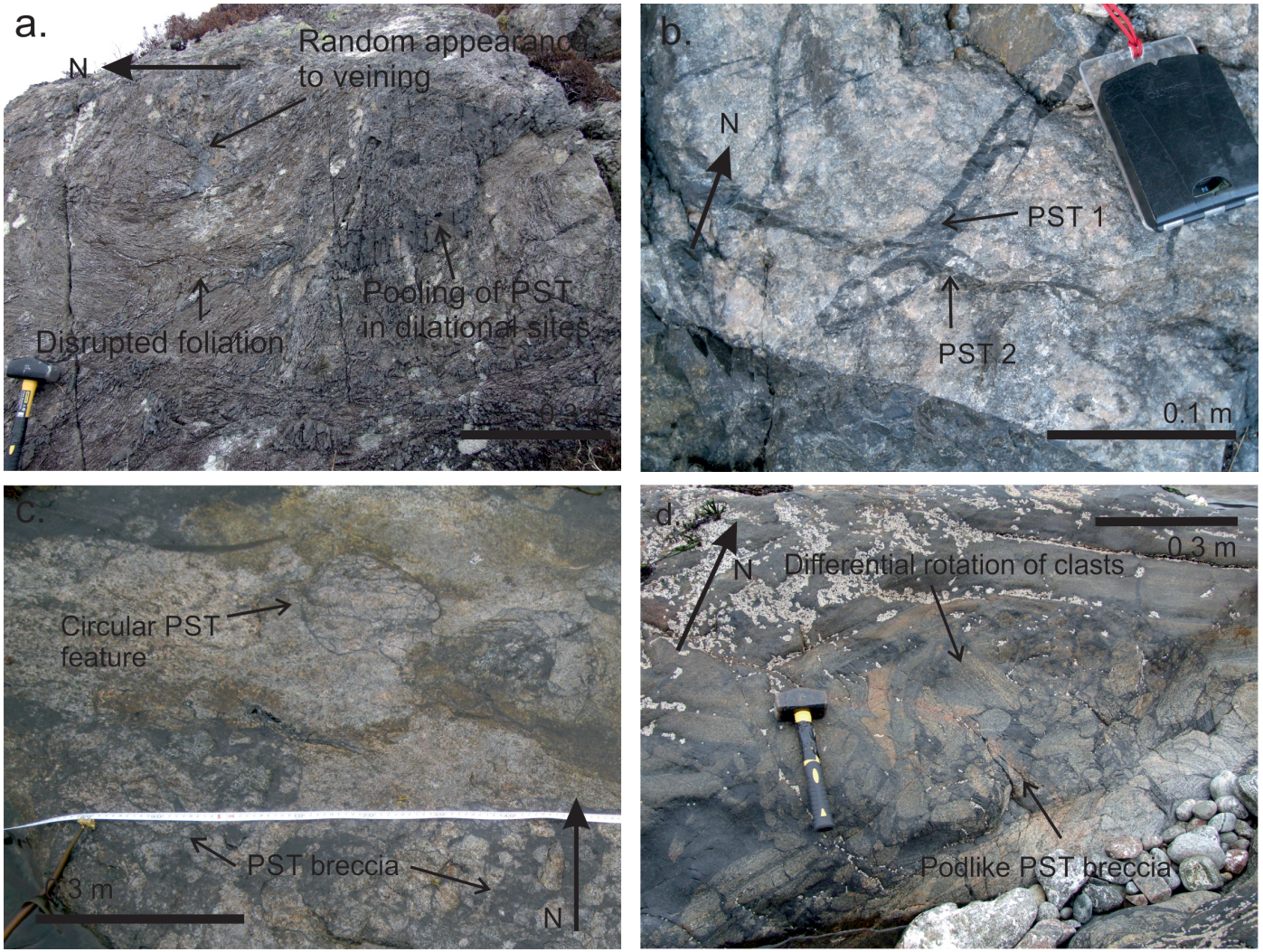

Figure 3.2: Field examples of pseudotachylyte vein geometries: a. Dense network of mixed pseudotachylyte fault and injection veins, Pairc, SE Lewis [13002 91716]; b. Cross-cutting epsiodes of pseudotachylyte (PST), Druim Reallasger, North Uist [86229 866653]; c. Rounded podlike features veined with pseudotachylyte , Áird a' Mhuile, South Uist [71125 829672]; d. Non-planar breccia body, Áird a' Mhuile, South Uist [7116 82957]

plane (Fig. 3.1a). Suites of injection veins and fault veins may occur together in chaotic-looking, densely veined pseudotachylyte networks (e.g. Fig. 3.2a). Non-planar pseudotachylytes also occur and may be curved varieties of the above, or in more extreme occurrences (Figs. 3.2c, 3.2d) may indicate different formation processes to planar variations. The pod-like set of veins in Fig. 3.2c, for example, is similar to a feature attributed to localised explosion associated with fault movement in impact-related pseudotachylyte bearing zones (Thompson and Spray (1992)).

3.3 Vein orientations

This section investigates the dominant pseudotachylyte - bearing fault orientations in the OHFZ, and looks for trends in injection vein orientation within the bulk dataset. These features are mapped out to allow consideration of spatial patterns across the fault zone. The objective is to provide an overview of pseudotachylyte bearing faults in the OHFZ, allowing inconsistencies to be explored in later analysis.

Planar pseudotachylyte features (i.e. fault veins, injection veins, paired shear bands, tabular breccia bodies and injection veins) are measured for dip and dip direction, and plotted as poles to planes on equal area stereonets using OpenStereo software (v 0.1.2, Grohmann and Campanha (2010)). Contours were constructed using the Kamb method on a 'low' grid density and a 250 step natural neighbour method.

Figure 3.3a shows the pseudotachylyte generation plane dataset. There is a cluster of fault veins that dips shallowly to moderately between NE through to SE, with 45% dipping between 000° and 090° (Fig. 3.3b). The mean dip direction is 051° and the modal dip direction is between 070-080°. Injection veins display a more scattered distribution (Fig. 3.3c). Broadly they define two sets dipping moderately to steeply towards the SE or the NW, which fits with the common observation that injections form at a high angle to the fault vein population (e.g. Sibson (1975), Grocott (1981), Di Toro et al. (2005a)) which were seen in Fig. 3.3a.

3.3.1 Variation along strike

The OHFZ can be split across the trace of the South Harris Shear Zone into the 'Northern' and 'Southern' sections (Butler (1995)). Fig. 3.4 shows that between these northern and southern sections, there is no appreciable difference in the distribution of fault vein orientations (Fig. 3.4a). However, there does appear to be some contrast in the injection vein distribution (Fig. 3.4b); where the southern section injections are clustered dipping more steeply NW and SE, the northern section injections, whilst scattered, dip more often moderately towards the NE or SW.

3.3.2 Variation between fault zone and country rock

Measurements taken in the fault zone are defined as those falling within 0.5 km horizontal distance normal to the basal fault trace in a westerly direction, and within the mapped OHFZ fault rock units or within 1.0 km normal to the basal fault trace in an easterly direction (whichever is furthest), as defined by 1:50 000 BGS mapping (British Geological Survey, 2013). The greater hanging wall distance allows for the development of faults above the mapped basal plane there, as well as the damage zone that occurs in both fault walls (Sibson (1977a)). Pseudotachylyte fault veins within the OHFZ dip predominantly towards the northeast, with maximum clustering at $33 \rightarrow 060$ (Fig. 3.5c). Few breccias have been recorded but two clusters appear, dipping NNE and ENE (Fig. 3.5c). Injection veins within the fault zone are highly scattered with no preferred orientation emerging (Fig. 3.5c).

Data from outside the defined fault zone are also presented for comparison (Fig. 3.5a). From the hanging wall side outwith the fault zone, few data are available, although pseudotachylyte veins (both fault veins and undifferentiated) tend to dip eastwards. Data from the footwall are more extensive due to the greater onshore outcrop west of the mapped fault zone. Fault veins across the footwall dip between NE through to ESE, predominantly at angles of 25 - 30° (Fig. 3.5a). This distribution is similar to that of fault veins within the fault zone and additionally the orientations of hanging wall fault veins too (Fig. 3.5). Also seen

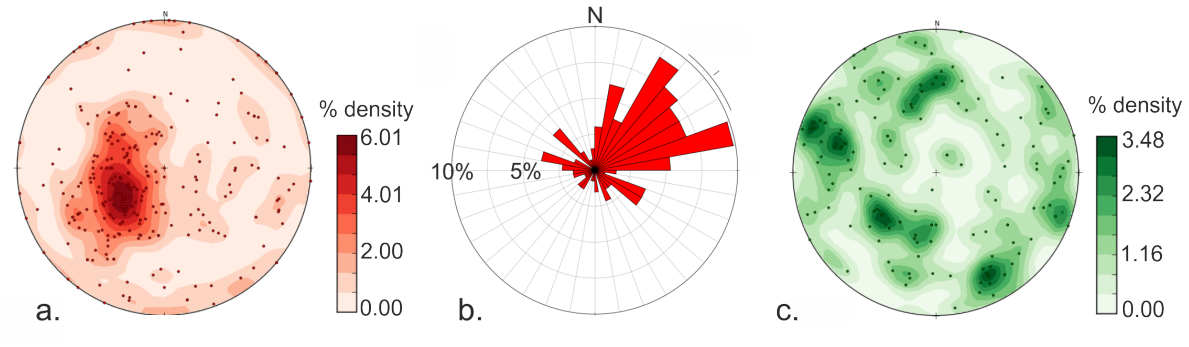

Figure 3.3: OHFZ orientations of pseudotachylyte veins: a. generation planes, poles to planes (n=278); b. Fault veins dip direction, rose diagram (n= 187); c. Injection veins, poles to planes (n=148).

in the footwall fault vein distribution is a loose cluster of SW to WNW dipping veins (Fig. 3.5). Many of these veins are located on Grimsay and are discussed in greater detail below. The SW dipping cluster of breccias reoccurs through the footwall, with the maximum density dipping 16 → 120. Although this orientation is dissimilar to the main cluster of fault veins in the footwall, it still falls within the wider range of occurrences. Footwall injection veins define two sweeping girdles dipping steeply towards the SE and the NW. This is in contrast to the injection veins within the fault zone (Fig. 3.5a), which rarely dip steeply in these directions. An additional cluster of injection veins dips moderately towards the NE.

3.3.3 Selected localities

As pseudotachylyte veins occur widely around the Western Isles, and not just within the mapped trace of the OHFZ, it is possible that one or more phases of pseudotachylyte generation occurred at different times and in different kinematic regimes to that normally associated with OHFZ movement. Pseudotachylyte orientations can be used to compare locations of high pseudotachylyte density outside the mapped trace of the OHFZ with those within the fault zone itself, to identify any structures of clearly different orientation.

The isle of Grimsay, between Benbecula and North Uist, exposes some pseudotachylyte bearing small faults in road-cuttings (e.g. [87100 855344, 85635 856193]). Fault veins of pseudotachylyte in some exposures dip between SW and NNW (Fig 3.6d), orientations rarely

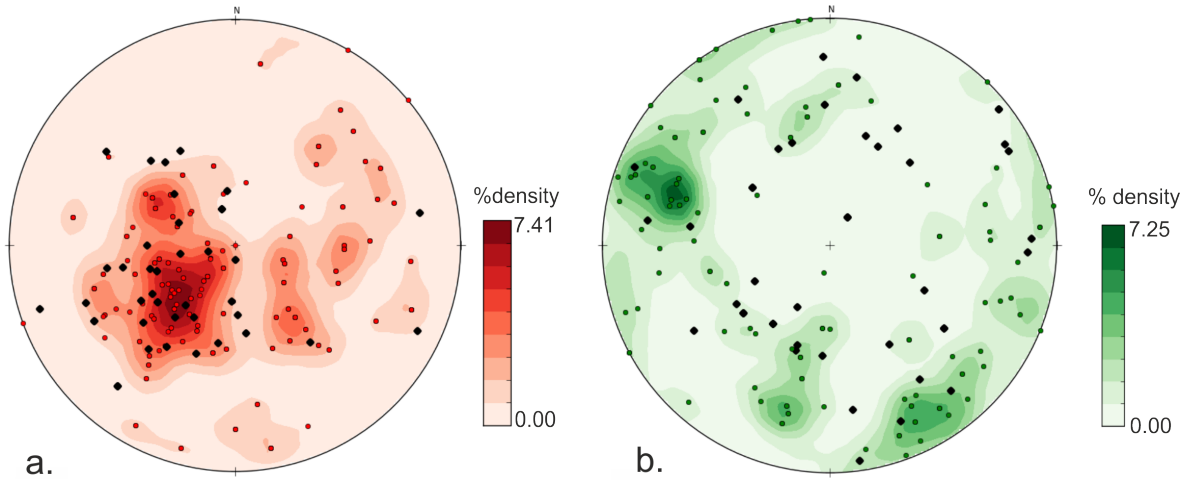

Figure 3.4: Comparison of orientations of pseudotachylyte generation planes and injection veins between the Northern and Southern sections of the OHFZ. a. Pseudotachylyte generation planes from Southern (dark red points, contoured, n = 219) and Northern (black points, n = 42) sections: b. Pseudotachylyte injection veins from Southern (light green points, contoured, n = 122) and Northern (black points, n = 43) sections. All points poles to planes.

seen in other areas studied. Although the basal fault of the OHFZ lies to the east of the studied exposures, forward propagating thrusts are mapped through this area (Fettes et al. (1981)). On examination of pseudotachylyte bearing faults, reverse offset of markers in the gneiss can be observed, confirming that pseudotachylyte generation here appears to be linked to top-to-the-SE thrusting on metre scale faults.

Abundant pseudotachylyte fault veins and large metre scale breccia bodies are exposed in a roadcut at Druim Reallasger, North Uist [86002 866553] (e.g. Fig. 3.1a,d). Again, this site sits >5 km westward from the basal trace of the OHFZ (fault perpendicular distance ∼ 2.5 km). These fault veins and breccia bodies dip consistently 20-30° towards the NE and injection veins dip steeply towards the ENE and WSW (Fig. 3.6a). Slip appears to be slightly oblique to the fault dip, as indicated by the injection vein orientation (Fig. 3.6a).

Pseudotachylyte is frequently observed on the west coast headlands of the southern isles of Barra and South Uist, where it forms dense arrays of breccias, fault veins and injection veins (e.g. Figs. 3.2d,e, 2.3b). Fault veins in this area dip between SE and NE with the more scattered orientations tending to dip back towards the NW through W to SW (Fig.

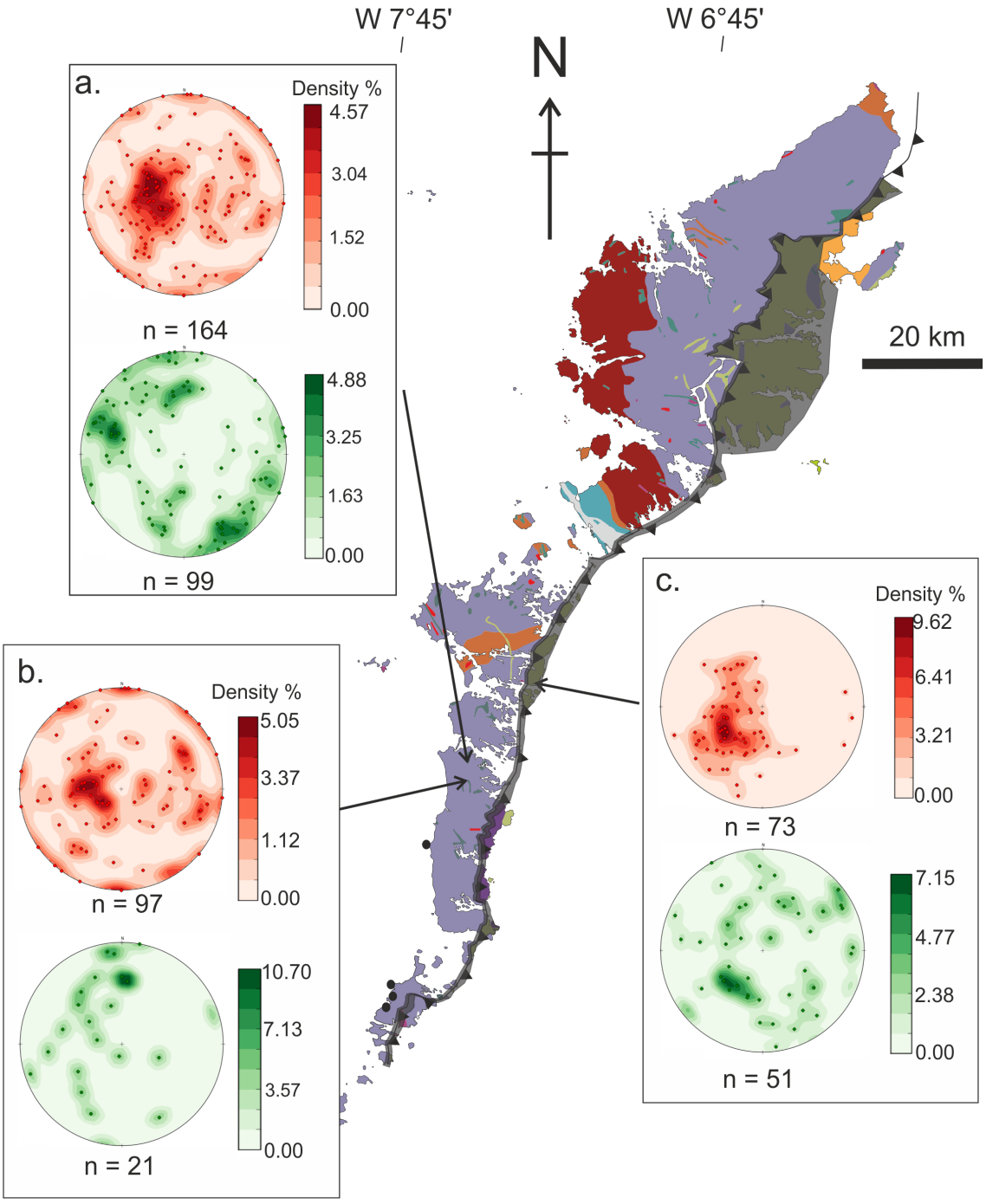

Figure 3.5: Orientations of pseudotachylyte generation planes (red points) and injection veins (green points) from: a. footwall of the OHFZ; b. footwall of OHFZ with data from west coast high pseudotachylyte volume localities removed (locations shown by black circles); c. mapped trace of OHFZ plus damage zone, as shaded on map. All points poles to planes.

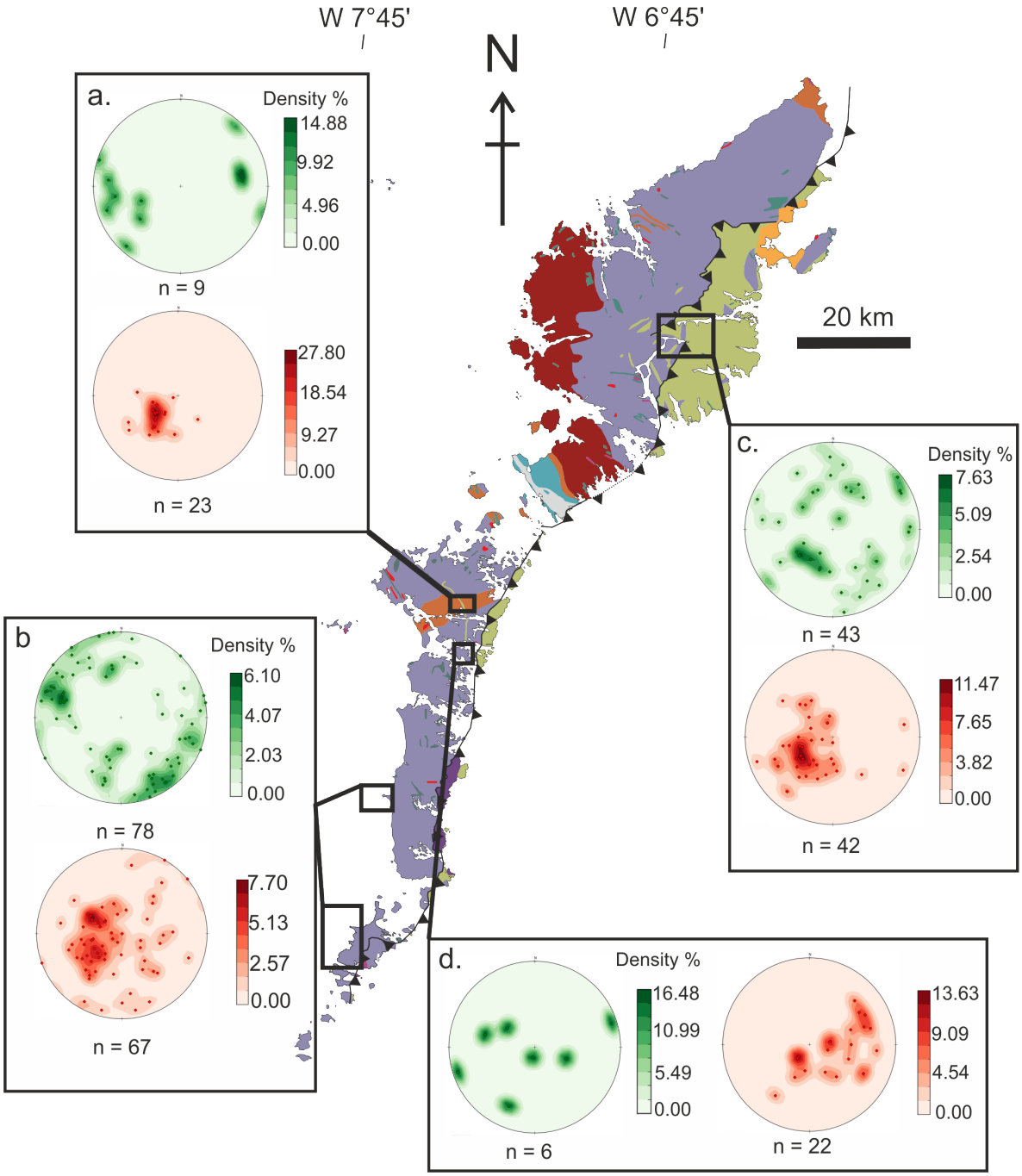

Figure 3.6: Orientations of pseudotachylyte generation planes (red points) and injection veins (green points) in selected Western Isles localities, including: a. A687 roadcut, Druim Reallasger, North Uist; b. 'West coast' localities including Bagh Halaman, Allathasdal, Aird Ghrein (all Barra) and Aird a' Mhuile (South Uist); c. SE Lewis (Pairc district) mylonitic zone; d. Grimsay. All points poles to planes.

3.6b). The orientation of the main easterly dipping fault vein cluster is therefore similar to fault vein distributions seen across the rest of the footwall and into the mapped fault zone of the OHFZ. Tabular breccia bodies are frequently well-exposed along these low-lying coastal localities and tend to dip towards the E or SE. Injection veins form steeply dipping SE and NW orientations. The large amount of data available from these localities has influenced the footwall subset seen in Fig. 3.5a. To compare these west coast localities with the 'background' orientations in the rest of the footwall, the footwall dataset is displayed again with the west coast data removed (Fig. 3.5b). Footwall injections tend to dip more shallowly towards the east than the west coast injections, and there are few westerly dipping examples compared to the west coast. Footwall breccias are in general more scattered than on the west coast, but the fault vein orientation is similar. These fault zone dips are also similar to those of the fault zone, albeit with the additional westerly dipping faults on the west coast.

3.3.4 Initial interpretation of pseudotachylyte fault orientations of the OHFZ

Pseudotachylyte in the OHFZ occurs on a wide range of fault dip directions, including a prominent E to NE dipping set. This is an expansion of the SE-ESE range expected from the regional scale structure of the OHFZ (Smythe et al. (1982)). There is no particular difference in orientation of pseudotachylyte veins between the 'Northern' and 'Southern' sections of the OHFZ (Fig. 3.4). Nor is there a division in pseudotachylyte orientations between the core of the fault zone and the footwall block of the eastern trace of the OHFZ, although the orientation of injection veins is less consistent in the hanging wall (Fig. 3.5). Within individual localities, more clustered distributions of injection veins exist, which may indicate the dominant slip direction of faulting, ideally normal to the injection veins (e.g. Swanson (1988)).

3.4 Host rock controls on pseudotachylyte faulting

As highlighted in section 3.3, pseudotachylyte faults in the OHFZ have a variety of orientations other than the SE to ESE dip usually associated with the OHFZ on a regional scale (e.g. from seismic surveys, Smythe et al. (1982)). This section therefore considers mechanisms that could potentially influence the orientation of pseudotachylyte -bearing faults in the OHFZ. One is the foliation present in the host rock, the Lewisian gneiss, and the other is a systematic pre-existent fracture system such as Riedel shears. Again, orientation of pseudotachylyte faults and veins are compared to foliation and expected Riedel configurations, to investigate if fault orientations are a feature of inheritance rather than reflecting the stress field(s).

3.4.1 Foliation

3.4.1.1 Approach and methodology

The dip of the OHFZ varies along strike, but on average is 20-30 ° towards the east to southeast. This dip is derived from observations made on non-pseudotachylyte bearing fault planes exposed within the OHFZ. In contrast, pseudotachylyte fault veins have a tendency to dip northeastwards as well as towards the east and southeast (Fig. 3.3a). Whilst this overlaps with part of the range of OHFZ faults, it is curious why many pseudotachylyte faults apparently favour a northeasterly dip. One reason for this may be that some periods of fault development fell under the control of other structural features, for example reactivating older, misaligned faults or by following the gneissic foliation. Faulting and fracturing may preferentially occur along foliation planes depending on the orientation of the foliation relative to the stress field, and the strength of the foliation plane relative to the strength of the whole rock (Fossen (2016)). This section investigates whether foliation planes influence the orientation of smaller OHFZ faults through a comparison of foliation and pseudotachylyte fault orientations.

The folded foliation in the Lewisian Complex is formed by gneissic mineral banding related to the Laxfordian tectonothermal event (Davies et al. (1975)). Therefore, foliation in

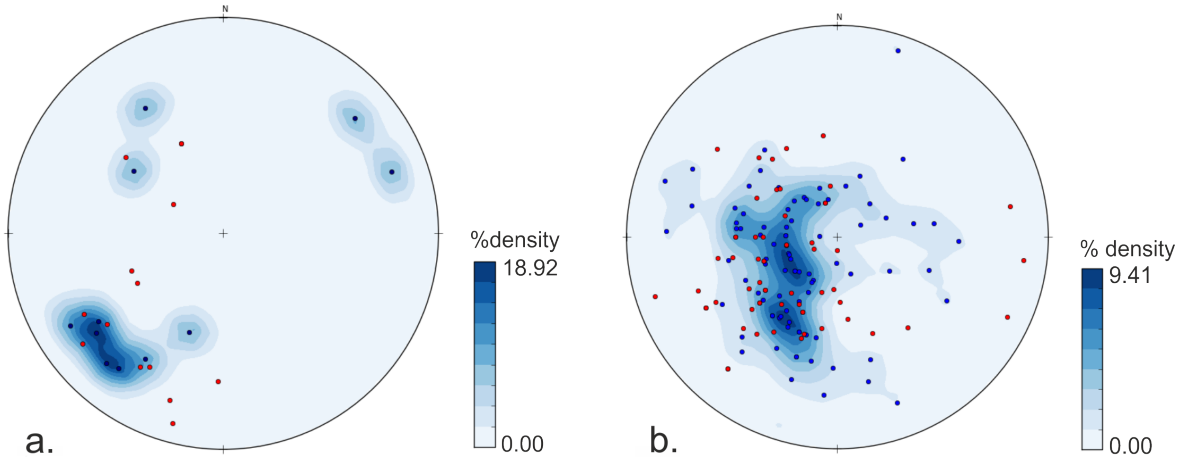

Figure 3.7: Comparison of pseudotachylyte generation planes (red points) and foliation (blue points, contoured) within the mapped OHFZ (see shaded area of Fig. 3.5) in: a. Footwall within the fault zone (foliation n=11, pseudotachylyte generation planes n=14); b. Hangingwall within the fault zone (Foliation n = 87, pseudotachylyte generation planes n = 59). All points poles to planes.

the Western Isles is both variable and unrelated to the OHFZ except where mylonitic foliation has developed, for example in SE Lewis (Fig. 2.3b).

3.4.1.2 Results

In the footwall to the fault zone, pseudotachylyte generation planes are distributed similarly to the foliation, with fault veins orientated close to the steeper NE dipping foliations (Fig. 3.7a). The hangingwall side of the fault zone, meanwhile, is characterized by a greater range of foliation dips, many of which trace a great circle consistent with the regional NW-SE fold axial planes, although it is not clear why this should be represented in the hangingwall and not the footwall (Fig. 3.7b). Despite these variations, pseudotachylyte generation plane orientations do again coincide with the foliation range, though they also show the scattered NE through to SE dipping range that is common to many of the local subsets.

To refine the comparison of foliation and pseudotachylyte faulting orientations, individual generation planes were compared to the immediate local foliation of the host rock. From Figure 3.8a, which shows the acute angle between tabular pseudotachylyte breccias and the

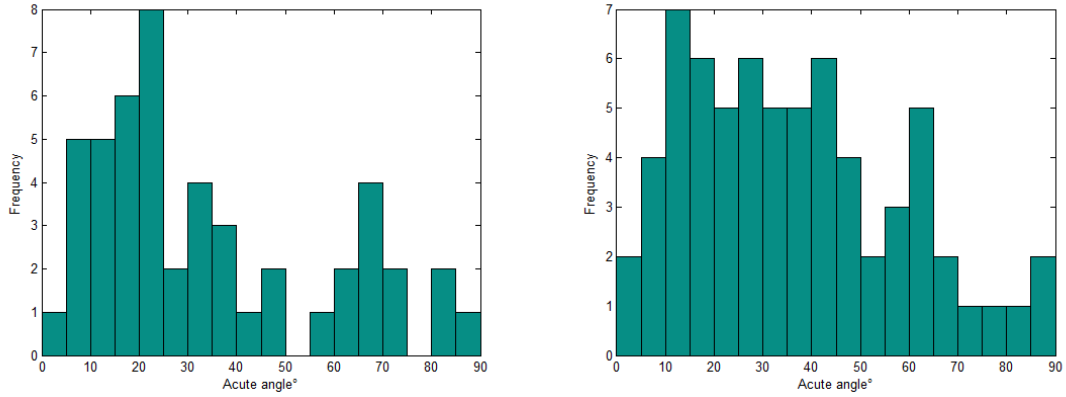

(a) (b)

Figure 3.8: Angular relations between pseudotachylyte generation planes and local foliation: a. Acute angle between pseudotachylyte breccia and local foliation (n=49); b. Acute angle between pseudotachylyte fault veins and local foliation (n=67)

surrounding foliation, it can be seen that many breccias are not parallel with the foliation and indeed often display a discordance of >10° (Fig. 3.8a). However, 51% form an angle of <25° with the foliation with a modal angular difference of 20-25°, though the mean is 34.2°. Fault veins form a broader distribution (Fig. 3.8b) but tend not to form at angles >65°. These data do not support control of pseudotachylyte generation plane orientations by foliation in general. The modal range of angular difference is 10-15° and the mean is 36.2°, slightly higher than for breccias.

3.4.2 Riedel shear systems

3.4.2.1 Approach and methodology

Another regional scale system that could exert control on orientation of pseudotachylyte veins would be a pre-existing fracture system that might produce faults at various orientations liable to reactivation, and that would allow injection into non co-seismic fracture directions. An example that would produce predictable orientations would be a system of Riedel-type shears associated with prior movement on the OHFZ. Idealised Riedel systems can be predicted given the dip and slip direction of the main fault, and the estimated strength of the rock. R, R', P and T planes are predicted for dip slip, left-lateral and right- lateral movement on a SE

dipping fault plane estimated at 20→120. These orientations are based on a modal average of fault plane orientations measured during this project. The angle of internal friction, ϕ, was calculated as 35.37 from a coefficient of friction, μ, of 0.71, given by Jaeger (1959) as a value for dry gneiss. The various planes were then defined as shown in Fig. 3.9 using the angular relationships given in Flodin and Aydin (2004).

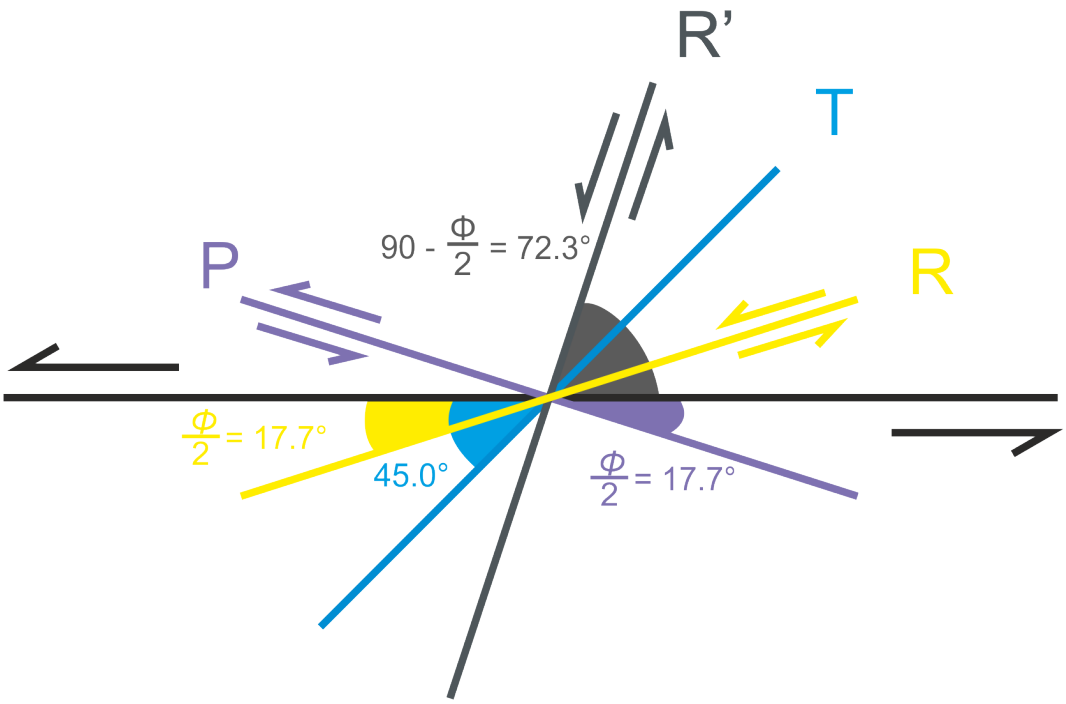

Figure 3.9: Predicted angles for Riedel-type shear plane development using relative angular relations from Flodin and Aydin (2004) and $\phi = 35.37$ (Jaeger 1959).

3.4.2.2 Results

The great circles of the calculated planes, and their poles, are shown in Figs. 3.10. Initially calculated for dip slip movement with a reverse sense, Fig. 3.10a superimposes measured pseudotachylyte generation planes and Fig. 3.10b superimposes measured pseudotachylyte injection veins. This dip-slip configuration of Riedel planes forms an array dipping with variable steepness towards the SE or NW, and while there may be generation planes that correspond to these planes, they cannot explain the cluster of pseudotachylyte generation planes that dip more towards the NE. Imposing strike slip movement on the same fault plane

produces Riedel planes dipping towards NE to SE (in the left lateral case, Fig. 3.10c-d) and SE to SW (in the right lateral case, Fig. 3.10e-f). Left lateral slip in particular produces planes that cover much of the same range as the broad cluster of measured pseudotachylyte generation planes (Fig. 3.10c). Injection veins might be expected to exploit pre-existent fracture planes, but the scatter of the injection data makes it difficult to match to any Riedel planes. However, in the left-lateral slip case, the T pole does coincide with a cluster of NE dipping injections.

An additional approach considers the angles between injection veins and their parent fault veins, where exposed. A histogram of acute angles between injection veins and their melt-generating fault vein is shown in Fig. 3.11. The modal angle is 80-90° and the mean 59.3°, showing a negatively skewed distribution that includes all possible angles over 10°. As Fig. 3.9 shows, the ideal angles that Riedel-type fractures should make with their parent shear plane are 17.7°, 45° and 72.3° for R and P shears, T fractures and R' (or X) shears respectively. Considering Fig. 3.11, the modal peak at 40-50° could therefore correspond to a T-shear orientation. A high number of injections also occur in the 70-75°, covering the 72.3° R' shear angle. Assigning these injection orientations (excluding T fractures) to the presence of Riedel shears, however, implies shear movement along the injection plane. The Riedel controlled examples should therefore be distinguishable by displacement.

3.4.3 Initial interpretation of host rock controls on fault orientation

Although many pseudotachylyte bearing faults may superficially appear foliation parallel in the field, in keeping with the bulk dataset comparison (Fig. 3.7), they are rarely exactly parallel when measured against the immediate foliation orientation (Fig. 3.8). It is therefore implied that pseudotachylyte faults do not exploit weak foliation planes and that this is not the reason why many pseudotachylyte faults dip northeastwards. The projection of the Riedel shear system is used to test whether a predictable fracture system could be already in place during pseudotachylyte -producing seismicity, so that fault planes and/or injection veins were encouraged to exploit pre-existent fractures in predictable orientations. Only if left-lateral strike slip movement along the regional OHFZ is envisaged do the various Riedel

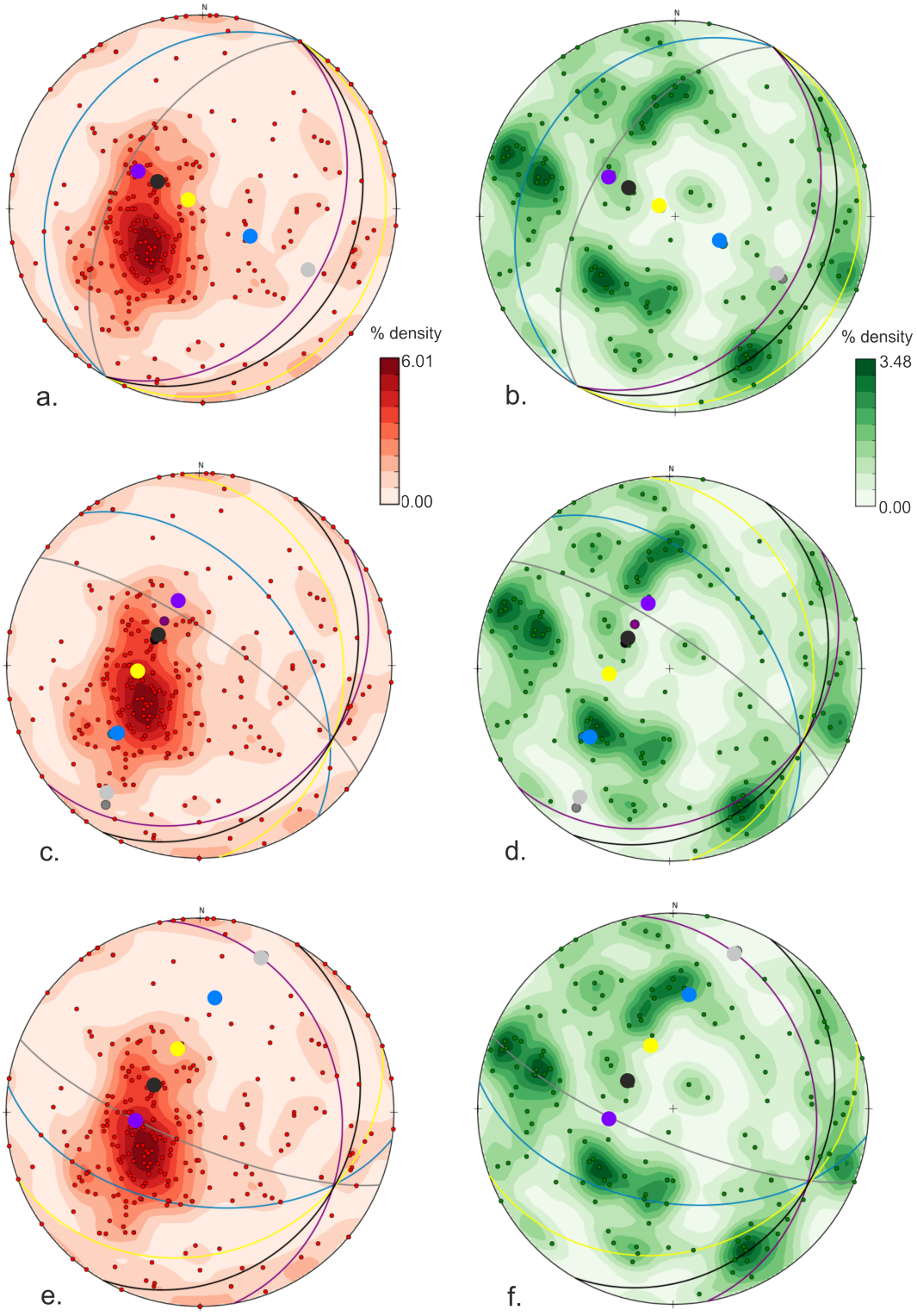

Figure 3.10: Comparison of idealised Riedel shear orientations (shown as both great circles and planes: black = averaged fault plane; yellow = R shear; blue = T fracture; purple = P shear; grey = R' shear) with pseudotachylyte generation planes (dark red poles and contours, n=278) and pseudotachylyte injection veins (green poles and contours, n=141). a.-b. show Riedel configuration based on a reverse (thrust) dip slip movement; c.-d. show Riedel configuration based on left lateral strike slip movement; e.-f. show based on right lateral strike slip movement.

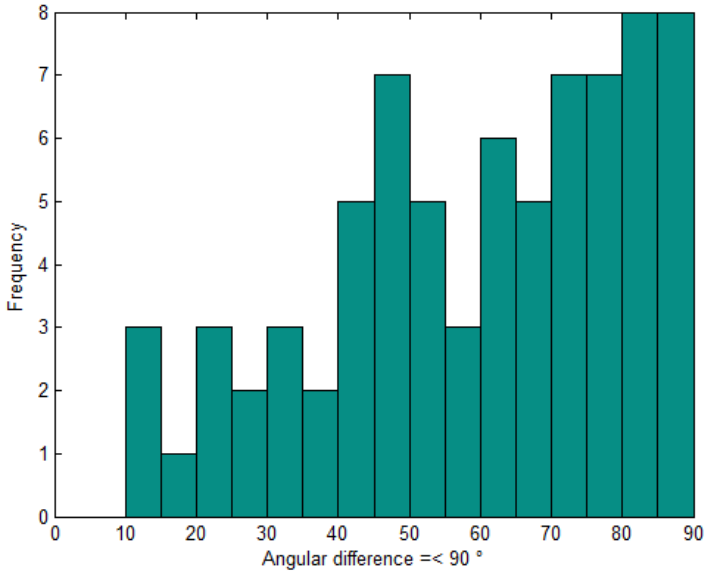

Figure 3.11: Acute angular difference between injection veins and their parent generation plane (n=75)

shears mimic the spread of the fault veins (Fig. 3.10), but this is not necessarily a causative effect. If regional oblique slip were invoked, any number of orientations could be covered depending on the balance of strike and dip slip. Pseudotachylyte in Riedel-type geometries between paired shears are observed in the OHFZ on the metre-scale, so it is not impossible that other pseudotachylyte faults measured here could fall under similar influence. However, it is unlikely to control the orientation of the complete fault vein orientation dataset.

3.5 En echelon pseudotachylyte arrays

Slip directions of pseudotachylyte faults are important to obtain if the history of seismicity in any fault zone is to be understood. Direct field evidence for the direction of fault offsets is unfortunately uncommon in the OHFZ, so that new approaches to deriving the trend of slip must be attempted. This section sets up a model to explain the observations of en echelon arrays of pseudotachylyte injection veins in the OHFZ. The model allows further inference of the slip direction and stress field during pseudotachylyte - generating seismic faulting.

3.5.1 Approach and methodology

In several localities around the Western Isles, linear arrays of segmented pseudotachylyte veins may exhibit en echelon characteristics (e.g. Fig. 3.12a). As no displacement is observed associated with individual veins or with the overall array, these veins are classified here as injection pseudotachylytes in tensile fractures. The long axis of individual veins may be parallel to, or at an angle with, the trend of the overall array. Curved vein tips are frequently observed where they approach or overlap with the adjacent vein (Figs. 3.12a, 3.13a), implying interaction via the modified tip stress fields (Pollard and Aydin (1984)). Some arrays are less well defined, with diffuse areas of parallel injection veins forming an array with uncertain trend (Fig. 3.12b). The stepping direction of individual segments is not always consistent within any one array. Occasionally these en echelon arrays cross-cut (Fig. 3.13a), suggesting that pseudotachylyte may have been generated in two or more differing stress fields.

These vein geometries correspond to models of fracturing and dyking (e.g. Pollard et al. (1982)) where a mode I tensile fracture may branch into twisted en echelon segments ahead of its propagating tip (Fig. 3.14). The twist is enforced by a rotation of the principal stresses around an axis parallel to the propagation direction of the parent fracture, the tip of which may experience mixed mode I/III shearing (Pollard et al. (1982)). The twist occurs in the direction that facilitates opening of the en echelon segments into the remote σ_3 direction; the opening direction of the segments is hence assumed to be perpendicular to the fracture walls (Hoek (1991)). The angle of twist, however, may be in reality less than the angle between the remote principal stress σ_3 direction and the opening direction of the parent fracture (Pollard et al. (1982)).

En echelon pseudotachylyte vein geometries have been noted before (Sibson (1975), Hoek (1991)) but have not so far been analysed as a structural feature of pseudotachylyte faults. To apply the fracture based en echelon models to pseudotachylytes, the parent fracture is assumed to be an injection vein, dominated by mode I propagation. This parent injection vein is rarely observed in the field in association with an visible en echelon array, but an

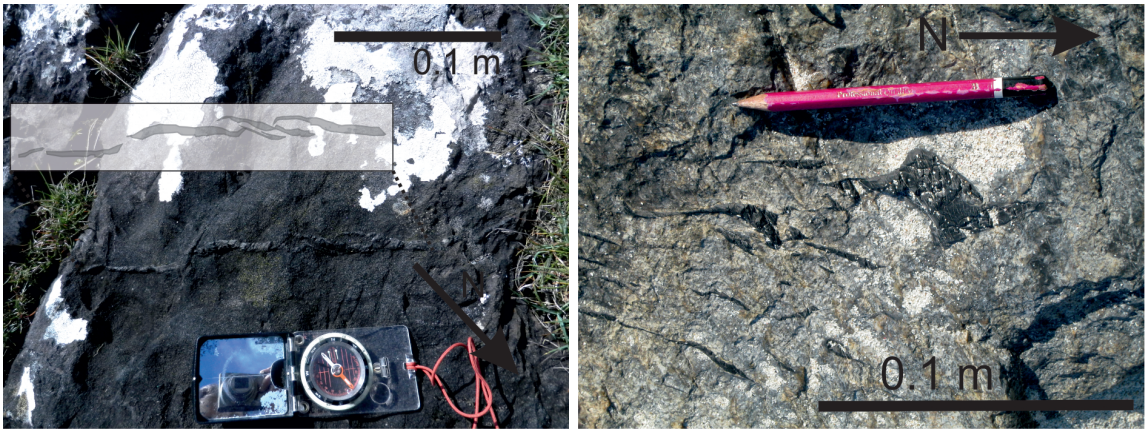

(a) (b)

Figure 3.12: Examples of en echelon pseudotachylyte injection vein arrays; a. Linear array of en echelon pseudotachylyte injection veins, Barra [70537 799802]; b. Diffuse array of en echelon pseudotachylyte veins, Barra [65687 803437]

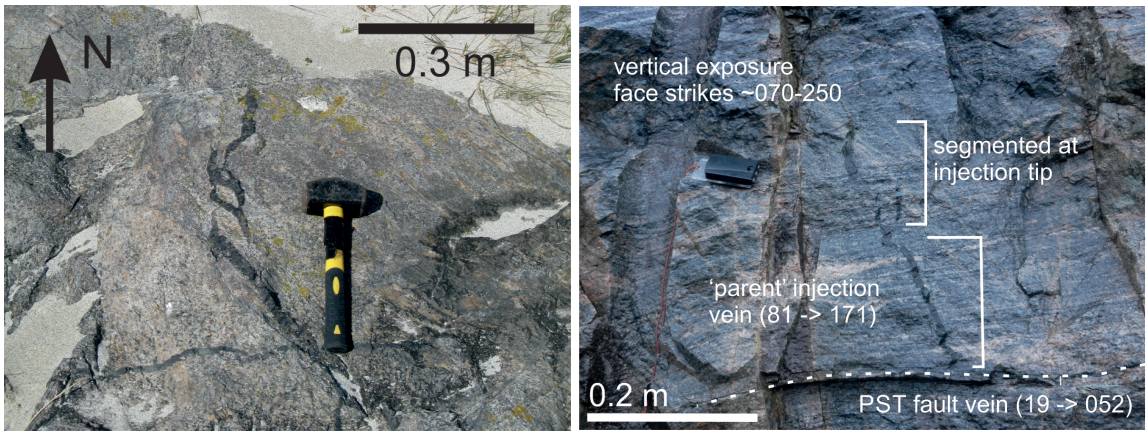

(a) (b)

Figure 3.13: a. Cross cutting arrays of en echelon pseudotachylyte injection veins, Barra [66008 803981]; b. Rare field example of segmenting injection vein seen with pseudotachylyte generating fault plane. Although the injection vein segmentation at the tip appears to be in the wrong plane for the model (Fig. 3.14), the misalignment of the exposure plane with regards to the dip and dip direction of the injection vein might alternatively cause segmentation parallel to the injection strike to be exposed in this way

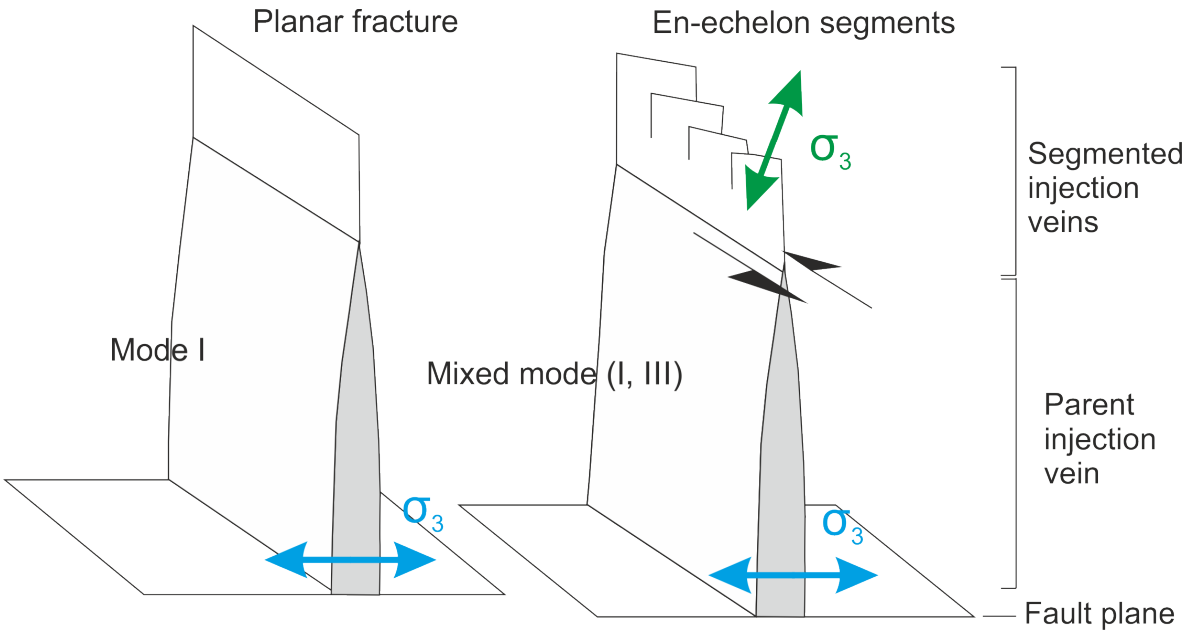

Figure 3.14: Model of en echelon fracture formation at tip of parent fracture. Stress field is reorientated around axis parallel to propagation (adapted from Clemente et al. (2007))



Figure 3.15: Hand specimen of pseudotachylyte vein showing splitting of single injection vein (note lack of offset) into en echelon branches

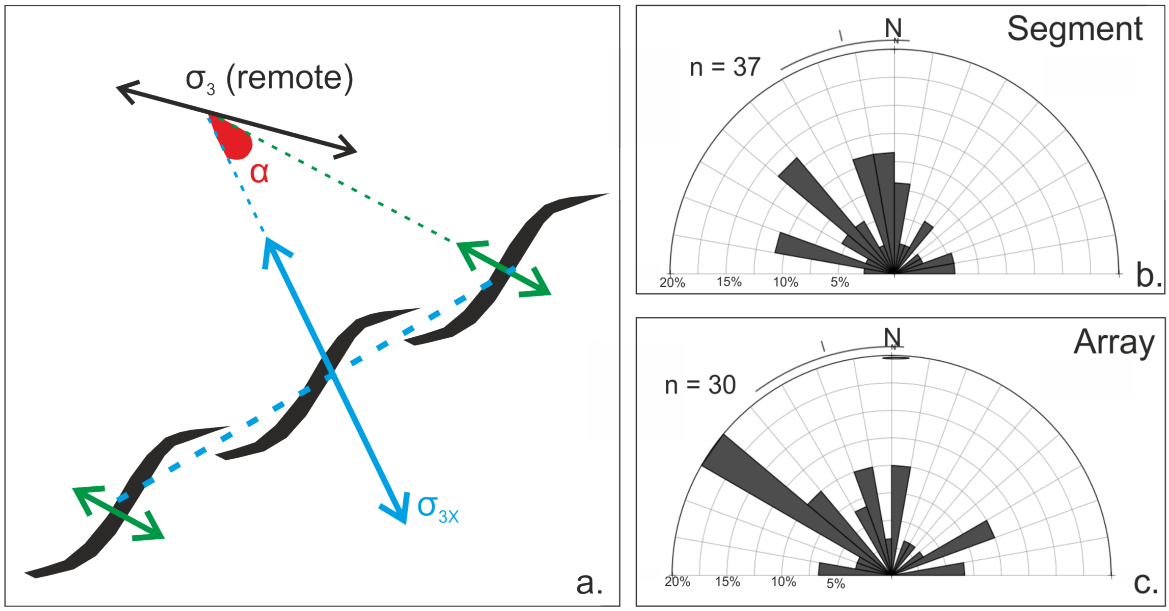

Figure 3.16: a. Schematic model showing relationship between opening direction of pseudotachylyte array, the opening direction of individual vein segments, and the remote minimum stress, assuming horizontal surface. The angle between the remote σ_3 and the local σ_{3x} may be greater than the calculated angle α; b. En echelon segment opening directions (n=37); c. Array opening directions (n=30).

example is seen in Fig. 3.13b and the continuity of a single injection vein branching into en echelon segments is seen across a pseudotachylyte bearing quartzofeldspathic gneiss pebble in Fig. 3.15. The en echelon segments propagate from the parent vein tip as it begins to branch (Figs. 3.15, 3.14). For each observed array, the strike (and dip, where possible) of the veins are measured, and the trend of the vein array taken. The opening directions are taken as normal to the margin of the vein segments and perpendicular to the trend of the vein array - the latter represents the opening of the parent injection vein (Fig. 3.16).

The opening of systematic pseudotachylyte tensile injection veins is thought to be controlled by the transient coseismic stress field at the propagating tip of the generation plane (Griffith et al. (2009b), Ngo et al. (2012), see Fig. 3.19), the assumption here being that these pseudotachylytes were not injected into pre-existent fractures. As the seismic fault tip propagates onwards from the created tensile injection, the influence of the fault tip transient

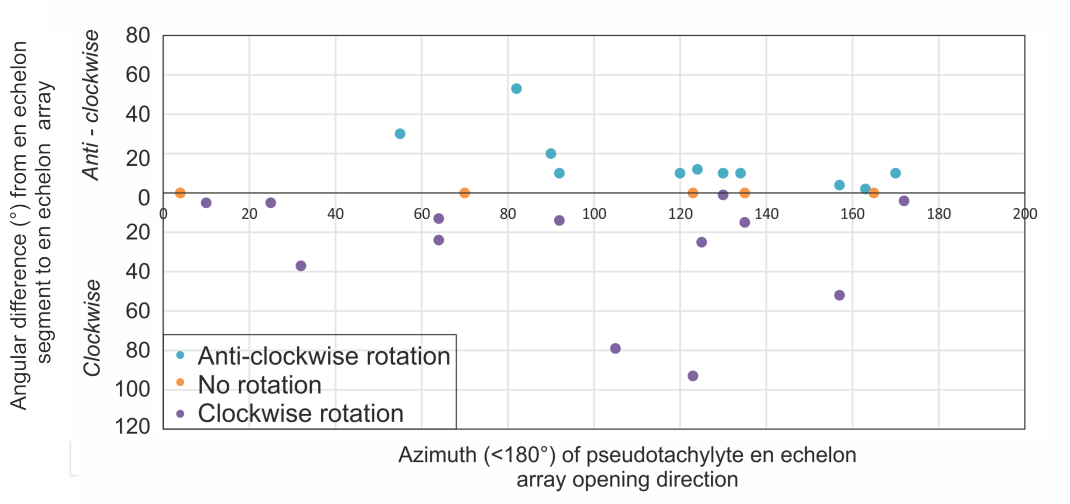

Figure 3.17: Direction and angle of rotation of en echelon array from individual segments, by opening trend of array (n=30)

stress field would be expected to diminish and the remote, static stress field once more become dominant. It is proposed here that this model can be combined with the en echelon fracture models (Fig. 3.14) for pseudotachylyte veins to create a coseismic, dynamic fracture model whereby the initial parent injection vein (Fig. 3.14) is initially subject to the coseismic fault tip stress field. As both the fault plane and the tensile injection offshoot propagate, the tip of the injection becomes spatially removed from the transient influence of the fault tip stress field, and so further tensile opening is increasingly influenced by the remote stress field, causing the twist and apparent shear. Hence the opening direction of the parent injection is thought to represent the rupture direction of the seismic slip, but the opening direction of the segmented injections is closer to the remote principle stresses, and should approach the orientation of the minimum principal stress σ_3. The angle α between the two opening directions is recorded as negative if the parent vein lies clockwise from the segments, and positive if it lies anti-clockwise. Clockwise rotation suggests left lateral shear (e.g. Fig. 3.16a) and anticlockwise, right-lateral shear. This method uses only two dimensions and, since many observations are from horizontal surfaces where the veins dip steeply downwards, is biased further towards an analysis restricted to the horizontal plane.

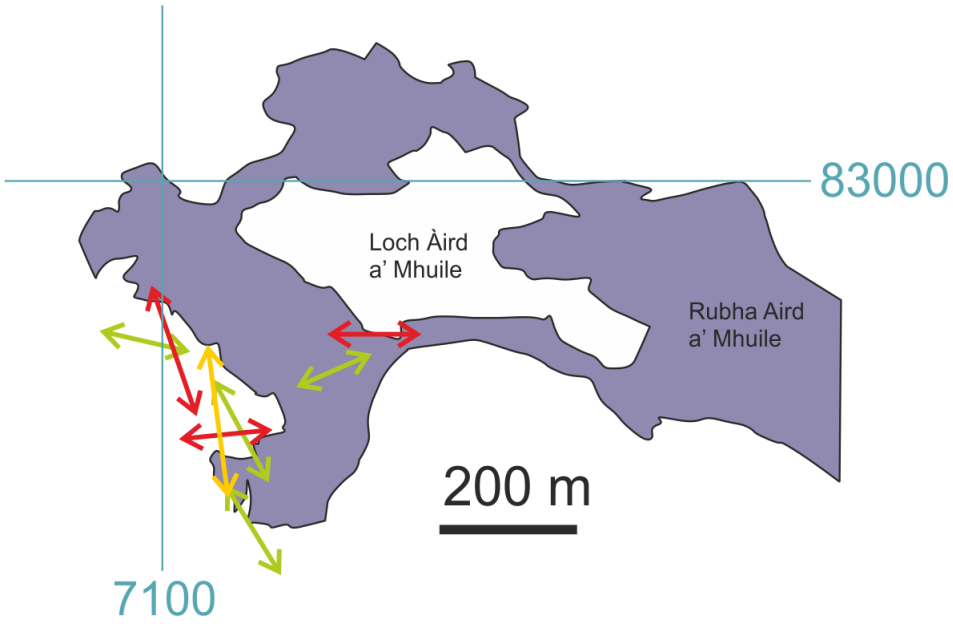

Figure 3.18: Map of Áird a' Mhuile, South Uist, showing direction of en echelon array opening directions (arrows) and direction of rotation of array relative to segments (green = clockwise, red = anti-clockwise, yellow = no rotation). Grid lines from British National grid are shown (Map data ©NERC 2015).

3.5.2 Orientations of local and regional stresses

The orientations of pseudotachylyte array trends and their constituent segment opening directions (Fig. 3.16a) were taken from 38 en echelon pseudotachylyte injection arrays from across the OHFZ. Rose diagrams displaying the opening directions of segmented veins and arrays are shown in Fig. 3.16b-c. The modal direction for the array opening direction is 120-130°, whereas segment opening directions have modal peaks at 000-010° and 130-140°, with more scatter at intermediate values.

3.5.3 Rotation of stress fields

Fig. 3.17 shows the difference in azimuth between the opening angles of rotated injection segments relative to the array. The number of observations falling into each subset are broadly similar (n=13, n=11 and n=6 for clockwise, anti-clockwise and no rotation respectively). Occurrences that display no rotation have a predominantly N-S opening direction although they also occur with other orientations. In the case that the array opening direction is rotated

anti-clockwise from the en echelon segments, array opening directions with the greatest rotation lie between the trends of 080-170° (or 260-350°) whilst segment opening directions fall between 070 -180° (or 250-000°). In the opposite case, where the array opening is rotated clockwise from the en echelon segments, the array opening directions are much more variable but have a peak in rotation between 120-130° (or 300-310°) and a second, minor peak at 060-070° (or 240-250°). Both arrays with anti-clockwise rotation and clockwise rotation are predominantly orientated $\leq 20°$ from the en echelon segments, although the clockwise rotated arrays show a greater spread of rotation to higher angles. Within any one field locality there is little consistency in opening directions. As can be seen, for example at the Àird a' Mhuile locality in South Uist (Fig. 3.18), arrays with similar orientations closely related in space may show opposite senses of rotation and shear. The additional observation of lack of consistent stepping direction within en echelon arrays might indicate that these arrays are not good representations of apparent shear direction.

3.5.4 Initial interpretation of en echelon pseudotachylyte injection veins

The opening direction perpendicular to the trend of pseudotachylyte en echelon arrays represents the opening direction of the parent injection vein (Figs. 3.14, 3.15). If the parent injection veins forms perpendicular to the transport direction on the fault, as is assumed in many models of pseudotachylyte faulting (e.g. Sibson (1975), Swanson (1988)), and confirmed by experimental and numerical studies (Griffith et al. (2009b), Ngo et al. (2012)), the array opening direction therefore indicates the trend of fault movement. It does not reveal the relative direction of movement between the fault walls. The cause of the twist to the opening direction of the individual en echelon segments within the array is proposed here to be the changing balance between coseismic and farfield stress fields (section 3.5.1). In this case, the opening direction of an individual array segment should approach the farfield minumum stress direction, or at least the minimum stress in the plane perpendicular to the plane of injection. NW-SE slip is dominantly indicated by the array opening directions (Fig. 3.16) but many areas show additional N-S or E-W trends (Fig. 3.18).

3.6 Field kinematic indicators

This section presents evidence used to infer slip directions on pseudotachylyte bearing faults, in order to complement the findings of section 3.5 above. Firstly, an additional model exploiting the orientation of pseudotachylyte injection veins, the off-fault tensile crack theory, is used to derive slip vectors on individual faults. This allows the principle axes of strain rate to be calculated and plotted, allowing grouping of fault slip directions from strain fields. These results are supported by available field and microstructural markers of fault displacement direction, although these are generally not common. Finally, the magnetic structure of a pseudotachylyte vein matrix is analysed for an additional indication of the slip direction.

3.6.1 Pseudotachylyte injection veins

3.6.1.1 Approach and methodology

The dynamic coseismic stress field localised around the propagating rupture tip has been observed to produce secondary tensile cracks (i.e. injection veins, in a pseudotachylyte system) of predictable inclination and orientation through experiments on analogue materials (Griffith et al. (2009a)), numerical modelling (Ngo et al. (2012)), and pseudotachylyte field observations (Di Toro et al. (2005a)). This is known as the off-fault tensile crack model, as used by Ngo et al. (2012). In all cases, these tensile fractures are observed to form on a single side of the fault - that through which the dynamic tensile field of the crack tip passes - and to form at inclined, but often high, angles to the propagating fault plane. The angle of inclination is controlled by slip velocity, the strength of the fault and of the host rock, the velocity weakening behaviour of the fault and the static stress state (Ngo et al. (2012)), but will form an acute angle to the fault plane that indicates the slip directivity, with the trend of slip perpendicular to the strike of the injection (Di Toro et al. (2005a)). Hence if the orientations of an injection vein and its generation plane are known, along with the knowledge of which side of the fault contains injections, the slip direction can be derived (Fig. 3.19d).

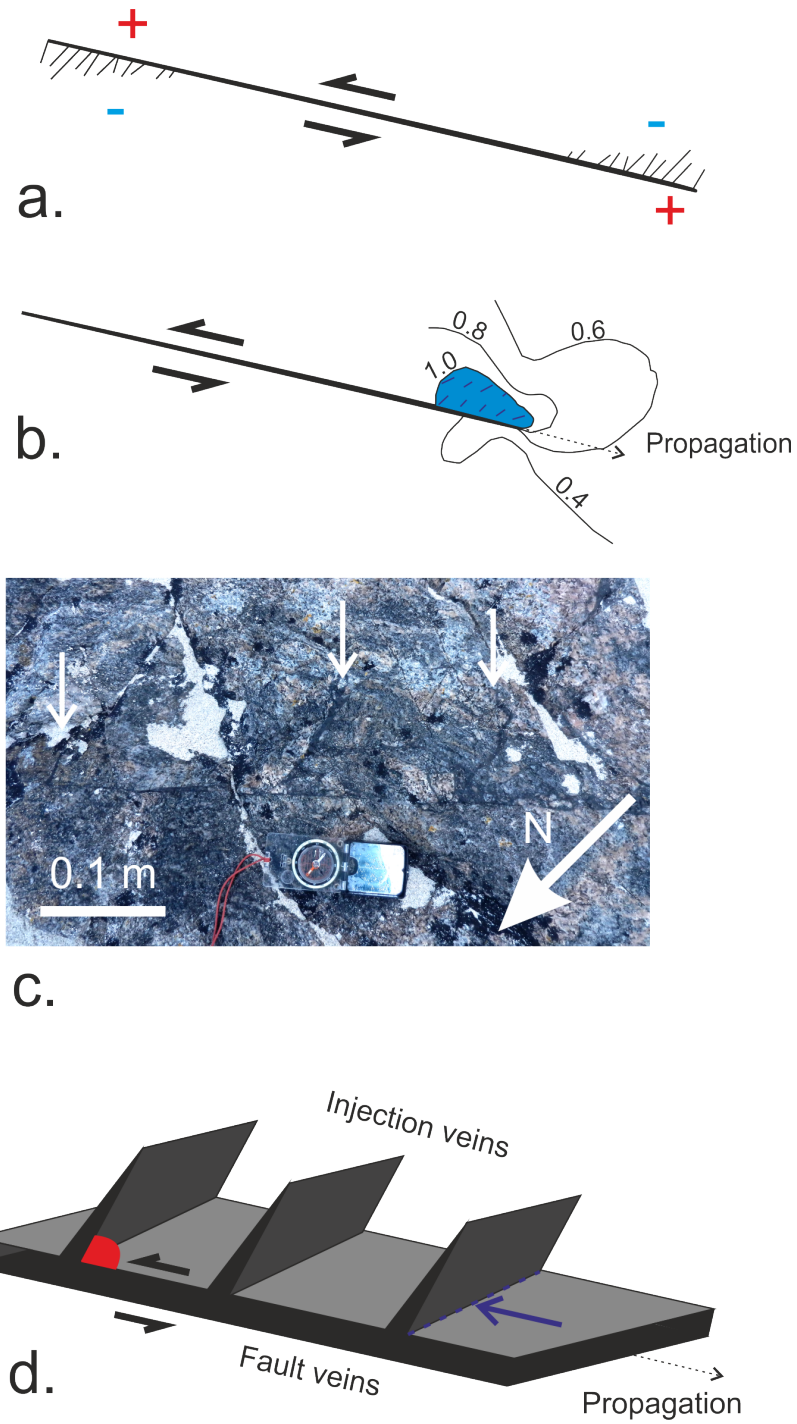

Figure 3.19: Model used to explain injection vein inclination and resulting calculations of slip direction: a. Tensile secondary fracturing generated near observed mode II crack tips in extension (after Dalguer et al. (2003)); b. Imposing a dominant rupture propagation direction at one tip of the crack may account for observations of pseudotachylyte injections on one side of the fault only. Contouring shows the ratio of the maximum shear stress to the critical shear stress, and the blue shaded area is therefore where tensile fractures are expected to form along orientations signified by the dark blue dashes. Contouring after Fig. 11b in Poliakov et al. (2002)); c. Example of inclined injection veins (indicated by arrows) at Allathasdal beach, Barra [65624 803536]; d. Model corresponding to c. showing direction of movement of injection-bearing wall based on injection inclination angle, and slip direction (blue arrow) based on resolved normal to injection.

Pseudotachylyte fault planes were selected for this study if they displayed multiple injection veins, preferably parallel and restricted to a single fault wall (e.g. Fig 3.19c). Additional examples with single injections were used if there were no injection features on the opposing fault margin and especially if adjacent, parallel pseudotachylyte fault veins displayed injection(s) on the equivalent fault wall in a similar orientation. The initial sample size was 75 fault vein - injection pairs. Angles between injection veins and their generation plane were calculated by converting the plane normals into directional components and finding the dot product, the cosine of the angle (Fig. 3.11). As seen in Fig. 3.8, the angular difference between injection veins and their generation plane form one peak around 45°, a value which could potentially represent Riedel shear T fractures. As Riedel shears may represent a differing fracturing process compared to the dynamic crack tip stress field, examples with angular differences between 40-50° were excluded from further analysis. The dominance of the higher angle inclinations relative to this excluded group (Fig. 3.11) is typical of other pseudotachylyte fault zones where the dynamic stress field model has been applied (e.g. Di Toro et al. (2005a)), so the application of it here seems reasonable. The slip direction was derived by finding the line of intersection between the injection vein and the fault plane, and projecting the normal to the intersection along the plane of the fault (Fig. 3.19d). By observing whether injections formed in the hanging wall or the footwall of each fault, and using the acute angle between the injection vein and the fault to distinguish in which direction that wall moved, the sense of slip can be gained across the fault. The misalignment of the slip vector from the orientation of the fault is also calculated here in reference to dip-slip movement as the perfect alignment. This was done using the 'angle between two lines' function of the Stereonet v9.5 program (Cardozo and Allmendinger (2013)).

With the slip direction recognised, it can be used much in the same way as a slip lineation for kinematic fault slip analysis (e.g. Petit (1987), Twiss and Unruh (1998)). Each fault vein plane and slip direction were plotted on a lower hemisphere stereonet to find the complementary fault plane at 90° to the fault vein. Bisecting these planes, and containing the lineation and fault pole, lies the 'movement plane' along which the P- and T- axes (maximum shortening and extensional axes, respectively) lie at 45° from the fault and complementary

planes. Fault arrays with different orientations but slipping under the same stress field (e.g. due to reactivation) can be analysed using this technique, as the compilation of their P- and T- axes allows the maxima to be calculated using Bingham statistics, which provide a probability distribution for the maxima of a set of directional data (Mardia (1975), Marrett and Allmendinger (1990)). These maxima represent the principal axes of incremental strain rate (Marrett and Allmendinger (1990)), which are not equivalent to the principal stress axes (Twiss and Unruh (1998)), but here they are used to construct a suggested focal-mechanism type diagram that is used to compare the remote stress regime for the inferred slip episodes with those concluded from other lines of evidence. This method was undertaken using the program FaultKin 6.5.0 (algorithms described in Marrett and Allmendinger (1990)).

The assumptions for this technique are instantaneous, infinitesimal and homogeneous strain across the fault array, and that each fault's slip movement should be parallel to the orientation of the maximum resolved strain rate of the large-scale remote strain tensor acting on the faults (Twiss and Unruh (1998)). For Bingham statistics to be valid where no magnitude of deformation at each fault is measured and accounted for, the direction of fault movement must be independent of the amount of slip (Marrett and Allmendinger (1990)). Progressive deformation and varying subsequent rotation of fault blocks dividing the spatial extent of the dataset can add error into determination of the strain rate axes (Gapais et al. (2000)) by varying the current geographical orientations of measured faults from fault block to fault block - this is a potential problem in the field area due to the known existence of later faulting, particularly Permo-Triassic normal faulting (Steel and Wilson (1975)) .

3.6.1.2 Results

Preferential pseudotachylyte injection into a single fault wall is observed in the OHFZ (e.g. Fig. 3.19c) as it has been for other pseudotachylyte bearing fault zones such as the Gole Larghe (Di Toro et al. (2005a)). The most dominantly single-sided-injection faults seem to be the simplest, straightest generation planes without interference from adjacent faults. Where regions of complexity occur along the fault, such as jogs and/or areas of brecciation, injec-

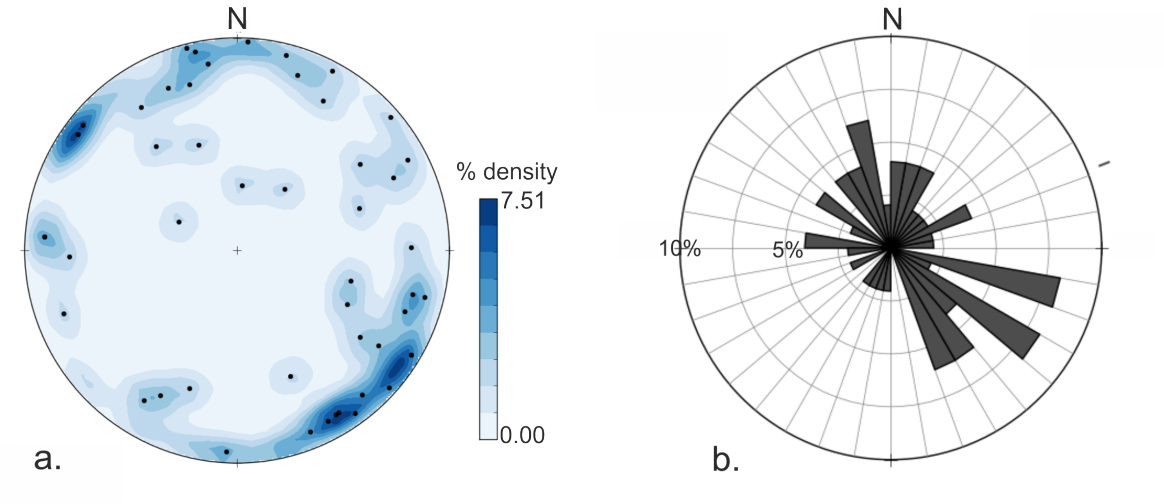

Figure 3.20: Slip directions calculated from injection vein-fault vein intersections: a. Stereonet of calculated slip directions (n=49); b. Rose of calculated slip directions (n=49).

tions may instead be seen forming on both sides. Slip vectors are calculated referring to the trajectory of the injection vein bearing fault wall, but are shown here (Fig. 3.20a) projected onto the lower hemisphere (i.e. down-dip plunges). Many of the slip vectors are shallow and plunge to the SE or the NW, despite the prevalence of NE dipping fault planes that were used in this study. A rose diagram (Fig. 3.20b) of the slip vector trends highlights this broad NW-SE group of transport directions and also suggests a smaller group of NNE-SSW vectors. This partitioning of slip trends can be seen in locations such as Malasgair, SE Lewis (Fig. 3.21) and Àird a' Mhuile, South Uist (Fig. 3.21). In NW Barra, however, the NNE-SSW set has not been recorded (Fig. 3.21).

Misalignment of the injection vein derived slip vector from dip slip movement on the fault veins is shown in Fig. 3.22. A small cluster of well-aligned slip vectors is shown in the peak between 0°-25°. However, the majority of slip vectors are at a high angle to ideal dip slip movement on these faults. This highlights the difference seen between the orientations of the fault veins and those of the slip vectors. The amount of misalignment does not vary consistently with location except in the Grimsay localities were misalignment to dip slip is generally low.

The slip analysis diagram (Fig. 3.23) shows the hangingwall movement directions plus cal-

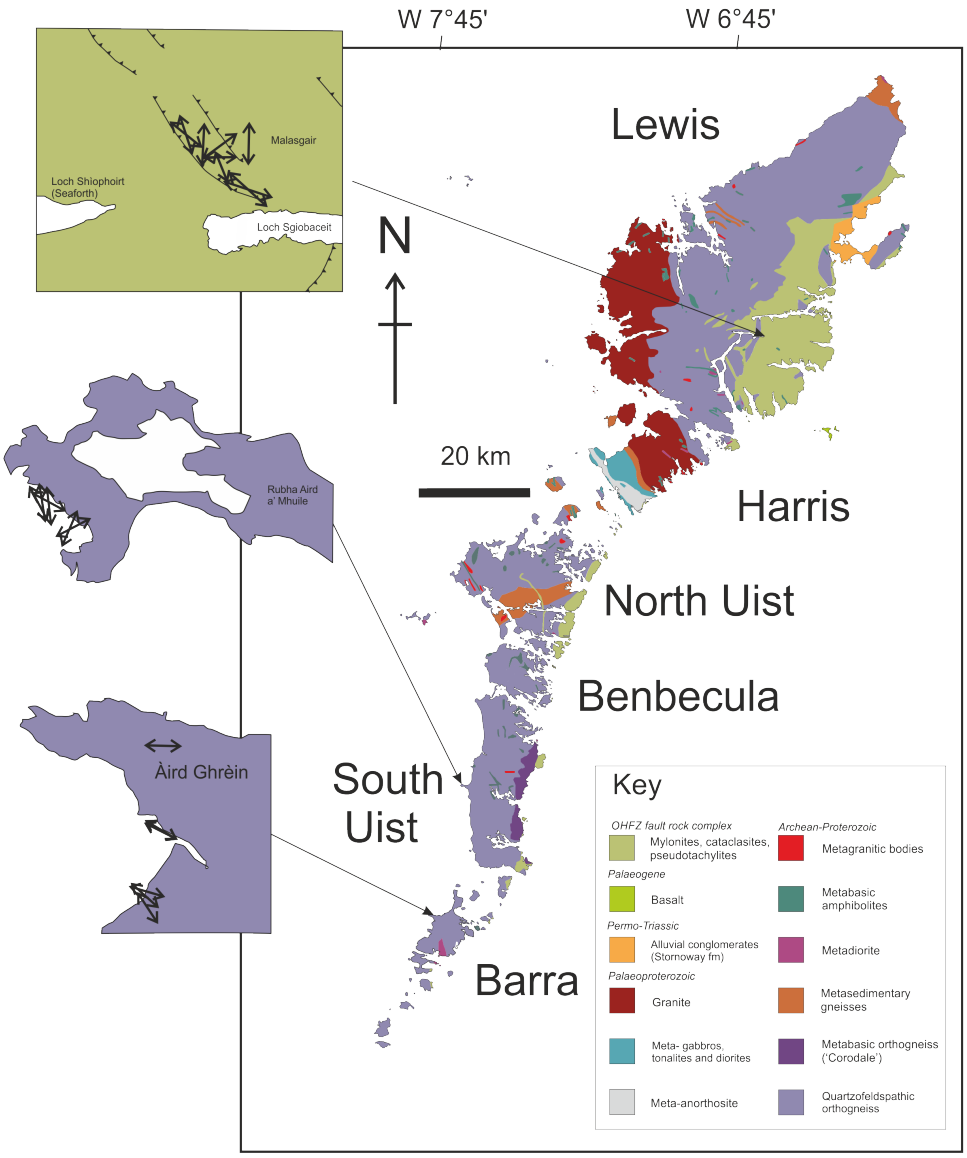

Figure 3.21: Map of selected localities in the Western Isles showing slip directions indicated by injection vein angles. Localities are: Ceann Shíophoirt (Seaforth Head), Lewis (top); Rubha Áird a' Mhuile, South Uist (middle); Áird Ghréin, Barra (bottom).

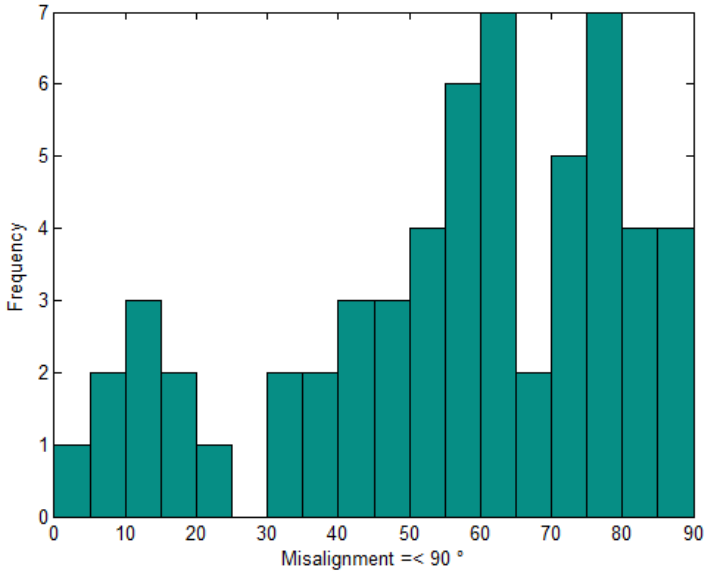

Figure 3.22: Misalignment of slip direction trend from dip slip movement on parent fault

culated P- and T- poles for this dataset. Viewing the dataset in bulk reveals no clear patterns. In an attempt to divide the bulk dataset, the two slip directions (NW-SE and NNE-SSW) determined above were isolated (Fig. 3.23). The N-S or NNE-SSW slip direction is defined by a small subset, with left lateral movement (Fig. 3.23a). For NW-SE slip, movement is dominantly top-to-NW, including more W and NNW orientations. Many form a distribution of P and T as shown in Fig. 3.23c, suggesting a dominantly reverse regime with an element of left lateral strike slip. This subset dominates analysis of the overall NW-SE slip set. The remaining observations in this subset define an extensional-right lateral stress field (Fig. 3.23d).

The kinematic analysis for individual faults using the off fault tensile crack model is shown in Fig. 3.24. Three groups of results are displayed: those showing reverse and reverse-oblique movement (Fig. 3.24a), those showing predominantly strike-slip movement (Fig. 3.24b) and those showing predominantly extensional slip (Fig. 3.24c). The majority of faults sampled for this analysis display reverse slip with some element of obliquity, as seen in Fig. 3.24a. These occur in many of the sites studied and include both SE and NE dipping fault planes. Strike slip movement (Fig. 3.24b) with NE-SW slip occurs on SE dipping faults which are predominantly left-lateral and located along the main fault zone in the east of the field area.

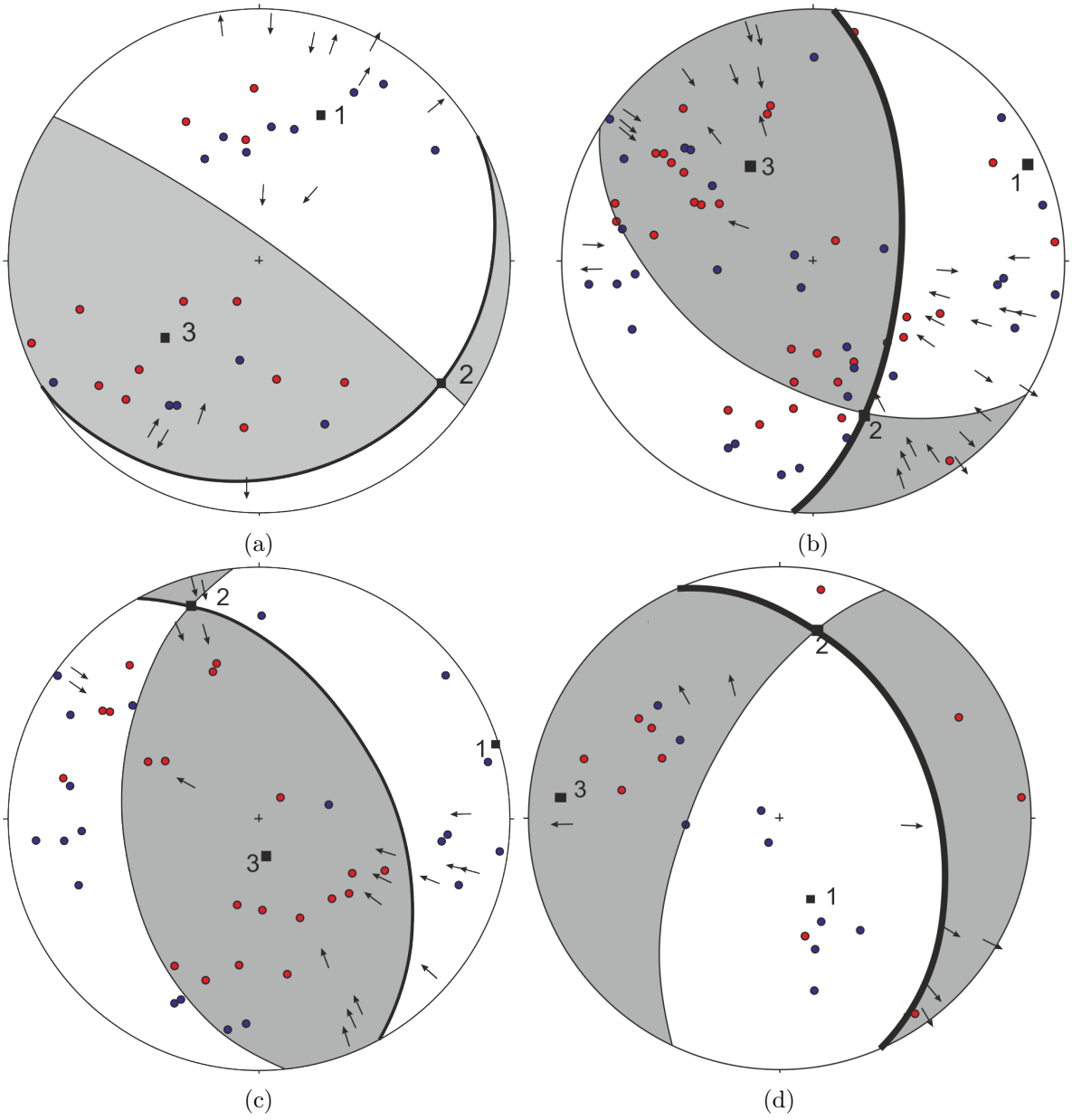

Figure 3.23: Kinematic analysis plots, showing hangingwall slip directions (arrows) and P- and T- axes (blue and red points respectively), the linked Bingham axes and the fault plane solution calculated thereof. The closest nodal plane to the observed fault dips is marked in bold, based on field data): a. NNE-SSW slipping faults; b. NW-SE slipping faults; c. NW-SE slip directions, group 1; d. NW-SE slip directions, group 2.

Other strike slip faults located west of the main fault zone are right-lateral on easterly dipping faults or are on faults dipping in more unusual orientations, for example south and southwest. Extensional faulting (Fig. 3.24c) is dominated by dip-slip movement, and occurs on faults dipping northeast and northwest.

3.6.2 Other kinematic indicators

There is typically little evidence along any given pseudotachylyte bearing fault vein to indicate which direction it may have slipped in, so opportunities to independently verify the slip vectors calculated above are rare. Possible indicators of slip sense may include asymmetric shape preferred orientation of clasts within pseudotachylyte veins or breccias, and offset markers around a fault vein - these observations are explored below for comparison with the slip vectors calculated above.

3.6.2.1 Field observations of offset

Faults with offset markers allow some estimation of slip direction, although these are apparent to the orientation of the exposure face. The sense of slip (reverse, normal etc.) may be recognised although the relative contribution of dip slip and strike slip on oblique-slip faults is difficult to judge. Twenty eight slip directions are reported in reference to the movement direction of the hanging wall in Fig. 3.26. These were recorded to the nearest 16-point compass reference for analysis - greater accuracy was considered inappropriate as the observed movement directions are already limited to apparent trends only. Both normal and reverse offsets are observed (Figs. 3.25a, 3.25b) and are present in the sample set in roughly equal numbers. As Fig. 3.26a shows, the dominant apparent slip directions are to the NW or SE followed by NE or SW. Normal faults show predominantly NW or SE hangingwall movement directions whilst reverse faults show several NE movements (Figs. 3.26b, 3.26c).

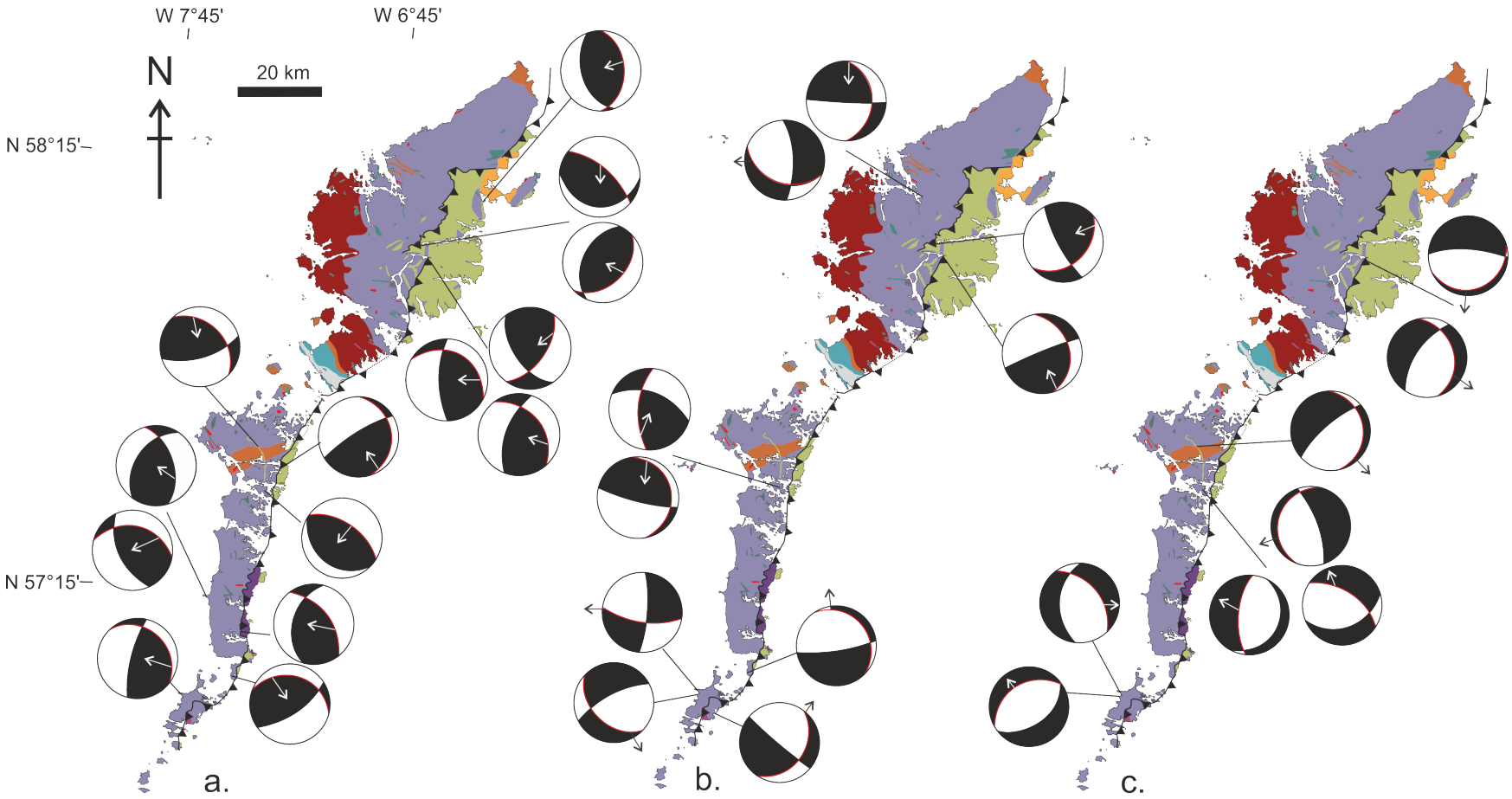

Figure 3.24: Focal-mechanisms showing fault dip (red great circle) and earthquake slip direction (arrows) calculated from application of off-fault tensile crack model to OHFZ pseudotachylytes : a. Locations of pseudotachylytes -bearing faults indicating reverse or oblique reverse slip sense; b. Locations of pseudotachylyte - bearing faults showing predominantly strike-slip movement sense; c. Locations of pseudotachylyte -bearing faults showing normal slip sense.

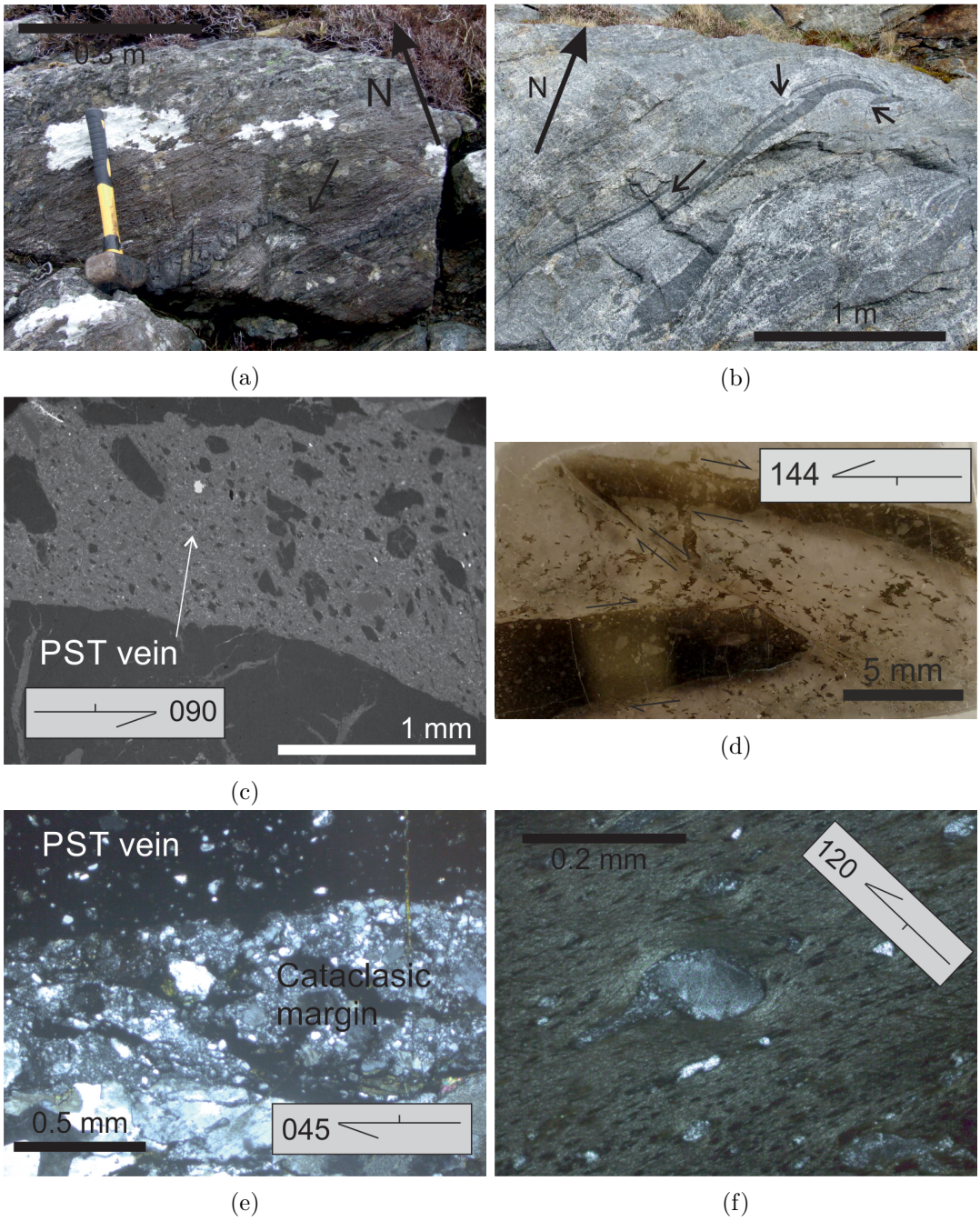

Figure 3.25: Field and microstructural evidence for pseudotachylyte fault slip direction: a. Pseudotachylyte bearing fault (arrowed) displaying apparent normal, top-down-to-ESE displacement. Offset marker layers include earlier phase of pseudotachylyte [130028 917107]; b. Pseudotachylyte bearing faults with reverse, top-up-to-NE offset of amphibolitic layering [85626 856188]; c. Pseudotachylyte vein imaged in BSE showing apparent shape preferred orientation of clasts, predominantly quartz (darker) and plagioclase. Top-to-left slip inferred. Sampled from [75694 823072]; d. Thin, late pseudotachylyte -bearing microfault cutting two earlier veins, with slip sense inferred from indicated microstructures. Sampled from [86263 856169]; e. Cataclasic margin of vein showing development of S-C foliation, exploited by pseudotachylyte ingress. Top-to-left movement indicated. Cross-polarised light. Sampled from [71321 829792]; f. δ- type geometry in recrystallising quartz clast in pseudotachylyte vein, with flow-banding. Top-to-right flow indicated. Cross polarised light, sampled from [67546 800681]

3.6.2.2 Microstructural pseudotachylyte slip indicators

There are several microstructures that may be present in pseudotachylyte veins that can act as indicators for the sense of slip. These are observed from optical work using the polarising light microscope, or from back-scattered electron (BSE) imaging using the scanning electron microscope (SEM). For this work, a beam accelerating voltage of 20 keV and spot size of 5 was used on a FEI Quanta 650 FEGSEM. Working distance was typically $\sim$ 10 mm. Thin sections and polished SEM blocks were cut from rock samples in various orientations; some relative to an 'average' southeastwards regional fault dip and some relative to local features in the rock, for example in order to cut through the veins perpendicularly. The method of sectioning parallel to the XZ plane, where the X- direction is the principal stretching lineation or transport direction and Z is perpendicular to foliation, was generally not used as the foliation and any lineations present within the host rock, on which such cuts are usually relative to, are older features (usually Laxfordian) unrelated to later activity on the OHFZ. The exception to this is where pseudotachylyte veins are found in mylonite or foliated cataclasites. The downside of being unable to use this approach is that, as the transport direction of the pseudotachylyte generation planes are not known, it is not necessarily captured truly in the plane of the cut. Slip directions inferred from these samples are therefore apparent directions and can only be measured in the plane of the cut. However, they do provide an approximation of the slip direction that can be compared to Fig. 3.20b, but cannot accurately differentiate between the two alternative trends across 180°.

These microstructural indicators include: offsets across fault veins (Fig. 3.25d); σ-type or δ-type clasts (surviving porphyroclasts of the host rock, Fig. 3.25f) where intracrystalline deformation can be linked to coseismic deformation, i.e. is different to the deformation state seen in the wall rock; the presence of a shape-preferred orientation (SPO) displayed by clasts within the vein (Fig. 3.25c); or by fabrics displayed at the margin of the vein, which may be cataclastic and display indicators such as S/C fabrics or σ-clasts (Fig. 3.25e). Where these are lacking, the deformation in the wall rock of the vein may also show kinematic indicators, but because these carry more risk of relating to earlier events the indicators more directly

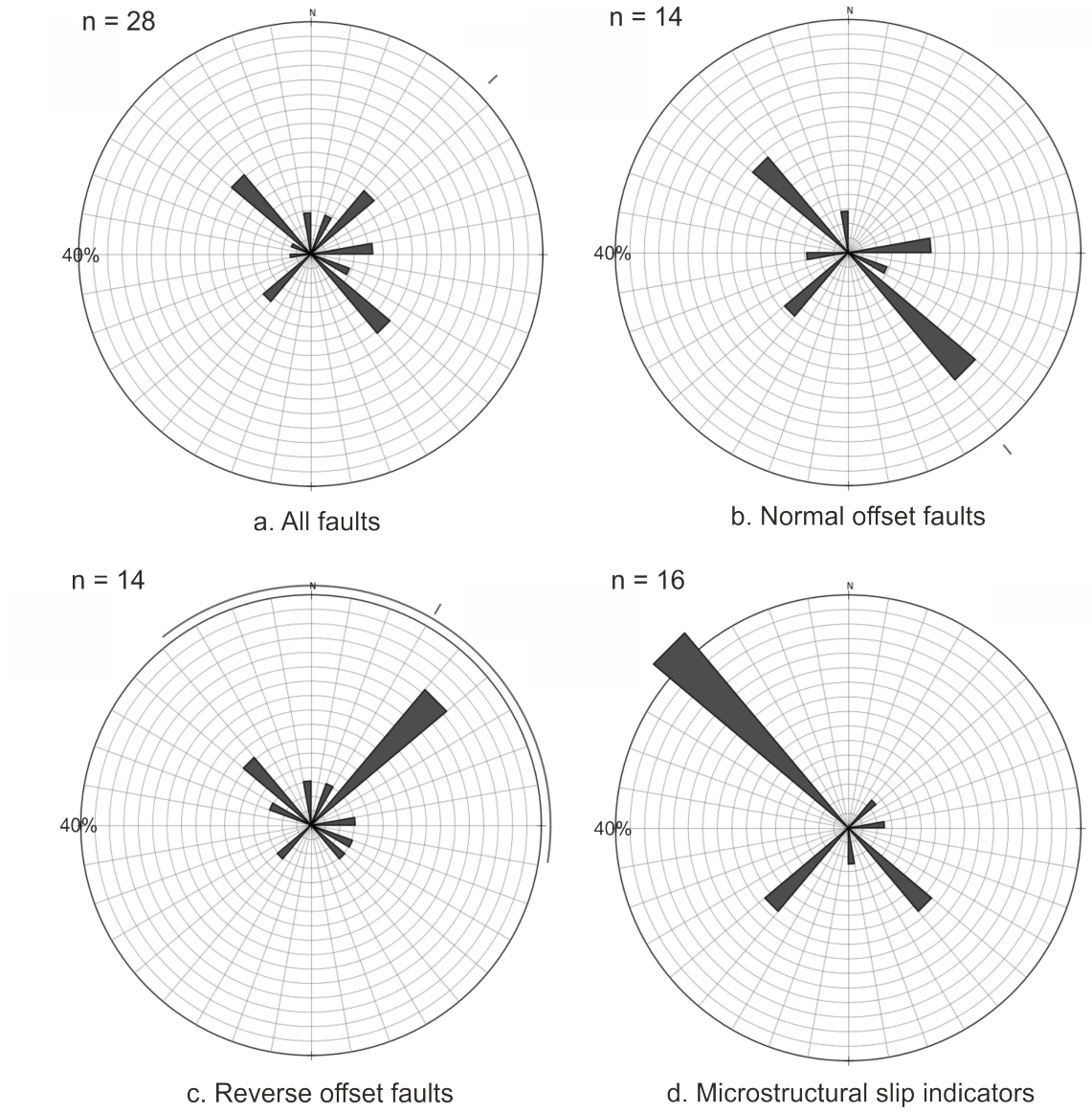

Figure 3.26: Apparent hangingwall movement directions from pseudotachylyte faults showing offset markers and microstructures: a. All observed faults; b. Normal offset faults; c. Reverse offset faults; d. Microstructural indications of slip direction.

related to the vein are preferred.

Observations of slip direction indicators were taken from 16 different generation plane samples, some with multiple sections and/or indicators. The slip directions are displayed in Fig. 3.26d, which displays the apparent movement direction of the hanging wall in these samples. The modal apparent slip direction is towards the NW, with intermediate peaks to the SW, SE and a minor peak to the NE. One section, G1 from Grimsay (Fig. 3.25d) displays

two parallel pseudotachylyte veins with the same slip sense cut by an oblique pseudotachylyte filled microfault. The sense of movement of the first phase of pseudotachylyte generation is top-to-the-NW and the second is top-to-the-SE. Both slip phases apparently utilise reverse movement.

3.6.2.3 Anisotropy of magnetic susceptibility

The magnetic susceptibility, K, is a multiplier of the inducing magnetic field, H, in its proportionality relation to the induced magnetization of a material (M), where that field is applied, as $M = K.H$ (Rochette et al. (1992)). The anisotropy of magnetic susceptibility (AMS) ellipsoid, a second rank tensor, may be controlled by preferred grain shapes in magnetite, or crystallographic orientations in other minerals (Borradaile and Henry (1997)), and as such is a useful fabric indicator that may display strain orientations or flow directions in tectonic (e.g. Benn (1994)) and magmatic (e.g. Bouillin et al. (1993), Magee et al. (2016)) or sedimentary rocks (Rees (1965),Hodson et al. (2016)) respectively. The principle axes of the AMS ellipsoid are defined as K_1, K_2, K_3.

In pseudotachylytes, magnetite is a common primary mineral crystallising in the pseudotachylyte matrix and often carries the highest natural remanent magnetisation (NRM) of the bulk assemblage (Nakamura et al. (2002)), as well as dominating the AMS signature. Rapid cooling of pseudotachylytes below the magnetite Curie temperature of 578°C means that the AMS ellipsoid represents the preferred shape of the magnetite as it crystallised during coseismic slip, assuming no later alteration and/or reheating of the rock body above the Curie temperature (Ferré et al. (2014)). AMS has therefore been used on pseudotachylytes to derive the coseismic slip direction (Scott and Spray (1999), Craddock and Magloughlin (2005), Garza et al. (2009), Ferré et al. (2015), Ferré et al. (2016)).

The AMS of a pseudotachylyte fault vein from the OHFZ, sample SU2 [71321 829729], was analysed in order to suggest the slip direction. Field and microstructural slip indicators for this fault vein are not unambiguous but are consistent. They include S-C type foliation

in the cataclasic vein margin (Fig. 3.25e) and the relative angle of the injection veins to the fault vein (as in section 3.6.1), both indicating top-to-northwest or west-northwest movement on the fault, which dips 28 → 80. Both of these examples are apparent directions, based on the planes of thin sectioning and exposure respectively.

The AMS analysis took place at Southern Illinois University using low-field magnetic susceptibility measurements on a KLY-4s Kappabridge magnetic susceptometer (Ferré et al. (2016)). The field strength was 450 A/m and the frequency 875 Hz. Seven 3.5 x 3.5 x 3.5 mm samples were analysed, a smaller size compared to many AMS studies as they were designed to reduce the inclusion of host rock and clasts with the pseudotachylyte matrix (Ferré et al. (2016)). Magnetic hysteresis was measured to evaluate the contribution from para- and diamagnetic minerals, using a Princeton Measurements vibrating sample magnetometer (VSM) 3900-04 and an applied field of <1 Tesla (Ferré et al. (2016)). The results for the orientations of K_1, K_2, K_3 are shown plotted in geographic space on an equal area stereonet.

The pseudotachylyte sample SU2 showed high values of mean magnetic susceptibility (K_m), with values of 52317 ± 11384 x 10^{-6} SI, and a low contribution from paramagnetic materials of 1.8%, indicating the dominance of magnetite in the AMS signal (Ferré et al. (2016)). The corrected degree of magnetic anisotropy, P', is 1.1 for this sample (Jelinek (1981), Ferré et al. (2016)). The principle axes of anisotropy are shown in Fig. 3.27, along with the great circle of the eastward dipping fault vein. Strong clustering of values from each of the seven samples shows that K_1 plunges 56/118°. The orientations of the principal axes of magnetic susceptibility (K_1, K_2, K_3) are plotted in Fig. 3.27a, along with the interpreted trend of slip movement. This is found from the pole to the intersection of the magnetic foliation (the plane through K_1 and K_2) which plunges 38→066°. This should be coincident with K_1 unless a component of pure shear is present, as is the case here (Ferré et al. (2016)). The slip sense across this pseudotachylyte fault is therefore top-to-WSW (Fig. 3.27).

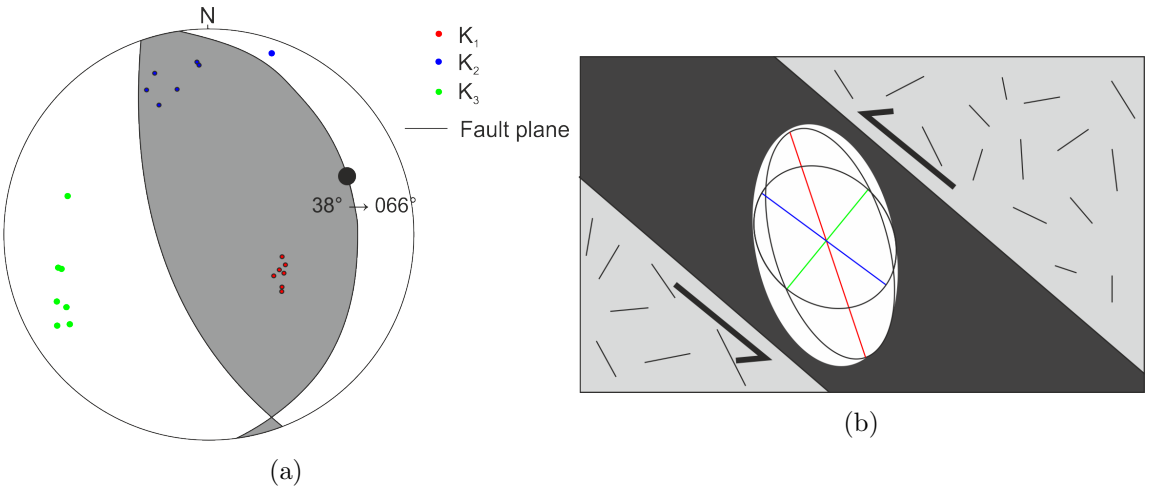

Figure 3.27: AMS results for sample SU2: a. Principal axes in geographic space of anisotropy of magnetic susceptibility ellipsoid for sample SU2, with interpreted slip trend (black circle), after Ferré et al. (2016). The orientation of the fault vein is shown by the great circle; b. schematic diagram showing interpreted slip direction of sampled fault plane.

3.6.3 Initial interpretation of kinematic indicators

These methods improve the results of section 3.5 because they present the relative movement, or slip sense, of the fault walls, rather than only the trend of slip direction. The most comprehensive approach is based on field observations of angles between injection and fault veins, using the off-fault tensile crack model. Although founded in previous field, experimental and numerical work explaining the phenomenon on pseudotachylyte bearing faults (Di Toro et al. (2005a), Griffith et al. (2009b), Ngo et al. (2012)), this is the first time the method has been used to derive slip directions from a set of pseudotachylyte bearing faults where fault movement is otherwise mostly unconstrained. The results reveal three major slip directions: top-up-to-NW, top-down-to-SE and top-to-NE (Figs. 3.21, 3.23). Additionally, it is clear that oblique slip occurs on many faults (Fig. 3.22, Fig. 3.24), since this method allows the fault dip to be integrated into the analysis, allowing focal - mechanism type diagrams to be produced (Fig. 3.24). Microstructural and field observations of slip support these results, where available (section 3.6.2, Fig. 3.26).

3.7 Discussion

3.7.1 Orientation of pseudotachylyte veins in the OHFZ

Although the bulk distribution of fault and injection vein orientation is varied (Figs. 3.3a, 3.3c), there are prevalent trends across many of the localities studied. A northeasterly dip is the modal orientation for pseudotachylyte fault veins across much of the field area. However, this orientation contrasts with the regional dip of the OHFZ, typically easterly to southeasterly dipping based both on regional scale seismic data (e.g. Smythe et al. (1982), Brewer et al. (1983)) and on field observations of major fault planes (Butler et al. (1995)).

Despite the differences between the northern and southern sections of the OHFZ, namely the increased volume of mylonite development in the north (Sibson (1977b)), there is no significant difference in the distribution of pseudotachylyte vein orientations between them (Fig. 3.4). Veins from within the mapped trace of the OHFZ, the 'fault zone' pseudotachylytes, show similar orientations of fault veins to the non-fault zone veins. Fault zone injection veins (Fig. 3.5c) are more widely scattered than in other locations. Whilst the faulting that generated the pseudotachylyte is consistent with pseudotachylyte faults outside the mapped fault zone, the preference of injection veins to form perpendicular to the slip direction (Ngo et al. (2012)) is disrupted here. This may be because increased density of damage in the fault zone (e.g. Vermilye and Scholz (1998)) had already produced a widespread fracture network which could then be exploited by pseudotachylyte injection off the generating fault plane. In the footwall, a similar fault vein distribution exists but the injection veins are more clustered (Fig. 3.5a). The dominance of NW and SE dipping injections suggests a slip direction along this trend, perpendicular to the injection strike. A minor cluster dipping NNE might indicate a second slip trend during a different phase of faulting.

3.7.2 Spatial variation in pseudotachylyte vein orientations

Locally consistent distributions of fault veins in localities such as Grimsay (Fig. 3.6) could relate to larger structures within the fault zone. In Grimsay, the pseudotachylyte bearing fault planes are well preserved and show little evidence (at this scale) of cataclasis, either preceding or subsequent to the pseudotachylyte generation phase. This suggests that pseudotachylyte faulting was a constrained event without later reactivation. Although the pseudotachylyte is locally densely distributed, the rock in the fault walls shows little sign of fault related deformation. $^{40}Ar/^{39}Ar$ dating of Grimsay pseudotachylytes has produced ages of 430 $\pm$ 6 Ma (Kelley et al. (1994)), consistent with Caledonian movement, and comparing favourably with the proposed age of thrusting on the main trace of the OHFZ (Sibson (1975)). These westerly dipping Grimsay faults could therefore be explained as antithetic backthrusts formed in the foreland of the main trace of the OHFZ to the east, being of parallel strike (Fig. 3.6) but opposing slip direction, well constrained by offset amphibolitic bands at the outcrop (Fig. 3.25b). Backthrusts can develop at the foreland propagating tip of a thrust wedge in a 'triangle zone' geometry, often overriding a blind thrust below, although this model is usually more applicable to thin-skinned style tectonics of sedimentary thrust wedges (Jones (1996)).

The west coast localities of Barra and South Uist display a modal trend of easterly dipping fault veins with variations to the NE and SE, but there are also a number that dip in the opposite direction (Fig. 3.6b). $^{40}Ar/^{39}Ar$ dating of a vein from one of these west coast localities in Áird Ghréin, NW Barra (Fig. 2.3), has concluded that two phases of pseudotachylyte were present; an initial $\sim$ 1200 Ma event and a subsequent $\sim$ 700 Ma event (Sherlock et al. (2009)). The injection veins from the west coast localities suggest slip on a NW-SE trend, including some more N-S trends and additionally a NNE-SSW cluster (Fig. 3.6b). The general footwall distribution (Fig. 3.5b) contains a shallower broadly east dipping (from S through to NE) set of injection veins than in the west coast localities, and has few westerly dipping examples. Overall, however, the pseudotachylytes on the west coast are concluded to relate to the same movement phases as the main trace of the OHFZ.

3.7.3 Controls on pseudotachylyte orientation

Preferential orientations for pseudotachylyte fault planes have been investigated with regard to the anisotropy of the rock (i.e. foliation, section 3.4.1), and to the potential presence of a regional scale structural system relating to the fault as with sets of Riedel shears (section 3.4.2). Whilst pseudotachylyte generation planes may commonly form at low angles to the foliation, there is not a preference for complete conformity; the number of observations where the pseudotachylyte generation plane has formed at angles $<10^{\circ}$ to the surrounding foliation is only 10% (Fig. 3.8b). Many of the field examples considered show discordant pseudotachylyte faults to support this interpretation (e.g. Figs. 3.1a-c). The possibility of fault orientations favouring the foliation dip over a more ideal direction is therefore discounted as having any overall significance in the OHFZ, in contrast to other pseudotachylyte bearing fault zones within gneissic hosts (Swanson (1988), Grocott (1981)). In these literature examples, the paired shear zone geometries have their bounding faults layer-parallel and the internal veins may pick Riedel shear geometries (Swanson (1988)). In the OHFZ, it is possible that the gneissic foliation does not in general present a sufficiently weak plane for slip to be preferentially resolved onto. In the mainland Lewisian, Beacom et al. (2001) note that brittle fracture zones (some containing pseudotachylyte) form in the location and orientation of older ductile shear zones, and Grocott (1981) matches the location of pseudotachylyte faults with the mostly strongly deformed gneisses in the Ikertôq shear belt, Greenland, so it seems more likely that pseudotachylyte faults should be foliation parallel where the fabric is stronger, and hence the foliation mechanically weaker, in regions of previous high strain rather than in the more uniformly foliated bulk rock.

Riedel-shear type fracture patterns are observed in the field within paired shear zones, as in West Greenland (Grocott 1981) and Maine, USA (Swanson (1988)). From the orientation data (Fig. 3.10) it is possible that pseudotachylyte faults were formed along fracture sets controlled by Riedel shear angles during a phase of overall left lateral strike slip on the OHFZ. However, it is difficult to show that the similarity in distribution is not coincidental. In addition, whilst left-lateral strike slip is a potential kinematic phase for the OHFZ (section

3.6.1.2), it is unlikely that all of the pseudotachylyte veins in the dataset used relate to that episode. A similar uncertainty relates to the comparison with injection veins (Fig. 3.11). The possible modal peak at T-shear orientations (45°) is convincing, but difficult to isolate as part of a Riedel system rather than an unrelated tensile fracture.

3.7.4 Slip direction

3.7.4.1 Validity of the en echelon array model

Pseudotachylyte en echelon arrays provide two sets of orientation information. Firstly, the orientation of the overall array is considered here to represent the orientation of the parent injection, which should be perpendicular to the slip direction of the generating fault and controlled by the dynamic fault tip stress field (Ngo et al. (2012)). Secondly, the orientation of individual en echelon pseudotachylyte segments forming the array are proposed here to rotate in response to the remote stress field as the influence of the dynamic fault tip stress field dies off in time and space. The slip trend indicated by the array opening direction is therefore predominantly NW-SE, with variations at N-S and ENE-WSW. This model is a proposed combination of en echelon mode I fracture models (e.g. Segall and Pollard (1980), Pollard and Aydin (1984), Clemente et al. (2007)) with coseismic mode II secondary fracturing models (Poliakov et al. (2002), Griffith et al. (2009b), Ngo et al. (2012)). This approach may be over-simplistic, and has not yet been strongly validated by field relationships as the pseudotachylyte fault (the mode II shear) and the initial 'parent' injection (the mode I tensile fracture) have only once been observed in the field (Fig. 3.13b) in the ideal geometry represented in Fig. 3.14. However, this can be attributed to the need to have three dimensional exposure to display both the plane containing fault and injection and the fault-parallel plane displaying the segmented pseudotachylyte injection segments. This latter is the plane most usually observed in the OHFZ. In addition, the segmentation of the injection vein into en echelon geometry is supported by Fig. 3.15.

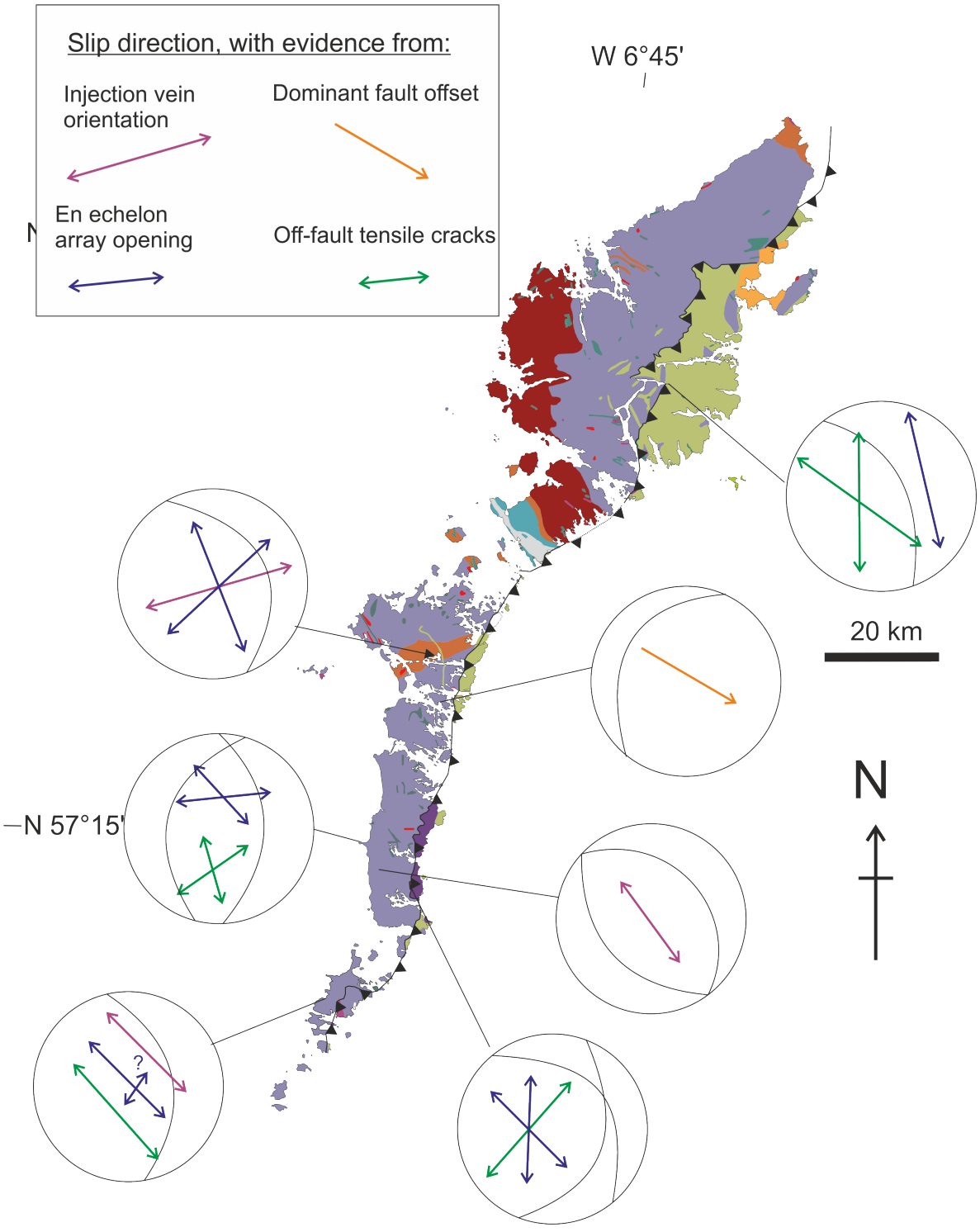

Figure 3.28: Schematic stereonet representation of dominant slip directions across the OHFZ region from various lines of evidence. Dominant dip direction of pseudotachylyte - bearing faults in each region is shown by the great circle.

3.7.4.2 Validity of the off-fault tensile crack model

Despite the lack of slip markers visible in the field across many pseudotachylyte bearing faults, this study has quantified the slip direction using two models based on dynamic fault tip stress fields and tensile injection. Firstly, the calculation of the slip vector based on the angle between the fault plane and the injection vein (section 3.6.1) and secondly, the use of en echelon pseudotachylyte injection veins to suggest the trend of slip (section 3.5). The former, the dynamic off-fault tensile crack model, is based on numerical models (Ngo et al. (2012)) and experiments (Griffith et al. (2009b)). It has previously been applied to pseudotachylyte fault zones by Di Toro et al. (2005a), used together with a numerical model that constrains rupture directivity, fracture energy and slip velocity on the Gole Larghe fault zone, Italy. In the present study, this model has been used simply to identify the variations in slip direction within a fault zone where this has been difficult to recognise through other approaches. In addition, the further processing of the angular relations (section 3.6.1.1) has allowed a slip vector to be calculated. This slip vector can be compared against the orientation of the fault and allows creation of a focal-mechanism type diagram (Fig. 3.23). The result of this approach is a three-dimensional analysis of slip, preferable to two dimensional field offsets and microstructural indicators (sections 3.6.2.1, 3.6.2.2), although these provide valuable ground-truthing to the injection vein based models.

Systematic repetition of injection veins along one side of a fault vein, as required for the off fault tensile crack model, has been observed to develop best along sections of faults removed from areas of complexity, such as overlapping faults or segments of brecciation. This observation suggests that interacting stress fields from multiple slip surfaces disrupt the formation of tensile fractures at propagating fault tips. This means that the approach outlined above is not easily applied along the main trace of the fault zone, where significant damage hampers the development of clear injection vein directionality. However, in common with Di Toro et al. (2005a), it is suggested that such analysis is a useful technique in many pseudotachylyte bearing fault zones, especially if other slip direction indicators are ambiguous or absent.

3.7.4.3 Evidence for multiple phase pseudotachylyte generation

Observations of multiple phases of pseudotachylyte formation across several localities (Sherlock et al. (2009)) are confirmed in this current work (e.g. Figs. 3.13a, 3.25a, 3.25d). Two cross-cutting en echelon arrays (Fig. 3.13a) show distinct slip directions, one NW-SE and one NNE-SSW (section 3.5). Although an E-W slip trend is shown in some locations in addition to the ubiquitous NW-SE trend (e.g. Fig. 3.18), the NNE–SSW direction appears the more common of these secondary trends based on injection veins, the off-fault tensile fracture model results and microstructural and field observations (Figs. 3.26, 3.28). Both of these slip directions are seen in almost all locations where such data have been collected - both within the fault trace and in outlying regions. The only locality studied where no example of the NNE-SSW (or alternatively more N-S) slip direction was calculated was the NW coast of Barra, where all ten observations record NW-SE slip only (Fig. 3.28). The west coast locality at Àird a' Mhuile, South Uist records both slip directions. Overall, this supports an argument for related movement between the OHFZ proper and these pseudotachylyte - rich outlying localities on the west coast, which have enough evidence for localised seismic faulting (i.e. pseudotachylyte bearing generation planes) to be considered as one or more major fault segments in their own right. The absence of the NNE-SSW slip sense in NW Barra suggests that not all of these fault segments were active simultaneously during all periods of seismic activity. Sibson (1975) considered the more scattered footwall pseudotachylyte faults to be a representation of the early OHFZ in the Uists and Barra, before a through-going fault zone was developed, and the matching kinematics displayed here support this view. However, progressive localisation with time has also taken place on these west coast fault strands, allowing the concentration of seismic, pseudotachylyte generating slip and encompassing two phases with differing fault kinematics.

Kinematic fault slip analyses plots suggest a third recognisable phase of pseudotachylyte generation (Fig. 3.23). NW-SE slipping faults are shown to have a distinct remote strain field from NNE-SSW dipping faults (Fig. 3.23). However, one way of reducing the scatter of T- and P- axes in the NW-SE slip dataset is to distinguish a predominantly compressional strain

field from a predominantly extensional one, dominated by top-up-to-NW and top-down-to-SE movement respectively. Traditionally, pseudotachylyte in the OHFZ has been linked to compressional top-to-the-NW reverse faulting in the OHFZ (e.g. Sibson (1980), Macaudière and Brown (1982) White (1996a), Imber et al. (2002)).

Other observations, particularly around South Uist and Barra where more significant strike slip and extensional reactivation of the OHFZ is seen (White (1996a), MacInnes et al. (2000), Osinski et al. (2001)), note pseudotachylyte along extensional faults in near proximity to compressional examples (Imber (1998), MacInnes et al. (2000), Osinski et al. (2001)). The slip directions for compressional examples are usually stated as NW-SE (Sibson (1980), White (1996a), Imber et al. (2002), Osinski et al. (2001)) or E-W (Macaudière and Brown (1982), Osinski et al. (2001)), and the observed extensional pseudotachylyte faults have a similar transport direction (MacInnes et al. (2000), Osinski et al. (2001)). This is exactly as the results for slip direction here display. NNE-SSW slip in OHFZ pseudotachylyte faults (Fig. 3.23a) has not been noted by previous workers, although a phase of left lateral strike slip is recorded in phyllonites in Lewis, North and South Uist (Butler et al. (1995)).

Although only showing apparent dips, field offsets (Fig. 3.26) suggest that extensional movement favours a NW or SE movement direction, whilst the NE or NNE slip direction is predominantly compressional with fewer antithetic slip observations towards the SW. Fig. 3.24c agrees with the predominantly NW-SE extension, with more NE dipping faults showing a small amount of oblique slip to facilitate this. The relative timings of the compressive and extensional phases are not well understood - Osinski et al. (2001) and Imber (1998) consider that both could occur during one dominant period of activity on the OHFZ, perhaps with extensional fault providing local space accommodation for the complex block movement of a major thrusting episode (Imber (1998)). In contrast, there is clear field evidence in Barra that extensional pseudotachylytes occur in steep normal faults that cut earlier low angle detachments (MacInnes et al. (2000)) - a fault set which is usually linked elsewhere to the latest Caledonian OHFZ activity, but which elsewhere cuts fluid-present detachments in extensional phyllonites and does not contain pseudotachylyte (Butler et al. (1995), Szulc et al. (2008)).

This late, steep extensional seismicity is corroborated by field observations shown in Fig. 3.25a, where a pseudotachylyte bearing normal fault offsets a shallower pseudotachylyte fault vein with uncertain displacement. Unfortunately, other constraints on the relative timing of the identified pseudotachylyte slip directions are generally limited for the OHFZ.

3.7.5 Orientation of remote stress and strain fields

En echelon segment opening directions should approximate the remote σ_{min}, which forms similar peaks trending NW-SE and N-S. The similarity of these results to those of the overall arrays is unsurprising when it is considered that the angles of rotation between the array and the segments tends to be low (Fig. 3.17). There is a lack of preferred rotation direction between the en echelon pseudotachylyte segments and the overall array, as seen in Fig. 3.17. It is therefore difficult to tell which direction relative to the array opening direction σ_{min} might lie. This is complicated further by the potential for more than one slip episode under differing stress fields to be present in the data. Fig. 3.17 also shows that although the best oriented arrays might be expected to show little rotation from the segments, there is no preferred trend for arrays with no rotation. Additionally, the most common array opening direction, NW-SE, may show both senses of rotation. Clockwise rotation of the array from the segments is representative of left lateral shear sense, and anti-clockwise of right lateral.

There may be an apparent pattern in the amount and direction of rotation (Fig. 3.17). Opening directions where consistently low angles of rotation are dominantly between 160 - 180° and 000-030° (and their western hemisphere equivalents, Fig. 3.17). This would suggest that the remote σ_{min} is roughly N-S.

Although it has been noted that the principle stress axes are unlikely to be parallel to the axes of principle strain rates shown in Fig. 3.23 (Twiss and Unruh (1998)), the stress field is here assumed to be compatible with the relative magnitudes of strain (i.e. ϵ_1 is broadly located in same quadrant as σ_1), allowing comparison of injection vein intersection results with the en echelon pseudotachylyte injection array analysis. Cross-cutting en echelon arrays indi-

cate that σ_{min} (in the horizontal plane) moved from a N-S round to a more E-W (or further) orientation. This would follow with the transition from the top-to-NW compression, where the minimum horizontal strain (ϵ_3) is oriented N-S and the maximum (ϵ_1) E-W, to top-to-SE extension where the minimum horizontal strain (ϵ_3) moves to an E-W configuration. This would support separate stages of movement for the compression and extension phases. The location of the principal strain axes in Figs. 3.23a and 3.23b suggest that the NNE-SSW and top-to-NW (NW-SE) slip episodes could be accommodated by a slight rotation of the strain axes, rather than a wholesale transition to a different remote strain field. This may represent progressive deformation and/or rotation of the OHFZ fault walls in response to regional scale displacements. Hence all the slip episodes recognised here could represent progressive stages of the same tectonic event.

3.7.6 Tectonic context of slip phases

The presence of pseudotachylyte along fault strands across the OHFZ indicates that seismic activity was a feature of the local tectonic regime during one or several periods of time during the development of the fault zone. Cross-cutting relationships observed in pseudotachylyte veins in the OHFZ (see Figs. 3.13a, 3.25a, also Sherlock et al. (2009)) and the identification of different slip directions and local stress regimes (section 3.5.2, Imber (1998), Osinski et al. (2001)) suggest that seismic activity in an environment conducive to pseudotachylyte generation took place over a number of discrete phases with differing stress fields and faulting regimes. Those identified here are: 1. top-up-to-NW compression; 2. top-to-NNE strike slip; and 3. top-down-to-SE or NW extension (section 3.7.4). Fig. 3.25a shows a pseudotachylyte - bearing normal fault cutting a shallower pseudotachylyte fault vein of uncertain slip sense, so that normal movement is inferred to be late. However, in general cross-cutting pseudotachylyte fault veins are not often observed, and the relative timing of these movements is initially somewhat uncertain. The wider developmental history of the OHFZ is used as a framework in which these events may be considered.

Top-to-NW ductile reverse movement is observed in a localised manner in South Uist (Os-

inski et al. (2001)) and Barra (MacInnes et al. (2000)), and to a much greater extent in the Northern Section of Sgalpaigh and Lewis (Sibson (1975), Imber et al. (2002)). In SE Lewis, some pseudotachylyte is observed to be ductiley sheared, concordant with the surrounding mylonite foliation, so that cyclical brittle seismicity and ductile shear is inferred (Sibson (1980), White (1996a)). This places the initial, resheared phase of pseudotachylyte into the ductile thrusting period that is most likely Grenvillian (i.e. $\sim$ 1100 Ma; Imber et al. (2001), Osinski et al. (2001), Imber et al. (2002) but cf. MacInnes et al. (2000)). The simplest and most frequent explanation for this common observation of sheared pseudotachylyte associated with mylonites is the downwards propagation of seismic slip into the depth range of ductile, amphibolite facies mylonitisation (Sibson (1980) in the OHFZ, Lin (2008), Mahapatro et al. (2009) and Leib et al. (2016) elsewhere). In the case of downwards propagation of seismic slip, there may also be unsheared pseudotachylytes produced concurrently at shallower levels in the seismogenic zone. This means that pseudotachylytes of a similar age to the Lewis mylonitised group may exist in other sections of the OHFZ because of the interpretation that the Northern section of the OHFZ is exhumed to a greater depth than the Southern section (Butler (1995)). However, these brittle equivalents could remain difficult to distinguish because a later, unsheared phase of pseudotachylyte that cuts through the Lewis OHFZ mylonites records the same northwesterly movement direction.

In addition, NW-SE extension and top-to-NE movement are also recorded by a number of pseudotachylytes (Figs. 3.18, 3.21, 3.23, 3.26). It has not been previously ascertained whether seismic pseudotachylyte generating activity was involved in these large scale fault movements due to the presence of the weak phyllonites, which contain the main evidence for these slip senses (e.g. Butler et al. (1995)). Top-to-NE strike slip is recorded in low grade phyllonitic mylonites in Sgalpaigh and the Uists and is considered to have occurred during the later Caledonian orogeny, subsequent to thrusting on the OHFZ (Butler et al. (1995)). However, the fluid-present conditions and ductile deformation recorded by these phyllonites are not likely to be conducive to the frictional failure needed for pseudotachylyte production (Imber et al. (1997)), and no brittle pseudotachylytes have been observed cutting through these phyllonite zones. Despite this, left-lateral strike-slip fpseudotachylyte faults are observed along

the OHFZ (Fig. 3.24b) with top-to-NE movement, implying that some sections of the fault zone may have continued to be mechanically strong during this time. Strike-slip reactivation was followed by a period of extensional activity, initially on low angle detachments and then steeper normal faults (Butler et al. (1995)). This succession from shallow to steep normal faulting has also been observed in Barra, where MacInnes et al. (2000) found pseudotachylyte developed along the steeper faults. This field evidence in Barra is important as it emphasises that fluid-present deformation and strike slip reactivation were not present along all strands of the OHFZ (MacInnes et al. (2000)). The observed normal pseudotachylyte faults in Fig. 3.24c occur on a range of fault dips between 19-60°, but the dominant dip-slip and NW-SE slip distinguishes extension as a probable separate slip phase to the more variable and oblique reverse slip faults, and hence most of the extensional pseudotachylyte faults are considered to belong to this same late phase as the example in Fig. 3.26 and the observations in Barra by MacInnes et al. (2000).

3.8 Chapter conclusions

The main conclusions from this chapter are:

- Pseudotachylyte bearing faults in the OHFZ are distributed around the Western Isles on faults exhibiting a range of orientations, dominantly NE, E or SE dipping. As the regional dip of the OHFZ is ESE to SE, this divergence is interesting;
- There is no great variation in pseudotachylyte fault dips along the strike of the OHFZ, or between the fault zone and the surrounding fault walls;
- Some oblique structures, especially if fault dip is consistent across a locality (e.g. Aisgernis, South Uist), may represent ramp or tear structures between ESE-SE dipping fault sections;
- Many other small pseudotachylyte bearing faults are also misaligned from the regional OHFZ dip, but there is no evidence that their orientation is influenced by foliation or predictable pre-existent fracture systems;

- Injection vein orientations can provide information on fault slip direction if surveyed systemically;
- Slip directions on OHFZ pseudotachylyte faults include top-to-NW, top-to-NE and top-to-SE;
- These slip directions represent dominantly reverse, left lateral strike slip and extensional faulting, respectively;
- Reverse faulting is generally oblique to some extent, extensional faulting is predominantly dip-slip. This is one reason why, although they occur on similarly orientated faults, these phases are considered separate kinematic episodes.
- Strike slip faulting can occur on faults in many directions, including as the oblique linking structures mentioned above. However, in the main fault zone they are predominately SE dipping and left-lateral, and this is considered as another kinematic phase, leading on from the oblique reverse slip.

Chapter 4

Characterisation of the depth and temperature of pseudotachylyte generation in the Outer Hebrides Fault Zone

4.1 Introduction

The chemical and physical behaviour of pseudotachylyte from its molten form through to crystallisation, and perhaps later alteration, records the evolution of the temperature of the pseudotachylyte bearing fault throughout the period of coseismic slip and beyond. Currently, the depth of pseudotachylyte -generating seismic activity in the Outher Hebrides Fault Zone is only loosely constrained between 5 - 10 km (Sibson and Toy (2006)) and the melt temperature is estimated around 1100°C (Sibson (1975)). Better constraints are needed, not only to improve understanding of the seismic environment in the OHFZ, but to improve the accuracy of parameters such as ambient temperature, coseismic temperature rise and depth that are often needed to quantify seismic energy terms. In this chapter, a mixture of semi-quantitative and quantitative approaches are used to successfully refine these values, based on

the compositional and microstructural features of OHFZ pseudotachylytes. The results allow a better understanding of the conditions of seismic activity identified in Chapter 3, facilitate comparisons to test the validity of experimental work in Chapter 5 and provide OHFZ specific parameters used to understand coseismic stress in Chapter 6.

The chapter begins with an outline of the techniques used, before presenting the results:

- Initially, the typical characteristics of OHFZ pseudotachylytes are described, in order to examine any systematic variations.
- Temperature analysis is supported by a study of the quenched crystal morphologies present in the pseudotachylyte. The relationship between cataclasites and pseudotachylytes are also examined, to investigate the balance of mechanical wear against thermal breakdown during coseismic slip.
- This approach is extended via analysis of pseudotachylyte host clast size populations and the ratio of survivor clasts to melt derived matrix in pseudotachylyte veins.
- The composition of the pseudotachylyte veins is then used to constrain the temperature and pressure of melt formation, initially through mineral and clast assemblages, followed by quantitative electron microprobe analysis and thermobarometry on pseudotachylyte matrix phases.

4.2 Methodology

4.2.1 Sample preparation and microscopy

The microstructural and compositional analysis involves both optical microscopy and scanning electron microscopy back-scattered electron (SEM BSE) imaging using a FEI Quanta 650 FEGSEM. BSE imaging was undertaken using an accelerating voltage of 20 keV and spot size of 5. Samples displayed here were prepared as thin sections, polished thin sections or polished blocks. Additional polishing with colloidal silica solution is required for the improved polishing of samples selected for analysis with electron backscatter diffraction (EBSD, Lloyd

(1987), Britton et al. (2016)).

Mineralogical and compositional analyses of pseudotachylyte phases, clasts and host rock minerals utilises a range of microscopy techniques. Optical microscopy is initially used to identify the mineralogy of larger crystals in the host rock and host rock clasts in the pseudotachylyte, but the small grain size of the pseudotachylyte matrix means that SEM techniques are necessary. Energy-dispersive X-ray spectroscopy (EDS) using Oxford Instruments' Aztec software is used to identify phases larger than 5 μm in diameter and to provide semi-quantitative analyses of the phase composition via the resultant spectra. An accelerating voltage of 20 keV, spot size of 5 and typical working distance of $\sim$ 12mm were used for EDS analysis. Electron backscatter diffraction (EBSD) analysis uses an 80mm X-Max SDD detector and KE Centaurus EBSD system, again with an accelerating voltage of 20 keV and spot size of 5. Results were plotted using Oxford Instruments' HKL Channel 5 software v.5.12.33.0. Measurements of spherulite shapes, and of clast area fractions, shape and size are processed from BSE images using the image analysis software ImageJ v.1.5g (Schneider et al. (2012)).

4.2.2 Quantitative compositional analysis

Major element analyses on pseudotachylyte samples from across the OHFZ were studied using the Cameca SX100 electron microprobe at the School of Geosciences, University of Edinburgh. Plagioclases and amphiboles in the vein and in the host rock were analysed; in total 165 analyses were taken. Adjacent amphibole and plagioclase crystals were analysed at each site, to ensure that exchange has likely happened between the two phases picked (Blundy and Holland (1990)). An accelerating voltage of 15 keV and spot size of 1 was used for analysis. Results are processed into weight percentages of oxides. The ideal analytical totals of total oxide weight percentages is >99.2 or <100.8 for plagioclase and >96.7% or <98.3% for amphibole, but those >98.5% or <101.5% for plagioclase and >96 or <99% for amphiboles were also considered, with caution. These ideal error bounds are derived from the $\pm$ 0.8% analytical error, whilst the ideal total of 97.5 % for amphiboles is due to an expected 2.5 % water content (Deer et al. (1992)). The use of additional analyses totaling outwith the $\pm$ 0.8%

error is due to the larger errors present in analysing resolution-limit crystal sizes present in pseudotachylytes, which results in a low number of datapoints if rejected. The analyses used are presented in Tables 4.1 and 4.2. Results are presented from the oxide weight percentages or as a calculation of the chemical formula, which is derived from the oxide weight % based on the number of anions plus a predicted number of O or OH (Deer et al. (1992)).

Vein phases in one of the samples analysed with EMPA, SU2, were also analysed using the EDS capabilities of the FEI Tecnai TF20 TEM at the Leeds Electron Microscopy and Spectroscopy centre, University of Leeds. For this technique, a 10 x 10 x 1 μm sized wafer was cut out of the pseudotachylyte vein sample (Wirth (2009)) using the focused ion beam (FIB) on the FEI Nova 200 NanoLab high resolution Field Emission Gun Scanning Electron Microscope at the University of Leeds. This wafer was then imaged in the TEM alongside EDS analysis, using an accelerating voltage of 200 keV.

4.2.3 Thermobarometry

Many published thermometers and barometers are available for both igneous and metamorphic assemblages (e.g. Ferry and Spear (1978), Kohn and Spear (1989), Blundy and Holland (1990), Ravna (2000), Klein and Koppe (2000)). Pseudotachylyte primary assemblages can be considered as igneous assemblages as they crystallise from melt. However, the melting and crystallisation processes are highly non-equilibrium under these circumstances due to the rapid heating and cooling experienced during fault slip. Non-equilibrium assemblages are unsuitable to use for geothermometry (Blundy and Holland (1990)). Alternatively, a devitrified or altered assemblage may crystallise within the pseudotachylyte once equilibrium conditions are restored, which would constrain a minimum temperature and pressure for pseudotachylyte generation. This study attempts to constrain temperature and pressure conditions during crystallisation or re-crystallisation of the OHFZ pseudotachylytes, and to test whether primary or devitrified assemblages are present, noting the continued uncertainty on this issue.

The hornblende-plagioclase thermometer was chosen due to the ubiquity of these phases in

Table 4.1: Major element analysis of pseudotachylyte vein amphiboles used for thermobarometry, with plagioclase X_An ratio. Analysis EDX9 was obtained using TEM EDS, all others are EMPA

VEIN							
Sample Number	*SU4*	*SU4*	*SU2*	*SU2*	*SU2*	*B7*	*B7*
Hbl analysis #	33/1	33/1	20/1	58/1	EDX9	17/1	25/1
SiO_2	43.57	43.57	49.09	57.33	47.34	49.46	48.79
TiO_2	1.00	1.00	0.88	1.13	0.00	0.74	0.41
Al_2O_3	16.13	16.13	8.15	17.75	10.89	10.46	11.02
FeO*	17.66	17.66	13.15	7.55	19.68	11.42	11.67
MgO	7.19	7.19	11.56	3.33	8.79	12.07	12.67
MnO	0.24	0.24	0.23	0.11	0.28	0.08	0.017
CaO	8.32	8.32	9.96	4.77	11.53	10.92	11.824
Na_2O	0.79	0.79	0.48	0.37	0.00	0.47	0.401
K_2O	3.77	3.77	2.53	3.70	1.50	1.24	0.33
F	0.06	0.06	0.49	0.18	0.00	0.13	0.04
Cl	0.10	0.10	0.16	0.06	0.00	0.04	0.01
Sum	98.82	98.82	96.68	96.28	100.00	97.03	97.18
Plag analysis #	30/1	31/1	23/1	59/1	EDX 1	22.00	22.00
X_{Ab}	0.56	0.61	0.54	0.07	0.63	0.71	0.71
X_{An}	0.44	0.39	0.47	0.93	0.37	0.29	0.29

Table 4.2: Major oxide analysis of host rock amphiboles used for thermobarometry, with plagioclase X_{An} ratio.

HOST																
Sample Number	*NU15*	*NU15*	*NU15*	*SU3*	*SU3*	*SU3*	*SU2*	*SU2*	*SU2*	*SU2*	*SU2*	*SU2*	*G1*	*SU4*	*SU4*	*SU4*
Hbl analysis #	3/1	4/1	5/1	34/1	32/1	33/1	2/1	4/1	9/1	14/1	15/1	16/1	4/1	15/1	13/1	14/1
SiO_2	45.95	46.21	46.23	41.52	41.36	40.81	41.12	41.28	40.15	40.90	41.28	41.43	42.28	44.04	43.45	43.41
TiO_2	0.88	0.87	0.87	1.00	1.29	1.57	3.63	1.37	1.28	1.41	1.48	1.51	1.19	0.22	0.22	0.22
Al_2O_3	10.25	10.33	10.42	11.78	11.94	11.47	12.15	11.56	11.73	11.53	11.48	11.48	11.71	12.05	12.92	12.21
FeO*	13.63	13.82	13.82	18.81	19.27	19.47	18.99	19.67	20.69	19.51	19.57	19.90	20.19	16.86	16.39	16.56
MgO	12.37	12.36	12.40	8.60	8.21	8.03	7.83	8.21	7.83	8.19	8.27	8.33	7.87	9.63	9.26	9.72
MnO	0.28	0.29	0.28	0.40	0.40	0.40	0.43	0.47	0.45	0.41	0.40	0.44	0.28	0.86	0.84	0.83
CaO	11.37	11.56	11.52	11.67	11.87	11.62	11.76	11.55	11.37	11.59	11.56	11.83	11.53	11.23	11.48	11.51
Na_2O	0.97	0.82	0.79	1.33	1.25	1.39	0.02	1.42	1.53	1.36	1.46	1.32	0.87	0.97	0.70	0.82
K_2O	0.69	0.67	0.68	1.51	1.56	1.57	1.63	1.64	1.70	1.64	1.62	1.54	1.28	0.98	1.06	1.01
F	0.11	0.14	0.15	0.17	0.13	0.16	0.18	0.15	0.16	0.19	0.20	0.18	0.07	0.09	0.06	0.09
Cl	0.00	0.01	0.01	0.15	0.14	0.13	0.23	0.21	0.25	0.23	0.24	0.23	0.16	0.03	0.04	0.04
Sum	96.48	97.07	96.15	96.91	97.40	96.62	97.92	97.54	97.12	96.95	97.55	98.175	97.42	96.97	96.44	96.42
Plag analysis #	2/1	2/1	2/1	37/1	37/1	37/1	7/1	7/1	11/1	19/1	19/1	19/1	1/1	16/1	16/1	16/1
X_{Ab}	0.47	0.47	0.47	0.66	0.66	0.66	0.51	0.51	0.54	0.58	0.58	0.58	0.53	0.54	0.54	0.54
X_{An}	0.53	0.53	0.53	0.34	0.34	0.34	0.49	0.49	0.46	0.42	0.42	0.42	0.47	0.47	0.46	0.46

pseudotachylyte veins sampled, the wide range of amphibole compositions that the thermometer is applicable to, and because it is valid for both igneous and metamorphic assemblages (Blundy and Holland (1990)). Aluminium in amphiboles may sit in the T1 site as Al^{iv} or in the M2 site as Al^{vi} (Deer et al. (1992)). The substitution of Al^{iv} can be shown to be both pressure and temperature dependent, and as much of the Al in amphiboles is Al^{iv} (Blundy and Holland (1990)), the total Al content is often used to relate to either temperature or pressure. Blundy and Holland (1990) argue that temperature is the major control on Al content. However, additional work has been able to isolate Al-in-hornblende as a geobarometer (e.g. Johnson and Rutherford (1989), Anderson and Smith (1995)).

The thermometer developed in Blundy and Holland (1990) uses a thermodynamic model based on two reactions representing the $NaAl^{iv} \rightleftharpoons \square$ Si substitution that use the phases amphibole, quartz and albite. The composition of co-existing plagioclase must therefore be known before applying the thermometer. An ideal plagioclase composition of $X_{Anorthite}$ <0.92, along with a temperature range of 500-1100°C and an amphibole content of <7.8 Si cations are the ideal constraints for using this thermometer (Blundy and Holland (1990)), and these are met by the samples used in this analysis. This technique was expanded on by Holland and Blundy (1994) to encompass both silica-saturated and undersaturated compositions, applicable in the temperature range 400-900°C and 500-900°C respectively for the two reactions used. These ranges cover temperature ranges that might be expected from devitrification or alteration of OHFZ pseudotachylytes , which formed in ambient temperatures that may have been >370°C (Osinski et al. (2001)), but do not cover the primary crystallisation temperatures of quartz and plagioclase (Spray (2010)).

EMPA and TEM EDS major element analyses of adjacent amphibole and plagioclase crystals were taken from the host rocks and pseudotachylyte veins of five samples, as described in section 4.2.2. The compositions of these are shown in Tables 4.1 and 4.2. The thermometers of Blundy and Holland (1990) and the two from Holland and Blundy (1994) are used to calibrate a temperature, using the spreadsheet 'Plagioclase-Hornblende geothermometry' supplied by the Mineralogical Society of America at *www.minsocam.org/MSA/RIM/RiM69_Ch04_hbld_plag_therm*

jla.xls. Pressures of 650 MPa based on Droop et al. (1999) who estimate metamorphic Laxfordian conditions on the mainland to have peaked at 650 ± 150 MPa, were input for the host rock analyses and a range of 130 - 330 MPa based on depth estimates of 4-10 km depth for pseudotachylyte generating faulting (Sibson (1975), Sibson and Toy (2006)) was applied to the vein analyses. Calculated pressures are also produced by the amphibole barometers of Schmidt (1992) and Anderson and Smith (1995).

4.2.4 Clast analysis

Unmelted clasts of host rock are frequently found in pseudotachylyte veins. These have variable size, similar to cataclasites and fault gouges which are often shown to have fractal or power law distributions (Blenkinsop (1991)). In pseudotachylytes the size distribution should be adjusted by the influence of melting and also by the size, type and spatial qualities of the pseudotachylyte vein sampled (Ray (2004)). The fraction of clasts in a given portion of pseudotachylyte vein, and the areas of the individual grains themselves, are measured using the image analysis program ImageJ (Schneider et al. (2012)) from 27 images taken from 19 samples (for clast size analysis) and 38 images from 19 samples (for the clast area to melt area ratio). Imaging at magnifications of 4x and occasionally 10x has produced images with resolutions of 0.82 and 0.32 microns per pixel, respectively. As the smallest clast size observed using BSE imaging is often on the order of 5 μm, the spatial resolution of imaging is not thought to be a problem. However, a few samples have clasts down to 1 μm, which may hence be unrecorded. Fragments smaller than the expected 5 μm, which may be real or may result from partial sampling of mid-shaded larger clasts during the thresholding method, are removed by filtering of the resulting image and of the measurements themselves. Multiple images are used for some samples with the average result being analysed. Errors were calculated by using one standard deviation.

The method of O'Hara (2001) is used to convert the ratio of clasts to pseudotachylyte matrix into a representation of thermal melting and mechanical wear processes. This approach is based on the equations for steady-state wear (W) - the mechanical breakdown of material

- and steady-state melt volume (M) from Scholz (1987) and Sibson (1975) respectively.

$$W = \frac{Ak\sigma_n u}{3h} \tag{4.1}$$

$$M = \frac{A\tau u}{q} \tag{4.2}$$

where A is the area of the fault; k is the wear coefficient; σ_n the normal stress; τ the shear stress; u the displacement; h a coefficient of hardness relevant to the strength of the asperities and q is the heat needed to melt the rock. The ratio of wear to melt where both are steady state is simplified to

$$\frac{W}{M} = \frac{kq}{3h\mu} \tag{4.3}$$

where μ is the coefficient of friction (O'Hara (2001)).

To relate these relationships to the temperature regime during coseismic slip, an assumption of adiabatic heating is carried. This appears theoretically valid due to the rapid generation and fall-off of the heating pulse, and because of the generally poor conductivity of rock - hence a slip rate (strain rate) above 0.1 m s^{-1} should ensure the process lies in the adiabatic regime (Spray (2010)).

When considering the total energy, E, during coseismic slip, the components are usually divided as (Scholz (2002)),

$$E = E_f + E_g + E_e + E_r \tag{4.4}$$

where E_f is the frictional work, E_g the gravitational work, E_e the fracture propagation work and E_r the work done to radiate seismic energy. E_e, E_g and often E_r may be variably considered negligible.

$$\frac{W}{M} = \frac{E_{wear}}{q} = \frac{T_{melt} - T_{ambient}}{T_{melt}} \tag{4.5}$$

where T_{melt} is the maximum temperature that the work facilitates on the fault plane, approximated by the melting temperature, and $T_{ambient}$ is the initial temperature of the rock before fault slip begins (O'Hara (2001)). This equation allows one of T_{melt} or $T_{ambient}$ to be

estimated if the other is known, as $\frac{W}{M}$ is estimated simply through the area ratio between clasts and melt within any pseudotachylyte vein (O'Hara (2001)). This method is applied to calculations of the clast to melt ratios in 19 OHFZ pseudotachylyte samples to test the constraints on T_{melt} and $T_{ambient}$ derived from compositional and microstructural approaches taken elsewhere in this chapter.

4.3 Results

4.3.1 Characteristic microstructures of pseudotachylyte veins

This section outlines the microstructures observed in OHFZ pseudotachylytes as evidence for a melt origin, for interaction with wear-processes and for the contribution of alteration or devitrification to the preservation of the primary structures and composition.

4.3.1.1 Typical microstructures

Pseudotachylyte veins under the microscope display many typical features regardless of the field scale geometry of the pseudotachylyte vein. The generation plane will cut through the host rock, forming a sharp transition at the margin (Fig. 4.1a). The host rock - generation plane contact is generally fairly straight, although steps in the margin are common (Fig. 4.1a). Injection veins branch off the main vein, often at a high angle, and protrude with varying lengths and thicknesses into the host rock. Tips of injection veins break down via segmentation or wing-crack like features (Fig. 4.1b). Injection veins often exploit earlier features in the host rock such as fractures, grain boundaries or easily deformed or melted minerals such as biotite. Pseudotachylyte breccias and some irregular shaped injection veins can show blocky, irregular shapes in thin section, similar to those seen at the outcrop scale.

Microscopic confirmation of the presence of melt-derived pseudotachylytes, rather than misidentified ultracataclasites, utilises the characteristic melt microstructures described in Maddock (1983), also on OHFZ samples. With regards to the surviving clasts of host rock

which are always found in the pseudotachylyte veins, the presence of embayments or rounded edges is often seen, particularly in plagioclase clasts but also in any other clast mineralogy (Fig. 4.2). Similar features occur as embayments or injection vein into vein margins.

In OHFZ pseudotachylyte samples analysed here, the vein matrix is never seen to be truly glassy under the highest SEM magnifications, although some appear so at lower magnifications and under the optical microscope. The finest grain sizes may be <1 μm in these superficially glassy regions, so that they are on the visible resolution limit of SEM imaging. Generally, pseudotachylyte vein phases rarely exceed ~ 50 μm in length, and are frequently much finer. The best developed crystalline phase tends to be plagioclase, which may form a range of crystal morphologies ranging from tabular microlaths through skeletal to more dendritic forms (Fig. 4.3a). These plagioclase crystals commonly show heterogeneous nucleation on host rock clasts of both plagioclase and quartz, and may form radiating microlites (Fig. 4.3b). Other pseudotachylyte vein phases such as hornblende, biotite and iron oxide tend to form along with further plagioclase as the interstitial phases, with less defined crystal shapes (Fig. 4.3a). Spherulites are seen in several samples with circular (spherical or ellipsoidal in 3D) morphologies which appear almost glassy but show exsolution of phases at high magnification - these spherulites form around a nucleus of crystalline phases, clasts or in isolation (Fig. 4.4).

4.3.1.2 Relationships between pseudotachylytes and cataclasites

If cataclasite and pseudotachylyte co-exist in a vein, it is important to recognise whether the cataclasite formed in an older slip event, so that the slip that generated pseudotachylyte occurred on a pre-existing fault, or whether the two fault rocks are synchronous, in which case some other explanation is required. In the sample SU3, a pseudotachylyte breccia, cataclasite and pseudotachylyte dominate different parts of the matrix (Fig. 4.5), although it appears that the finest groundmass fraction of the cataclasic part contains low volumes of crystallised melt, having thin, lath like plagioclase and hornblende. In simple planar fault veins, too, the clast component can increase so much at the margins of the vein that it appears to be almost entirely cataclasite (Fig. 4.7). Alongside the changing clast percentage, crystal size decreases

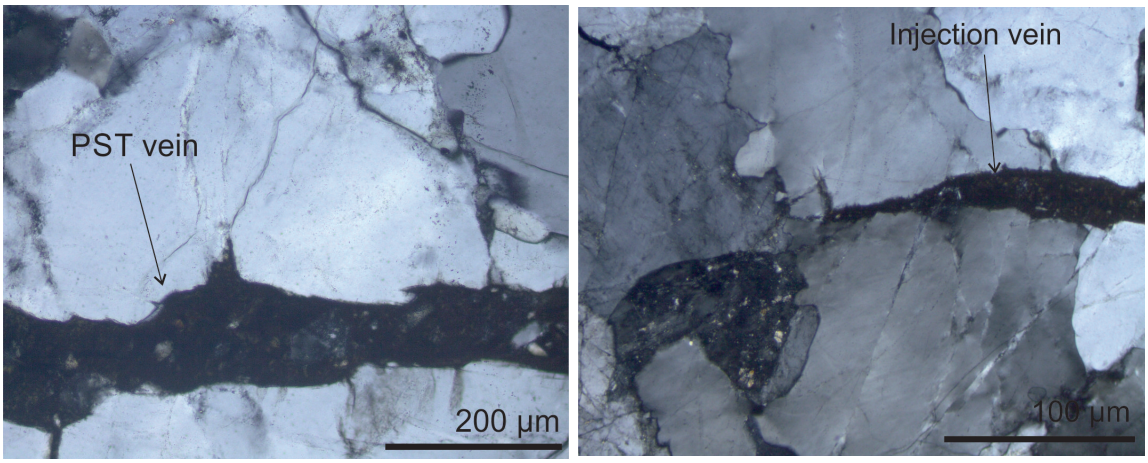

(a) (b)

Figure 4.1: Features of pseudotachylyte veins cutting through host rock: a. Cross polarised light image of pseudotachylyte vein cutting through quartzofeldspathic host rock. Steps in the vein boundaries are seen at regular intervals, along with small injections exploiting microfractures (sample SU4); b. Cross polarised light image of tip of injection vein, showing small branch at tip. Irregularities in vein margin are seen controlled by grain boundaries and microcracks (SU4).

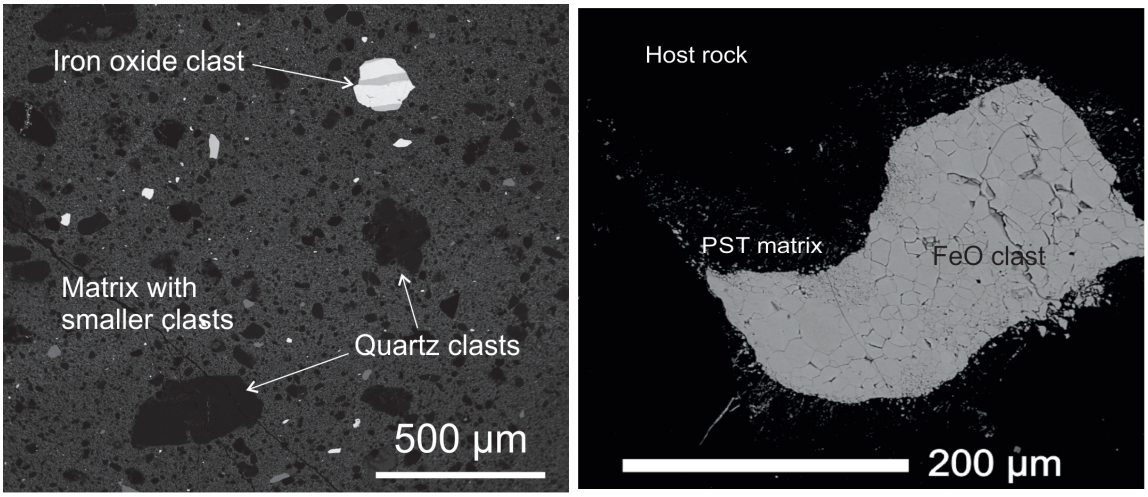

(a) (b)

Figure 4.2: Melt derived features of clasts in pseudotachylyte veins: a. BSE image of sample SU2, large clasts are an iron oxide (pale) and quartz (dark) showing melting-derived embayments. Smaller clasts predominantly quartz, iron oxide and plagioclase b. BSE image of an iron oxide clast being deformed both by mechanical spalling and thermal melt embayment within small pseudotachylyte pocket (SU4).

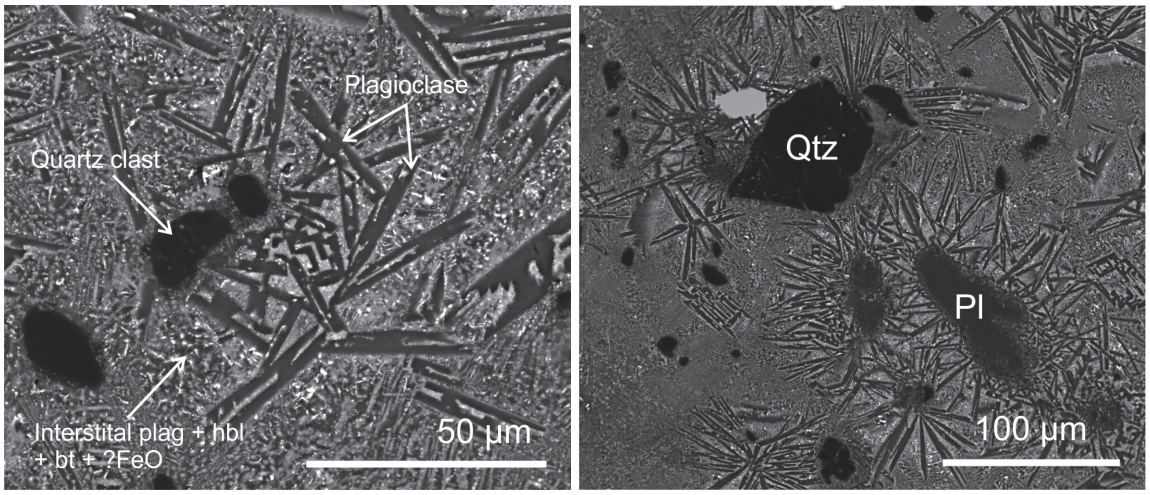

(a) (b)

Figure 4.3: Pseudotachylyte matrix phases: a. Skeletal plagioclase microlaths crystallising in the matrix of pseudotachylyte in sample SU2. The interstitial matrix is composed of plagioclase (plag), amphibole (hbl), biotite (bt) and iron oxide (FeO); b. Typical radiating microlitic texture of plagioclase microlaths in SU2 nucleating around clasts of quartz (darkest grey in BSE image) and plagioclase (second darkest grey)

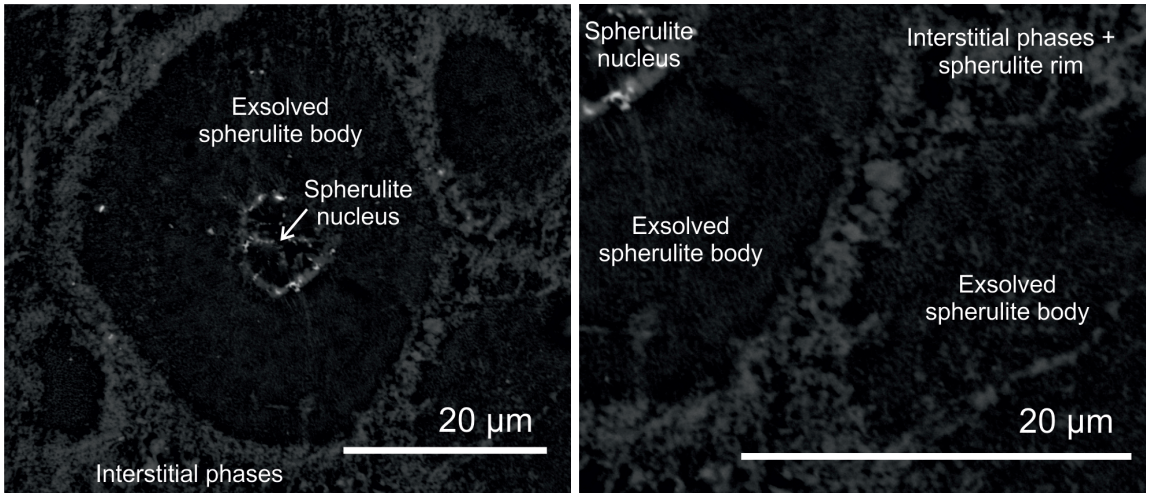

(a) (b)

Figure 4.4: Spherulites in pseudotachylyte veins: a. Individual, zoned spherulite typical of those seen in sample B7; b. Magnified image of 4.4a showing stringy exsolution of light and dark phases in body of spherulite (B7).

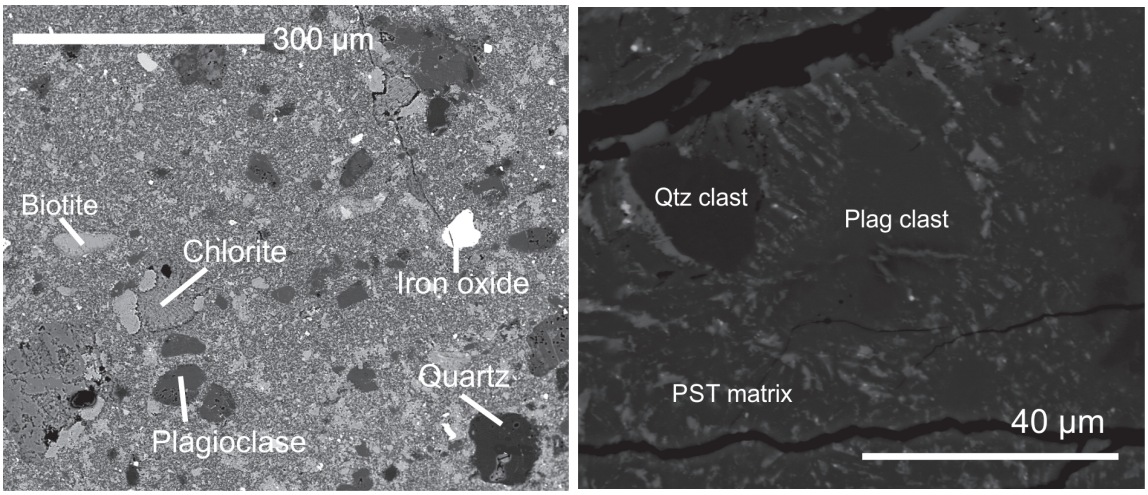

(a) (b)

Figure 4.5: Cataclasite - melt relations within pseudotachylyte veins: a. BSE image showing variety of clast mineralogies in a dominant cataclastic in part of matrix of sample SU3; b. BSE image of melt-derived crystalline texture identified in the matrix of the breccia in sample SU3.

from the centre towards the wall and the crystal morphology also changes from radiating skeletal or spherulitic forms in the vein centre through to more tabular, and increasingly more equant, crystals towards the walls (Fig. 4.7).

In contrast, other samples have a a sharp margin, rather than a gradual transition, between the cataclasite and pseudotachylyte which may obviously truncate fabrics in the older cataclasite (Fig. 4.6a). The presence of pre-existing cataclasite is common in the rocks hosting the pseudotachylyte in many samples, including those previously mylonitised. However, the pseudotachylyte vein is often non-parallel to that cataclasite bands. Where the two are parallel, the pseudotachylyte may cut through the centre of the cataclasite zone, or to one side so that cataclasite is observed only on one wall of the pseudotachylyte (Fig. 4.6b).

4.3.1.3 Primary and devitrification microstructures

Many of the microstructures and crystal morphologies observed are ambiguous as to whether they formed during primary crystallisation, devitrification of a primary glass, or due to later alteration. Distinction is important if compositions are to be used for temperature and pres-

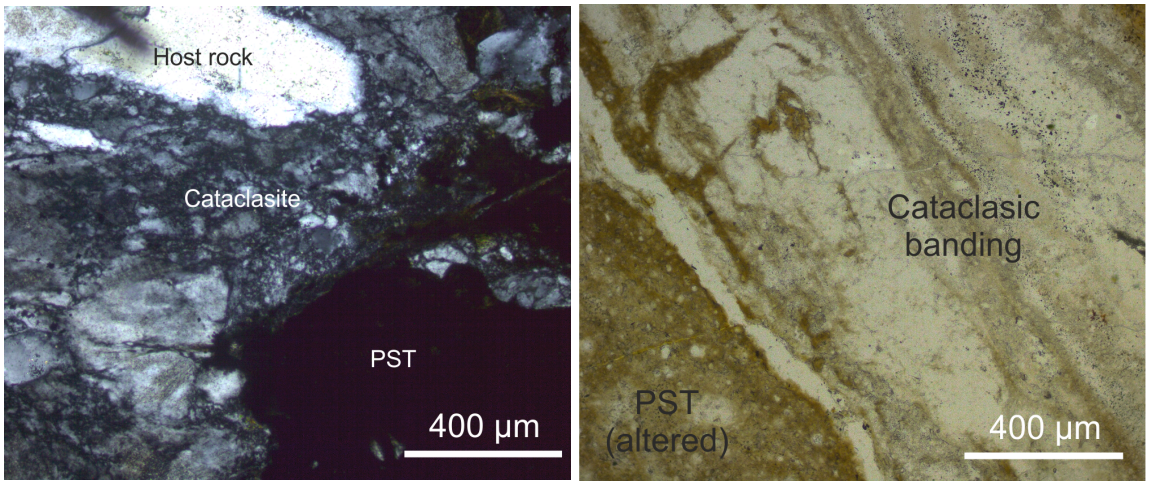

(a) (b)

Figure 4.6: Relations between pseudotachylyte veins and previous brittle structures: a. Pseudotachylyte cuts through margin with pre-existent cataclasite, sample SU2; b. Pseudotachylyte vein parallel to, and assumed to be reactivating, cataclasic banding in sample NU22.

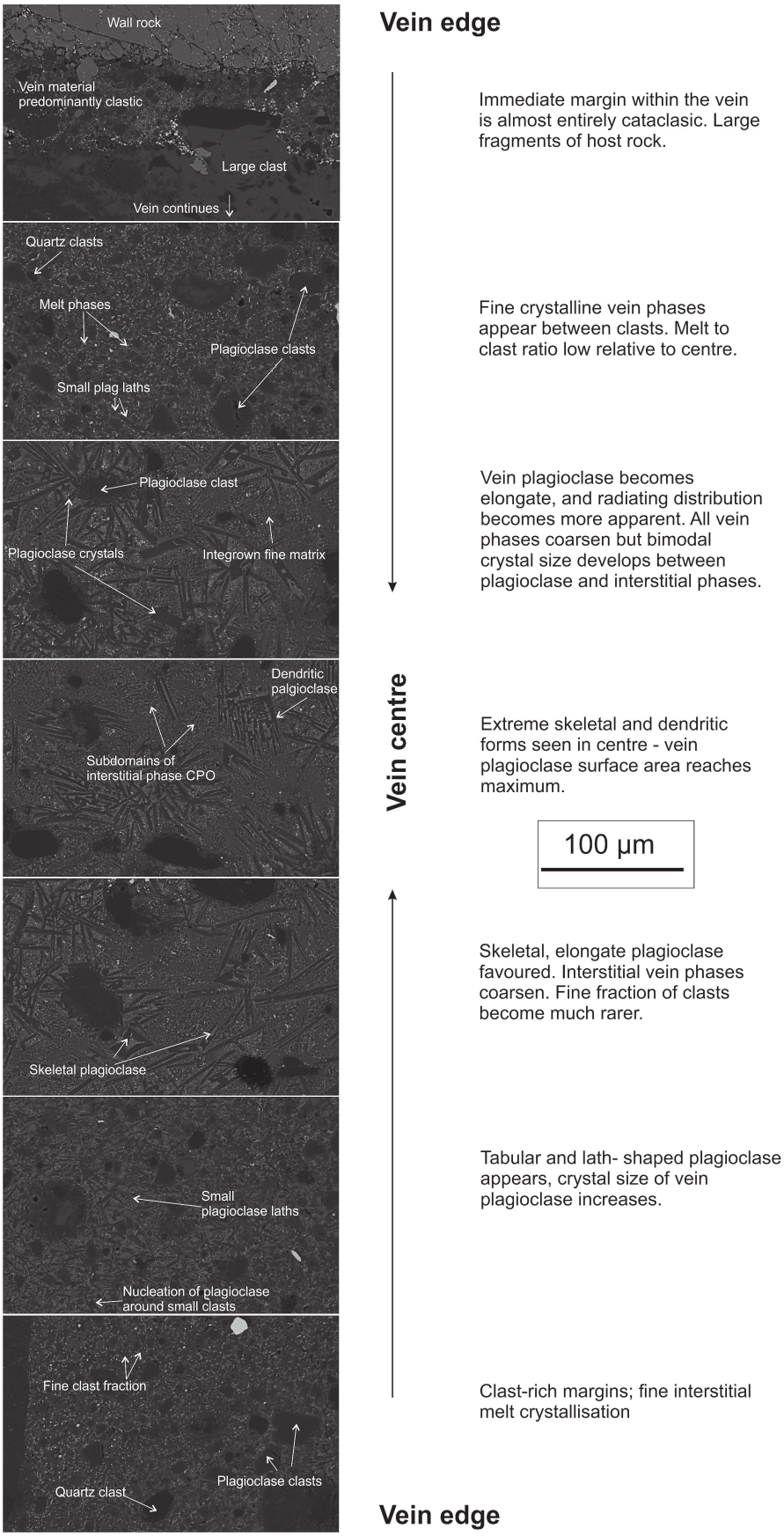

Figure 4.7: Transect through $\sim$ 2 mm wide fault vein in sample SU2 showing changing clast and crystalline textures across vein

sure constraints. This section outlines the evidence for preservation of primary crystallisation in OHFZ pseudotachylytes.

Rapid undercooling (quench) textures in OHFZ pseudotachylytes include diffusion fronts around spherical features (Fig. 4.8a), skeletal crystals (Fig. 4.3a), radiating microlath structures (Fig. 4.3b) and spherulitic textures (Fig. 4.4). However, several microstructures are common to both primary undercooling textures and devitrification, including spherulites and dendritic crystals (e.g. Lofgren (1971), Lofgren (1974)). Pseudotachylytes are often referred to as glassy but in practice there is no physical reason why the presence of glass should be expected unless the rate and magnitude of undercooling below the solidus temperature specifically favoured it (Lofgren (1974)).

Spherulites in the pseudotachylyte matrix tend to appear circular and often undeformed in the sectioned plane. An exception, sample B7, has spherulites with radial cracks, filled with material continuous with that on the edges of each spherulite (Fig. 4.9b). Shape analysis on spherulites across this sample determine that few spherulites are circular in 2D; in fact the modal axial ratio is 0.7 (Fig. 4.10a). Fig. 4.9a shows the variation in the shape of the spherulites as they grow together, with several more elongate examples forming in 'chains' of attached individual spherulites. Analysis of preferred spherulite orientation in Fig. 4.10b shows the clockwise angle between the major axis of the best-fit ellipse for each spherulite and the vein wall. A wide variety of orientations are present. However, maxima parallel, perpendicular, and at a small angle ($\sim$30°) to the vein wall can be identified (Fig. 4.10b).

In Fig. 4.9b typical conjugate cracks are seen in some of the spherulites. These intersect at angles of $\sim$60 (or 120)° or closer to 90°. The long axes of spherulites are rarely aligned with these orientations (Fig. 4.10b). The fractures are often seen in the orientation shown in Fig. 4.9b, where the bisector of the obtuse microfracture intersection is perpendicular to the wall. In macroscopic Andersonian faulting this would represent the minimum compressive stress, but actually the offsets show extension parallel to the wall (Fig. 4.9b), suggesting that the spherulites have been compressed perpendicular to the wall (Fig. 4.9a). A similar effect

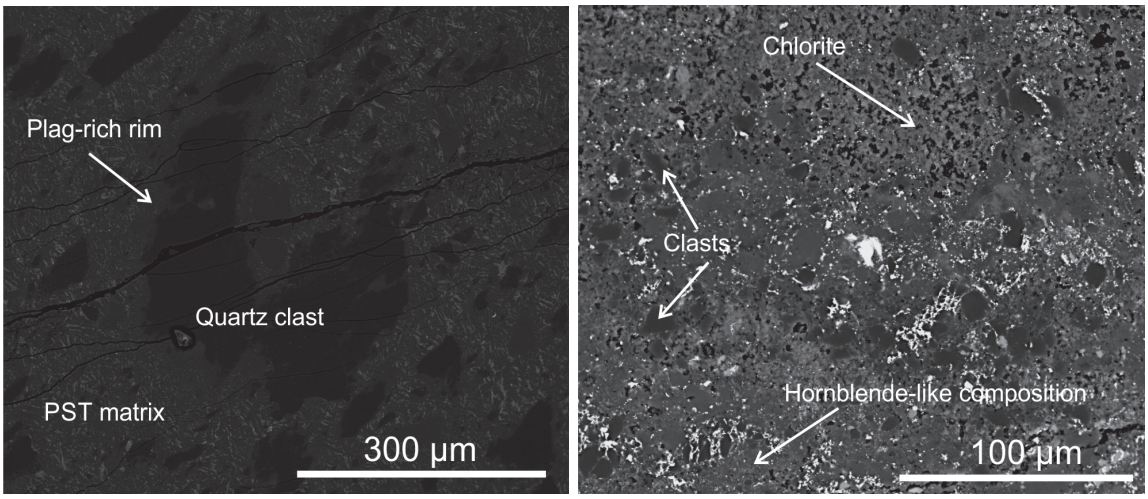

(a) (b)

Figure 4.8: Textures of pseudotachylyte crystallisation and alteration: a. Quartz clasts with haloes of plagioclase-rich aphanitic vein material, SU3; b. Altered pseudotachylyte in sample SU9.

is seen in the 'chains' of small spherulites, which also have their long axis parallel to the wall (Fig. 4.9a).

Despite the occasional presence of flow-banding, there is an absence of shape-preferred orientation (SPO) in the crystalline phases of pseudotachylyte samples from the OHFZ. This can most clearly be seen in the frequency of microlathes of plagioclase radiating in all directions, or in the random alignment of plagioclase in more holocrystalline vein matrices (Figs. 4.3b). This random alignment is shown in the EBSD analysis of the radiating plagioclase of sample SU2 (Fig. 4.11) where the Euler colour map shows that the elongate plagioclase radiates around the clast. The colour of the microlathes in Fig 4.11b is variable within any one area but may change steadily around a clast, hence there is no crystallographic preferred orientation (CPO) present.

4.3.2 Crystalline textures and undercooling

Several of the crystalline textures already discussed above, particularly spherulites, skeletal and acicular forms, plus the extremely fine interstitial matrix, are representative of rapidly

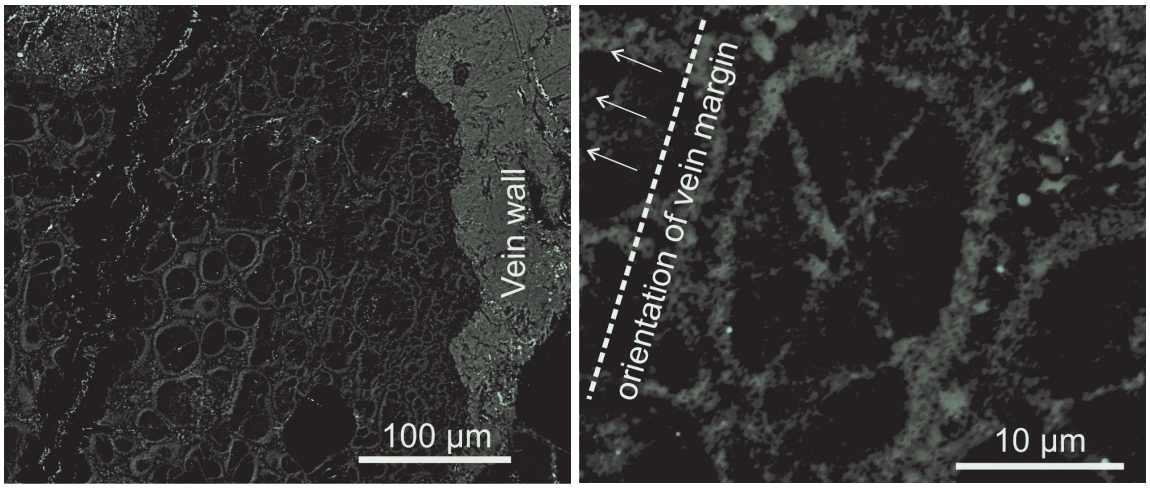

(a) (b)

Figure 4.9: Deformation of pseudotachylyte spherulites: a. Texture of spherulitic matrix in sample B7, showing fining of spherulites towards wall, some seemingly elongated parallel to wall and small 'chains' of conjoined spherulites, also wall-parallel; b. Spherulite showing conjugate cracks and their orientation relative to the vein wall, sample B7.

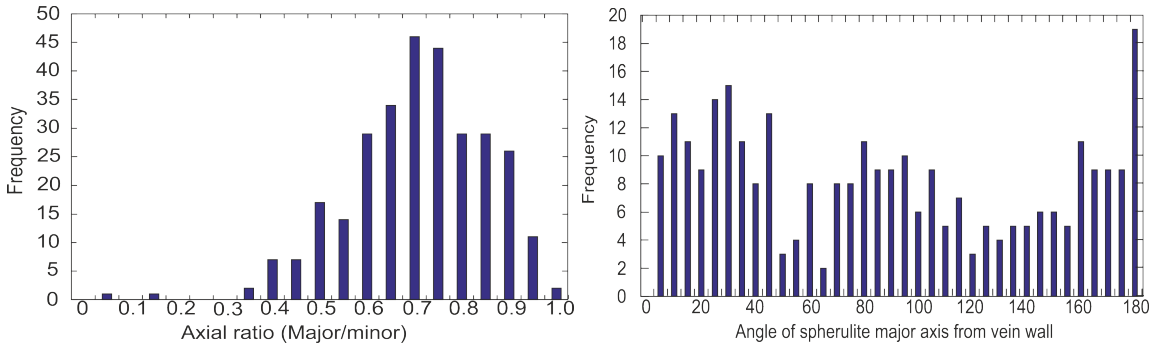

(a) (b)

Figure 4.10: Analysis of spherulite geometry in pseudotachylyte sample B7: a. Histogram of axial ratios seen in spherulites in sample B7; b. Histogram of the orientation of spherulite long axes relative to the vein wall in sample B7 (near vertical in images).

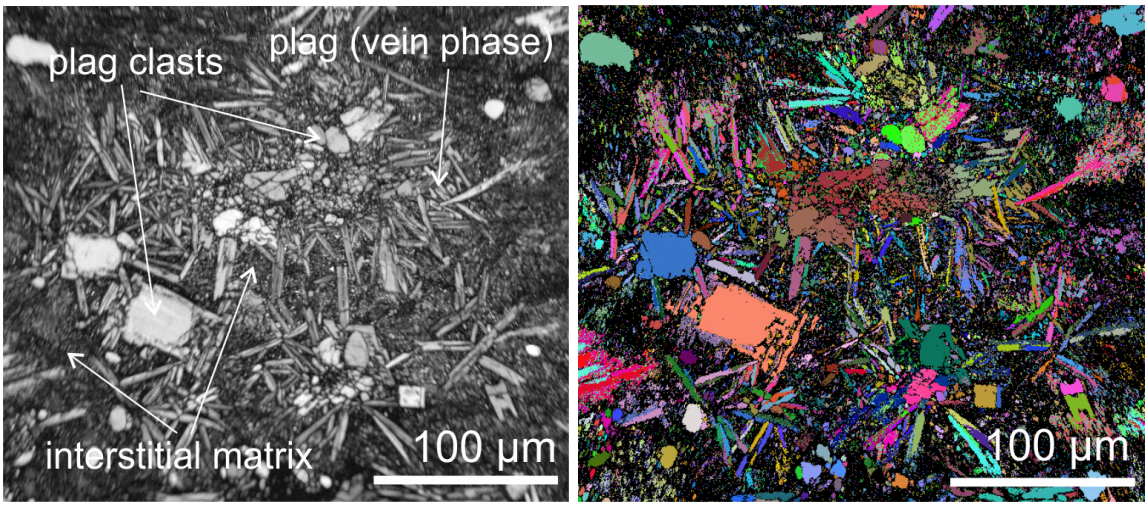

(a) (b)

Figure 4.11: EBSD imaging of pseudotachylyte vein SU2: a. Band contrast image of pseudotachylyte vein matrix in sample SU2. Fragmented plagioclase clasts are surrounded by radiating laths of crystallising plagioclase, between which is formed a mixed interstital unresolvable matrix of amphibole, iron oxides, plagioclase and possibly biotite; b. Colour map of Euler angles over the area shown in Fig. 4.11a. Colour represents lattice preferred orientation.

undercooled melts (Lofgren (1974)). The crystal shape, which in these pseudotachylytes most readily presents the best forms in plagioclase, can be indicative of the magnitude of undercooling, as Fig. 4.12 shows. Based on this graph, and knowing the composition of the plagioclase - which is constrained to $X_{Anorthite}$ = 0.23-0.34 in samples analysed by EMPA, and an oligoclase-andesine range more generally - allows some estimation of the change in temperature (Δ T) during crystallisation.

Pseudotachylyte in sample SU4, where best preserved, displays tabular, almost skeletal plagioclases often in a radiate texture (Fig. 4.14). Using the SU4 plagioclase compositions ($X_{Anorthite}$ = 0.23-0.28), ΔT is predicted to be between 800-870 °C (Fig. 4.12). Sample SU2 has higher average plagioclase Ca content ($X_{Anorthite}$ =0.28-0.34). The pseudotachylyte vein in sample SU2 is in general better preserved, and has been studied in more detail than sample SU4. Broad variations across the vein are shown in Fig. 4.7. These different crystal morphologies can be linked to differences in the magnitudes of undercooling (Fig. 4.12). A progression is seen from fine, tabular plagioclase near the margin of the vein, through skeletal, elongate forms to some internally branching dendritic forms in the vein centre (Fig. 4.7).

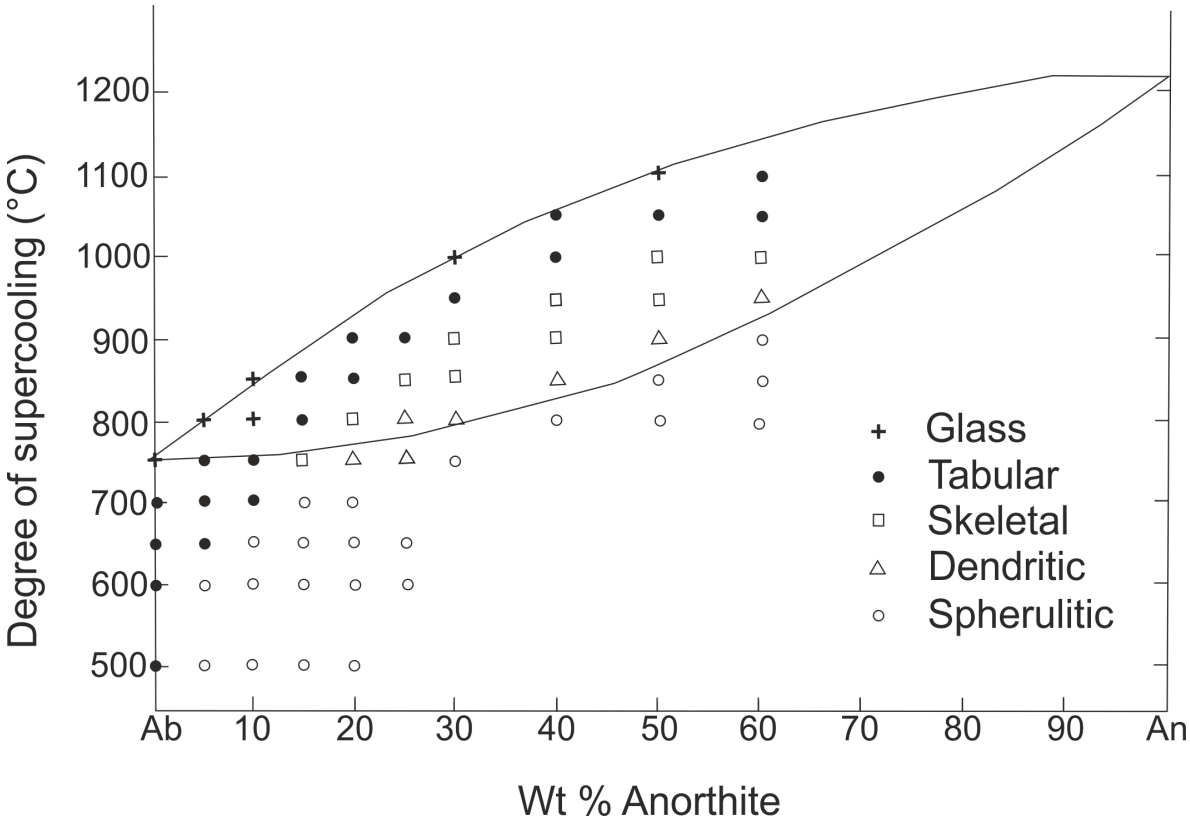

Figure 4.12: Plot showing experimental results of Lofgren (1974), displaying the crystal morphologies of plagioclase compositions expected from differing magnitudes of undercooling.

This progression shows variable undercooling (Fig. 4.13), from 915-1000°C near the wall to 752-843°C in the centre of the vein. The maximum ΔT of 1000 °C provides a minimum melt temperature, using the ambient conditions of 230-370°C in the southern section of the OHFZ (Osinski et al. (2001), Imber et al. (2002)), where sample SU2 originates, of 1230-1370°C.

4.3.2.1 Initial interpretations of microstructural results

Evidence for a melt origin are seen in these pseudotachylyte samples, according to the classification of (Maddock (1983)). A common observation is rounding and embayments in quartz and plagioclase, which is attributed to the effects of partial melting and heating (Gibbs-Thompson effect) on these clasts (Hirose and Shimamoto (2005)). Similarly, the embayments into amphibole and biotite in the vein wall are due to preferential melting of these minerals at their lower single-crystal melting temperatures (Spray (2010)).

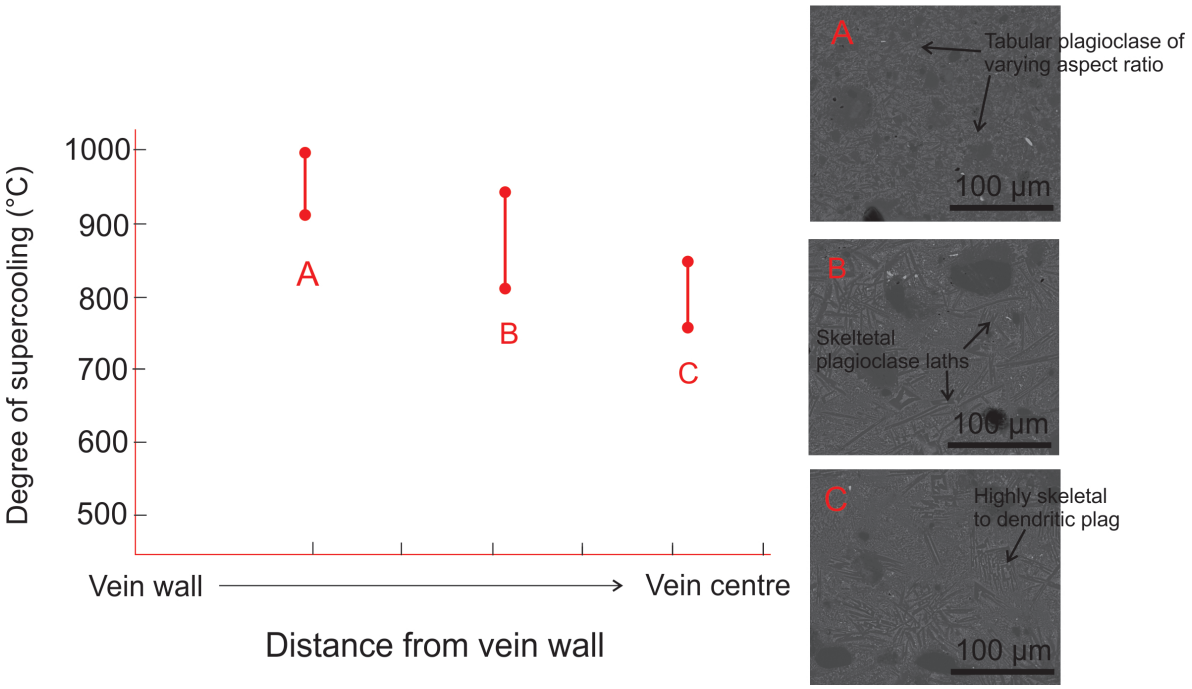

Figure 4.13: Schematic diagram showing change in Δ T with position in vein (SU2) based on experimental data from Lofgren (1974)

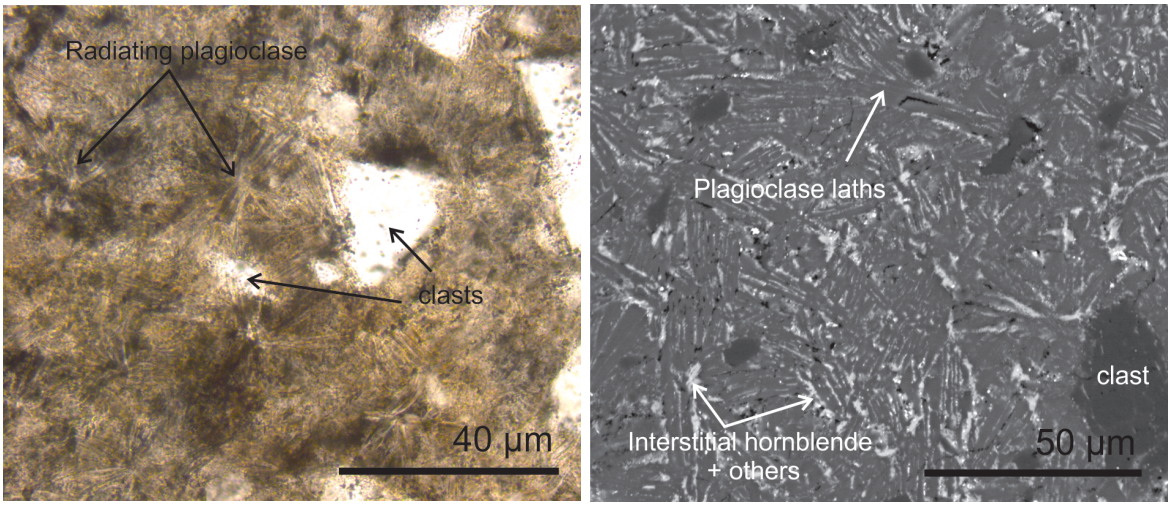

(a) (b)

Figure 4.14: Pseudotachylyte matrix of sample SU4: a. Plane polarised light image of radiating plagioclase laths (white) in brown matrix of pseudotachylyte in sample SU4; b. BSE image of radiating plagioclase laths in matrix of pseudotachylyte in sample SU4.

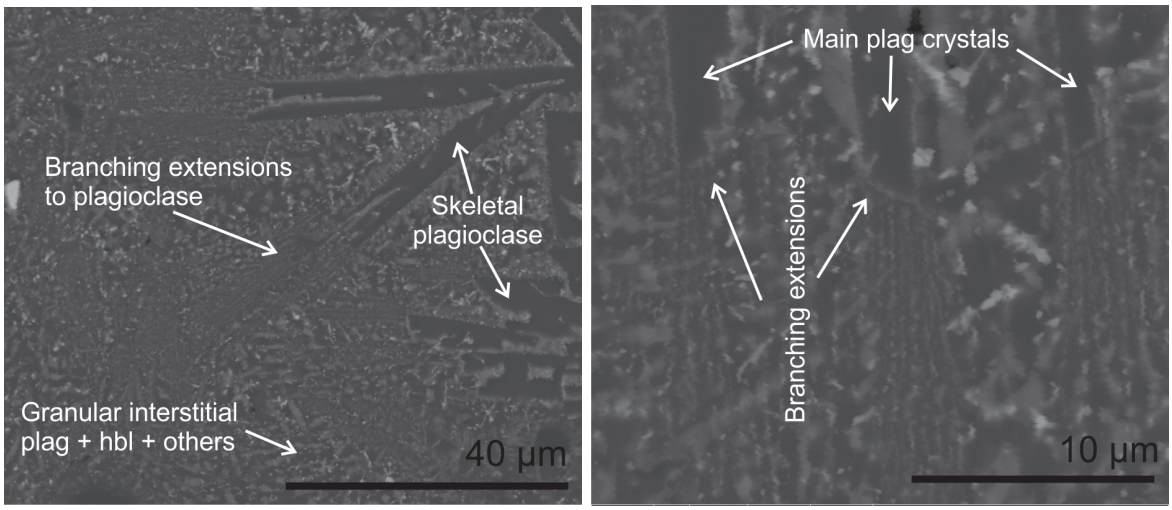

(a) (b)

Figure 4.15: Branching spray morphology of undercooled plagioclase in pseudotachylyte vein: a. BSE image of pseudotachylyte in sample SU2 showing branching sprays of continued growth from elongate skeletal plagioclase laths; b. High magnification image of branching sprays.

Gradual and sharp transitions between pseudotachylyte veins and cataclasite represent different processes. Where the cataclasite is dominant near the margin of the vein, but gradually decreases into the centre (e.g. Fig. 4.7), represents a transition in the amount of melting relative to mechanical breakdown of the fault walls. This could be influenced by temperature gradient across the vein, as margins cool due to conduction of frictional heat into the wall rock, and the progressive damage of the fault walls concentrating the broken down material in their vicinity. The presence of a temperature gradient across the vein is supported by the changing crystal morphology along the same transect (Fig. 4.7, also Lofgren (1974), Di Toro and Pennacchioni (2004)). Hence, pseudotachylyte and cataclasite are synchronous in this case. In the examples where the transition between pseudotachylyte and cataclasite is sharp, or cataclasite is present outside of and parallel to the pseudotachylyte vein (Fig. 4.6b), the cataclasite is a precursor to the frictional melting event. However, the number of samples where pseudotachylyte is observed to cut through a parallel band of cataclasite, i.e. reactivates a pre-existent fault plane, is relatively small.

The varying crystal forms of plagioclase across the pseudotachylyte vein in the sample

SU2 are consistent with a model of rapid undercooling of a melt where heat is lost at the vein margins, giving a variable temperature and cooling profile. It is likely that sample SU2 preserves the primary crystalline texture in the skeletal plagioclase phenocrysts. A minimum peak melt temperature of 1230-1350°C is derived from addition of the magnitude of undercooling to minimu ambient temperature. This range is consistent with the lower range of estimates from clast mineralogy.

Many of the crystal morphologies identified in section 4.3.1.3 as typical of rapid undercooling expected in pseudotachylyte veins (Caggianelli et al. (2005)) are potentially ambiguous because they may also form during devitrification. However, the deformed spherulites in sample B7 (Fig. 4.4) and their SPO relate not to slip or flow direction in the molten pseudotachylyte, but to a vein perpendicular force such as the post-seismic vein closure. As the fractures are filled with material similar to the spherulite rim, the compressive force must be synchronous with the latest stages of crystallisation. If the compression does result from vein closure on solidification, then the spherulites are primary structures. It is possible that devitrification was partial in many samples, with primary glassy patches devitrifying and primary crystals being preserved. This could be the case in, for example, sample SU2 which displays skeletal to dendritic radiating plagioclase microlaths surrounded by a much finer, anhedral and equant matrix of plagioclase and hornblende (Fig. 4.3a). Further support for primary plagioclase laths is provided by the observed transition to more tabular crystal morphologies towards the vein walls, which fits well with the expected variation in undercooling (Lofgren (1974)) due to the temperature profile across the vein (Di Toro and Pennacchioni (2004)). Additionally, although the spherulites in Fig. 4.4 seem primary, the body of the spherulite displays very fine intergrowth textures (Fig. 4.4b) which could result from later crystallisation of a mixed glass. In contrast, the pseudotachylyte sample in Fig. 4.8b shows a patchy texture, often associated with chlorite. This is related to fluid-present alteration, so that the primary assemblage is obviously not preserved. However, other than these examples, many samples carry remaining uncertainty over whether they preserve primary supercooling or later devitrification microstructures.

4.3.3 Clasts as markers of temperature and deformation processes

Survivor clasts of the host rock are ubiquitous in all pseudotachylyte samples taken for this study. The mineralogy of the clasts can vary, depending on the extent of melting and temperature of the melt, and the volume of clasts commonly changes between veins or even along different sections of the same vein (section 4.3.1.2). The proportion of unmelted host rock clasts to relative to the pseudotachylyte matrix, once melt, represents the balance between wear and melting processes.

4.3.3.1 Mineralogy of clasts

Clasts seen in the OHFZ pseudotachylyte samples are predominantly quartz and plagioclase. Other contributions may include potassium feldspar, zircon and iron oxides, depending on what is present in the host rock (Fig. 4.2). The main variation in the quartzofeldspathic host rock mineralogy of sampled pseudotachylytes is the amount of hornblende and biotite, but an increase in these minerals does not affect the dominance of quartz and plagioclase as clasts. The presence of amphibole, biotite or chlorite as clasts is generally indicative that the fault rock is predominantly cataclasite or ultracataclasite, as in Fig 4.5a. Microstructures in the clasts present in pseudotachylytes indicate the maximum temperatures reached during frictional heating. Fig. 4.2a shows two large clasts, of quartz and iron oxide, with the quartz in particular showing marked concave embayments. Fig. 4.2b illustrates a similar feature in an iron oxide clast. Although mechanical spalling can be seen, especially on the lower edge, the largest modifier of the initial grain shape is the large concave indentation in the upper surface. Around the clast, redistribution of Fe - rich phases are seen crystallising throughout the pseudotachylyte matrix.

4.3.3.2 Size distribution of clast populations

Results for clast areas measured using image analysis were plotted on a log-log plot from which the D-value, or fractal dimension, can be derived using a regression line on the main

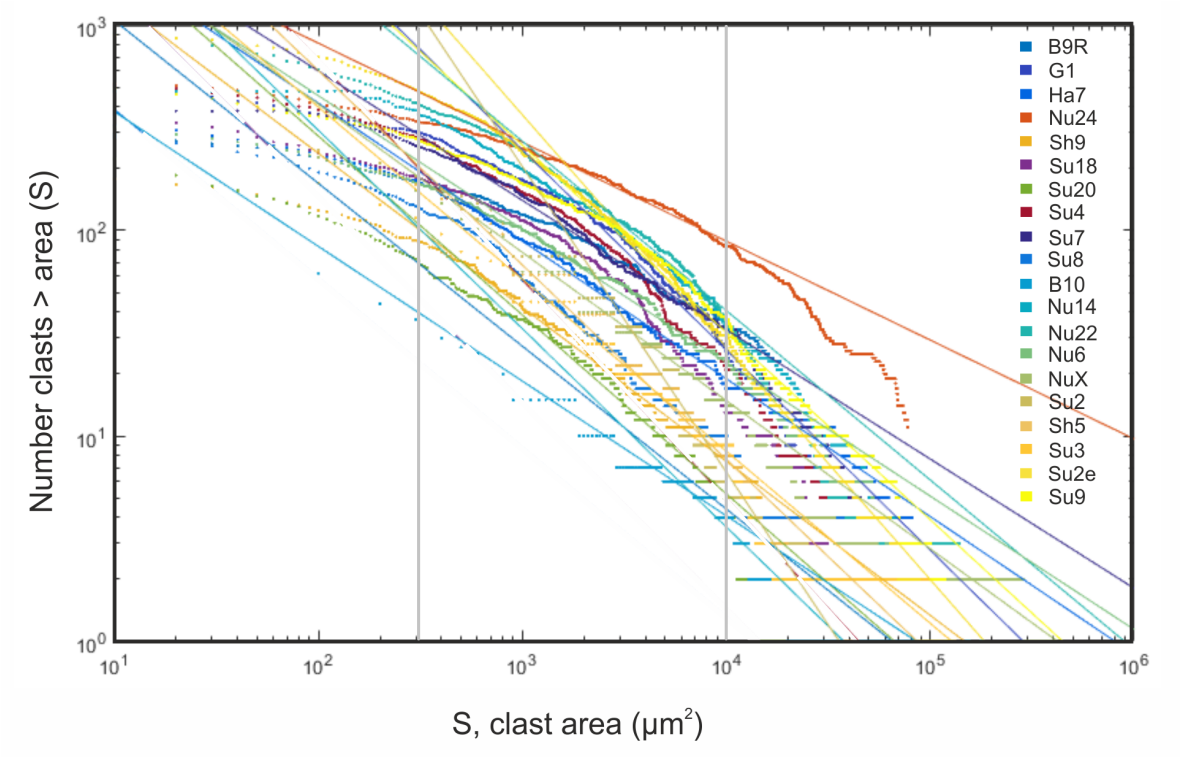

Figure 4.16: Frequency of clast sizes in pseudotachylyte samples. Shown on a log-log scale, the distribution for each pseudotachylyte vein is represented as the number of clasts larger than the specified area. Grey lines indicate the typical fractal range although this may vary for individual samples lying outside the main distribution.

section of the distribution (Blenkinsop (1991)). The results form a broad range with clusters of overlapping distributions flanked by overlapping outliers (Fig. 4.16). All distributions show a fall-off at either end, which is probably related to limitations in observational resolution. Clasts which are only partially included in the image are not measured during the analysis process and this means that many larger clasts are not included.

The fractal D-value is calculated from the gradient of the 'linear' portion of the log-log distribution (Fig. 4.16). The gradient can be described by the power law $N \propto S^{-D}$, where N is the number of clasts larger than area S (Ray (1999)). D-values for these samples are displayed in Fig. 4.17. Although the mean D-value is 0.801 $\pm$0.18 (to 1 s.d.), it seems that several values lie between 0.7 - 0.9, with others higher. There appears to be no correlation between the type of vein and the D-value, although the sample set is small. This is the two-dimensional D-value (D_{2D}); the 3D equivalent can be calculated as $D_{2D} + 1$ (Sammis et al.

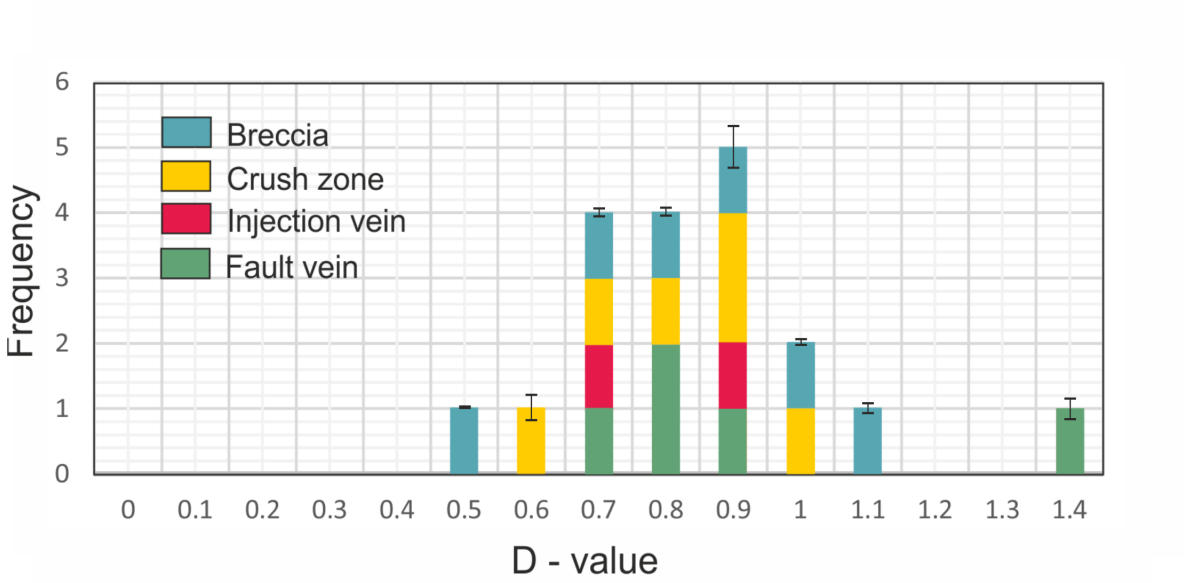

Figure 4.17: Fractal D-values (2D) indicated by Fig. 4.16. Error bars represent ± 1 standard deviation error for measurements on each sample, totalled for each bin.

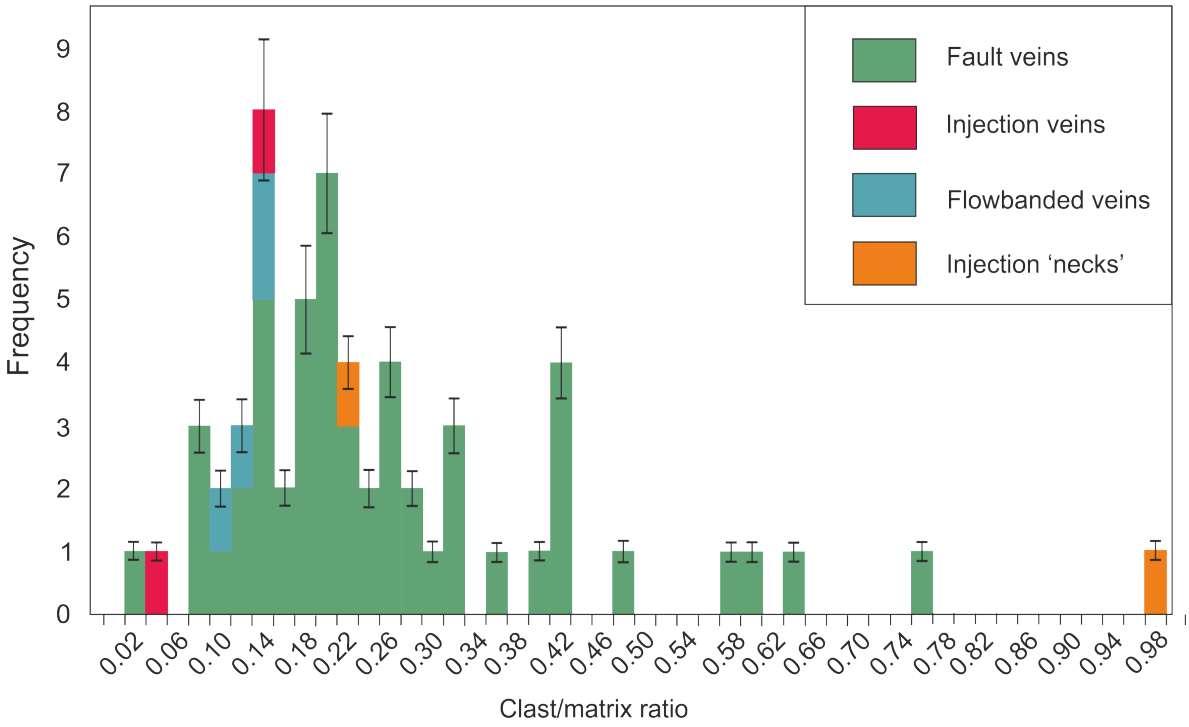

Figure 4.18: Ratio of wear to melt processes (based on the ratio of clasts to melt) in pseudotachylyte samples from different contexts. Error bars represent 1 s.d. for each sample from multiple measurememnts summed per bin.

(1987)).

The ratio of clasts to matrix, representing the balance of wear and melting processes (O'Hara (2001)), is calculated here using method. A ratio approaching 1 corresponds to predominantly clast material, with the quantity of pseudotachylyte matrix (melt) increasing as the value approaches zero. Out of 38 images assessed, a mean of 0.249± 0.21 (1 s.d.) was calculated between the range 0.09-0.65 (Fig. 4.18).

4.3.3.3 Application of the geothermometer

The range of clast to melt ratios is also reflected in Fig. 4.19, which visualises results from the relationship given in Eq. 4.5. Results shown here use a mean ratio from each sample. A higher ratio of clasts, relative to pseudotachylyte matrix, gives a steeper line on Fig. 4.19. The suggested melt temperature (T_{melt}) range of 1250-1550°C is indicated - this includes higher temperatures that may occur transiently above the range concluded in section 4.3.2. From this input, the range of ambient temperatures ($T_{ambient}$) predicted by the graphed change in melt temperature to be between 720-1225°C (Fig. 4.19. If instead the ambient temperature is used for the input value to predict the melt temperature, for example using a value of 350°C (Imber et al. (2002)), the resultant range of predicted T_{melt} is only 490-670°C (Fig. **??**. When the error range produced from adding or subtracting one standard deviation from each sample's $\frac{W}{M}$ is also considered, the possible range for $T_{ambient}$ when T_{melt} is in the range 1250-1550°C becomes 240-1390°C.

4.3.3.4 Initial interpretation of clast observations

A range of melt derived microstructures have been identified and allow determination of pseudotachylytes from cataclasites in OHFZ fault rock samples. Where well-preserved, the pseudotachylyte matrix is often very fine grained and may contain crystalline forms such as skeletal grains and spherulites that may have resulted from rapid undercooling and quenched crystallisation. Melt features identified in various clast mineralogies constrain melt tempera-

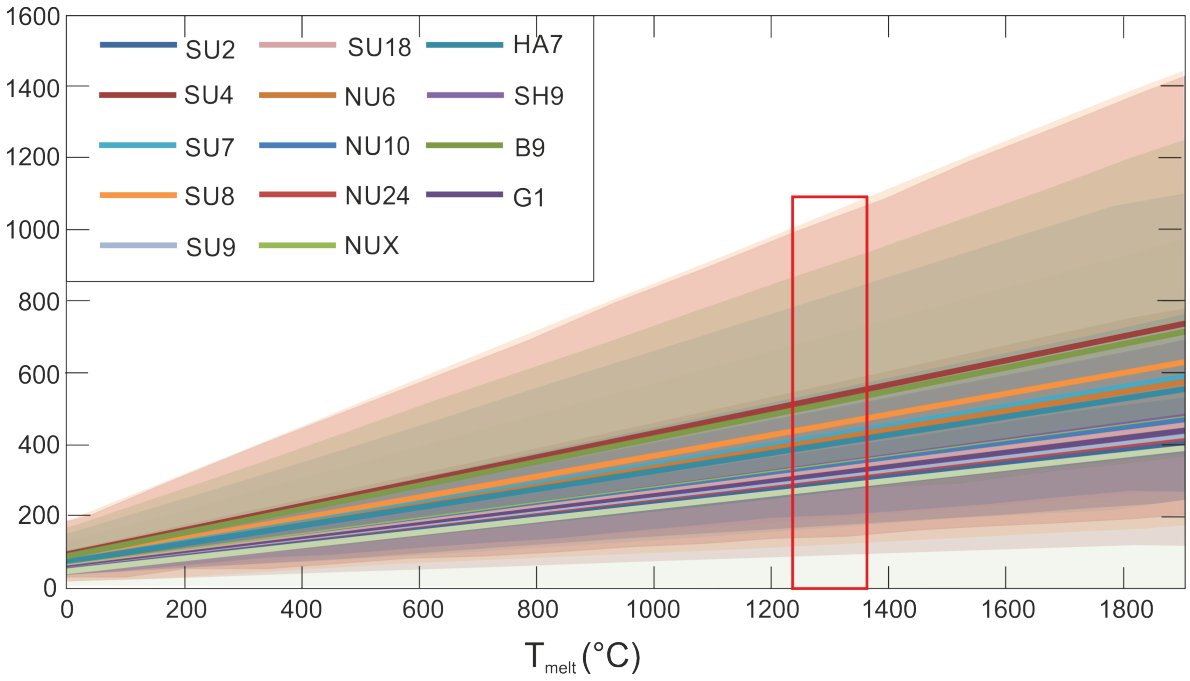

Figure 4.19: Plot after O'Hara (2001) showing results for OHFZ pseudotachylyte samples based on measured wear-to-melt ratios. Coloured envelopes outline error of one standard deviation on the $\frac{W}{M}$ ratio. Red box outlines range considered where T$_melt$ = 1230-1350°C.

ture to 1250-1550°C - although this represents a lower bound for the peak melt temperature, it is expected to be reached only transiently and locally as the clasts are not able to completely melt. The heterogoneity of temperatures across a fault vein is highlighted by the concurrence of both a pseudotachylyte crystalline matrix and cataclasite at different points in a fault vein, with a spectrum of clast to melt ratios in between.

This agrees with the range of values for both clast to melt ($\frac{W}{M}$) ratios and clast size distributions from various pseudotachylyte veins which show a lot of variability that is not necessarily dependent on the type of vein (injection, fault) sampled - the balance between mechanical wear and cataclasis and the thermal input and melting is likely to be variably distributed within a single vein and unique to that vein in comparison to another. This may explain why the geothermometer method using the $\frac{W}{M}$ ratios produces a large range of predicted temperature values.

Temperatures predicted for T$_{ambient}$ using the geothermometer method are all much higher than many published estimates (e.g. Imber et al. (2002), Szulc et al. (2008)) and mostly too high to be feasible. The samples with the highest $\frac{W}{M}$ values give the lowest estimates, with

575 °C being suggested for a T_{melt} value of 1000°C, but the higher T_{melt} estimates of 1250-1550°C indicated by melting of clast mineralogies tend to indicate ambient temperatures high enough for bulk rock melting, far above the constraints on ambient temperatures for any pseudotachylyte producing activity on the OHFZ, even the early resheared phase thought to have formed within the brittle-ductile transition zone (Fettes et al. (1992), White (1996a)).

Error in the calculation of $\frac{W}{M}$ is variable but is large enough on samples with higher $\frac{W}{M}$ values that the predicted range for $T_{ambient}$ includes values down to 240°C, which is in the range of estimates of OHFZ ambient temperatures given by Szulc et al. (2008). However, the size of the error means that the usefulness of the predicted temperature range is limited. A major source of error is highlighted by standard deviation calculations where multiple images of the same sample have been analysed, and these indicate that clast content can be variable along the vein. This variety of clast content within an individual pseudotachylyte has already been observed in samples, for example sample SU2 where clasts increase towards the wall (Fig. 4.7) and in sample SU3 where the clast content increases in parts to almost a complete cataclasite (Fig. 4.5). This variety is quantified in Fig. 4.18 which indicates that the type of pseudotachylyte vein does not necessarily indicate the clast ratio. Hence, the calculation of temperatures using the geothermometer method of O'Hara (2001) is overly subjective to the part of the pseudotachylyte vein selected for calculation of the clast to melt ratio.

Pseudotachylyte clasts in OHFZ samples are predominantly quartz and feldspar, in common with many other reports of pseudotachylytes both in the OHFZ and in exhumed fault zones worldwide, in a variety of host rocks (e.g. Maddock (1983), Lin (1999), Fabbri et al. (2000), O'Hara (2001), Di Toro and Pennacchioni (2004), Rowe et al. (2005), Bestmann et al. (2011)). Rounded clast shapes are common and are interpreted to be a consequence of melting (Sibson (1975), Lin (1999)). The observation of limited melting of quartz clasts but somewhat more prevalent melting of plagioclase clasts is common in many samples and provides a rough estimate of the maximum melt temperature, as a proxy for the maximum frictional heat produced. The single-crystal melting temperature of plagioclase is 1100°C for pure albite and 1550°C for pure anorthosite (Spray (2010)), and for iron oxide is 1600°C for magnetite

(Spray (2010)) and 1539°C for haematite (Lide (2004)). If heated rapidly enough, quartz could melt as β-quartz at around 1550°C, or otherwise as β-christabolite at 1750°C (Petzold and Hinz (1976)). Noting the common oligoclase(-andesine, occasionally) composition of the plagioclase, as with the wall rock phase, the melting temperature relevant to the plagioclase clasts is likely to be ∼1250°C. This grants a minimum range of the melt temperature between 1250-1550°C.

Samples such as SU3, which show variation from this typical clast mineralogy by locally preserving biotite clasts (Fig. 4.5a), illustrate that the heat flow can vary between pseudotachylyte veins and within an individual body of fault rock. The sample SU3 also has a high clast to melt ratio in the region shown in Fig. 4.5a, which is another measure of the heat flow and thermal melting processes relative to purely mechanical wear (O'Hara (2001)). SU3 is sampled from a breccia body at least 0.5 m in width, and does exhibit some regions of greater melt content (Fig. 4.5b). Such large volumes of fault rock are likely to be dominated by melt transport and cataclasic wear (Bjørnerud and Magloughlin (2004)) because of the dilational nature of many breccia bodies and because local frictional heat production is restricted to the bounding faults and to abrasion between clasts. The survival of biotite in Fig. 4.5a implies that temperatures did not rise locally much above 650°C for a sufficient period.

4.3.4 Composition of OHFZ pseudotachylytes

The composition of pseudotachylyte samples from the OHFZ is described mineralogically, and alteration assemblages identified that provide constraints on the minimum ambient temperature and depth of pseudotachylyte generating seismic faulting. The potential for heterogeneous melt composition across a pseudotachylyte vein is looked for, in order to constrain the best regions for quantitative analysis. Quantitative major element analysis is then presented, which will be further used for thermobarometry. The macro and micro-structure and composition of the pseudotachylyte samples studied for this work are tabulated in Appendix A, Table A: A.1 and Table A:A.2.

4.3.4.1 Typical mineralogy of pseudotachylyte matrix phases

Minerals crystallised in the matrices of OHFZ pseudotachylytes sampled in this study are predominantly identified as amphiboles and plagioclases. The presence of these phases is relatively independent of their respective proportions in the host rock mineralogy. Interpretation of EDS spectra suggests that the amphiboles are almost always hornblende or magnesiohornblende, whilst the plagioclase is typically within the oligoclase range. Other ubiquitous phases include an iron oxide. Individual crystals may occasionally appear to be zoned, although at this small scale the change in BSE shade could also be an edge effect due to uneven polishing over the crystal. Other phases which appear as crystalline phases in the OHFZ pseudotachylytes include biotite, which may occur either instead of, or with, hornblende, and pyrope garnet. The latter is only seen in pseudotachylyte within host rocks which may also contain garnets themselves, though not all garnet-bearing host rocks necessarily produce pseudotachylyte garnet phases. Where garnet is present, it tends to be on the scale of ~ 5 μm or less, so that uncertainty is added to its recognition by the resolution limit of the EDS method.

4.3.4.2 Heterogeneous compositions within pseudotachylyte veins

It can be seen that pseudotachylyte generation planes sampled in this study tend to have well-mixed assemblages across any vein, with the typical phases evenly spread irrespective of the local minerals in the adjacent wall. This behaviour is to be expected in the centre of fault veins where displacement of the walls and flow of the melt mean limited coupling between the initial position of a point in the fault and the initially adjacent wall mineral. However, some smaller branches show a different composition to that of the main vein. An example of this is found in sample SU4, where an injection vein into a plagioclase crystal (Fig. 4.20a) is much more plagioclase rich than the bulk composition of the main vein.

Other apparent injection veins which appear to be filled with amorphous material record a biotite composition - these can often be tracked to the breakdown of biotite either directly on the wall of the vein or some distance into the host rock (Fig. 4.20b). The biotite melt does

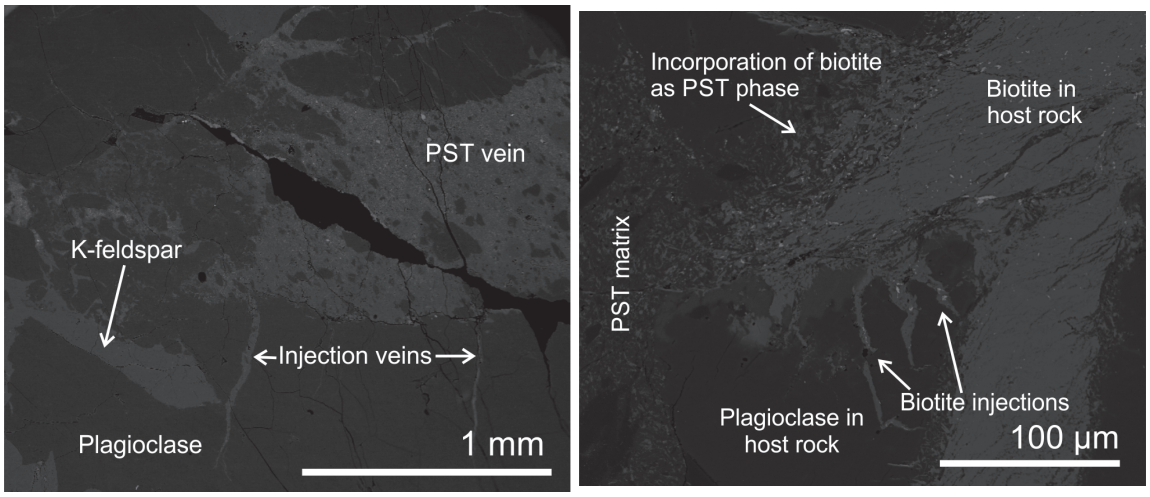

(a) (b)

Figure 4.20: Examples of pseudotachylyte matrix heterogeneity: a. View of main pseudotachylyte vein in sample SU4, with thin injections seen formed especially from its lower margin. These cut through plagioclase in the host rock, and are filled with a more plagioclase rich melt composition relative to material in the main vein; b. Breakdown of a biotite crystal in the margin of a pseudotachylyte vein, sample SU3. Melted biotite material is seen injecting back into the host rock, rather than contributing to the main pseudotachylyte matrix which is seen to the left. The matrix does however appear enriched in biotite near to the host grain.

not appear to mix well with the bulk melt of the pseudotachylyte vein, as seen in Fig. 4.20b, where a biotite melting in the wall injects into the surrounding host crystals the contribution into the crystalline phases of the main vein of recrystallised biotite seems limited to the immediately adjacent area.

An additional example of localised variation in melt phases may occur when clasts of less common composition experience limited melting and the surrounding area therefore enriched in the input elements, for example in Fig. 4.2b where a clast of iron oxide provides excess iron to the surrounding matrix which crystallises as the Fe-rich bright phase. Possibly there is limited melt flow around this clast, which sits in a spatially restricted pocket of the pseudotachylyte vein. Alternatively, perhaps because of the relatively high crystallisation temperature of iron oxides (1539-1600 °C, Spray (2010), Lide (2004)) which may be only transiently reached, the iron is not able to diffuse into the wider vein before crystallisation.

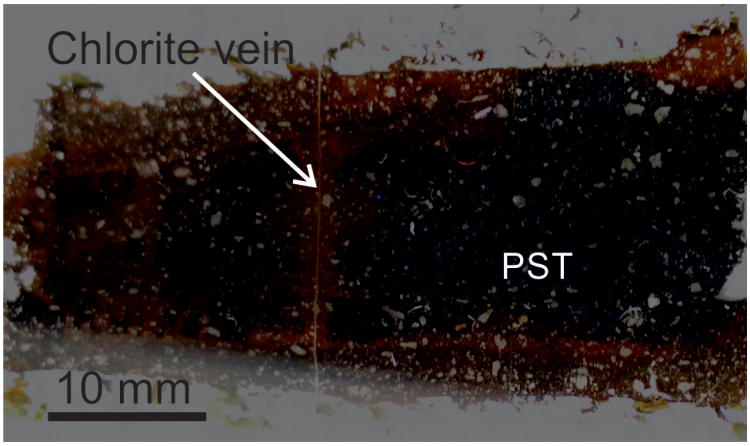

(a)

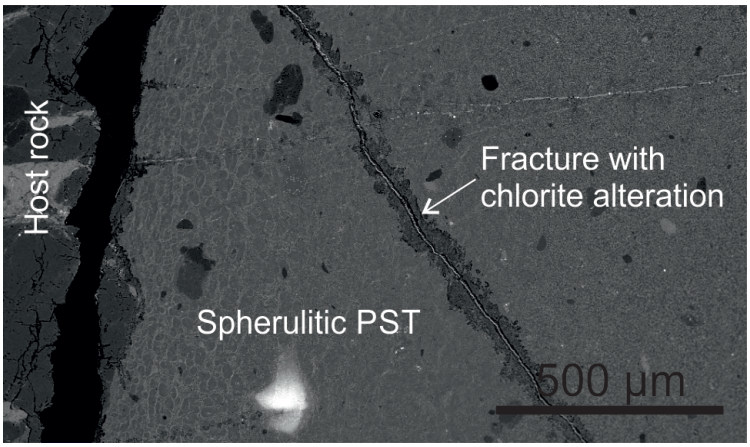

(b)

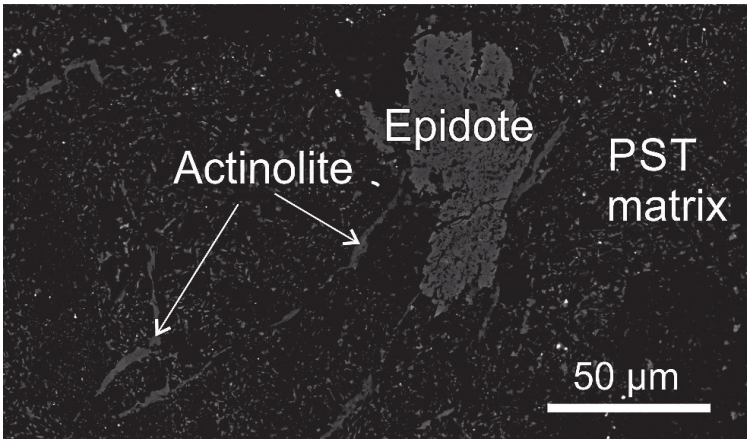

(c)

Figure 4.21: Evidence for secondary alteration in pseudotachylyte veins: a. Reddish - brown alteration of pseudotachylyte fault vein is seen to concentrate around vein edges and around chlorite-filled fracture that cross-cuts pseudotachylyte . Photo of SU2 polished section; b. Chlorite-filled fracture cuts across pseudotachylyte vein in sample B7. The host rock is seen to the left of the crack; c. Large secondary epidote overgrowing vein-like structures filled with actinolite cutting through the pseudotachylyte matrix of sample HA10. BSE image.

4.3.4.3 Alteration of pseudotachylyte

Several veins contain additional phases that may suggest alteration of the primary assemblage. The most ubiquitous are veins, predominantly of chlorite, cross-cutting the pseudotachylyte or catalcasite veins (Fig. 4.21b). Albite veins may also be seen (Fig. 4.21c). Assemblages that grow within the pseudotachylyte veins commonly include chlorite, epidote-clinozoisite, and occasionally actinolite, pumpellyite and albite (Fig. 4.21c). This secondary assemblage of epidote-clinozoisite + chlorite ± actinolite ± albite ± pumpellyite represent higher temperature phrenite-pumpellyite up into greenschist facies alteration conditions (Best (2009)).

Alteration (excluding cross-cutting mineral veins) is confined to the pseudotachylyte veins, with the host rocks away from the deformed margins maintaining their Laxfordian amphibolite facies assemblages (or granulite, where appropriate). Many of these secondary minerals are hydrated. Colour changes can often be seen around fractures and margins of pseudotachylyte veins (Fig. 4.21a). The timing of the alteration is shown as episodic in sample HA10, from near Roineabhal in southwest Harris (Fig. 4.21c), where parallel, slightly discontinuous veins of actinolite cut through the pseudotachylyte vein, but are overgrown by epidote, which forms large $\sim$ 50 μm patches across both the pseudotachylyte and actinolite veins. In turn, the epidote patches are cut by chlorite veins, parallel to the original actinolite veining suggesting reuse of the same pathways (Fig. 4.21c).

4.3.4.4 Quantitative composition of pseudotachylyte vein phases

Compositions of vein and host rock plagioclases are shown on a ternary plot in Fig. 4.22. Host rock plagioclase compositions are generally consistent between the samples analysed, which are are all typical Lewisian quartzofeldspathic gneisses. One anorthite rich host rock plagioclase composition is seen (Fig. 4.22), the cause of this is unknown. The vein plagioclase tends to be systematically more potassium rich than the plagioclase in the host by $\sim$ <5 % weight. Two analyses plot between 50-70 % orthoclase. Generally these would plot outside the range of possible feldspar compositions, but at temperatures as high as 1100°C, feldspars can

encompass some of these ternary compositions (Fig. 4.22, Fuhrmann and Lindsley (1988)). The two low albite ternary compositions, which include a host and a vein sample, are probably analyses over both components of anti-perthite (exsolved potassium feldspar hosted in albite), which is observed to occur in the host rock. This highlights the presence of potassium-rich feldspars as well as plagioclase as a vein phase in these samples.

Vein plagioclase analyses obtained via TEM EDS are also shown on Fig. 4.22. The sample analysed by TEM, SU2, was also analysed using EMPA and the reported compositions are very similar, although the amount of potassium calculated is slightly lower in the TEM EDS analyses. TEM EDS analysed plagioclases exhibit slightly lower content of Na than the host phases, as do the vein plagioclases analysed by EMPA. The TEM EDS analysis also identifies a potassium rich feldspar which lies in some proximity to the potassium feldspar vein phase picked up in the EMPA results (Fig. 4.22).

Compositions of vein and host rock amphiboles are shown in Fig. 4.23. There is already variation between analyses across the host rocks, and the amphiboles crystallising in the vein are much less similar to their host rock equivalents than the plagioclases are. A range of FeO-MgO ratios exist in the host rocks (Fig. 4.23a), and the pseudotachylyte vein amphiboles are scattered both within and around this trend. However, the majority lie within the existing trend of ratios and the pseudotachylyte amphibole is generally more Fe- rich and less Mg- rich than its parent host rock. In terms of Na_2O and K_2O, there is again variation between the host rock samples but also a large difference between the host amphiboles and the pseudotachylyte vein amphiboles (Fig. 4.23b). The vein amphiboles have a tendency to contain less Na_2O and more K_2O than their parent host rock amphiboles. This reduction in sodium is also shown alongside a reduction in calcium in Fig. 4.23c, although once more the pseudotachylyte phases are highly scattered.

In Fig. 4.23d, the ratio of weight percentage SiO_2 to Al_2O_3 is shown. The host rock amphiboles have a relatively clustered set of compositions, but the pseudotachylyte crystals are again scattered. For the majority of samples there is an increase in Al_2O_3 and also in

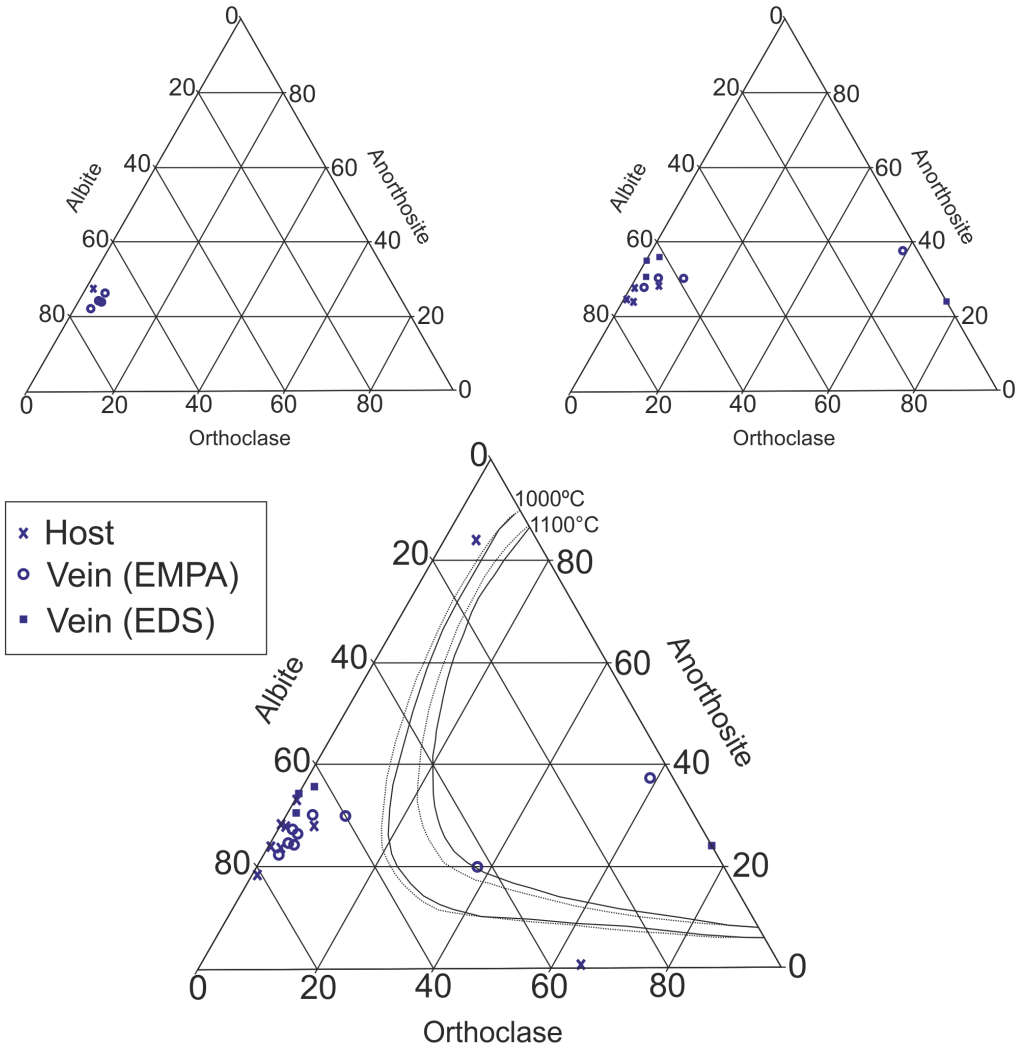

Figure 4.22: Ternary diagrams showing composition of plagioclase in host rock and vein phase crystals. Analysis undertaken using EMPA unless specified otherwise. Top left: Host and vein plagioclase compositions from sample SU4. Top right: Host and vein plagioclase and potassium feldspar compositions from sample SU2. Bottom: Feldspar compositions from all samples analysed. Isotherms between the plagioclase - alkali feldpar solid solution series and the feldspar immiscibility gap (dashed line: 100 MPa, solid line: 500 MPa) are shown at 1000°C and 1100°C (Fuhrmann and Lindsley (1988)).

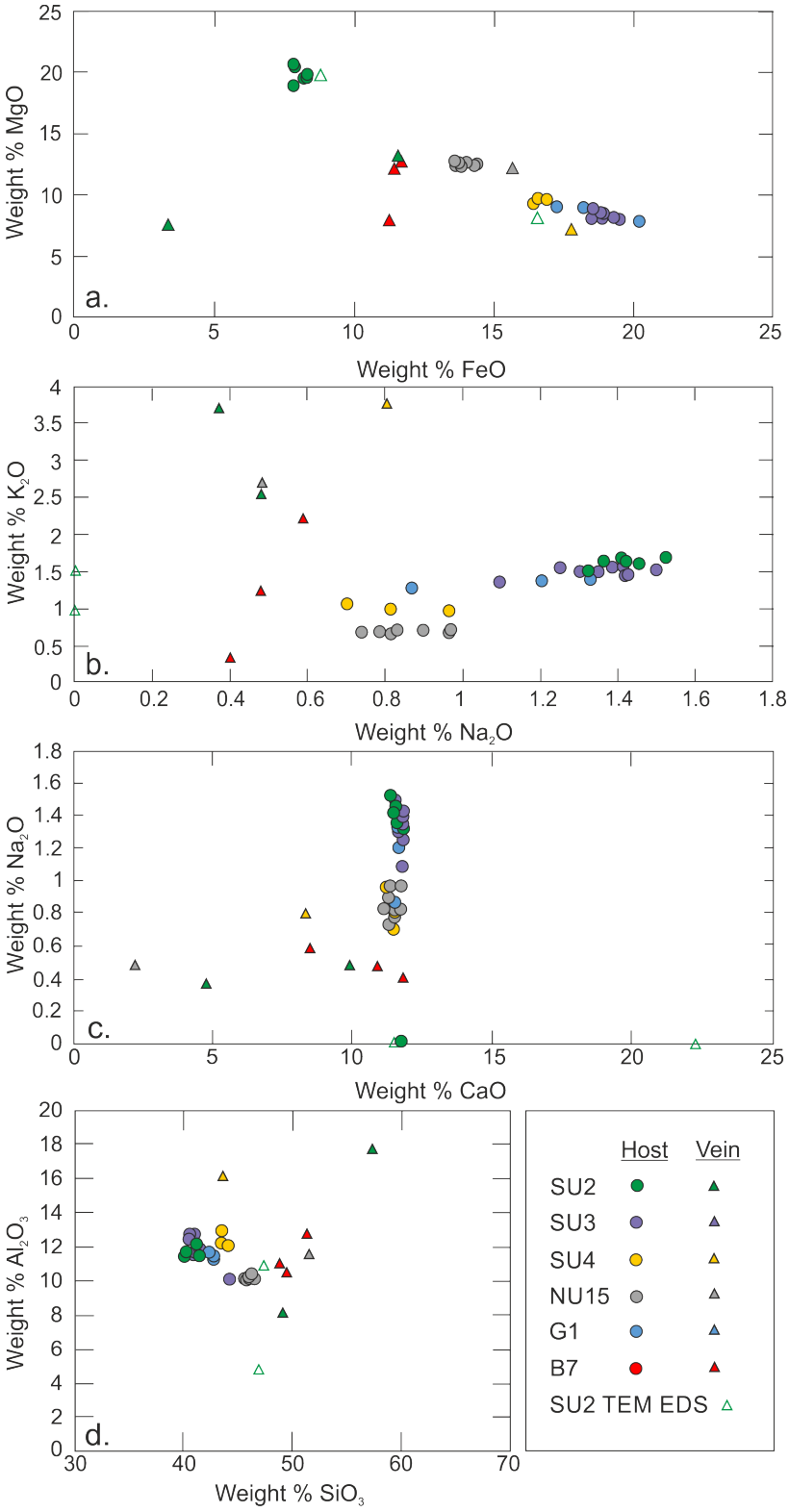

Figure 4.23: a. Weight percentages of FeO and MgO in host and vein amphiboles; b. Weight percentages of Na_2O and K_2O in host and vein amphiboles; c. Weight percentages of CaO and Na_2O in host and vein amphiboles; d. Weight percentages of SiO_2 and Al_2O_3 in host and vein amphiboles. Analyses from EMPA filled shapes, analyses from TEM EDS open shapes.

SiO_2. In all of these relationships there is no systematic value of change between a host rock amphibole and the version that crystallises in the pseudotachylyte, even if the general trend in composition change is followed.

Two TEM EDS analyses of vein amphiboles from sample SU2 are also shown in Fig. 4.23. The location of the sampling points during analysis lying on amphiboles is not completely certain. Nevertheless, both analyses sit on the general trend of inverse proportion between FeO and MgO (Fig. 4.23a). The EDS results show lower K_2O than the SU2 EMPA analyses, but sit within the range of other samples (Fig. 4.23b). When Al_2O_3 is compared with SiO_2, both TEM results join an apparent trend where both oxide contents increase, in contrast with the host phases which form a cluster (Fig. 4.23d). These TEM amphibole analyses are often dissimilar to the EMPA results of SU2 vein amphiboles, but the two vein EMPA analyses are themselves too dissimilar to make the variation with the EDS results seem meaningful.

Likely mineral formula are calculated from the major element analyses. Vein plagioclase analyses classify in the oligase and andesine fields, as expected from having a similar or more calcic composition than the oligoclase host plagioclases (Fig. 4.22). The calculated formulas of the amphiboles in the host rocks, although somewhat variable, define them as hornblendes, being in the range of $(Na, K)_{0.2-0.4}Ca_2(Mg, Fe, Al)_5Si_{6.5-7.5}Al_{0.5-1.5}O_{22}(OH)_2$. The vein amphibole phase is also a hornblende, usually with more overall Na + K , more Si and less Ca as described above. A typical formula range is $(Na, K)_{0.3-0.52}Ca_{1.4-1.9}(Mg, Fe, Al)_5Si_{7.0-7.8}Al_{0.2-1.0}O_{22}(OH)_2$. Other phases recognised quantitatively using EMPA are biotite (Mg-rich phlogopite) and a garnet of pyrope-grossular composition, although the reading for Al is low ($Ca_{1.4}Mg_{1.5}Al_{1.1}Si_{3.4}O_{12}$). TEM EDS also identified biotite of a more iron rich annite composition than identified by the EMPA analysis. The relationships between the vein phase crystals in the sample SU2 are shown in Fig. 4.24, a brightfield TEM image of the EDS sampled area. The interstitial nature of the potassium feldspar, biotite and hornblende compared to the larger plagioclase is clearly seen, and this high-resolution imaging, along with the EDS, has highlighted that biotite may be more common as a vein phase than was identified using SEM analysis.

4.3.4.5 Initial interpretation of compositional results

Pseudotachylyte compositional heterogeneity highlights specific processes that occur during slip. For example, the plagioclase rich injection vein contained within a plagioclase crystal might imply that frictional slip and offset occured across the injection fracture, rather than being a purely tensile crack with melt influx from the main vein (section 4.3.4.2). The breakdown of biotite crystals to produce biotite melt, poorly mixed into the main pseudotachylyte (Fig. 4.20b), suggests an element of in situ melting, especially as some examples are not adjacent to the slip zone. This allows a transient coseismic isotherm to be mapped out across a melting biotite, parallel to the fault wall, at 650°C, the biotite melting temperature (Spray (2010)). Additional variation comes from secondary alteration, which proves a useful constraint on conditions subsequent to pseudotachylyte generation. Greenschist facies alteration assemblages (4.3.4.3) broadly constrain a minimum ambient temperature of 300-500°C (Best (2009)), equivalent to depths of 12 - 20 km based on a geotherm of 25°C km^{-1}. Alteration assemblages involve hydrous minerals, and hence the retrogression is assumed to be fluid assisted. This is supported by the localised nature of alteration to pseudotachylyte veins and to vein margins and fractures in particular (Fig. 4.21a). The extent of samples showing this alteration assemblage includes several samples from the 'crush zone' regions of the OHFZ in North Uist, where greenschist facies fluid ingress is known to have affected the fault rock assemblages (Imber (1998)), but also in samples taken from, for example, the west coast of South Uist, where wholesale retrograde alteration is not observed at the field scale (SU3). Other samples taken in the vicinity (SU2) preserve the primary pseudotachylyte vein assemblage, so could be either a post-alteration generation phase or could just represent the heterogeneous distribution of fluid-facilitated alteration. The presence of chlorite veins, however, is common in many otherwise unaltered pseudotachylyte veins (Fig. 4.21b).

Pseudotachylyte melt phases show variable compositions that differ slightly from their equivalents in the host rock. The overall composition of the pseudotachylyte, not including the clasts, is more basic than that of the host, due to the limited melting of quartz and to some

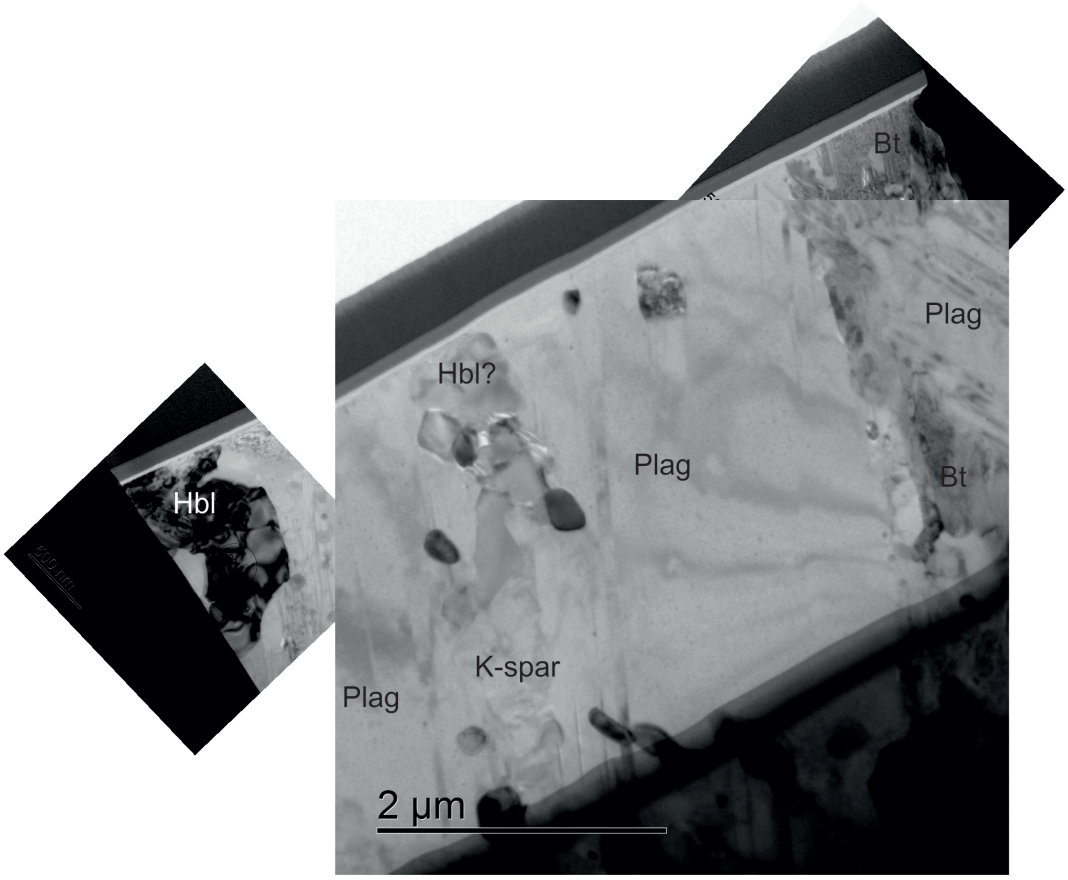

Figure 4.24: TEM brightfield image of crystalline vein phases in sample SU2

extent plagioclase. Melting was, therefore, partial and non-equilibrium. Trends of increasing potassium and decreasing sodium in plagioclase, increasing potassium, aluminium and silica and decreasing sodium and calcium in amphiboles are observed between the host rock phases and the pseudotachylyte vein phases. These compositions do not allow direct estimation of the ambient or melt temperatures during seismic activity and pseudotachylyte formation.

Quantitative analysis of pseudotachylyte mineral chemistry was undertaken using both EMPA and TEM EDS methods, allowing comparison of the use of both techniques for pseudotachylyte phase analysis. The main problem with acquiring reliable analyses from pseudotachylyte matrices is the small crystal size, being often at or below the spatial resolution limit of $\sim$5 μm for the SEM and hence the electron microprobe, also at $\sim$5 μm. This causes problems analysing the composition of fine interstital phases that are expected to occur, specifically biotite, potassium rich feldspars and iron oxides. The spatial resolution of the TEM is more

appropriate for the pseudotachylyte grain size. However, the analytical accuracy of TEM-EDS is lower than that of EMPA. The interplay of these factors is apparent in the results presented in this study. On one hand, the greater resolution of the TEM allowed identification of crystalline biotite in the pseudotachylyte matrix, which was usually only suspected using SEM EDS as part of the unresolved matrix background spectra. TEM brightfield imaging (Fig. 4.24) also provides valuable information on the crystalline nature of a pseudotachylyte matrix that is subresolution on the SEM, and shows the textural relationships between different phases. (e.g. Fig. 4.24). However, the lower detection limits affect the reported compositions of plagioclase and hornblende for sample SU2 (Figs. 4.22, 4.23). In Fig. 4.22, the EDS-derived values plot lower on the albite and orthoclase componants relative to the EMPA points, reflecting the zero or near-zero values recorded for Na_2O and K_2O in the EDS results. These two oxides are particularly noticeable because their weight % as recorded by EMPA is already low. This effect shows up again in Fig. 4.23b and Fig. 4.23c where the EDS points plot away from the EMPA points on the axes. This analytical error is propagated into the thermobarometry (section 4.3.5), because the thermometry calculation used involves X_{Na} of amphibole sites and also the X_{Albite} of the plagioclase (Holland and Blundy (1994)), as the amount of total Al is coupled to Na via the substitution $NaAl^{iv} \rightleftharpoons \square$ Si. The Al_2SiO_3 TEM EDS result may also be inaccurate, and is certainly lower in one analysis (at 4.8%) to the EMPA equivalents (8.1%, 17.7%), which although vary, bound the range recorded for other samples.

4.3.5 Thermobarometry

Fig. 4.25a shows the pressure - temperature distribution estimated for the Lewisian host rocks from hornblende-plagioclase thermobarometry (section 4.2.3). The Anderson and Smith (1995) method has been used to calculate pressure, along with thermometer 'B' of Holland and Blundy (1994), which is favoured as being applicable to the greatest range of amphibole compositions. Also presented are the temperatures calculated using the Holland and Blundy (1994) 'B' thermometer and an input pressure of 650 MPa. Many of the results fall into the amphibolite or granulite facies expected from the Laxfordian tectonothermal event, and the

pressures calculated in using the Anderson and Smith (1995) barometer are mostly within error of the 650 MPa calculated by Droop et al. (1999) (Fig. 4.25a). The sample SU2, from Àird a' Mhuile, on the west coast of South Uist, shows a temperatures into the granulite facies, apart from a single analysis point which plots in the greenschist facies using both barometry methods (Fig. 4.25a).

Analysis of vein phases uses a restricted dataset due to the difficulty of obtaining good analytical results from crystals at the resolution limit. The study focuses on three pseudotachylyte veins, in samples SU2, SU4, and B7. SU2 and B7 are thought to partially preserve primary crystallisation in the form of skeletal radiating plagioclase or spherulites (section 4.3.1.3), but the finer matrix phases which are analysed for composition may be a devitrification assemblage. SU4 presents radiating plagioclase microlites that could be either devitrification or primary crystallisation texture (Fig. 4.14b). In Fig. 4.25b, the results from the Holland and Blundy (1994) thermometer and both the Anderson and Smith (1995) and Schmidt (1992) barometers are displayed. For samples B7 and SU4 the two barometers produce results within error of each other. Results for B7 fall in the range 480-483 ± 50 °C and 489- 589 ± 72 MPa (Fig. 4.25b). Results for SU4 are higher grade, 606-636 ± 50°C and 1050-1129 ± 76 MPa. Analyses of SU2 are similar to those for B7, in the range 381±48 - 546±63 °C and 383±60-595± 62 MPa. Additional temperatures were also calculated for each analysis using input pressures of 150 and 330 MPa, the expected lithostatic stress bounds for the previosuly predicted depth range of 5-10 km (Sibson and Toy (2006)). Although these arbitrary pressures are lower than any calculated values, the temperature ranges for B7 and SU2 are much the same. For SU4, however, temperatures are much lower than those calculated and shown in Fig. 4.25b, around 350-450°C.

4.3.6 Initial interpretation of thermobarometry

The thermobarometry on the host rock phases confirms that the pressure calculation of Droop et al. (1999), which was based on the mainland Scotland Lewisian, is also broadly applicable to the quartzofeldspathic gneisses in the Western Isles. These temperature and pressure data are useful as there are few quantitative values for Laxfordian metamorphism in the Western

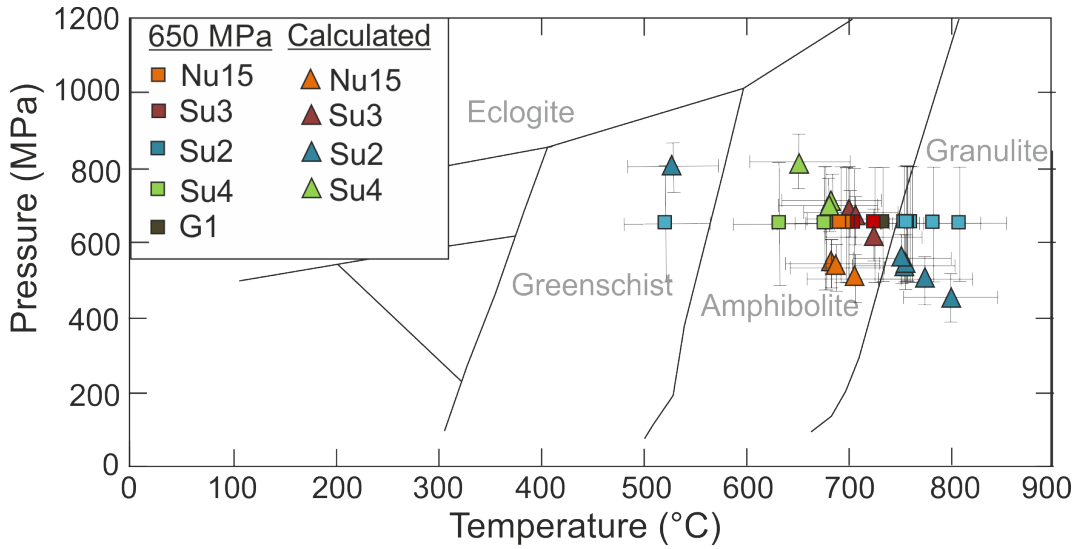

(a) Temperatures and pressures for host rock amphibole - plagioclase predicted by thermometer 'B' of Holland and Blundy (1994) and the barometer of Anderson and Smith (1995). Temperatures are also plotted using the same thermometer using an standard input pressure of 650 MPa

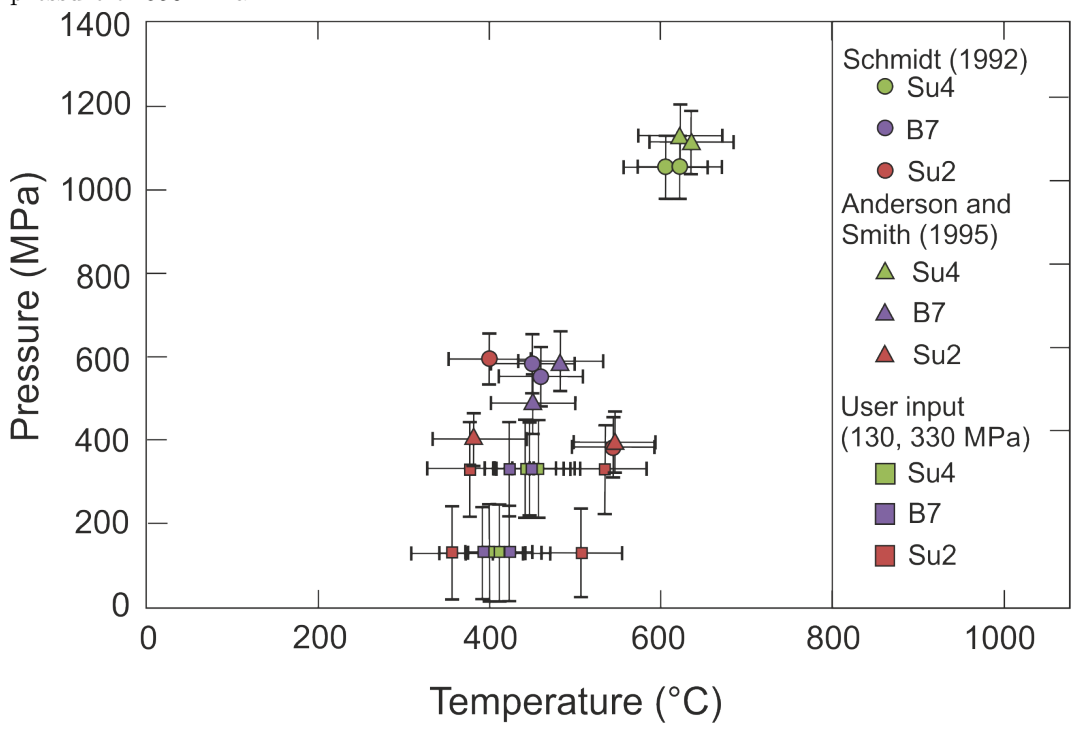

(b) Temperatures and pressures for pseudotachylyte vein amphibole - plagioclase predicted by thermometer 'B' of Holland and Blundy (1994) and the barometer of Schmidt (1992). Temperatures are also plotted using the same thermometer for input pressures of 130 and 330 MPa

Figure 4.25

Isles gneisses. Additionally, they provide an upper limit on ambient pressures interpreted from pseudotachylyte thermobarometry. The results support the common identification of amphibolite facies assemblages in the Western Isles Lewisian (Fettes et al. (1992)). However, the granulite facies results for SU2 are interesting as both SU2 and SU3 are sourced from the pseudotachylyte - rich locality of Àird a' Mhuile on the western coast of South Uist, yet the two record different metamorphic facies (Fig. 4.25a). The nearest major granulite facies unit in the Western Isles is the Corodale Gneiss on the east coast of South Uist, and in the hanging wall of the OHFZ (Fig. 2.7). Either the two are tectonically juxtaposed by the faulting recorded by the pseudotachylytes or the sample SU2 represents a slither of relict Lewisian that survived Laxfordian overprinting, which is known to occur in localised instances (Fettes et al. (1992)). The SU2 outlier at greenschist temperatures in Fig. 4.25a is the same analysis with unusually low sodium values in Fig. 4.23c. It is not known why the sodium value is low but the resultant thermobarometry results for this analysis point are not considered valid.

The applicability of thermobarometry to pseudotachylyte vein phases was discussed briefly in section 4.2.3. From the results (Fig. 4.25b), the thermometry produces a cluster of points for both SU2 and B7 between 400 - 550°C. Such a temperature could represent the mineralogy produced by devitrification of the primary glass, being too low for proposed melt temperatures of 1250 -1370°C (e.g. sections 4.3.2, 4.3.3.4) which would define the maximum primary crystallisation temperature. Sample SU4 records higher temperatures and particularly pressures. The temperature range is not high enough to invoke coseismic slip temperatures, during which high transient stresses that might also be experienced. Additionally, the pressure is as high, or higher, than the analyses of the host rock (Figs. 4.25b, 4.25a). In Fig. 4.23, the main deviation from other pseudotachylyte analyses for the amphibole used from sample SU4 is the high potassium values. However, an analysis from sample SU2 has similarly high potassium content without resulting in the high pressure values seen for SU4 (Fig. 4.25b) so it is unclear what has caused this.

Uncertainty arises from the variability of the amphibole compositions as seen in Fig. 4.23, which strongly suggest that these phases are not, in fact, an equilibrium assemblage,

diminishing the likeliness of it being a late alteration assemblage. However, relatively immediate devitrification may present such analyses if the crystals equilibrate only relative to the local glass volume, where the glass is poorly mixed across the vein and compositions are heterogeneous. Devitrification also needs to occur before the pseudotachylyte cools down to ambient temperatures, which may have been lower. Ambient temperatures for brittle thrusting are constrained to >300°C by the greenschist alteration assemblages (section 4.3.4.3), to >370±20°C (Osinski et al. (2001)) or >230±20°C (Szulc et al. (2008)) by published analyses.

4.4 Discussion

4.4.1 Temperature and pressure conditions of pseudotachylyte generation

4.4.1.1 Melt temperature

Melt temperature is used as a proxy for coseismic fault temperature, which in turn can be used to calculate the heat input and link to the seismic energy budget (e.g. Sibson (1975), Di Toro et al. (2005b)). Peak melt temperature during coseismic slip has been constrained in this study to at least 1230-1370°C (sections 4.3.2, 4.3.3.1). Similar assemblages of host clasts, particularly partially melted plagioclase and to a lesser melting extent quartz, are seen across many of the pseudotachylytes from the OHFZ (section 4.3.3.1). It is reasonable to infer, therefore, that melt temperature reached at least 1250°C, the melting temperature of oligoclase (Spray (2010)) across the fault zone. To account for melting of high temperature clasts such as quartz and iron oxide, it is envisaged that the melt temperature may transiently peak at 1600°C for a limited time period, which also restricts the complete melting of plagioclase clasts.1550°C remains the lowest melting temperature possible for quartz (Petzold and Hinz (1976)), which is observed to display some limited melt absorption in parts of OHFZ pseudotachylyte veins (Fig. 4.2a). Such temperatures are modelled to be possible in the case of an appropriate slip duration of $\sim$ 6 s (Caggianelli et al. (2005)). Another factor in the temperature rise could be the latent heat of crystallisation released preferentially around clasts due to the tendency for nucleation upon their rims, which may push the local temperature high enough for the melting temperatures to be reached. Temperatures over 1250°C

cannot be maintained sufficiently long to completely melt plagioclase, as it is often found as survivor clasts in the melt (Fig. 4.2a) and as resistant asperities in the slip zone wall (Fig. 5.8).

Models of pseudotachylyte melt temperature agree that the maximum temperature is only transiently reached (McKenzie and Brune (1972), Caggianelli et al. (2005)). Spatial variation in peak temperature is also a feature of pseudotachylyte fault veins, both within the individual vein, with isotherms parallel to the margin as evidenced by changes in clast content and in crystallisation geometries near the walls (Fig. 4.7, Nielsen et al. (2008)), and between generation veins that might be closely related in time and space. This is seen in the varying balance of thermal and mechanical processes indicated by varying clast fraction and mineralogy (sections 4.3.1.2, 4.3.3.2) and is likely influenced by all manner of fault heterogeneity, including dilational jogs, frequency of off-fault injection and local wallrock mineral fractions. This was seen clearly in a pseudotachylyte breccia (Fig. 4.5a). Breccias may experience a wide spectrum of peak temperatures throughout their matrix because of their large volume to frictional wear surface (the outer boundary and abrading clasts) ratio. This fits with the models of Bjørnerud and Magloughlin (2004) where breccias are subject to low-pressure draw-in of pseudotachylyte generated elsewhere along a fault, rather than producing enough friction to fill their matrix volume with pseudotachylyte generated within the breccia.

4.4.1.2 Ambient temperature, pressure and depth

Pseudotachylyte samples from the OHFZ have secondary alteration assemblages that constrain the minimum ambient temperature of pseudotachylyte faulting to greenschist facies conditions (section 4.3.4.3) between 300-500°C (Best (2009)). No better constraint is available within this range from this study, but the lower bound supports other minimum temperatures of 230-370°C taken from published sources (Sibson (1975), Osinski et al. (2001), Imber et al. (2002), Szulc et al. (2008)). Many of these sources also analyse greenschist facies alteration and deformation features in the OHFZ. Additionally, when the calculated amount of melt cooling is added to an ambient temperature estimate of 250-350°C, the predicted melt temperature is very similar to that predicted by other approaches, for example clast mineralogy

(sections 4.3.2, 4.3.3.1). This suggests that the lower range of the greenschist facies estimate made here is valid as an ambient temperature for at least one phase of pseudotachylyte faulting.

300-350°C equates to depths of 12-14 km at a geotherm of 25°C km^{-1}. In the case of active thrust tectonics an elevated geotherm, perhaps 30°C km^{-1}, could result in such temperatures occurring at shallower depths of 10-11.5 km. This is at the upper end of the OHFZ pseudotachylyte generation depth range estimated in Sibson and Toy (2006), but is based on similar evidence as that outlined in Sibson (1975), specifically the field expression of greenschist facies, fluid present alteration, which is best seen in the low grade mylonites that cut the older OHFZ and rework pseudotachylytes in the east of South Uist, and the widespread greenschist facies hydrothermal alteration of the OHFZ faults in North Uist particularity (see Chapter 2).

Pseudotachylyte generation is interpreted to have been multiphase based on field evidence (Chapter 3, e.g. Fig. 3.13a). This is in addition to the mylonitised pseudotachylyte phase of the northern section (Sibson (1980), White (1996a)). If these generation phases relate to different tectonic regimes and generation at different depths, it is likely that several ambient temperatures and pressures might be represented across the pseudotachylyte population. The number of samples analysed in section 4.3.5 is too limited to lend itself to a thorough study of such variations that may or may not occur, with the samples SU2 and SU4 sourced from reverse faults and the sample B7 having uncertain movement sense (Appendix A). However, within the three samples analysed there is a notable difference in temperature and pressure between the sample SU4 and the samples B7 and SU2, which record $\sim$ 600-630 °C and $\sim$ 400-550°C respectively. At 1050-1129 MPa pressure, sample SU4 represents depths of 35-37 km. The depth of samples SU2 and B7 is in the range 11 - 20 km. The resultant depth of SU4 is beyond the depth of pseudotachylytes seen in many fault zones outside of subduction zones or brittle faulting in eclogite facies (Lund and Austrheim (2003), Austrheim and Andersen (2004)) and seems unlikely to be realistic for the OHFZ, being deeper than the metamorphic grade of the host rock allows (section 4.3.5). Depths for SU2 and B7 cover a large range but are useful in that they support the higher end of, or deeper than, the literature estimate of

5-10 km for OHFZ pseudotachylyte formation (Sibson and Toy (2006)). The higher end of the depth range suggested by this barometry, perhaps at depths >15 km, is not considered realistic because during and above the brittle-ductile transition expected at these depths, plastic behaviour of quartz and of the rock would be expected to occur. This is not observed in these samples, which record localised brittle faulting and damage in line with the deformation seen at the field scale of the southern section of the OHFZ from which they are sourced.

The mylonitised pseudotachylytes are thought to have formed around the brittle-ductile transition at depths of 13-18 km (Fettes et al. (1992), White (1996b)) and to date to ∼1000 Ma (Butler et al. (1995)) or perhaps earlier (Imber et al. (2001), Osinski et al. (2001)). The pseudotachylytes studied here, preserved in their brittle form, have a depth range that encompasses this. It may be that they are the same generation, as the now resheared northern pseudotachylytes, but the southern section of the OHFZ was uplifted into the brittle regime preventing mylonitisation. This scenario will be discussed further in Chapter 7.

Direct estimates of depth were attempted using geobarometry on amphibole-plagioclase compositions in the pseudotachylyte matrix (section 4.3.5). Both the Schmidt (Schmidt (1992)) and Anderson-Smith (Anderson and Smith (1995)) barometry results produce pressures indicating depths of 11 - 20km for samples B7, a fault vein pseudotachylyte from eastern Barra on the major OHFZ fault jog, and SU2, a tip-to-W reverse fault vein from the west coast of South Uist. Therefore, both samples are within the range of both the proposed ∼ 10 km of preserved brittle pseudotachylyte faulting and the 13-18 km depth resheared pseudotachylyte generating seismicity mentioned above. In this work, better constraints from the barometry analysis are unfortunately limited by the limited number of valid analyses available.

The 30 km equivalent pressure calculated from amphibole-plagioclase barometry for sample SU4 (section 4.3.5) is a note of caution for accepting these barometry derived depths, as 30 km is much higher than pseudotachylytes are typically generated outside of subduction zone settings (Sibson and Toy (2006)) and greater than the equivalent depth of metamorphism of the host rock assemblage (∼800 MPa, Fig. 4.25a) through which it cuts. An outline of the problems with using thermobarometric models on pseudotachylytes, and a discussion

of what the temperatures and pressures represent, has been included in sections 4.2.3 and 7.2.1. As stated there, primary crystallisation is a disequilibrium process. Tectonic activity might be a cause of increasing stress in one or more directions above the lithostatic value, as suggested by (Wenk and Weiss (1982)) who also calculated unrealistically large pressures from pseudotachylyte pyroxene barometry. However, if as suggested in section 7.2.1, the thermometry values represent devitrification conditions soon after slip, stress would be expected to be relieved by the seismic stress drop, and so the meaning of these pressures become less clear.

4.4.2 Evaluation of thermal and cataclasic processes

Cataclasite occurs alongside pseudotachylytes in several forms. Pre-existent cataclasite may be cut through or completely reactivated by the pseudotachylyte forming faults (e.g. 4.6b), but it is not constrained how far in advance the cataclasite formed. For example, the cataclasite that appears in parts of the margin (host rock side) in sample SU2 (Fig. 4.6a) is overprinted by undeformed biotite, which suggests that some period of possibly fluid-facilitated retrogressive reactions had time to occur prior to the presumably anhydrous pseudotachylyte producing event. However, the S-C type foliation in the cataclasite indicates a parallel slip direction to that of the pseudotachylyte bearing fault. Other samples occasionally show simple reactivation of a cataclasite-bearing fault (e.g. Fig. 4.6b). Although the host rock is invariably brittly deformed to some extent, many other examples show little apparent relationship between localised cataclasite bands and the later pseudotachylyte bearing fault. Nevertheless, cataclasite and pseudotachylyte have been recognised here as coexisting within a pseudotachylyte generation plane and indicate that cataclasic wear is synchronous with frictional melting during coseismic slip.

The variable division between mechanical (cataclasis) and thermal (melting) breakdown processes is illustrated by the calculation of wear-to-melt ratios (section 4.3.3.2). The ratio of clasts to melt-derived matrix has a clear modal average (Fig. 4.18) but shows significant variation within some samples. Although the number of vein types other than fault veins is low, injection veins tend to have lower wear-melt ratios, consistent with the results of O'Hara

(2001). This may be considered a factor of the differing processes acting across differing parts of the pseudotachylyte vein system. Transport of melt into cracks, without local shearing and hence cataclasis, would indeed be expected to produce a low clast:melt ratio if the approximation to wear:melting is applied (O'Hara (2001)). Considering only fault veins, the play off between mechanical processes and thermal processes is both variable and inherently coupled.

Meanwhile, coseismic heat production is controlled by the maintenance of frictional strength as well as a contribution from latent heat of crystallisation (Lofgren (1974)). The former is prolonged if routes for melt escape off the generation plane are available (Bjørnerud and Magloughlin (2004)), otherwise the strength of the fault will diminish to that of a melt lubricated surface or the shear strength of the melt if no asperities remain in contact. The temperature profile will therefore be quite unique to each vein geometry. Latent heat (or enthalpy) of crystallisation is effectively a release of heat from the system, and can be significant, equivalent to >100°C (Best (2009)). Neither of these effects are accounted for in the 'geothermometer' method of O'Hara (2001). In addition, calculated values for the proportion of clasts to matrix are low, with a mean of 0.24 (section 4.3.3.2) compared to values found for various faults in O'Hara (2001)), where ratios of 0.5-0.7 are reported for fault veins. Only fault veins from an eclogite facies fault in the Bergen Arc, Norway, produce ratios below 0.2. However, reports for the ratio of clasts to the total pseudotachylyte vein area (i.e. clasts and melt) are 0.25 for pseudotachylytes from the OHFZ (Maddock (1983)), 0.17 from the Homestake Shear Zone, Colorado (Allen et al. (2002)) and 0.2 for pseudotachylytes from the Gole Larghe fault (Di Toro et al. (2005b)), both comparable to the results of this study. It seems, therefore, that the ratios reported in O'Hara (2001) are perhaps the more unusual.

The 'Geothermometer' method developed by O'Hara (2001) is used here to analyse the OHFZ pseudotachylytes using the wear:melt ratio, and the results displayed in Fig. 4.19. The temperatures predicted for ambient and met conditions are unrealistic unless the extremes of the large errors are considered. Other observations detailed in this chapter have provided causes for this, as discussed in the above paragraphs. Primarily these are that the 'Geothermometer' method depends on the measured ratio of clasts to pseudotachylyte matrix in the

pseudotachylyte vein (wear to melt ratio), but this ratio has been shown to vary spatially within individual pseudotachylyte veins and between different types of pseudotachylyte veins. The inferred synchronous production of cataclasite and pseudotachylyte is a reflection of the complex coupling of the thermal and mechanical coseismic slip processes which will evolve through the coseismic slip period and depend on unique fault parameters such as fault geometry, magnitude of displacement, slip velocity and fault mineralogy (e.g. Sibson (1975)). The use of measurements from different parts of the pseudotachylyte sample will average the spatial variation, although ths contributes to the large errors, but the observed wear:melt ratio reflects the final state at solidification and should not necessarily be expected to indicate a peak melt temperature. The complexity of the relationship between coseismic thermal and cataclasic processes, along with the unusually high wear to melt ratios reported in the original study of O'Hara (2001), may explain the unrealistic results produced by this method both within this study, and as previosuly suggested by the findings of Di Toro and Pennacchioni (2004), Torvela and Ehlers (2010), Warr et al. (2010) and Cirrincione et al. (2012)).

Size distributions of OHFZ pseudotachylyte clast populations show D-values (2D) between 0.48-1.31 (Fig. 4.17). A number of studies on pseudotachylytes are available for comparison. For impact-generated pseudotachylytes, expected to be higher than fault-generated pseudotachylytes, D-values are 1.29-1.89 (Hisada (2004)). Reported fault-generated examples include 1.5 from the Musgrave Ranges, Australia (Shimamoto and Nagahama (1992)), 0.89-1.35 in pseudotachylytes from Rajastan, western India (Ray (1999)), and 1.75-2.65 in the Gole Larghe fault zone, Italian Alps (Di Toro and Pennacchioni (2005)). The results obtained in this study therefore fall within the comparable literature range, albeit lying mainly towards the lower end. As noted by Di Toro and Pennacchioni (2005), the often limited range over which the distribution curve is sufficiently straight for calculation of the power law relationship is variable between studies. The fewer orders of magnitude are covered by the distribution, the more the error increases. In the OHFZ results, there are approximately two orders over which the curves yield a power law (Fig. 4.16). The fall-off from a power law distribution at the finest clast sizes, observed in other pseudotachylyes, is also seen in results presented here (Fig. 4.16). Where this can be shown to be a real effect, rather than a resolution limit, it is concluded to

be evidence of preferential melting of the finer fraction (Shimamoto and Nagahama (1992)) due to the increased likelihood of the entire clast being heated to the melt temperature via heat conduction from the melt (Ray (2004)).

4.4.3 Compositional effects

The composition of pseudotachylyte plagioclase is relatively consistent both within a sample and between different samples (section 4.3.4.4). Consistency in the pseudotachylyte vein plagioclase may be controlled by the limited variation in host-rock plagioclase between many of the samples across the OHFZ. An exception to this is where meta-anorthosites and meta-gabbros appear in the South Harris Igneous Complex, and a sample from the anorthosite shows labrodorite composition for both host and vein plagioclase. The quantitative results show that the pseudotachylyte plagioclase is more potassium rich and, in the case of sample SU2, slightly poorer in sodium than the host phase. Lower sodium content, in effect greater $X_{Anorthite}$, may be a signifier of the less SiO_2 rich compositions observed in may pseudotachylytes relative to their host rocks (e.g. Sibson (1975), Lin and Shimamoto (1998), Camacho et al. (1995)). Potassium content, meanwhile, will increase with the temperature of crystallisation (Sen (1959)), such that the pseudotachylyte phases are expected (as observed) to show higher K content than their amphibolite facies metamorphosed host rock.

In contrast, pseudotachylyte vein amphiboles show wider compositional variation with respect to both the host rock, and to other analyses from the same sample (Fig. 4.23). The typical crystalline texture of pseudotachylytes in the OHFZ, where plagioclase forms the largest, most developed crystals and all other phases (including additional plagioclase) are interstitial (e.g. Fig. 4.3a), suggests that the plagioclase phenocrysts crystallise first and are able to sample the melt to maintain a more consistent and ideal composition. Evidence for the rapid growth of plagioclase, driven by diffusion gradients, is seen in the elongate, branching morphology (Fig. 4.15a). Later phases, including hornblende, crystallise from a depleted melt which may be spatially restricted for diffusive sampling by the distribution of clasts and plagioclase crystals, so that non-ideal compositions are produced that may vary over different

sites in the vein. The crystallisation process, as well as the melting, therefore remains out of equilibrium.

Some major element trends record relationships characteristic of igneous rocks due to similar fractionation processes. In pseudotachylyte amphiboles, FeO increases at the expense of MgO (Fig. 4.23a). OHFZ pseudotachylyte amphiboles see the FeO content vary between them by up to 10%, but within a sample the records here are relatively consistent (Fig. 4.23a). Pseudotachylyte amphiboles tend to be more Mg rich and lower in Fe than their host rock amphibole (i.e. are less evolved). The trend of Mg-Fe replacement in pseudotachylytes is consistent irrespective of how far the host deviates from this trend. In contrast, the Na_2O vs K_2O trend is perhaps stronger in the host rock amphibole (Fig. 4.23b), although this may be a feature of more sample points. The trend for the pseudotachylyte phase is that Na_2O increases slightly (between 0.4 and 0.8 weight %) whilst K_2O also increases from 0.3 to 3.8 weight %. Na_2O is almost always lower in the pseudotachylyte than in the host phase from any sample. The proportion of K to Na in the *A* site of amphibole is thought to be temperature related, with increasing K substitution as temperature is increased (Helz (1979)). The results here do not suggest that Na is lost with increasing K content, but the trend is weak overall. In contrast, whilst CaO is almost constant through all host rock amphiboles, it is variable in the vein phases (Fig. 4.23c). Some of the relationships between pseudotachylyte amphiboles and their host rocks may be related to the bulk composition of the melt. For example, the preferential melting of biotites may enrich the melt in potassium, and hence the crystallising amphiboles, as biotites are inferred to crystallise late due to their smaller grain size (rarely identified under SEM) and lower melting temperature (Spray (2010)).

4.4.4 Timing of crystallisation

Spherulites in sample B7 are shortened perpendicular to the vein margin (section 4.3.1.3). As the fill in the fractures has the same composition as some of the spherulitic zones, it implies that these microfractures, and the compression, occurred during crystallisation, albeit when the spherulite was solid enough to deform in a localised brittle manner. Otherwise, spherulites

only show weak and variable elongation directions, or best-fit long axis orientation, which suggests they formed after flow of the melt had ceased. One explanation for this compression direction is closure of the vein walls, which would fix the timing of crystallisation and deformation of the spherulite to the end of seismic slip and/or the immediate postseismic period. In this case, the primary assemblage and crystalline textures are preserved in sample B7. No preferred shape orientation of vein phases is seen in any sample, with plagioclase laths especially showing random or radiating distributions. However, the results seen in section 3.6.2.3 suggest that information on the flow direction is stored in the anisotropy of magnetic susceptibility of magnetic and paramagnetic phases (Ferré et al. (2016)). EBSD results suggest that this is not reflected in the lattice preferred orientations of the non-magnetic plagioclase lathes (Fig. 4.11). Crystallisation of all phases is therefore inferred to begin late in the coseismic period, once flow of the melt has desisted.

4.5 Chapter conclusions

This chapter has sought to constrain parameters relating to conditions of seismic, pseudotachylyte -generating pseudotachylyte in the Outer Hebrides Fault Zone, including melt temperature, ambient temperature and depth. In doing so, the evidence for the occurrence for primary crystallisation, devitrification and alteration in pseudotachylyte veins has been considered, and the relationship of cataclasite and host rock clasts in pseudotachylyte, both products of wear, analysed for implications on the energy balance between mechanical and thermal processes during coseismic slip. The main conclusions of this chapter are:

- Melt temperature in OHFZ pseudotachylytes was 1230-1370°C and probably transiently highe, based on evidence from clast assemblages and quench textures;
- Ambient temperature for OHFZ pseudotachylyte faulting was in the range 230°C - 350°C as indicated by later greenschist alteration assemblages and by the amount of undercooling represented by quench crystallisation textures ;
- The depth of some pseudotachylyte generating events in the OHFZ was >10 km, based

on these ambient temperatures and on the results of amphibole-plagioclase thermobarometry;

- Although multiple pseudotachylyte generation episodes are inferred in Chapter 3, it has not been possible to differentiate these from any difference in depth of foration or of composition;

- Primary crystallisation features are preserved in OHFZ pseudotachylytes although parts of the vein may be partially devitrified - hence the results obtained in this chapter (barring the alteration assemblaages) relate to the parameters of seismic slip;

- Equant minerals in the pseudotachylyte finer matrix may represent devitrification on cooling of partially glassy pseudotachylyte towards ambient temperatures, as recorded by thermometry;

- Crystallisation in pseudotachylyte typically occurs after slip has ended so that little evidence for flow direction is preserved in the crystal geometry;

- Temperature gradients across a pseudotachylyte vein may be identified by varying proportions of cataclasite/clasts and melt derived matrix, which can be synchronously produced. This means that inferences based on clast volume fractions are overly sensitive to the part of the vein sampled, and may not give meaningful results.

Chapter 5

Experimental investigation of coseismic strength of pseudotachylyte faults in the Outer Hebrides Fault Zone

5.1 Introduction

Whilst the Outer Hebrides Fault Zone (OHFZ) is dominantly hosted by quartzofeldspathic gneiss, it does cut through other lithologies along strike, including the Corodale two-pyroxene gneiss unit which is juxtaposed as the hanging wall in South Uist against the quartzofeldspathic gneisses of the footwall (Fig. 2.7). This juxtaposition of different lithologies across the fault is a common feature of large, active fault zones globally, and reverse faults in particular - for example, plate boundaries at the Himalaya (Yin and Harrison (2000), Parsons et al. (2016)); the Alpine Fault, New Zealand (Suggate and Grindley (1972)); the Insubric Line and Penninic Front, European Alps (Schmid and Kissling (2000)); the San Andreas (Chester et al. (2005)); and generally all subduction zones (e.g. Heaton and Hartzell (1987), Jordan et al. (1983)).

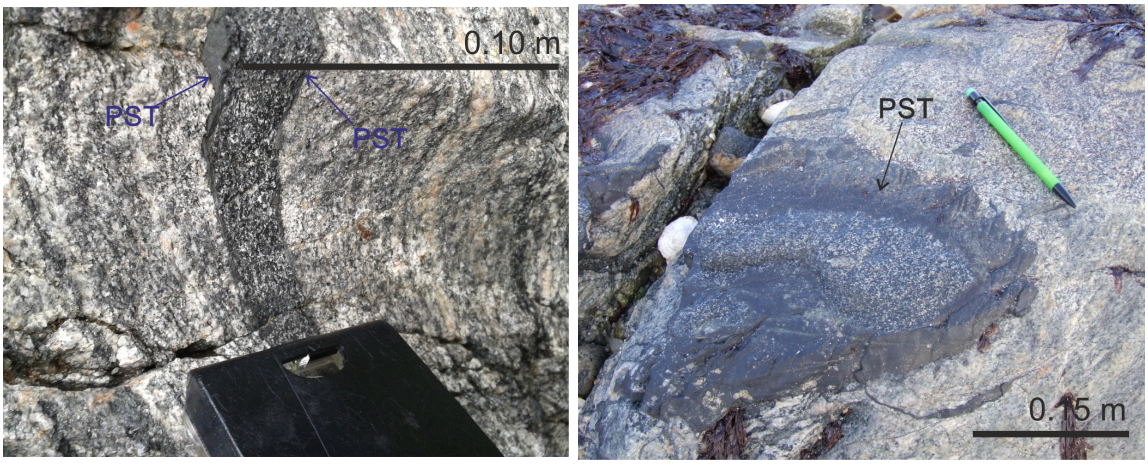

(a) (b)

Figure 5.1: Field examples of pseudotachylyte development along boundaries between quartzofeldspathic and amphibolitic bodies: a. Ferry terminal, Eriskay [78479 810203]: Development of pseudotachylyte along planar boundaries of amibolitic band in gneiss; b. Bágh Halaman, Barra [64518 800376]: Pseudotachylyte layer formed around pod-like amphibolite body (metamorphosed intrusion) and associated irregular pseudotachylyte veining into quartzofeldspathic rock.

The presence of different lithologies might be expected to modify the along-strike mechanical behaviour of slip. If coseismic processes such as melting, which are controlled by the thermal and mechanical properties of the minerals present, are able to occur, these in turn can modify the seismic behaviour of the fault (e.g. weakening and stress drop, see Chapter 7). Predictions of coseismic behaviour become complex if two differing rock types are in contact across the fault (e.g. Ben-Zion and Andrews (1998), Berg and Skar (2005)).

The region of the OHFZ in South Uist where the Corodale gneiss appears in the hanging wall also displays high volumes of pseudotachylyte in the crush zone. It has been speculated (Butler et al. (1995), Osinski et al. (2001)) that this is due to the mineralogy of the Corodale gneiss being susceptible to melting. On a smaller scale, contacts between broadly meta-basic and meta-felsic lithologies are also seen at the margins of the Younger Basic intrusions or amphibolitic banding within the gneiss. Pseudotachylyte is frequently observed along these mostly planar boundaries, and commonly injects into the meta-basic intrusion (Fig. 5.1). These once-basic intrusions are now amphibolites due to Laxfordian metamorphism (Cliff et al. (1998)). As amphiboles are known to be preferentially melted (Spray (2010)), it may

be suggested that the mineralogy of the meta-basic dykes encouraged the formation of pseudotachylyte melt along their boundaries.

To investigate the slip behaviours of different lithologies along the OHFZ, an experimental approach is undertaken. Earthquake slip rates can be recreated using high velocity rotary shear rigs and commonly produce frictional melts from crystalline samples (e.g. Spray (1988), Hirose and Shimamoto (2003), Di Toro et al. (2006a), Del Gaudio et al. (2009)). Samples of OHFZ host rocks were deformed experimentally to investigate the slip behaviour of different lithologies, of mixed-lithology faults, and the contribution to melting of differing mineralogies. Deformed samples were sectioned and analysed using optical and scanning electron microscopy (SEM) methods to assess the presence of melt structures (i.e. pseudotachylyte), and also to compare the similarity of experimental and natural samples. This allowed evaluation of how well natural faulting processes can be recreated in the laboratory. Profiles of the slip zone margin geometry were traced from micrograph transects and used to investigate the differing roughness of the slip zone in the various lithologies, and evaluate the mineralogical and microstructural controls. The compositions of the experimental pseudotachylyte matrices analysed with electron microprobe techniques (EMPA) were used to compare the relative input of each wall rock in mixed lithology cores and to allow calculation of the viscosity of the melts, which serves to explain the differing fault strength behaviours of the various lithologies during slip. This allows comparison with the mechanical result taken during the experiments.

5.2 Methods

5.2.1 Field sampling

Samples were taken from the field area with the aim of representing typical OHFZ host lithologies. The following rock samples were obtained: quartzofeldspathic gneiss, meta-basic gneiss, Corodale gneiss and mylonitic quartzofeldspathic gneiss. The ideal criteria for sample selection were: a large sized coherent sample (>15x10x10 cm, or similar) to allow coring of the sample to the drill's full extent, and to increase the available volume that is unaffected

by weathering effects; a sample as undeformed as possible by visible or smaller fracturing, to reduce the chance of the sample disintegrating either during preparation or under the applied load of the experiment; and as homogeneous a sample as possible to reduce the influence of mineralogical variation between individual cores of the same rock type. As the probability of finding undamaged volumes of rock is difficult near the main trace of the OHFZ, samples were commonly sourced away from any fault and were often boulders broken off the main rock exposure, i.e. unorientated and not in situ. Although the quartzofeldspathic rock can be highly variable across the OHFZ in terms of mineral proportions (specifically, amphibole and biotite content) and texture (strength of gneissic banding), the quartzofeldspathic samples chosen represent a typical version, with average strength of fabric and mineral fractions (Table 5.1).

5.2.2 Sample characteristics

The mineralogical compositions of the rock types are displayed in Table 5.1. These modal proportions were measured using a combination of whole rock X-ray diffraction (XRD) and optical and SEM mineralogy. All samples have a modal grain size of 1 mm. The quartzofeldspathic and meta-basic gneisses have a granular texture, with a very weak shape preferred orientation picked out by alignment of the long axis (average axial ratio ~ 2) of quartz and plagioclase in the meta-basic sample, and hornblende in the quartzofeldspathic sample. The Corodale gneiss sample is protomylonitic in part and additionally contains microfractures and bands of cataclasite or fragmentation.

Table 5.1: Modal percentages of lithologies sampled for experimental study

Lithology	**Plagioclase**	**K-feldspar**	**Quartz**	**Hornblende**	**OPX**	**CPX**	**Biotite**	**Chlorite**
Quartzofeldspathic gneiss	49.3%	7.8%	11.0%	9.6%	-	-	6.8%	15.5%
Metabasic gneiss	57.7%	7.8%	7.1%	27.5 %	-	-	-	-
Corodale gneiss	50%	-	10%	10%	15%	5%	10%	-

The following configurations of cores were deformed as displayed in Table 5.2. The combinations were chosen to provide 'end-member' compositions of quartzofeldspathic and meta-basic gneisses plus an intermediate mixed core and to refine this mixed configuration to represent an actual contact seen in the field by presenting the Corodale unit and the quartzofeldspathic unit.

Table 5.2: Configurations of cores used in experiments

Core 1	Core 2	Axial load (MPa)	Slip velocity (ms^{-1})	Runs	#	Displacements (m)
Meta-basic	Meta-basic	18	1.3	1	R1	2.8
Quartzofeldspathic	Quartzofeldspathic	18	1.3	1	R2	3.1
Meta-basic	Quartzofeldspathic	18	1.3	3	R3, R6, R7	1.8, 5.7, 6.0
Corodale	Quartzofeldspathic	18	1.3	1	R5	5.2

5.2.3 Experimental procedure

The apparatus used was the Low to High Velocity Rotary Shear Apparatus (LHVRSA) at Durham University (Fig. 5.2, e.g De Paola et al. (2015)). This apparatus is capable of slip speeds between 0.001 ma^{-1} to 1.0 ms^{-1}, and can apply an axial normal pressure of up to 20 MPa. Samples were prepared for experiments using a core drill and lathe. Cores were drilled and lathed to 24.9 mm diameter and 35-40 mm in length. The cores were placed in the sample holders, which have a hollow diameter of 25 mm (Fig. 5.2). Samples less than the ideal diameter by a few tens of microns had a layer of tape added to their base, to allow them to be held securely in the sample holder. A Teflon ring was added to the exposed section of core for some confinement, and placed just below the slip zone to allow material above to be removed by shortening of the sample, so that the rings on opposing cores should not come into contact with each other (Fig. 5.2). The sample, Teflon ring and sample holder were marked so that rotational slip of the sample with respect to either of the others could be tracked. Once both cores were attached in the sample holder to the respective arms of the rig, their alignment was checked with respect to the flatness of the slip surfaces that would come into contact with each other. This was done by bringing the cores into contact with each other and visually observing uneven parts where light could be seen. If there was misalignment under

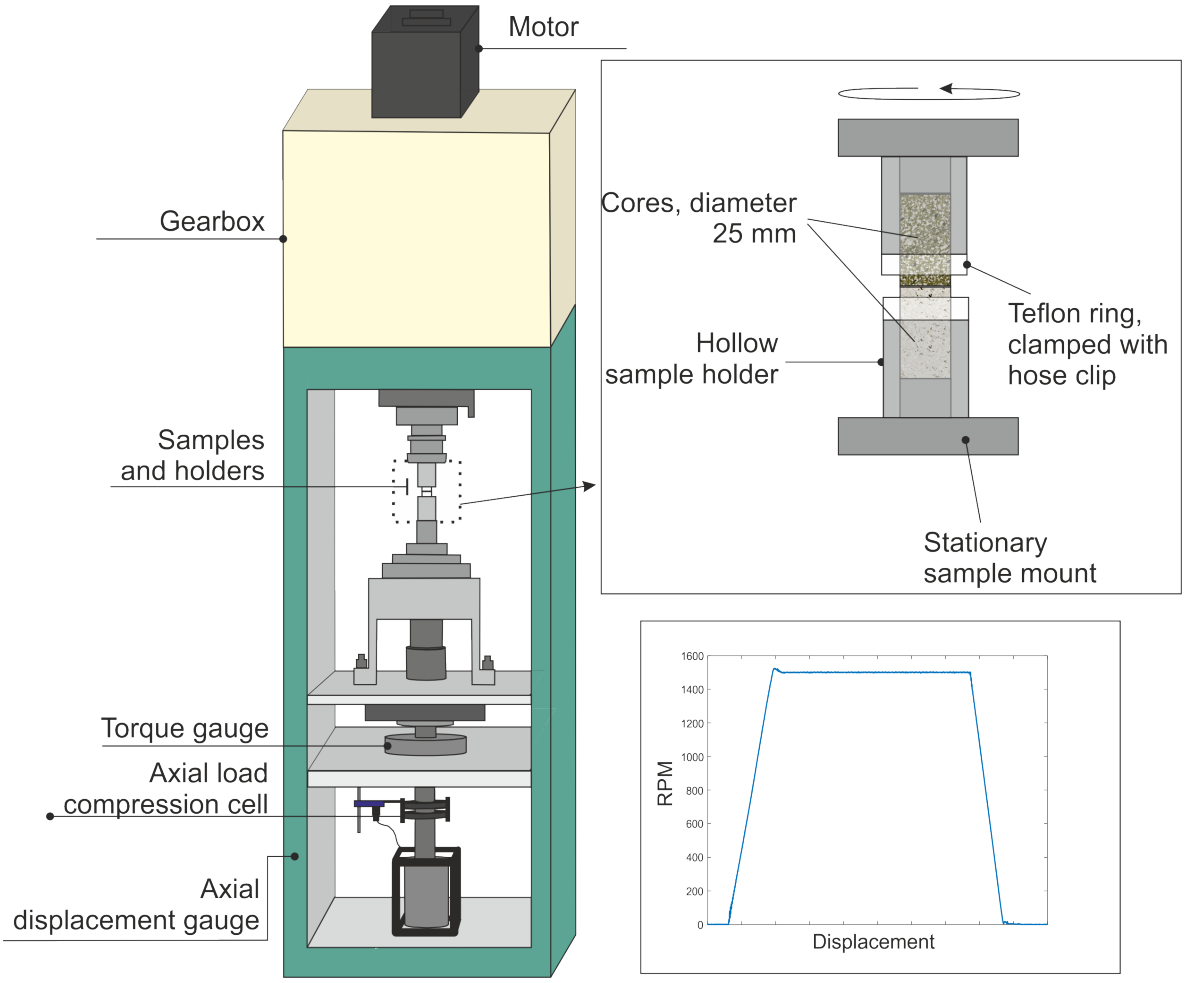

Figure 5.2: Configuration of the Low to High Velocity Rotary Shear Apparatus (LHVRSA) at Durham University, with detail of sample holders and a typical slip velocity profile.

minimal load at contact, but none when the applied load was increased to 0.5 MPa, this was deemed acceptable as the much greater pressure the experiments would be run at (18 MPa) was expected to keep the entirety of the slip surfaces in contact pre-slip. Misaligned cores were ground off until alignment was achieved.

All experiments were run under the same conditions. Samples were dry and were initially at room temperature. Slip speed acceleration was of the 'trapezium' type (Fig. 5.2), accelerating rapidly to a constant velocity of 1.3 ms^{-1} before equally rapid deceleration to stationary once molten material was observed. This resulted in rotational displacements ranging from 2.8 - 6.0 m. The terms 'velocity' and 'displacement' used here, both of which vary with

radial position within the cylindrical sample, refer to the equivalent velocity and equivalent displacement which represent values at points at $\frac{2}{3}$ of the radius. All experiments were run under an axial load of 18 MPa, close to the maximum possible with the LHVRSA.

After the experiment had finished, the melt was allowed to cool to weld the two cores together, and the welded core as a whole was removed from the sample holder. Ejected, solidified melt material was also collected from around the rig for analysis. Because the slip velocity and displacement increase from zero at the centre to a maximum at the circumference, the cores were sectioned along a chord cut one third of the way into the diameter to attempt to capture the maximum slip, being as closely parallel to the slip direction as possible whilst still displaying a usable width of material. Sections cut across the centre of the cores were also made, to capture the perpendicular to the slip direction. The cores were impregnated with resin before cutting to keep the material together during sawing. Two samples (R1, R2) had split along the welded slip zone immediately after the experiment, but being fortunately single-lithology samples, and with varying extents of the slip zone preserved, were analysed with the same methods. Optical and polished sections were produced for use with optical, SEM and EMPA methods (see section 4.2.1).

5.2.4 Analysis of slip zone roughness

The geometry, or roughness, of the slip surface profiles are quantified using similar methods to those outlined in Lee and Bruhn (1996) and Brodsky et al. (2016), where a fast Fourier transform algorithm is applied to investigate the dominant wavelengths of asperity present. The profiles of the slip zone margins are traced from a set of thin section and SEM images that traverse the slip zone. All samples were photographed at 20x magnification on the optical microscope, and at various other scales on the optical microscope and/or SEM, from sections cut one third and halfway through the core samples. The traced profiles of the slip zone margins are digitised and processed in Matlab. An example of the processing flow is shown in Fig. 5.3. The linear best fit line is calculated and subtracted from the profile to remove trends away from the horizontal and to move the profile down to straddle the x-axis (Fig. 5.3a),

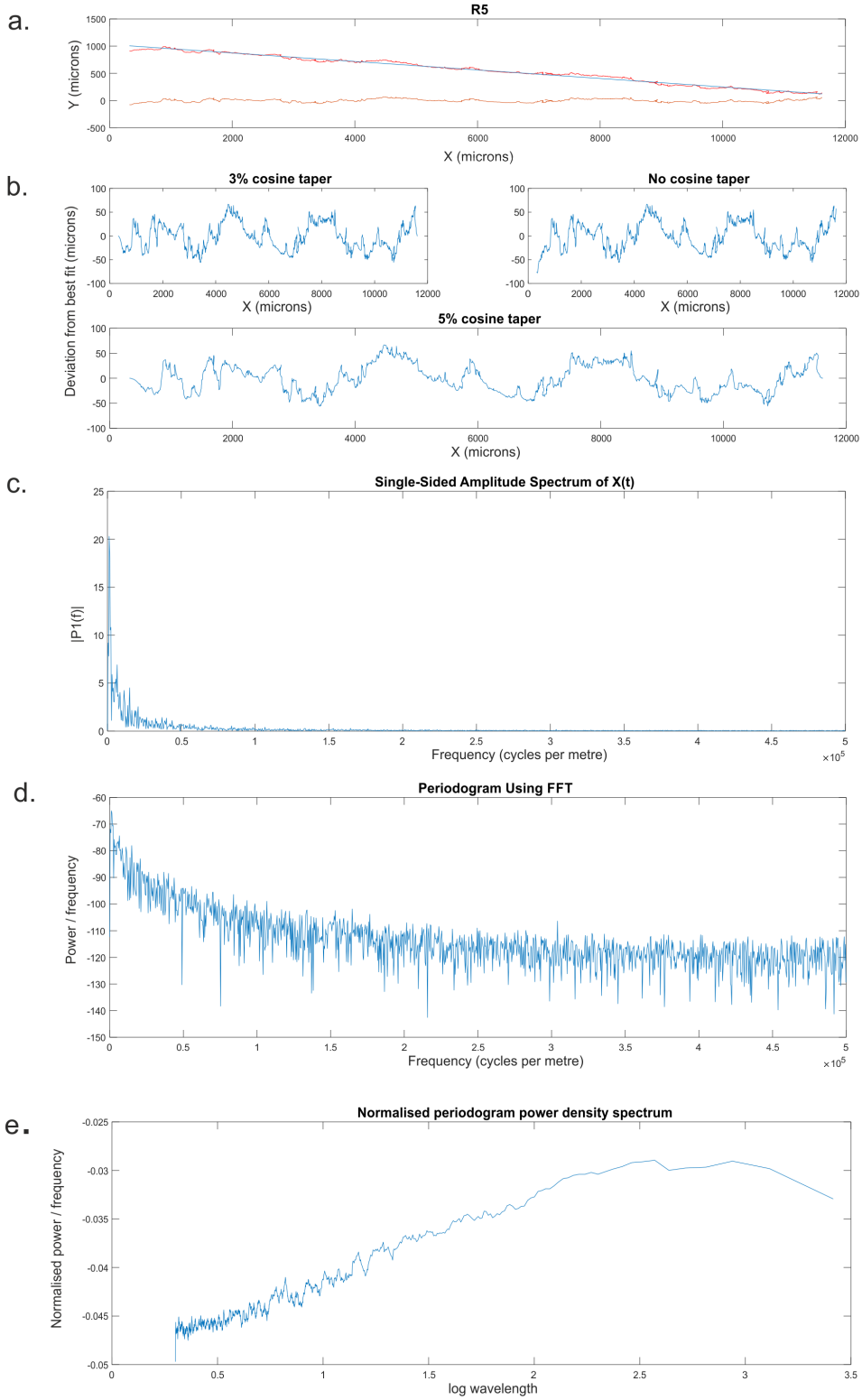

Figure 5.3: Example of process used to generate roughness analysis: a. slip zone profile is picked and digitised, then detrended using the best fit line; b. Cosine tapers are added to the end of the profile, which smooths edge effects in the forthcoming power spectral analysis. The 5% taper was chosen; c. the discrete Fourier transform is applied to the profile; d. The peridogram method is applied to produce the power spectral density, squaring the power at each frequency; e. the periodogram is normalised, displayed on logarithmic axes, displayed against wavelength and smoothed.

which removes arbitrary positioning and rotations of the profiles introduced whilst tracing from micrographs. A 5% cosine taper is added to the ends of each profile in order to reduce leakage of the power spectrum at the finite edges of the profile (Fig. 5.3b) when the discrete Fourier transform is applied. The single-sided amplitude spectrum produced by the Fourier transform (Fig. 5.3c) is approximated to the power spectral density using a periodogram method, squaring the amplitude at each frequency (Fig. 5.3d). The power spectral density produced for each sample is normalised over the length of the profile to better allow comparison of different length samples, and then plotted against wavelength. Curves are smoothed using a moving average with bins at 1% frequency intervals. The gradient and intercept of the curves are calculated and compared.

5.2.5 Compositional Analysis

Electron microprobe analysis (EMPA) on the JEOL 82e electron microprobe at the University of Leeds was used to quantify the composition of the experimental pseudotachylyte matrix, as whole rock analyses techniques would have also sampled the clasts. Manual sampling ensured the analysis spot sampled precisely the desired location, to reduce as much as possible any influence from clasts, which are widely distributed through these pseudotachylytes. Time dependent intensity corrections were run to account for the loss of sodium and potassium from the interaction volume. For these glass analyses, an accelerating voltage of 20 keV and a spot size of 2 were used. Energy-dispersive X-ray spectroscopy (EDS) analyses, initially taken as a preliminary approximation of the matrix composition, were also compared with the EMPA results. Since the EDS is generally only used as a semi-quantitative technique - due to lack of calibration standards, and weight percentage totals being often significantly less than the ideal - these results were only included after comparison of equivalent EMPA and EDS analyses produced very similar results. To improve reliability, several EDS analyses (>6 for each sample) were averaged for a mean result, normalised and then processed into an oxide weight percentage for comparison with the EMPA results. In contrast, EMPA results are presented as individual analyses to indicate any variation in composition across the pseudotachylyte veins from which analyses were taken.

5.2.6 Viscosity modelling

Calculation of the viscosity of the pseudotachylyte whilst molten allows the strength of the pseudotachylyte bearing fault plane during seismic slip to be estimated, and the effect of differing melt compositions investigated. The method used to model the viscosity (η) of the experimental melts follows that outlined in Shaw (1972), and has previously been applied to pseudotachylytes (e.g. Spray (1993), Ujiie et al. (2007)). The viscosity of the molten matrix (η_m) is modelled across the temperature range 250 - 1700°C, to encompass the possible temperatures experienced by the experimental samples. EMPA oxide weight percentages for each sample are transformed into mole fractions, and then multiplied by the 'characteristic slope' constant of the viscosity-temperature relationship for each oxide in a binary system with SiO_2 (see Table. 1 of Shaw (1972)), divided by the total SiO_2 content of the analysis. These values are summed to evaluate the gradient of the multicomponent system in viscosity-temperature space. An uncertainty in this technique is that the content of H_2O, to which the viscosity is highly sensitive, must be approximated. To do this, the difference in weight percentage between the analysis total and 100% is used as the fraction of volatiles lost. The melt is expected to be hydrous due to the preferential melting of hydrous minerals such as hornblende and biotite. Other volatiles, such as SO_2 and CO_2, are not expected to be significant, so that the loss value is attributed to H_2O alone. Weight percentages of H_2O are calculated as 5.9%, 2.2%, and 1.6% for R2, R5 and R7 respectively - the value for R2 is perhaps high, but the values for R5 and R7 are similar to those obtained from OHFZ pseudotachylytes by Spray (1993).

In order to produce a viscosity value for the pseudotachylyte matrix at a given temperature, the relationships of viscosity versus temperature (T) for several oxide systems are averaged to intecept at a single point, the co-ordinates of which are approximated by Shaw (1972) at (1.50, -6.40). Here, x = $10^4/T$ and y = ln η_m, so that the viscosity temperature dependence for the calculated slope value can be displayed using the relationship from Shaw (1972),

$$ln\eta_m = s.\frac{10^4}{T} - c_t + c_\eta \tag{5.1}$$

where s is the slope gradient calculated for the relevant composition, T is the temperature in Kelvin, and c_t and c_η are the intercept values mentioned above. The matrix viscosity can then be calculated at any temperature.

As these samples are glassy, there is no need to account for the growth of a solid crystal fraction which would affect the viscosity. However, these experimental samples, in common with natural pseudotachylytes, contain clasts that remain solid during melting, and to account for their behaviour the calculated matrix viscosity (η_m) must be adjusted to a suspension viscosity (η_s). The method used follows the empirical findings of Kitano et al. (1981). Firstly, a shape factor (A) is calculated that represents the typical shape of the clasts,

$$A = 0.54 - 0.0125r \tag{5.2}$$

where r is the aspect ratio of the clast. This was calculated for all experimental samples via image analysis on BSE images, using the same sample set as for the analysis of the clast fraction and the clast size distribution (Section 5.3.1.2). A best-fit ellipse is fitted to each recognised clast and, for the calculation of r, the major axis is divided by the minor. The shape factor (A) is then used to divide the clast fraction (ϕ) as (Kitano et al. (1981)),

$$\eta_s = \eta_m(1 - \frac{\phi}{A})^{-2} \tag{5.3}$$

In addition to clasts, these experimental samples contain varying volumes of vesicles where degassing has occurred. Vesicles also contribute to the viscosity of the melt, providing degassing occurred during slip. The effect of gas bubbles on pseudotachylyte viscosity is discussed by Spray (1993) and Ujiie et al. (2007), who both deduce that if the vesicle volume fraction in the vein is <5%, then the modification of the suspension velocity is insignificant. The vesicle fraction is analysed for these samples using a mean value from image analysis measurements. For samples R2 and R5, the fraction is <5%. However, for R7, the mean value is 7.7%, so that the vesicles must be taken into account. To do this, the following

relationship is used (Bagdassarov and Dingwell (1992)),

$$\eta_v = \frac{\eta_s}{1 + C\phi_v} \tag{5.4}$$

where η_v is the suspension viscosity incorporating vesicle effects, C is a constant of 22.4 $\pm$ 2.9 and ϕ_v is the volume fraction of vesicles in the vein. It should be noted that, especially in sample R7, the density of vesiculation is highly variable across the pseudotachylyte slip zone. High concentrations occur notably at the free edges, which were excluded from measurements, but also throughout the vein. The assumption of heterogeneous viscosity across the vein, which underpins the approach given here, is perhaps questionable, but averaging of vein composition and clast content is also applied so that the approach is consistent.

The viscosity should be related to the steady state shear strength (τ_{ss}) via,

$$\tau_{ss} = \eta \frac{V}{2\omega} \tag{5.5}$$

where V is the slip rate and ω is the halfwidth of the slipzone (Nielsen et al. (2008)). This relationship is based on the provision that the strength of the fault is sustained by viscous shear behavior of the melt in the slip zone once steady-state shear applies. The slip velocity is 1.3 ms^{-1} throughout, and the halfwidth is measured as an average from the profiles of the slip zones sampled at 150 μm increments.

5.3 Results

All samples were observed to produce melt during the experiments, generating a molten layer within the slip zone which was extruded outwards from the sample. This occurred after a few seconds of slip, and the experiments were halted shortly afterwards. Following the experiments, samples were extracted for examination, as follows.

5.3.1 Microstructural development

5.3.1.1 Structures within experimental pseudotachylytes

Experimental samples reveal a welded slip zone filled with the solidified melt produced during high velocity slip. The slip zone is bounded by wall rock margins that vary from planar to highly irregular, and injection veins may occur. The pseudotachylyte filling the slip zone contains clasts of host rock, as observed in natural samples. The matrix of the vein material is glassy in all samples except one, R1 (Fig. 5.4a-b). This sample, a single lithology meta-basic core, consists of ~ 1 μm or smaller particles of amphibole-type composition. These show consistent interfacial angles and are occasionally euhedral, so that they are interpreted as crystal grown from the pseudotachylyte rather than ultracataclasite clasts (Fig. 5.4a). Some clasts in R1 appear to have rims of new material, where crystals have nucleated upon their surface (Fig. 5.4a) which supports the production of a melt over cataclasis, as does the observation of molten material during the experiment. In other samples, the matrix is amorphous across the entire vein (Fig. 5.4b) and the colour and structure of the matrix appears mostly homogeneous. An exception occurs where biotite has locally melted - this feature is discussed below.

Clasts are rounded to angular and consist of quartz, plagioclase, potassium feldspar and hornblende. Pyroxenes are also observed in the sample involving pyroxene-bearing Corodale gneiss. Cracks in the slip zone material are often intra-clast or form around the clast edge. Some clasts appear to have a cellular texture (Fig. 5.4c-d), with internal 'spots' at the same atomic-number contrast tone as the external matrix. This occurs on both quartz and plagioclase clasts, and may be internal melting of the clast. Melting from the clast rim inwards, which is more common, is observed in the rounded shapes of clasts and also in convex embayments (Figs. 5.4, a, c-d). Plagioclase clasts, particularly in the plagioclase rich matrix of R2, may have an alteration rim revealed by differences in atomic-number contrast, suggesting alteration during partial melting of those clasts.

Vesicles are also present in these experimental pseudotachylytes. These are largest and most prevalent at the edges of the sample, where melt extrudes out of the free surface. Within

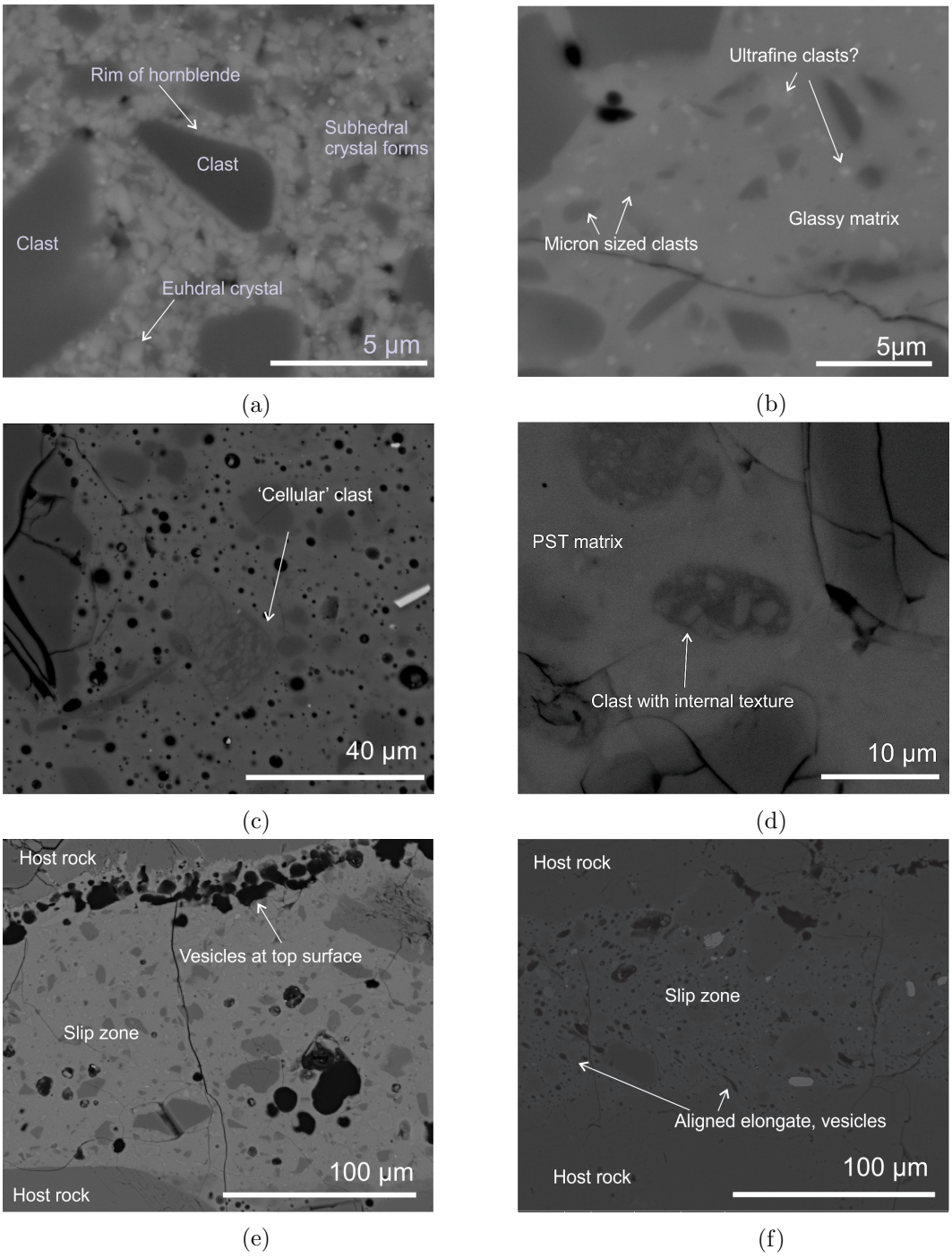

Figure 5.4: Selected microstructures of experimental pseudotachylytes : a. Metabasic core (R1): slip zone showing crystallisation of <1 μm hornblende as matrix and nucleation of hornblende crystals around central clast of plagioclase; b. Metabasic - quartzofeldspathic core (R3): More typical glassy matrix; c. Corodale - quartzofeldspathic core (R5): rounded plagioclase clast showing apparent internal breakdown in 'cellular' texture; d. Quartzofeldspathic core (R2): rounded quartz clast with similar apparent internal breakdown, lacking more regular cell-type structure; e. Metabasic - quartzofeldspathic core (R7): Vesicles are distributed at margin of slip zone; f. Corodale - quartzofeldspathic core (R5): elongation of vesicles allows alignment to be observed and shear direction inferred.

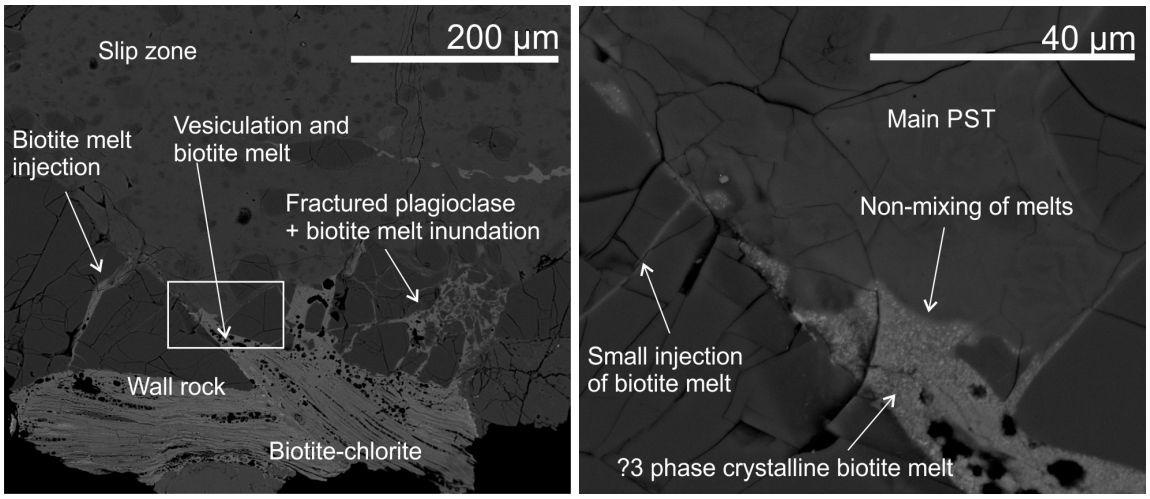

(a) (b)

Figure 5.5: Vesicle distribution in experimentally generated pseudotachylytes : a. Quartzofeldspathic - quartzofeldspathic core (R2): Intergrown biotite and chlorite in the wall rock breaks down to produce a dominantly biotite melt seen injecting into surrounding wall minerals. Vesicles present within the crystal show that this breakdown is also internal as well as at the slip zone margin; b. Quartzofeldspathic - quartzofeldspathic core (R2): Close up of boxed area shown in Fig. 5.5a. Three phases can be seen crystallised in the biotite melt, but are not resolvable for compositional analysis. The biotite melt does not mix with the main melt body of the slip zone.

the vein, they are variable and more common in some samples than others. For example, the single lithology quartzofeldspathic core (R2) has few vesicles, whereas the cores containing significant hornblende (e.g. R1, R3, R6, R7) have many more. R1, the crystalline sample, has a few, small vesicles, which may be related to the incorporation of volatiles in to the crystal lattices. Occasionally, the vesicles can be observed clustered at the surface of the pseudotachylyte vein, at the margin with the host rock (Fig. 5.4e). This occurs most frequently when the wall rock mineral that the vesicles are adjacent to is hornblende, but not always, as observed in Fig. 5.4e where plagioclase is the wall mineral. Vesicles only appear to show significant elongation and/or a preferred shape direction in part of one sample, R5 (Fig. 5.4f). However, vesicles in all samples have a mean aspect ratio of >1, with R3 showing 2.1 and R5, R6 and R7 showing 1.2 - 1.5. There is no preferential orientation of the long axis indicated in these results.

Within the host rock, biotite or intergrown biotite-chlorite is observed to have partially broken down. These breakdown zones occur both on the margins of the slip zone and within

crystals set back from the slip surface. The breakdown product is injected into the surrounding host rock and into shattered clasts, and consists of a crystalline matrix with three phases distinguishable by their differing atomic-number contrast tones (5.5a). These are <1 μm and so are not resolvable for EDS or EMPA compositional analysis. EDS analyses taken therefore provide a bulk composition for the breakdown product, which is essentially a biotite spectra, and so the breakdown product is interpreted as a melt derived from the biotite. This melt does not mix well with the main vein melt, which in places is observed to partially intrude into injection veins of the biotite-melt (Fig. 5.5a). The biotite appears to have melted entirely in-situ, with the movement of the biotite melt limited to injection veins. This biotite melt is also vesicular, with bubbles lacking a preferred alignment, and contains clasts that may be produced by the fracturing of surrounding host rock grains. In some cases these grains are completely shattered and penetrated by the biotite melt (Fig. 5.5a).

5.3.1.2 Clast content

Image analysis was used to analyse the proportion of clasts and the range of clasts sizes present in the pseduotachylyte. BSE SEM images were used in order to capture the finer clast fraction, which were not resolvable with optical techniques. The area ratio of the pseudotachylyte formed of clast material ranges from 0.24 - 0.39 (Table 5.3). The smallest clast size is limited during the image analysis process by a threshold to exclude noise, but falls as low as 0.05 μm^2. Similarly, the largest clasts present may not be captured by the imaging, especially at higher magnifications, but is recorded up to $\sim$ 3000 μm^2.

The distribution of clast sizes is similar between all samples. The two-dimensional D-value (the fractal dimension, see section 4.3.3.2) is extracted from the straight line portion of the logarithmic cumulative distribution (Fig. 5.6), and the results are shown in Table 5.3. The samples with at least one meta-basic core have D-values between -1.0 and -1.3, whereas the quartzofeldspathic -quartzofeldspathic core and the quartzofeldspathic - Corodale cores have values of -0.85 and -0.86 respectively.

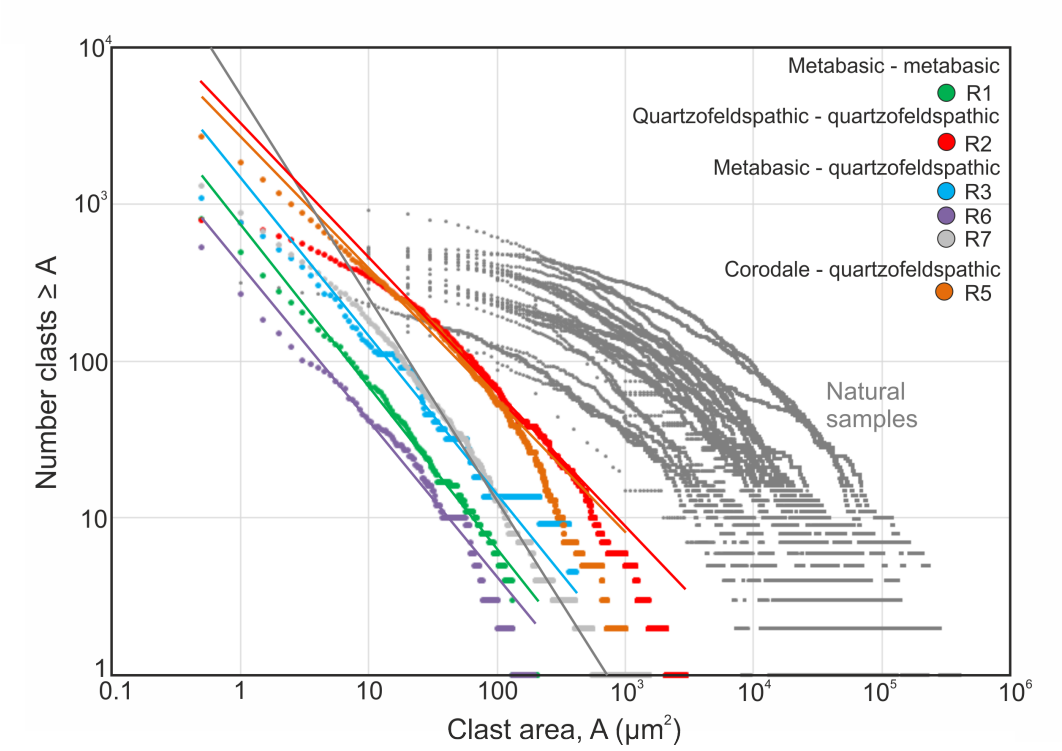

Figure 5.6: Size distribution of clasts in experimental pseudotachylytes with natural pseudotachylyte results included for comparison. Solid lines indicate best fit lines to experimental results, used to gain the fractal dimension D; the extent of best-fit line indicate the fractal range considered to fit the line.

Table 5.3: Clast analysis from experimental pseudotachylytes . Errors on clast % are ± 1 s.d. and errors on D-values represent observation uncertainties of $1\mu m^2$.

Core configuration	Run	Mean clast %	D-value
Metabasic-Metabasic	R1	0.24±0.05	-1.04±-0.49
Quartzofeldspathic - quartzofeldspathic	R2	0.29±0.04	-0.86±-0.41
Metabasic - quartzofeldspathic	R3, R6, R7	0.40±0.06, 0.27±0.06, 0.26±0.04	-1.015±0.05, -1.00±0.41, -1.30±0.28
Corodale - quartzofeldspathic	R5	0.25±0.04	-0.85±0.47

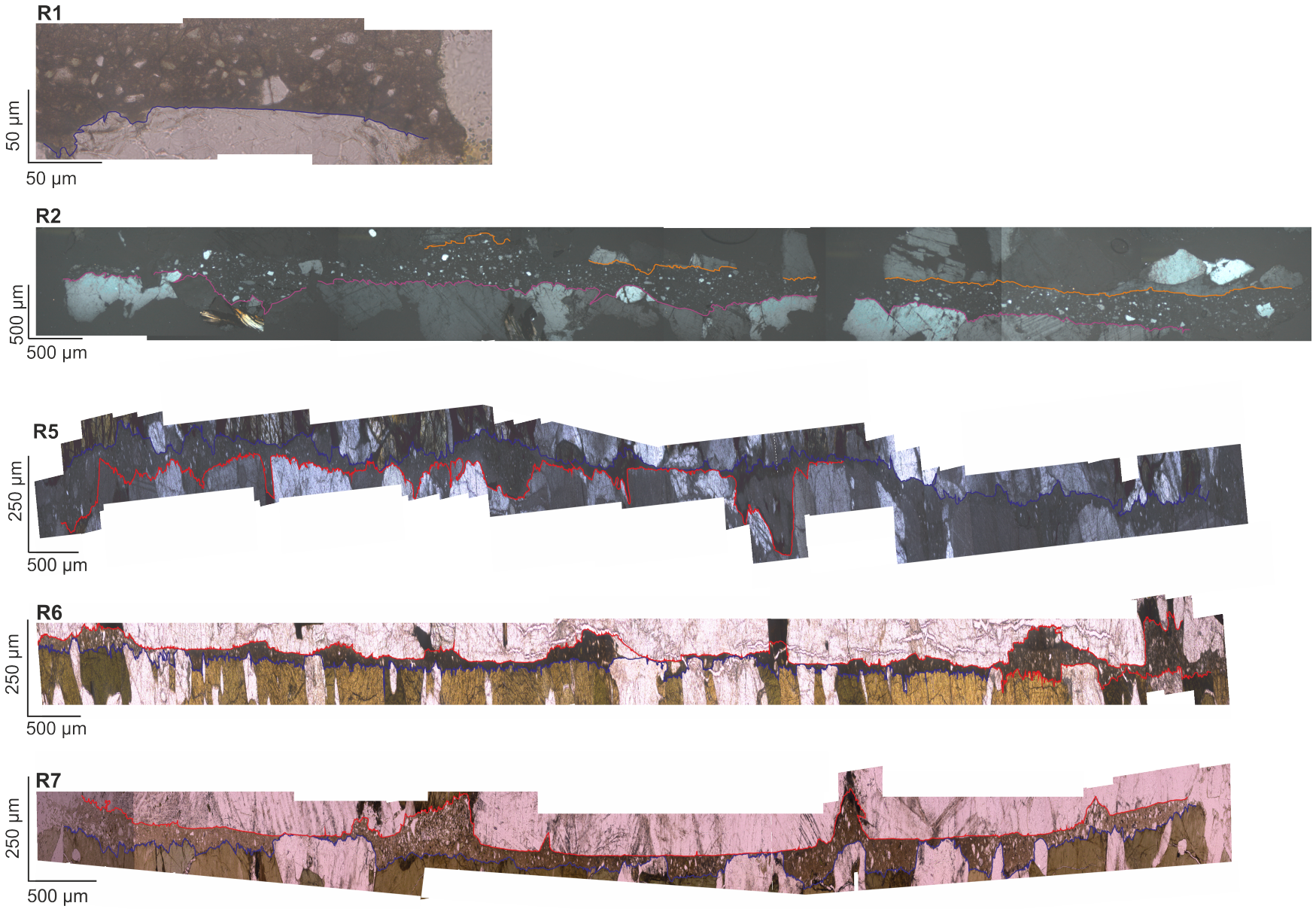

Figure 5.7: Selection of profiles of slip zone margins in experimental samples

5.3.1.3 Slip zone thickness and observed roughness

The profiles of the slip zone margins are highly irregular across the slip zone (Fig. 5.7). The width of the slip zone can be measured where the margins of the slip zone are preserved against the pseudotachylyte, and show variation from $\sim$ 380 μm width down to 1 μm. These changes in width occur rapidly on the length scale of the grain size.

One of the reasons for this irregularity is the preferential melting of biotite and amphibole relative to quartz and plagioclase in particular. This relationship is revealed in the embayment into the wall rock where these minerals occur (Fig. 5.8a-b). This appears to exert a significant control on the distribution across the slip zone of the wider pockets of pseudotachylyte. In the cores containing the meta-basic sample, amphibole is regularly distributed throughout the rock, so that the cut slip surface intersects one every 0.5 - 1.0 mm on average. The embayments in the side of the slip surface containing the meta-basic gneiss therefore occur at the same interval (Fig. 5.7). The contrast with the quartzofeldspathic gneiss can be seen in the mixed quartzofeldspathic - meta-basic cores, where the side of the slip zone consisting of quartzofeldspathic gneiss is generally smoother and has large embayments occurring more irregularly and typically at intervals >1 mm (Fig. 5.7). In contrast, the more resistant minerals such as plagioclase and, where found, pyroxenes, may cause necking of the vein to submicron widths, continuing over the length of juxtaposition of two resistant wall minerals facing each other across the vein (Fig. 5.8b).

A finer scale of roughness (10 - 50 μm) is influenced by weaknesses present within and between individual grains in the host rock. Small embayments into the host rock, or further progression into an injection vein, are often observed at features such as grain boundaries and pre-existing micro-fractures (Fig. 5.8c). On the intra-crystal scale, cleavage plane angles are replicated in the roughness of the slip zone margin, where fragments have been sheared off along them as planes of weakness (Fig. 5.8d).

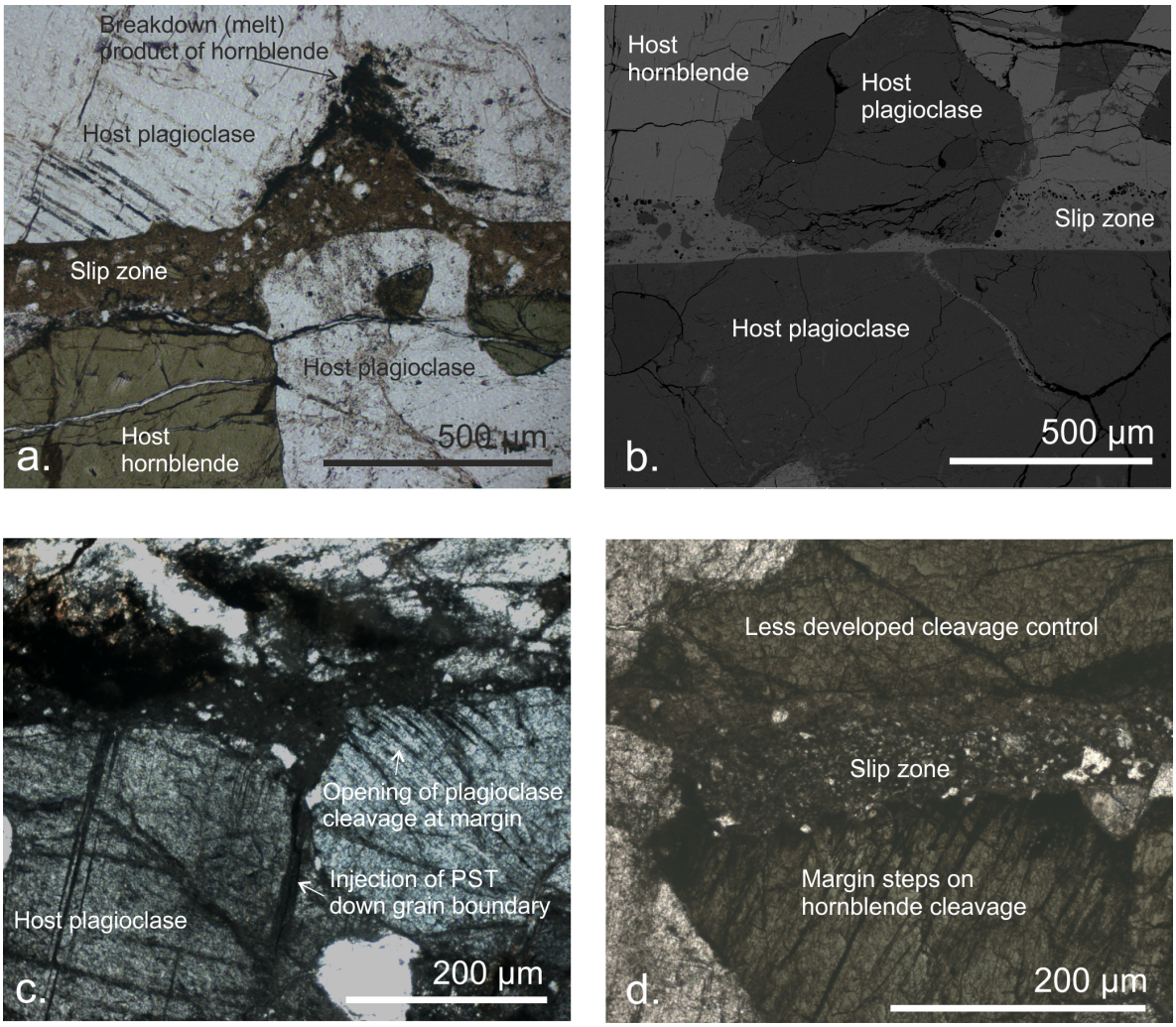

Figure 5.8: Preferential melting and pre-existent weak planes as controls on roughness: a. Metabasic - quartzofeldspathic core (R7): Differential hardness and melting potential of hornblende creates variable slip zone width, with hornblende embayed and plagioclase protruding. Opposite plagioclase lies embayment with traces of opaque material signifying complete breakdown/melt of a hornblende or biotite, equivalent to the process in Fig. 5.5; b. Metabasic-quartzofeldspathic core (R7): Contrast between ower margin planar plagioclase surface against the variable profile of the upper margin. Juxtaposition of two resistant minerals often causes extreme thinning of the slip zone to only some microns wide; c. Corodale- quartzofeldspathic core (R5): Grain boundary between adjacent minerals - both plagioclase, but at differing orientations as can be seen from the cleavage angle - utilised for injection of pseudotachylyte . Cleavage opened at margin; d. Metabasic- quartzofeldspathic core (R7): Cleavage planes in hornblende picked out by shape of margin, due to plucking or shearing.

5.3.1.4 Quantifying roughnesses of experimental slip zones

The peak on power spectral densities (Fig. 5.9) represents the most common frequency of asperity - all samples show that the largest wavelength asperities occur more frequently (Fig. 5.9). A peak, or the beginning of a plateau, appears at values of log (wavelength) = 2.5 to 3 μm, or asperity wavelengths between 300-1000 μm. The higher the position of the overall profile on the power spectral density scale, the greater the roughness of the surface. The two lowest lines on Fig. 5.9, representing the two quartzofeldspathic hosted slip margins of sample R2, are quite distinct from each other but are both lower in position to the other samples. The profiles from quartzofeldspathic slip zone margins that were run against different rock types in the mixed lithology cores share a similar range of slope and intercept between them but sit at higher power and are shallower than the single-lithology quartzofeldspathic core R2. Similarly, there is a noticeable difference in power between the single-lithology metabasic core R1 and the metabasic sides of the mixed cores R6 and R7, which again sit at higher power spectral densities. The profiles shown in Fig. 5.9 are from samples imaged optically at 20x magnification, apart from the samples R1 and R2 which have limited preservation and are difficult to see optically, respectively. Additional profiles imaged at various other magnifications show a similar relative order of power spectral densities, with the single-lithology samples sitting below the mixed-lithology samples, but the absolute values of each profile at equivalent wavelengths vary somewhat.

5.3.1.5 Initial interpretation of microstructural results

Some features of these experimentally produced pseudotachylytes have not been recognised in the natural pseudotachylyte samples from the Western Isles. Natural pseudotachylytes are rarely truly glassy, whereas all except one of these experimental samples are. This is likely to be due to the experimental conditions, where the ambient temperature is room temperature rather than >250°C. Faster cooling along greater temperature gradients favour the formation of glass over crystalline quench textures (Lofgren (1974)). Alternatively, the natural samples may have been glassy initially before devitrifying into the crystalline forms now observed. In

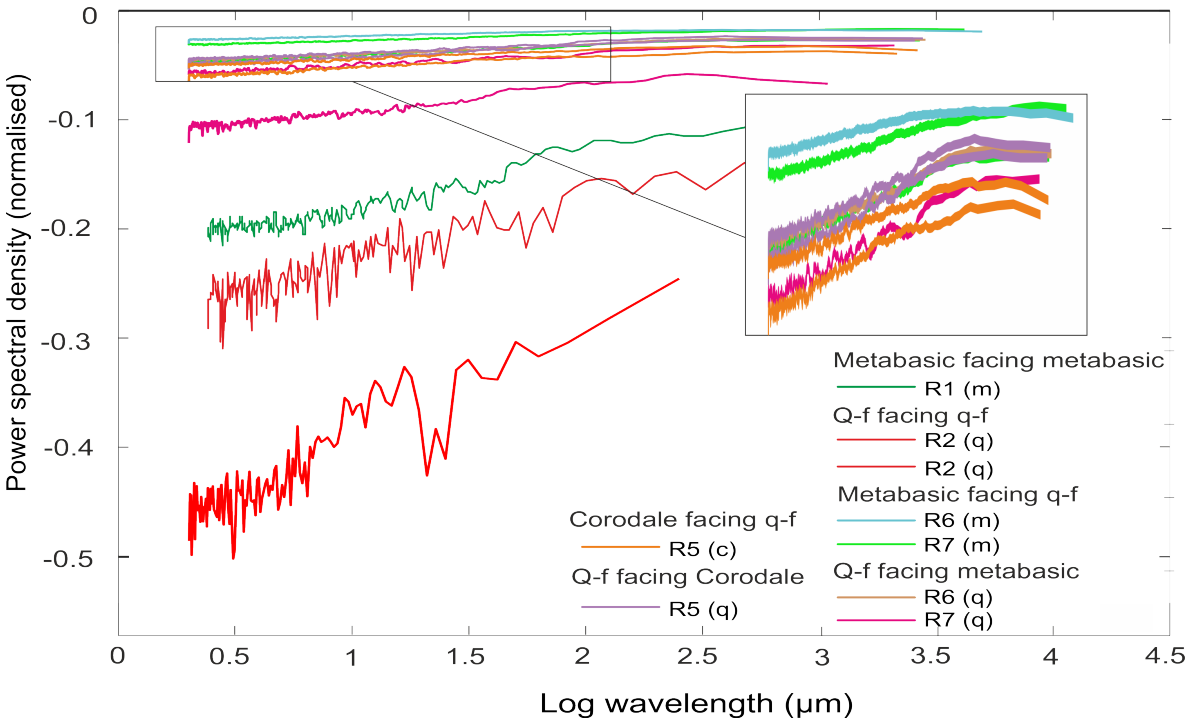

Figure 5.9: Power spectral densities for roughness of slip zone profiles highlighted in Fig. 5.7, normalised and presented against wavelength of the asperity.

general, experimental pseudotachylytes are typically reported as glassy (Lin and Shimamoto (1998), Hirose (2005), Di Toro et al. (2006a)), although Spray (1988) produced acicular, radiating and spherulitic crystals in glassy matrix, similar to natural pseudotachylytes, and replicated them in Spray (1993). Olivine microlites have also been reported by Del Gaudio et al. (2009).

The other feature not observed in natural samples are vesicles, which are common in the experiments containing the metabasic gneiss. This metabasic sample contains a high proportion of the hydrous mineral hornblende. The vesicles are therefore expected to consist predominantly of exsolved water. Natural pseudotachylytes, however, are also found in host rocks containing significant hornblende, and also biotite, another hydrous mineral. The distribution of vesicles in the experimental pseudotachylytes, notably where melt extrudes at the free edges of the slip zone and also strung along the slip zone margins of the pseudotachylyte, suggests that relatively low pressure experimental conditions allow the volatiles to exsolve out of the melt. In the natural case the confining pressure is too high and the volatiles become

instead incorporated during crystallisation of the melt.

As well as the main melt bodies, several of these samples show localised melting of biotite and hornblende, sometimes remote from the slip zone. The single-crystal melting temperatures for biotite and hornblende are 650°C and 750°C respectively (Spray (2010)), so that the presence of these partly melted minerals in the wall acts as an isotherm for conduction of frictional heat away from the fault. In the sample R7, host rock hornblende has melted in-situ in two occurrences at ~ 75 and ~ 90 μm perpendicular distance from the vein wall. It is more common, however, to observe this localised melt production at the margins of the slip zone in association with biotite (or biotite-chlorite intergrowths), where the melt is interpreted to have formed earlier than, and to have had limited mixing with, the main melt body.

Quantification of the roughness using spectral analysis has shown that there are differences in roughness behaviour between different lithologies and between equivalent lithologies in single- and mixed-lithology cores. The relationships are however uncertain due to the lack of consistency in displacements between experiments, which also correlates with the variation in roughness. Additionally, the single-lithology meta-basic core only has a very limited length of slip margin preserved, so that the results may not be representative of its entire length.

Generally in fault zones, the roughness, at the field scale at least, is expected to decrease with slip (Brodsky et al. (2011)). The roughness evolution of experimental samples differs significantly from natural faults in that rotary shear sample preparation involves smoothing of the slip surface as much as possible before deformation is invoked, whereas natural faults begin each slip event with some degree of roughness. Absolute values for intecept vary with the magnification and detail available for the digitising of the slip zone margin, so that the values are only meaningful when compared relatively with samples picked at the same scale. Qualitatively, the mixed fault profiles do seem to show different roughness between the metabasic and quartzofeldspathic walls due to the distribution of easily melted minerals. This lends support to the contribution of lithology in determining roughness.

5.3.2 Compositional analysis of experimentally produced melts

Variable compositions of the melts produced by different core configurations are initially indicated by the differing plain light colours of the slip zone pseudotachylyte. Under plane polarised light, the pseudotachylyte produced by the single lithology quartzofeldspathic core, R2 is colourless and is difficult to distinguish from the plagioclase and quartz that dominated the clasts and the host rock margins. In contrast, the pseudotachylyte of the mixed metabasic - quartzofeldspathic and Corodale - quartzofeldspathic cores is a moderate brown (Fig. 5.8a), and the metabasic core a dark brown-black. Under cross polarisation, all the pseudotachylyte samples appear dark and opaque.

Major element compositions for these experimental pseudotachylytes are displayed in Fig. 5.10. Results from the more accurate EMPA method are displayed as solid lines, but the EDS results, dashed lines, compare favourably. Broadly, two groups of melt can be distinguished - the high aluminium, low ferromagnesian pseudotachylyte of the quartzofeldspathic and the Corodale - quartzofeldspathic cores, which approximate a plagioclase composition, and the more ferromagnesium rich metabasic and mixed metabasic - quartzofeldspathic cores, which appear to be dominated by an amphibole-type composition (Fig. 5.10).

In Fig. 5.11, the SiO_2 vs Na_2O + K_2O weight percentages are plotted onto an igneous melt classification (Best (2009)). The EDS points again match the EMPA points favourably, although EDS may overestimate the SiO_2 content by a few percent. This comparison increases confidence in the placement of EDS points for samples where EMPA is not available (samples R1, R3). The EMPA data, which represent individual analyses from across the vein, are relatively clustered indicating that the pseudotachylyte matrix composition in the slip zone is in general somewhat homogeneous. This is supported by more numerous semi-quantitative EDS analyses, which show little variation with changing location either transverse or parallel to the slip zone margins. The main source of compositional heterogeneity remains the unmixed biotite melts discussed above (section 5.3.1.1). A range of melt compositions has been produced by the various sample configurations. Under this classification, the quartzofeldspathic

core produces an evolved trachy-dacite, and the mixed Corodale - quartzofeldspathic core a slightly less silica rich version. The metabasic core has produced a basaltic melt, and the three mixed metabasic - quartzofeldspathic cores, a more alkali and silica-rich basalt. These mixed samples form on a mixing line between the wholly quartzofeldspathic and metabasic melts, but lie much closer to the metabasic sample. Even the mixed Corodale - quartzofeldspathic sample lies on this projected line, despite the Corodale gneiss having a different mineralogy to the standard metabasic core, but lies along the more evolved section of the range. The two mixed metabasic (amphibolite) - quartzofeldspathic samples (R6, R7) for which EMPA analyses are available replicate each other well.

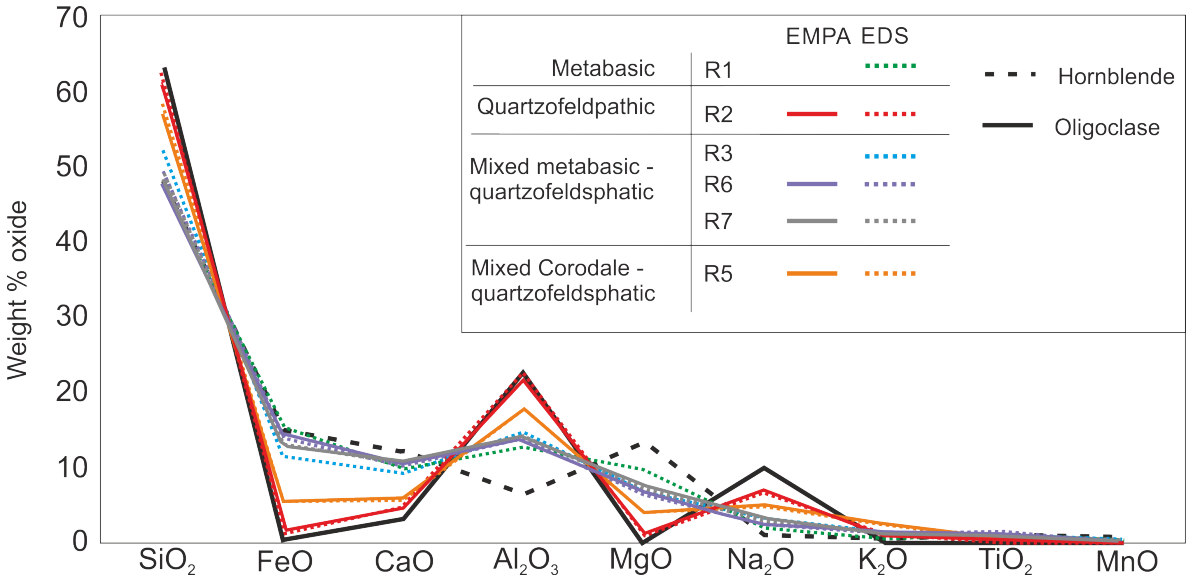

Figure 5.10: Major element oxide analyses taken using EDS and EMPA methods. Also shown are the analyses for oligoclase and a relatively Mg-rich hornblende (from Deer et al. (1992)).

5.3.2.1 Melt viscosities

Melt viscosities were calculated for experimental samples R2, R5, and R7 (see Table 5.2). Suspension viscosities for these samples are plotted against temperature in Fig. 5.12. In a melt temperature range from 1250-1550°C, viscosities vary from 704 - 8734 Pa s for R2, 735-9905 Pa s for R5, and 29 - 252 Pa s for R7. Although the viscosity varies over an order of magnitude across this temperature interval, the samples R2 and R3 have similar values,

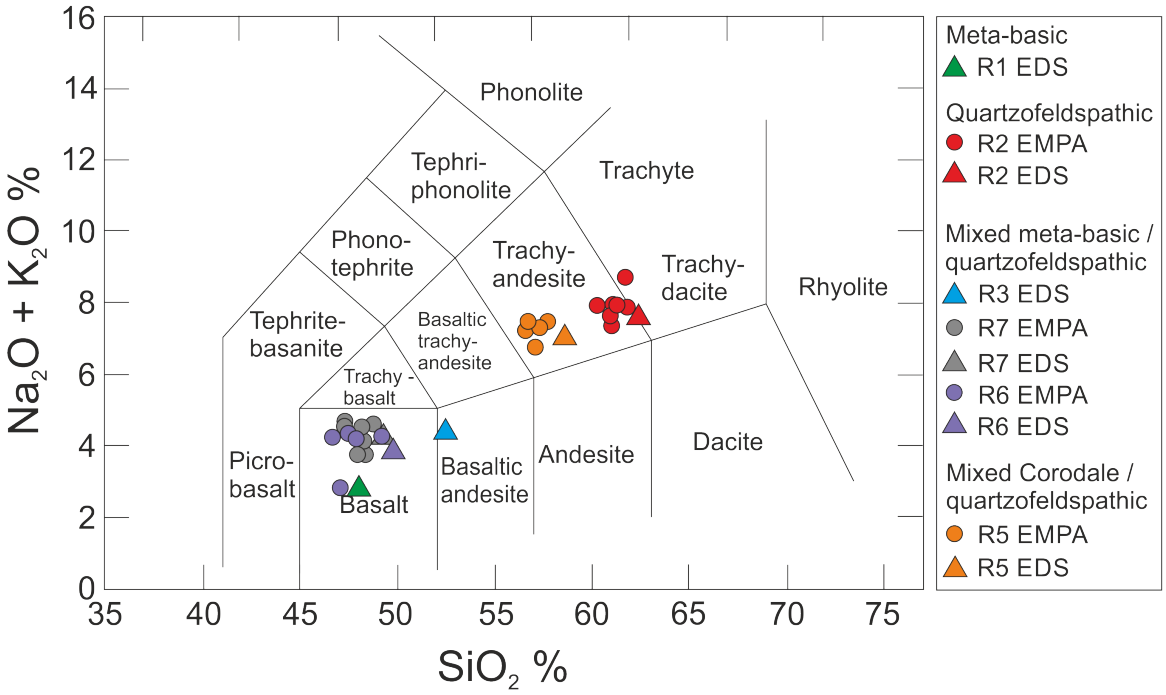

Figure 5.11: Analyses from EDS and EMPA for SiO_2 vs Na_2O + K_2O of experimental pseudotachylytes , overlain on a typical classification of igneous extrusive rocks (Best (2009)).

whereas R7 is much lower (Fig. 5.12). An adjustment for significant vesicle content, which acts to decrease viscosity, has been applied to R7. Even with this correction the suspension viscosity over the same temperature range is 80 - 687 Pa s, an order of magnitude lower than R2 and R5 (Fig. 5.12). Shear strengths calculated from these viscosities using Equation 6.6 range from 7.8 - 96.4 MPa for R2, 13.9 - 187.6 MPa for R5, and 0.4 - 3.5 MPa for R7 over the temperature interval 1250 - 1550°C.

5.3.2.2 Initial interpretation of compositional results

The melt in the single-lithology quartzofeldspathic core sample R2 shows a major-element profile very close to that of oligoclase, which is the plagioclase composition expected from the host and from natural OHFZ pseudotachylyte melts. The mixed Corodale - quartzofeldspathic core is also dominated by this plagioclase composition, but is a little more influenced by the higher FeO, MgO and lower Al_2O_3 content of the more hornblende dominated melts. The Corodale gneiss does contain hornblende, although not much more than the quartzofelds-

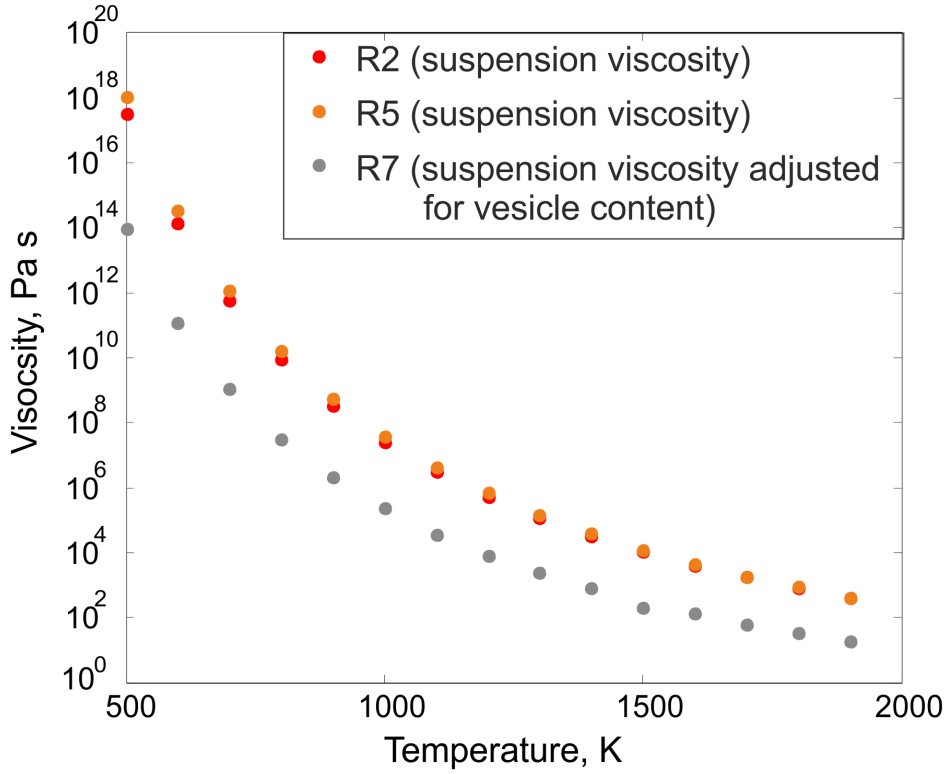

Figure 5.12: Relationship of suspension viscosity with temperature for a singe lithology quartzofeldspathic core (R2), the Corodale - quartzofeldspathic mixed core (R5) and metabasic - quartzofeldspathic mixed core (R7). The latter is a vesicle-adjusted suspension viscosity, due to the >0.05 vesicle fraction.

pathic gneiss, but a little more biotite is also present. The pyroxenes in the Corodale gneiss appear mechanically hard, and do not participate significantly in melting; rather, they form resistant asperities on the slip zone margin or clasts in the pseudotachylyte. The melts formed with a metabasic component differ from a complete hornblende composition most noticeably at the Al_2O_3 and MgO oxide percentages, so that it seems likely that these melts represent a mixture of plagioclase and amphibole compositions, similar to the natural pseudotachylyte samples of the OHFZ (section 4.3.4). This is borne out by the crystallisation of the melt in sample R1, which has apparently produced hornblende as the major phase with interstitial components that may include plagioclase, having a similar Z-contrast to the plagioclase clasts. All experimental melts have somewhat higher potassium content than either the oligoclase or hornblende ideal compositions (Fig. 5.10), which is likely due to contributions from biotite and/or potassium feldspar where present in the host samples.

The overall composition of the melts ranges from approximately basaltic to andesitic, as shown in Fig. 5.11. As has been discussed, the 'basaltic' R1 melt has actually crystallised hornblende, rather than the pyroxene expected in a true basalt. Frictional melting experiments have shown that pyroxene-plagioclase assemblages can crystallise from melting amphibolite host rock (Spray (1988)), and it is not immediately obvious why these differences occur. It is possible that the melt composition could exsolve augite, rather than hornblende, with plagioclase. However, the melt compositions of all experiments described here have iron contents that cannot be explained as a mixing between augite and plagioclase, whilst higher iron clinopyroxenes tend to have too low CaO and MgO for these results. The projection of the compositions onto the classification in Fig. 5.11 is a little artificial considering that the 'basaltic' samples would not be recognised as such considering their mineralogy, but it serves to show the trends in silica vs alkali content of the experimental melts. These trends are driven by the variation in core lithology, with reduced availability of preferentially melted hornblende or biotite leading to increased silica content in the melt, as frictional heating is driven high enough, with less initial melt lubrication, to drive plagioclase and quartz to melt. The inclusion of the Corodale-quartzofeldspathic sample R5 within the range might suggest that the proportion of the minerals biotite and hornblende are the controlling factor, no matter if the rest if the rock mineralogy differs. Progressive displacement is also expected to change melt composition, through increasing input of resistant minerals such as quartz and plagioclase, driving melt composition towards more silica rich compositions as melting proceeds. However, it has been reported elsewhere that the compositional evolution with slip is more complex, involving changes in many major elements at different times, although consistency begins to appear around the steady state section of coseismic slip evolution (Hirose (2005)).

The viscosity range predicted covers two orders of magnitude, due to the poorly constrained range of estimates for the peak melt temperature. Viscosities will also change throughout slip due to the evolution of temperature and melt composition (Hirose (2005)). A significant factor of melt composition is water content, which viscosity is highly sensitive to, but which carries measurement uncertainties in this analysis (see section 5.2.6). The im-

pact of deformation on suspension viscosity, which is noted to decrease under strain (Metzner (1985)), has not been considered here.

5.3.3 Mechanical results

Mechanical results from these experiments show weakening of the slip zone during slip (Fig. 5.13). As these experiments were designed to study microstructural development rather than to produce reliable mechanical analysis, the interpretation of these graphs is of limited reliability. However, they are may be used in combination with the microstructural and compositional variations described previously.

All samples produce a pronounced peak in the frictional coefficient before weakening, with further slip down to a steady state value. The most reliable part of the experimental data is the steady state slip phase, which is less vulnerable to the effects of noise. For the single-lithology metabasic gneiss experiment (R1), the steady state frictional coefficient $\mu_{ss} = 0.10$, and for the single-lithology quartzofeldspathic gneiss experiment (R2) $\mu_{ss} = 0.13$. The steady state value of μ for the mixed quartzofeldspathic gneiss-metabasic gneiss experiments (R6, R7) was 0.96. The steady state frictional coefficient for the mixed Corodale gneiss - quartzofeldspathic gneiss core (R5) is similar to the single-lithology quartzofeldspathic gneiss with a value of $\mu_{ss} = 0.13$. The peaks, which represent the second peaks present in frictional sliding curves such as these, may occur at different offsets and over different wavelengths. The peak frictional coefficients, which range from μ=0.15 to μ= 0.38, tend to show lower strengths for experiments using metabasic samples. However, these values are sensitive to the conditions of the experiment set up, and are not considered reliable, especially when some lack repeats.

5.4 Discussion

The composition and microstructures on a slip zone evolve interdependently during slip, and both control and reflect the strength and deformation behaviour of the fault during the slip

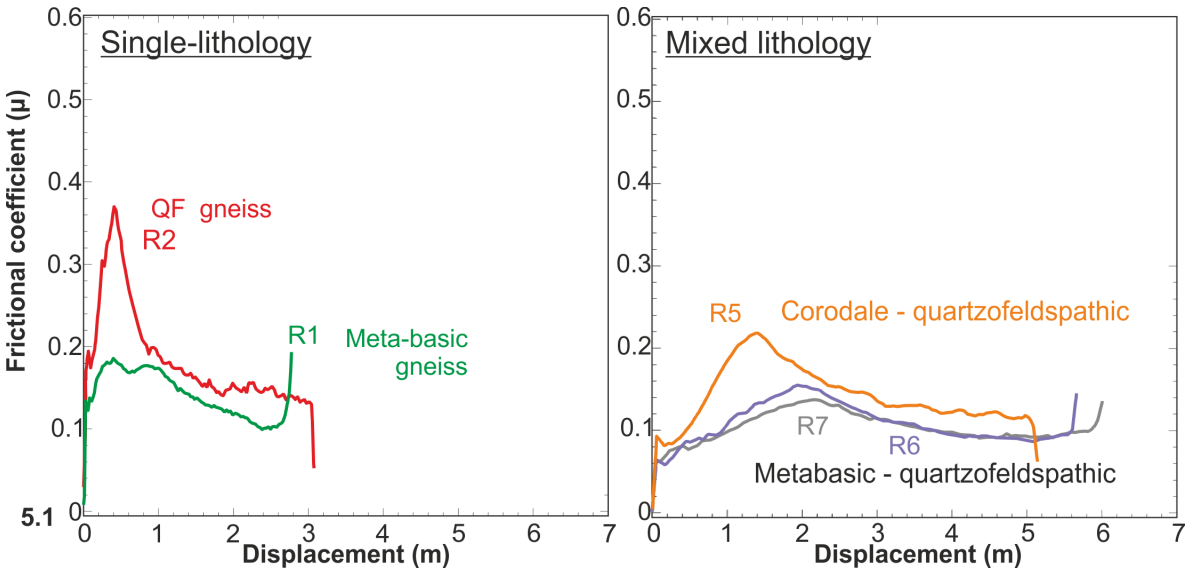

Figure 5.13: Mechanical results for many of the experiments run during this study, shown as frictional coefficient (μ) against displacement.

period. The production of frictional melts at seismic slip rates has been studied experimentally for a number of years (e.g. Spray (1987), Tsutsumi and Shimamoto (1997), Hirose and Shimamoto (2003), Di Toro et al. (2006b), Lavallée et al. (2015)), but this study adds to this existing body of work by also looking at faults formed between different lithologies. This discussion, therefore, focuses particularly on the behaviour controlled by the mineralogy of the host rock and the effects of mixed-mineralogy.

5.4.1 Fault zone roughness

In many aspects, the microstructural characteristics of these experimental melts are comparable to natural pseudotachylytes formed from similar rocks in the OHFZ. For example, the preferential melting of amphiboles and biotites causing embayments into the walls of the host and the associated irregularity and roughness in the profile of the slip zone is seen often in the natural fault vein pseudotachylytes (Fig. 4.20b). Small injection veins do develop in the experimental slip zones but less systematically than in natural samples. This is related to both the small length scale of the experimental samples and the lack of a transient stress field associated with the propagating rupture front, because the experimental samples slip on a

pre-cut failure surface. The tensile stresses associated with the passage of the crack tip are thought to be responsible for the secondary fractures facilitating injection veins (Ngo et al. (2012), see section 3.6.1). The exploitation of weaknesses in the wallrock, such as grain boundaries and microfractures to form embayments or injection veins, is also a common feature in both natural and experimental pseudotachylytes. Grain boundaries often become exploited as cracks where two different minerals, or the same minerals in differing crystalline orientations, are juxtaposed due to differential or anisotropic thermal expansion of the crystals in response to heat conduction into the wall from the frictional heat source (Fig. 5.8c).

Another plane of weakness that frequently controls the sub-grain scale vein roughness is cleavage, particularly in plagioclase and hornblendes which compose a significant proportion of these samples (Fig. 5.8d). The margins of the host rock are abraded along cleavage planes, and hence form a regular and predictable roughness for the length of the grain, although dependent on the grain size and orientation of each crystal. Because the orientation of the cleavage planes relative to the slip zone controls how well the shear stress is resolved onto the cleavage plane in order to shear off material from it, the fabric of the whole rock becomes significant. If the rock has little fabric, and there is no crystal preferred orientation (CPO), the orientation of individual crystals is essentially random and therefore the exploitation of cleavage and its influence on the roughness of the slip zone also varies randomly along the slip zone margin. If there is a preferred orientation that presents the cleavage at exploitable angles relative to the slip zone, this wavelength of cleavage controlled roughness will pervade across the slip margin, or at least where that mineral occurs in the wall. Furthermore, if the fabric comprises a mineral banding, the slip zone margins may be dominated by a certain cleavage set with a consistent orientation if a CPO is also present, in which case the impact of cleavage on roughness may persist for a significant part of the fault if it lies banding- parallel. Of the rock types in the OHFZ, including the samples deformed in these experiments, only the mylonitic rocks tend to have a strong CPO fabric, although the quartzofeldspathic gneiss has variable strength mineral banding. The cleavage - scale roughness geometry therefore varies from grain to grain (Fig. 5.7).

The roughness of the slip zone can therefore be controlled mineralogically by the mineral fractions of the rock, the distribution of those minerals along the slip plane and the orientation of those minerals. The changing proportion of preferentially melted hornblende in OHFZ rocks appears to be a major control on the grain-scale roughness that develops during slip. This is partially due to preferential frictional melting forming often concave embayments into the hornblende, relative to the prominent feldspars and quartz. Mechanical wear is another process that preferentially breaks down hornblende, as evidenced by the large number of hornblende clasts, at the smaller end of the clast fraction (section 5.3.1.2). These combine to produce the fault zone profiles in Fig. 5.7. The hornblende-rich metabasic samples tend to have greater roughness than the quartzofeldspathic samples (section 5.3.1.4), because of the higher number of embayed hornblende. The dominant wavelength of asperity is similar between the rock types, probably because the grain size, fabric, and range of minerals are the same in the metabasic and quartzofeldspathic gneiss samples.

The different roughness developed when a different lithology is juxtaposed across the fault implies that the evolution of roughness is linked to the geometry of opposing fault wall. This is likely due to some function of adhesive wear mechanisms as asperities develop from resistant minerals in the opposing wall, mismatched in distribution and perhaps size between the two rock types. Increasing mismatch should lead to decreased contact area between the fault walls, encouraging the reduction of friction along the fault (Scholz (2002)). Additionally, several differences in asperity properties will develop in the different lithologies which will impact on the overall strength of the fault and also the wear on the opposing wall (Fig. 5.14). This behaviour at the microscale should be replicated on natural faults juxtaposing lithologies, although quantitative extrapolation of these results to natural faults is complicated by the difference in scaling of damage (Power et al. (1988)) and the tendency of natural faults to smooth with slip (Brodsky et al. (2011)), whereas ground experimental fault surfaces initially become rougher.

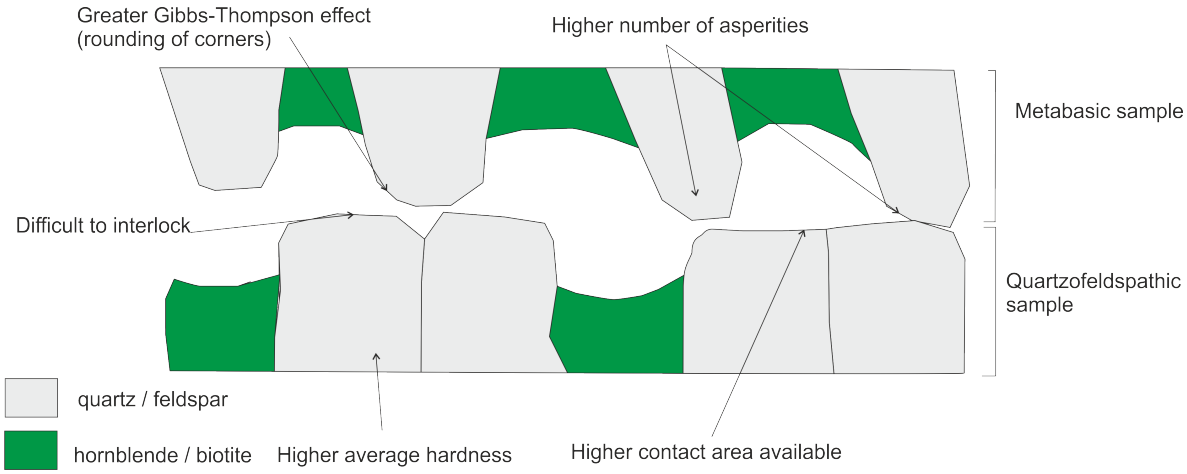

Figure 5.14: Schematic diagram of fault between quartzofeldspathic and amphibolitic metabasic samples, based on Fig. 5.7, highlighting the differences in asperity and slip zone properties that might be expected to influence wear of the opposing fault wall differently to if the same-lithology was juxtaposed.

5.4.2 Melt heterogeneity

The main melt body has been shown to be fairly well mixed, with limited variation between EMPA analysis points at different locations within the vein (Fig. 5.11), so it is curious that incorporation of the biotite melt has been so limited (Fig. 5.5). Biotite has the lowest single crystal melting temperature of the minerals found in these samples (Spray (2010)), so would be expected to melt first and remain molten during the duration of slip. Shortening of the sample during the experiment ranged between 0.10 - 1.21 mm, with a mean of 0.65 mm. This is a minimum for the amount of host rock material removed from the margins as it does not include that volume replaced by the width of melt in the slip zone. Considering the average grain size in many of these samples is $\sim$ 1 mm, these shortening values indicate that the current slip zone margins expose parts of the crystal, or new crystals, that were not at the slip interface when slip began. It seems likely, therefore, that these biotites at the slip zone margin, along with those lying within the wallrock, began melting relatively late during slip, depending on the rate of thermal conduction. Shortening of each wall exposed the biotite melt to the main slip zone, but had insufficient time to mix with the main vein. This process is restricted to biotite and hornblende because it appears that the wall rock temperatures do not increase enough to melt the other minerals present - dominantly quartz, feldspars and

pyroxenes - unless they are directly in the slip zone at the frictional heat source. The nanocrystalline grain size of parts of the biotite melt, in comparison to the glassy main melt zone, also indicates a lesser degree of undercooling (Lofgren (1974)), i.e. from a reduced maximum temperature. This could be controlled either by late melt production, beginning after peak fault temperature is reached, and/or initial non-proximity of the biotite from the heat source of the slip zone. In many cases the biotite melt has injected into and appears to have heavily fractured surrounding crystals, which suggests the melt was initially confined and pressurised rather than able to escape on the unconfined slip zone. In Fig. 5.15a, a slip zone cuts down into the host rock above an in-situ melting hornblende crystal, which may have facilitated the change in slip zone geometry by fracturing the rock above.

This in-situ melting of wall rock minerals away from the slip zone, and the fracturing and injection of the melt into the surrounding rock, is a feature that is also observed in natural pseudotachylyte samples from the OHFZ (Fig. 5.15b). This behavior emphasises how thermally driven decomposition of individual minerals feeds back into the mechanical deformation of the rock, influencing the geometry of the slip zone and the dynamic strength of the wallrock.

5.4.3 Clast content

In general, a finer, nanoscale clast fraction is found in the experimental pseudotachylytes which is not present in natural samples. In addition, the overall area proportion of clasts in the vein is on average higher in the experimental samples than in natural OHFZ pseudotachylytes, with respective averages of 0.29 ± 0.05 and 0.19 ± 0.07 with one standard deviation error. The melting of the smaller fraction, thought to be necessary for removal of these grain sizes in natural pseudotachylytes (Shimamoto and Nagahama (1992)), is perhaps not as well-developed a process during experimental melting. This may be due to factors such as a limited slip period (and hence heating duration) in the experiments (2-5 seconds) compared with natural slip periods (0.1-100 seconds, dependent on size, Kanamori and Brodsky (2004)), or alternatively other controls such as the limited normal loading in the experimental set-up. The relative loss in the finer fraction in natural samples is clearly seen in Fig. 5.6, where the distribution

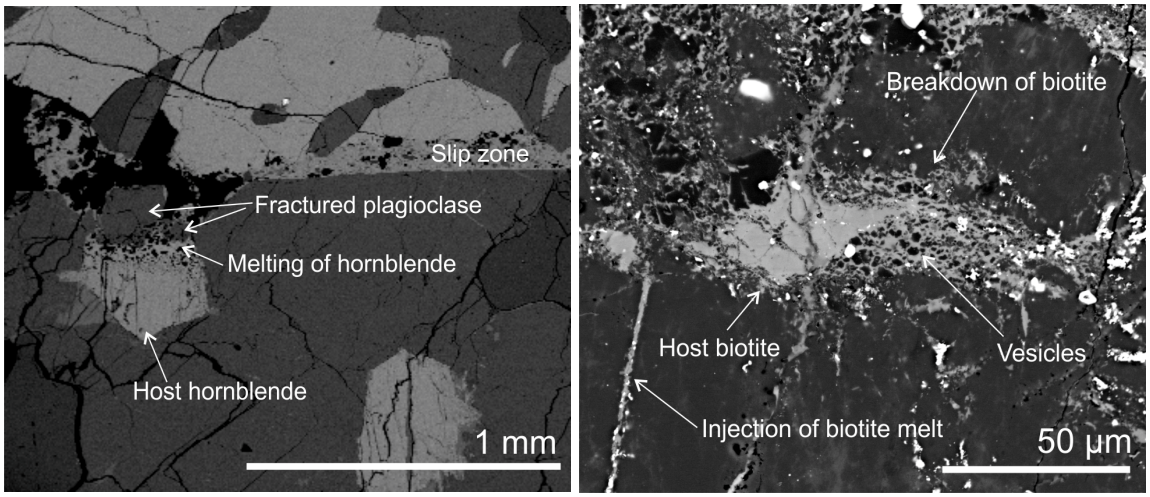

(a) (b)

Figure 5.15: Host rock biotites and hornblendes melting in situ, in both natural and experimental samples: a. Metabasic- quartzofeldspathic core (R7): hornblende in quartzofeldspathic wall of mixed core, removed from slip zone, melting in situ on slip zone side. Above, the plagioclase crystal is highly fractured and the slip zone cuts down towards it; b. Wall rock to natural pseudotachylyte sample SU3 showing biotite grain breaking down in situ. Glassy melt injects into surrounding crystals and vesicles are present.

of natural clasts populations falls away from the power law at the finest sizes, whereas the experimental samples maintain the power law trend and generally extend to smaller area values.

The D-values, taken from the gradient of the power law best-fit trend, are however in a similar range when comparing the experimental and natural samples. Within the experimental samples, there appears to be a division between those samples that are at least partially composed of the amphibolite rich meta-basic sample (R1, R3, R6, R7), which have a D-value somewhat >1, and those which do not, where D is ~ 0.85 (Fig. 5.6). As the higher D-value represents a steeper trend to the power law - i.e. a higher proportion of the total clasts found at the finest section - this may be due to mineralogical control. Amphiboles, along with biotites if present, are mechanically the weakest mineral found in these assemblages (based on fracture toughness, Spray 2010). Hence they are most likely to be ground into the smallest particles in a fault rock. Amphibole clasts are very rarely seen in natural samples, which is likely due to the combined effect of preferential melting of both amphiboles in general (Spray, 2010) and the fine fraction regardless of mineralogy. In natural samples, therefore, it is un-

certain whether the influence of mineralogy on clast content and size distribution would be preserved and recognised as it has been in the experimental samples.

5.4.4 Composition of experimental pseudotachylytes

There are obvious variations in the melt composition between single and mixed lithology cores which indicate mixing between the two end-member single lithology cores (Fig. 5.11). The mixed quartzofeldspathic - metabasic pseudotachylytes (R5, R6, R7) can therefore be understood as a mix of the melts produced by the metabasic and quartzofeldspathic single-lithology cores, but are dominated by the metabasic component, causing the major element distribution to look much like the single-lithology metabasic melt. The more hornblende-like composition of all melts with a metabasic core (R1, R3, R6, R7) indicates that the preferential melting of the more numerous hornblendes found in the metabasic sample is probably a cause of this (Fig. 5.10). Interestingly, although the quartzofeldspathic sample does contain hornblende in the host core, the melt produced is very different to that of the metabasic-influenced melts. This is presumably because there is not enough hornblende in the quartzofeldspathic sample to dominate the melt composition, and since the most prevalent mineral is instead plagioclase, this comes to dominate the melt even as a resistant mineral (Fig. 5.10).

Whole rock analyses for natural OHFZ pseudotachylytes are not available from this study, but literature values are used for comparison. These analyses were summerised in Table 2.2. It is specified in many of these publications that the host rock is quartzofeldspathic gneiss - whilst this covers a wide range of compositions, it is assumed that the data should be most appropriately compared with the quartzofeldspathic gneiss sample of this study. The work of Macaudière et al. (1985), also presented in Table 2.2, was restricted to the South Harris anorthosites, so is not considered again here. One experimental pseudotachylyte whole rock analysis using OHFZ samples has been published by Spray (1993), along with two comparable natural examples. The experimental pseudotachylyte has much higher iron content, and lower silica, than any of the experimental results presented here. The two natural samples, however, are a good fit, for the most part closer to the major element oxide profiles of R2 and R5 than

the pseudotachylytes produced with metabasic samples. The same is true for the analyses of Sibson (1975) and Maddock (1992), which cover the range between the quartzofeldspathic dominated and metabasic dominated experimental melts. These experiments, then, have successfully replicated the broad compositional trends of the OHFZ's natural pseudotachylytes, despite the differing conditions of pressure and ambient temperature imposed by laboratory conditions.

5.4.5 Viscosity and shear strength

Viscosity of melt suspensions are expected to decrease as the deformation rate increases (Metzner (1985)), although the rate of change is not a factor here as all experiments were run under a constant slip rate of 1.3 ms^{-1}. Hence, the values calculated for viscosity represent maxima (Fig. 5.12) that should vary throughout slip. These values are in a similar range to calculations for natural OHFZ pseudotachylytes (Sibson (1975), Spray (1993)), natural pseudotachylytes from other fault zones (Philpotts and Miller (1963)), and experimental pseudotachylytes (Spray (1993), Hirose (2005)). The mixed core with a metabasic component (R7) produced viscosities an order of magnitude below those for the quartzofeldspathic and quartzofeldspathic - Corodale cores at equivalent temperature, which matches the experimental values of Spray (1993) and Hirose (2005) who worked on dolorite and gabbro samples respectively.

The shear strengths calculated for the melts, based on viscosity, can be compared to those recorded in the mechanical data. As discussed, the viscosity during the slip episode changes dynamically. It must therefore be estimated which stage of slip the estimated viscosity values relate to, which is most readily achieved using temperature estimates. The peak temperature is likely to occur after a second or so of slip (Caggianelli et al. (2005)), after the frictional peak is reached. Taking this temperature to be 1550°C, the predicted shear stresses are are 7 MPa, 13 MPa and 0.4 MPa for the samples R2, R5 and R7, compared with the mechanical results of around 6.8 MPa, 5.9 MPa and 2.6 MPa for the same samples at peak friction (Fig. 5.13). The predicted examples are therefore comparable with the observed range of shear stresses, and

also captures the reduced shear strength (and viscosity) of the metabasic mixed core R7. This effect is related to the relatively low silica values (Fig. 5.11) and more basic melt composition in comparison with samples R2 and R5. The mechanical results suggest steady state shear strengths of 1.5-3.0 MPa for all these samples, so that the slip zone temperature must remain more or less consistent over this slip period in order to keep the viscosities equivalently low. Hirose (2005) have shown through experiments at progressively larger displacements that the effects of changing melt composition, clast content, vesicle content, temperature and shear through increasing slip tend to produce a peak viscosity just after the frictional peak, before a viscosity reduction into the steady state phase. This behaviour seems necessary if the viscosity is to be linked to the changing shear strength. Such a link requires the assumption that a through-going melt layer is supporting the slip zone and controlling its strength, which may only come into effect during the weakening and steady state phases (Del Gaudio et al. (2009)). The shear stress prediction at peak friction is therefore a minimum, as frictional strength of the fault zone still applies.

5.4.6 Distribution of pseudotachylyte in the Outer Hebrides Fault Zone

Variation in lithology along the strike of a fault zone is expected to influence fault strength and the deformation processes possible during faulting. If other environmental conditions allow seismic slip to generate pseudotachylyte, lithology will exert some control on melt generation in terms of: a) the ease with which the minerals present melt, dependent on their fracture toughness and melting/breakdown temperature (Spray (2010)); and b) the distribution of easily melted minerals in particular will control the geometrical evolution of the slip surface (i.e. the roughness and existence of asperities), which in turn controls the frictional development during slip (section 5.4.1).

In the OHFZ, two major lithological changes from the typical quartzofeldspathic gneiss occur along the mapped strike of the fault. In South Harris, the fault zone cuts anorthosite, although the fault zone has only limited onshore exposure. Further south, the hanging wall is composed of two-pyroxene Corodale gneiss. Because of these changes in lithology, and

also because the fault zone in South Uist contains a well developed crush zone with plentiful pseudotachylyte, some workers have linked the prevalence of pseudotachylyte to the presence of Corodale gneiss in the fault wall (Butler (1995), Osinski et al. (2001)). However, this is not borne out by the mineralogy of the Corodale gneiss or by high velocity experiments on Corodale Gneiss samples (Chapter 5). Whilst hornblende is present, none of the major minerals in the Corodale gneiss (Table 5.1) are particularly susceptible to melting, with relatively high melting temperatures and fracture toughnesses (Spray (2010)). This interpretation is supported by experimentally deformed samples, where the core containing Corodale gneiss did not preferentially melt relative to the core of quartzofeldspathic gneiss (sections 5.3.1.3, 5.3.2). The assumption that the Corodale is susceptible to pseudotachylyte production probably arises from references to it as a meta-basic gneiss (e.g. Osinski et al. (2001)), a term also applied to the amphibolite bodies in the Western Isles, which in contrast are mineralogically pre-disposed to melt easily (section 5.3.2). An alternative influence may be the fabric of the Corodale Gneiss, which is partially protomylonitised. However, the influence of previous deformation on slip behaviour has not been investigated in this study. Thus, the simplest explanation for the widespread presence of pseudotachylyte in this South Uist locality, in line with the presence of an intense crush zone also containing cataclasite (Butler (1995)), is repeated slip along this segment of the fault zone.

In contrast, the frequent occurrence of pseudotachylyte along the boundaries of amphibolite meta-basic units (usually small metamorphosed intrusions) in the Western Isles is due to the amphibole-rich mineralogy of the meta-basic unit, as has previously been suggested (Sibson (1975)). This results from the combined properties of low fracture toughness, which encourages mechanical breakdown, and relatively low melting temperatures of amphibole below those regularly achieved by faults during coseismic slip (e.g. Sibson (1975), Di Toro et al. (2005b)). Slip along the contact may initiate due to increased strain and strain rate along the mechanical boundary between the quartzofeldspathic and metabasic gniesses (Sibson (1980)). Observations of pseudotachylyte following the curved, lensoid contacts of some of these metabasite bodies supports this hypothesis (Fig. 5.1b). However, once slip begins, the production of melt from is favoured by the amphibole-rich mineralogy. Again, this is an

example of the evolution of slip surfaces controlled by a lithological contrast across the fault. Faults along these contacts, where near-planar, are likely to be foliation parallel, as many of these amphibolitised dykes are now concordant (Mason and Brewer (2004)). This may contribute partially as to why some (but not necessarily the majority) pseudotachylyte faults lie near-parallel to foliation (Fig. 3.7).

5.5 Chapter conclusions

- These experiments have studied the effects of different lithologies from the OHFZ on the microstructures and composition of pseudotachylyte fault zones, and have sought to understand how these behave when two different lithologies may be juxtaposed across such a fault. The pseudotachylyte compositions, and many of the microstructures, that have been produced experimentally have proven similar to those observed in natural OHFZ pseudotachylyte samples, increasing confidence that the interpretation of processes made here can be also applied to the natural case.

- The preferential melting of hornblende (also biotite) is represented in these results by the contrast in compositions between melt produced by a metabasic, amphibole-rich host and a quartzofeldspathic host, the latter being much more 'evolved' under igneous melt classification. This influences melt properties such as the viscosity, which is lower in the more basic melts, and hence the strength of the melt which will control the coseismic strength of the fault during later stages of slip. The composition of the host rock is therefore represented in the magnitude of coseismic weakening behaviour of the fault.

- When two different lithologies are juxtaposed across a fault, the melt composition will be a mixture of the melts that would have been produced by the end member compositions, but will be closer to the melt of the rock type with greater proportions of easily melted minerals at the fault plane. The resultant strength behaviour of that melt will therefore approximate the more easily melted end member as well, rather than an average of the two contributing rock types. The roughness of the fault profile is a microstructural component that is controlled not only by the mineralogy of the host rock, but also

the distribution and orientation of those minerals. The different roughness signature of differing lithologies can be seen in the mixed experiments. However, these profiles in the mixed cores are not the same roughness as those of single-lithology cores of the relevant rock type, but are modified presumably by the mechanical wear and roughness properties of the opposing, differing rock type and by the behaviour of the mixed melt produced.

- The properties of fault hosting rocks, and of the fault itself, are highly dynamic throughout the slip period and therefore can be difficult to predict. This work shows that lithology is an important control on the evolution of such properties through slip, and not just on the initial static rock properties. However, it is likely that other factors such as pre-existent damage will also have similar influences on slip behaviour, and this has not yet been fully explored.

Chapter 6

Coseismic strength of pseudotachylyte bearing faults

6.1 Introduction

During coseismic slip, the dynamic shear strength of a fault progressively decreases, causing a stress change along the fault. This stress drop behaviour is important for consideration of the seismic energy budget and the probability of future slip events. The weakening effect may be due to several mechanisms, including: thermal pressurisation (Lachenbruch (1980)), flash heating (Rice (2006)), melt lubrication (Spray (1993)), fluid lubrication (Brodsky and Kanamori (2001)), nanoparticle lubrication (Han et al. (2011), De Paola et al. (2010)), gel lubrication (Di Toro and Pennacchioni (2004)), thermal decomposition (Han et al. (2007)) and acoustic fluidisation (Melosh (1996)). The weakening behaviour is important for understanding the magnitude of the stress drop and how it relates to displacement during coseismic slip. The issue of whether stress drop should scale with seismic moment or not is still debated, despite the wealth of seismic parameter data available for major modern earthquakes.

Pseudotachylytes are well-suited to calculations involving earthquake energy budgets due to the constraints linking the temperature rise along the fault, discussed in Chapter 4, to the heat energy generated during slip and hence the coseismic frictional work. The behaviour of

individual earthquakes can be described by a range of seismic parameters including dynamic weakening, magnitude and stress drop, comparing data from several fault zones. Experimental and seismological approaches can produce differing results due to the contrast in observation scale (Hirose and Shimamoto (2005)), and field based studies provide a link between these. In this chapter, field observations of the thickness of pseudotachylyte along a fault with known displacement are used in combination with the thermal properties of the pseudotachylyte to calculate the average dynamic shear strength. Combining data from several faults provides an estimate of the typical slip weakening behaviour of the fault zone. Here, data from four different fault zones, including the OHFZ, are collated to compare the properties and controls on variability in slip behaviour. The average coseismic shear strength is calculated for each pseudotachylyte bearing fault, and from this the strength of the Outer Hebrides Fault Zone (OHFZ) is also derived. Stress drops and seismic magnitudes are also calculated for faults in the datasets and compared with literature values for modern earthquakes.

The chapter begins with an outline of the methods used, including a description of the data used and derivation of the equations used in this approach. The first results presented are the relationship between pseudotachylyte thickness and fault displacement which represents the development of melt generation with slip. Next, the average dynamic shear stress is calculated, and also compared with displacement to consider the dynamic weakening behaviour. The shear strengths of the fault zones are derived from this data, and compared to a Mohr-Coulomb analysis. Moment magnitudes, static and dynamic stress drops are calculated for individual faults. Theses results facilitate discussion as to the differences in seismic behaviour between different fault zones, and testing of models of seismic stress evolution.

6.2 Methods

The approach in this chapter begins with the derivation from field measurements of the average coseismic shear strength, as outlined by Di Toro et al. (2005b). The assignment of thermal properties for the typical rock type in each fault zone are based either on published values or

calculated from the mineralogy, as detailed below. The assumptions and limitations of field measurements are also considered, before the theory behind the calculation of the average dynamic shear stress is outlined. Methods for calculating moment magnitude and both static and dynamic stress drops are also explained.

6.2.1 Data sources and geological context

For the approach used here, observations of the average thickness of the pseudotachylyte vein and a measured displacement are needed for each pseudotachylyte fault vein. These measurements have been taken both from field observations of the OHFZ made during this study, and from available published sources. These additional sources include: from the OHFZ, Sibson (1975), Hirose and Shimamoto (2005) and Nielsen et al. (2010a); from the Gole Larghe fault zone (Italian Alps) Di Toro et al. (2005b); from the Otago normal fault zone (New Zealand) Barker (2005) and from the Hatagawa fault zone (NE Japan) Takagi et al. (2000). Data published in Sibson (1975), Hirose and Shimamoto (2005), Barker (2005) and Takagi et al. (2000) are in the form of values for vein thickness and displacement, or apparent separation, and required the estimation of thermal properties based on the rock type allowing calculation of the dynamic shear stress. Shear stresses for the Gole Larghe Fault Zone reported in Di Toro et al. (2005b) were used directly for this work. Shear stress values for the OHFZ were also published in Nielsen et al. (2010a), but for consistency were recalculated using the same input parameters for density, heat capacity etc. as for the rest of the OHFZ observations used in this chapter.

The geological context for the fault zones analysed, including a simplified version for the OHFZ, are displayed in Table 6.1. A range of fault types (strike slip, reverse, normal) are covered by this dataset and there is some variation in lithology, although all bar the Otago normal faults are hosted in rocks of broadly granitic composition. The pseudotachylytes described by Takagi et al. (2000) in the Hatagawa fault zone have been subsequently mylonitised, which adds some uncertainty to the validity in this analysis.

Table 6.1: Comparison of geological setting of fault zones used from published studies for analysis of dynamic shear stress: OHFZ (Kelley et al. (1994), Butler et al. (1995), Sherlock et al. (2009)), Gole Larghe fault zone (Di Toro et al. (2005b)), Otago normal fault zone (Barker (2005)) and the Hatagawa fault zone (Takagi et al. (2000))

	Outer Hebrides Fault Zone (OHFZ)	**Gole Larghe Fault Zone (GLFZ)**	**Otago Fault Zone (OFZ)**	**Hatagawa fault zone (HFZ)**
Geographical location	NW Scotland, UK	Italian Alps	South Island, New Zealand	Abukuma Mountains, NE Japan
Fault kinematics	Thrust (reactivated in other senses)	Strike slip	Normal	Strike slip
Depth of seismicity	5-10 km (15+ in northern section)	9-11 km	6-12 km	10-15 km
Rock Type	Felsic gneiss	Granitoid	Quartz-plag-mica schist	Granite

6.2.2 Assignment of rock properties

The calculation of average dynamic shear stress requires the input of several parameters including: the specific heat capacity (C_p, J kg^{-1} °C^{-1}), latent heat of melting (H, J kg^{-1}), density (ρ, kg m^{-3}), change in temperature between the ambient host rock and the coseismic fault temperature, which is proxied by the melt temperature (ΔT, °C), and the proportion of clasts in the vein (ϕ). These values are provided by some of the published datasets and are calculated here for the others, including the new OHFZ data measured during this study. The properties ρ, H and C_p refer to the unmelted rock, since it is assumed that the values for each are equivalent to those for the melt (Di Toro et al. (2005b)).

The proportion of clasts, ϕ, is expressed as an area fraction as it is calculated from thin section or polished block micrographs. OHFZ samples were measured using image analysis, via the process previously described in section 4.2.4. In chapter 4, the ratio of clasts to matrix was reported (section 4.3.3.2) which is modified here as the ratio of clast area from the total vein area. The mean ratio of clast area with respect to total vein area from 39 samples is 0.19. This value is applied to the published results for the OHFZ of Sibson (1975), Hirose and Shimamoto (2005) and Nielsen et al. (2010a). For the Gole Larghe fault zone, Di Toro et al. (2005b) have stated that $\phi = 0.2$. As 0.2 was similar to the value measured for the

OHFZ samples it was taken as a typical value for pseudotachylyte fault veins and used for clast proportions in both the Otago normal fault zone and the Hatagawa fault zone (Table 6.2).

Rock density is calculated for the OHFZ based on typical mineral proportions for the quartzofeldspathic gneiss that hosts the faults measured in this work. Proportions of quartz, plagioclase, potassium feldspar, biotite, hornblende and pyroxene were measured from four typical thin sectioned samples using the optical microscope and then averaged. The volume percentage for each mineral was then multiplied by the mineral density (taken from Wenk and Bulakh (2004)), and all were summed. The resultant whole rock density is shown in Table 6.2 along with those for the Gole Larghe and Otago faults. No published value for density in the Hatagawa fault zone was found; however, considering that the granitic lithology is expected to be most similar to that of the Gole Larghe, the same value was also applied to the Hatagawa.

Latent heat and specific heat capacity were calculated for the OHFZ using data from the mineral databases of Robie and Waldbaum (1968), Holland and Powell (1990) and Schön (1983). These values were derived at atmospheric pressure, but are available at a range of temperature intervals. The value for C_p was chosen at an appropriate temperature and converted from J mol^{-1} K^{-1} to J kg^{-1} $°C^{-1}$ using the molecular weight. The appropriate temperature was picked as the closest to the midpoint of the heating interval between the ambient temperature (here picked as 350°C) and the melting temperature of the mineral. This choice is based on the argument that C_p increases linearly with T so that the midpoint in the temperature range presents an effective average (O'Hara (2001)). These values of C_p for the constituent minerals were then multiplied by the mineral fraction. Latent heat values (H) were obtained from O'Hara (2001), converted to the appropriate units and calculated for the whole rock in the same manner. Values for all fault zones are given in Table 6.2. The Otago fault zone has no available latent heat estimate, but considering the similarity of its heat capacity with that of the Gole Larghe, the same latent heat was used. Neither of these parameters has been defined for the Hatagawa, and both values from the Gole Large are substituted based on the similar mineralogy of the two fault zones.

Table 6.2: Input parameters used in this chapter. Sources from: [1] Di Toro et al. (2005b), [2] Barker (2005), [3] Breeding and Ague (2002), [4]Bjørnerud (2010),[5] Imber et al. (2002), [6] calculated here, [7] justified in text

Property	Units	**OHFZ**	**Gole Larghe**	**Otago**	**Hatagawa**
Clast proportion (ϕ)		0.19[6]	0.2 [1]	0.2[7]	0.2[7]
Rock density (ρ)	kg m^{-3}	2725 [6]	2350[1]	2750[3]	2350[7]
Latent heat (H)	J kg^{-1}	3.26 x 10^5 [6]	3.24 x 10^5 [1]	3.24 x 10^5 [7]	3.24 x 10^5[7]
Heat capacity (C_p)	J kg^{-1} $°C^{-1}$	1222 [6]	1200[1]	1200 [2]	1200[7]
Ambient temperature ($T_{ambient}$)	°C	350 [5]	250 [1]	200 [4]	350 [7]
Melt temperature (T_{melt})	° C	1250 [6]	1450 [1]	1000 [2]	1450[7]
Temperature change (ΔT)	°C	900	1200	800	1100

The change in temperature (ΔT) varies for each fault zone depending on estimates for the ambient temperature and melt temperature (Table 6.2). The OHFZ values chosen are a lower estimate of the peak melt temperature and a mid-range estimate within the constraints on ambient temperature (section 4.4.1) so that the resultant ΔT is approaching a minimum possible value. For the Hatagawa fault zone, temperature constraints are not published, however the ambient conditions are noted as greenschist facies (Takagi et al. (2000)) so for $T_{ambient}$ a midrange greenschist facies temperature of 350°C is assigned. For T_{melt} a value of 1450°C is used, due to the similarity of the mineralogy and fault depth to the Gole Larghe fault zone.

6.2.3 Field data collection

Measurements required from field observations are the thickness of the pseudotachylyte fault vein (t) and the displacement on the fault (d). The best practices and limitations of field data collection are well covered in Di Toro et al. (2005b) but the pertinent points, including those relevant to the context of the OHFZ, are reassessed here.

A significant limitation across the OHFZ is that the plane exposing the true displacement is rarely observed. The values given for displacement here are therefore apparent separations as measured on the given plane of exposure. The use of separations are also specified in the datasets of Sibson (1975), Nielsen et al. (2010a), Di Toro et al. (2005b), Takagi et al. (2000) and for some of the observations in Barker (2005). In addition, although the Lewisian

gneisses are typically banded, the matching of distinctive marker bands across a fault is often uncertain. Pseudotachylyte veins are therefore selectively sampled based on whether an offset was clearly discernible.

The thickness of pseudotachylyte veins is one of the common causes of error in these field measurements. The ideal pseudotachylyte fault vein has a constant thickness and lacks injection veins, which act to reduce the effective thickness by extracting melt off the fault plane (Di Toro et al. (2005b)). This ideal is rarely met, as pseudotachylyte veins fill the rough geometry of faults including jogs, and injection veins are common on all pseudotachylyte bearing faults (Di Toro et al. (2005b)). One method of increasing accuracy of measurements on pseudotachylyte faults is to take the melt area, including injection veins, and to normalise the figure over the length of the fault vein, as described in Di Toro et al. (2005b). However, this method was not employed in data collection in the OHFZ since the exposure often restricts observing the full length of the fault. Faults with significant injections or thickness changes were therefore rejected from further analysis.

Another source of error in the field that varies between fault zones is the dominant orientation of exposure. In the Gole Larghe fault zone, the faults are near-vertical and the once glaciated, dominantly horizontal exposure surface means that displacements and thicknesses are observed close to their true values (Di Toro et al. (2005b)). In the OHFZ, faults tend to dip moderately, often in a broadly easterly direction (see section 3.3). The exposure is variable, ranging from small but flat beach rocks to near vertical cliff-like sections. The angle of apparent exposure is therefore very variable and the uncertainty in observing true thickness and displacement can be significant. This situation is probably the case in many dip-slip fault zones including the Otago normal fault zone. To account for this uncertainty, an upper error of + 0.1 m is included with all displacement measurements used in this work, including those sourced from the literature. This accounts for the fact that the observed, apparent dispacement will always be the lower estimate of true displacement, and for the fact that the observed displacement on any fault is rarely greater than 0.1 m, except in the Gole Larghe where the approximation to true displacement in more certain anyway.

A further constraint for selection of faults for analysis in the field is that the displacement observed must be generated during the single slip episode that produced the pseudotachylyte. This is not always expected in complex, well-evolved fault zones, where slip may localise repeatedly on the same slip plane. In the Gole Larghe fault zone, it has been shown by Di Toro et al. (2005b) that several pseudotachylyte fault veins overprint a pre-existing cataclasite, so that some part of the measured displacement may have occurred before the pseudotachylyte was generated. Efforts are reported in Barker (2005), and were made during the collection of the new OHFZ data, to avoid faults with indications of additional slip episodes but this is often difficult to do without subsequent microscopic investigation.

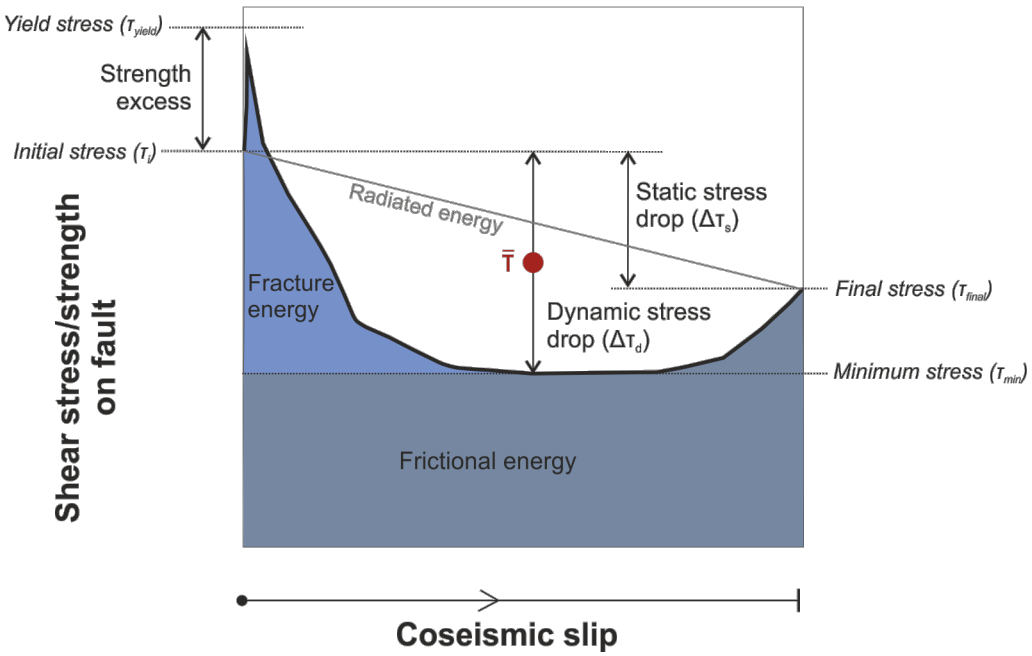

Figure 6.1: Schematic diagram illustrating change of shear stress (black curve) along a fault (averaged per unit area) during a single episode of seismic slip. Terms used in this chapter are defined here. After Niemeijer et al. (2012).

6.2.4 Theoretical derivation of average shear stress

The energy used to overcome friction during seismic slip, E_f, forms a significant part of the overall energy budget of an earthquake (Eq. 1.2, Scholz (2002)),.

Assuming the work undertaken to overcome friction is entirely converted to heat energy, through adiabatic heating (O'Hara (2001)), the rise in temperature on the fault is also directly related to the mechanical work. Hence (Sibson (1975)),

$$E_f \approx Q = H + C_p \Delta T \tag{6.1}$$

where Q is the total heat energy input, H the latent heat of melting, C_p the heat capacity, and ΔT the change in temperature between ambient conditions and the coseismic melt. The average dynamic shear stress ($\bar{\tau}$) is related to Q via (Di Toro et al. (2005b)),

$$\bar{\tau} = \rho Q \frac{t}{d} \tag{6.2}$$

The term average dynamic shear stress refers to an average value in the falling shear stress during coseismic slip (Fig. 6.1). It is defined as the midpoint between the initial shear strength, τ_i, and the minimum shear strength experienced by the fault during the slip episode, τ_{min} (e.g. Beeler (2006)).

Combining Equations 6.1 and 6.2,

$$\bar{\tau} = \rho(H + C_p \Delta T) \frac{t}{d} \tag{6.3}$$

where $\bar{\tau}$ is the average dynamic shear stress (in Pa). This derivation is modified by adding a term to remove the fraction of surviving host rock clasts (ϕ) in the vein from the thermodynamic calculations (Di Toro et al. (2005b) as they take no part in the melting process, so that,

$$\bar{\tau} = \rho(H(1 - \phi) + C_p \Delta T) \frac{t}{d} \tag{6.4}$$

6.2.5 Analysis of fault strength, earthquake magnitude and seismic stress drops

6.2.5.1 Fault strength

The brittle yield shear strength (τ_{yield}) is a measure of fault strength in terms of the critical shear stress needed to induce brittle failure (Fig. 6.1). It is useful for characterising the properties of the fault zone and for estimating the applied stresses needed for failure. Yield shear stress can be estimated from the array of pseudotachylyte data by observing and/or extrapolating values of $\bar{\tau}$ on the smallest displacement faults. As the displacement approaches zero then $\bar{\tau}$ should approach τ_{yield} (Fig. 6.1). The values of $\bar{\tau}$ at the smallest displacements available therefore provide an estimate of the strength of the host rocks at failure, and these strengths are compared across the different fault zones.

To further develop analysis for the OHFZ, a Mohr's circle construct was developed. Mohr-Coulomb models represent graphically the strength of the rock and the stress state of the crust. The failure line may represent either the frictional strength of an existing fault ($\tau = \mu\sigma_n$, where τ is shear stress, μ is the frictional coefficient and σ_n is normal stress), or the formation and slip of a new fault in intact rock ($\tau = \mu\sigma_n + C$, where C is a factor of cohesion). Here, both failure modes are considered. Typical values of $\mu = 0.6$ and $C = 50$ MPa are used for the Mohr - Coulomb behavior of intact rock, and a range of $\mu = 0.6$-0.85 is considered for frictional sliding (Byerlee (1978)).

For the Outer Hebrides Fault Zone, an Andersonian reverse faulting stress field is assumed, so that the vertical principal stress is the minimum principal stress (σ_3) which is also assumed equivalent to lithostatic pressure (P_L, Fossen (2016)). Lithostatic pressure is calculated from the rock density (ρ), gravitational constant (g) and depth (h). A typical rock density for the Lewisian gneiss is 2.7 kg m^{-3}, based on calculations made in section 6.2.2. The depth range for OHFZ pseudotachylyte -generating seismicity is suggested to be 5-10 km (Sibson and Toy (2006)). These minimum and maximum bounds are used to calculate the minimum and maximum lithostatic pressures of $P_L = \sigma_3 =$132 MPa and $P_L = \sigma_3 = 265$ MPa respectively.

The maximum principal stress (σ_1) is initially calculated from σ_3 using the approximation

$$\sigma_3 = \frac{\nu.\sigma_1}{1-\nu} \tag{6.5}$$

where ν is Poisson's ratio, set at a typical value of 0.25 (Jaeger and Cook (1979)). The calculated values of σ_1 and σ_3 are used to construct the Mohr's circle for lithostatic pressure at 5 km and 10 km depth. Normal stress is not adjusted for pore pressure, as the fault system is thought to be fluid-absent during the pseudotachylyte generating seismic activity (Sibson (1975)). The average dip on the OHFZ, $\sim 25°$, is used for an existing failure surface. The shear stress resolved along the fault plane can be calculated as (Jaeger and Cook (1979)),

$$\tau = \frac{\sigma_{max} - \sigma_{min}}{2} sin2\theta \tag{6.6}$$

where θ is the angle between the plane normal and σ_{max}.

6.2.5.2 Seismic moment and magnitude

The seismic moment of each earthquake recorded by individual pseudotachylyte veins is derivable if the displacement is known. The seismic moment can be defined as (Kanamori and Brodsky (2004)),

$$M_0 = d.G.A \tag{6.7}$$

where M_0 is the seismic moment (Nm), d is displacement (m), G is the shear modulus (Pa) and A is the rupture area (m^2). The shear modulus can be estimated from typical values appropriate to the rock type, but the area of each fault where pseudotachylyte is measured, or even the fault length, are not easily obtained in the field and are not available for any of the published datasets. However, seismological data show a power law relationship between the seismic moment and the fault slip area (Fig. 6.2, Aki (1972), Kanamori and Anderson (1975), Gibowicz et al. (1991), Wells and Coppersmith (1994), Nadeau and Johnson (1998), Abercrombie and Rice (2005), Imanishi and Ellsworth (2006) and Lin et al. (2012), and

references therein). These sources were used to collate fault area data over a range of moment magnitudes and tectonic regimes. Although some authors suggest a division of the trend based on fault movement sense, tectonic context or earthquake magnitude (Wells and Coppersmith (1994), Kanamori and Anderson (1975), Abercrombie and Rice (2005)), there is no obvious differentiation based on these parameters once all the data are collated (Fig. 6.2). A best fit power-law regression reveals A = 0.0013 M_0 $^{0.5868}$. The R^2 value is 0.92, and in general the various datasets fit well onto this trendline. The exception is that of Nadeau and Johnson (1998) which track a steeper exponent of $\sim$ 0.81.

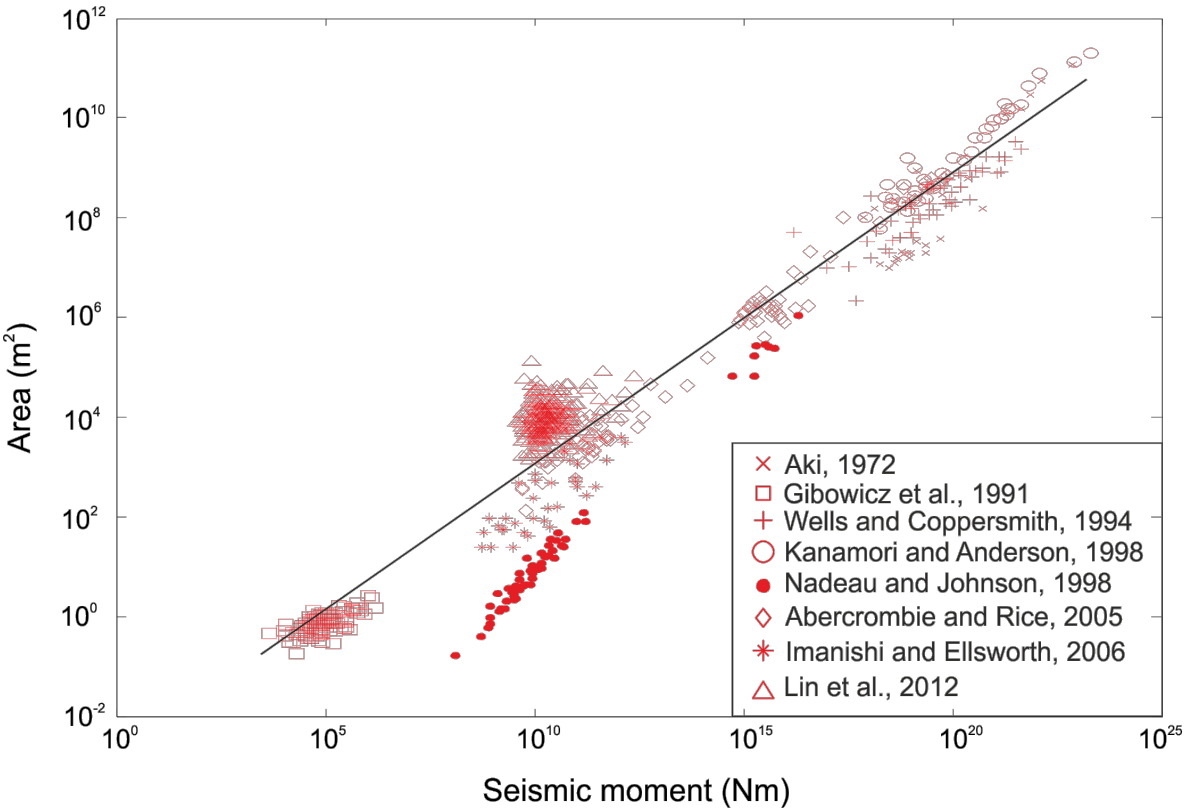

Figure 6.2: Plot of seismic moment against fault slip area with data from the publications used to estimate the scaling law (see text). The best fit line is also indicated for the power law A = 0.0013 M_0 $^{0.5868}$

The relationship between rupture area and seismic moment is substituted into Equation 6.7 to give,

$$M_0 = (0.0013d.G)^{\frac{1}{1-0.5868}} \tag{6.8}$$

This equation provides a scaled estimation of the slip area from the measured displacement.

The seismic moment is converted to the moment magnitude (M_W) using the relationship (Kanamori and Brodsky (2004)),

$$M_W = \frac{logM_0}{1.5} - 6.07 \tag{6.9}$$

6.2.5.3 Stress drops

The displacement and area of a fault can also be used to calculate the static shear stress drop, $\Delta\tau_s$ (Fig. 6.1), if it is assumed that the rupture is perfectly circular (Borok (1959)),

$$\Delta\tau_s = \frac{7\pi}{16} G \frac{d}{r} \tag{6.10}$$

Here, r is the fault radius in metres, which is estimated from the area via $r = (\frac{A}{\pi})^{\frac{1}{2}}$ due to the assumption of a circular fault.

Since the average dynamic shear stress, $\bar{\tau}$, is defined as the midpoint of τ_{yield} and τ_{min}, the dynamic shear stress drop, $\Delta\tau_d$ (Fig. 6.1), is calculated using the assumptions that $\tau_{yield} \approx \tau_i$ (initial shear stress, see Fig. 6.1) and since $\Delta\tau_d = \tau_i$ - τ_{min},

$$\Delta\tau_d = 2(\tau_{yield} - \bar{\tau}) \tag{6.11}$$

which can be calculated as τ_{yield} and $\bar{\tau}$ are both known.

The differences between $\Delta\tau_d$ and $\Delta\tau_s$ are compared to each other against the calculated seismic moment, along with published data of static stress drops from Abercrombie and Rice (2005) and Baltay et al. (2011).

6.3 Results

6.3.1 Average dynamic shear stress

The relationship between pseudotachylyte fault vein thickness (t) and displacement (d) is shown in Fig. 6.3. In general, the thickness increases with displacement, the ratio of which is the basis of Equation. 6.4 in relating the amount of pseudotachylyte in a vein to the energy budget of the earthquake. The trend flattens at displacements >0.1 m. Although the larger displacement range is dominated by the data of Di Toro et al. (2005b), there are sufficient points from other datasets following a similar trend to suggest that this is a real feature and not mis-calibration between datasets. At displacements <0.1 m, the data are best fit by a power law of $t = 0.0154\ d^{0.877}$ ($R^2 = 0.47$). At displacements >0.1 m, the data is best fit by a linear curve of $t = 0.0006\ d + 0.0029$ but the data is highly scattered and $R^2 = 0.125$. Whichever the type of trend, the increase of thickness with displacement in this portion is barely discernible.

Values calculated for the average dynamic shear stress, $\bar{\tau}$, are plotted against displacement for each data set on a log-log graph in Fig. 6.4. A decrease in $\bar{\tau}$ is seen with increasing displacement. The data are best fit by a power law of $\bar{\tau} = 11.95\ d^{-0.56}$ where $R^2 = 0.599$. Values of $\bar{\tau}$ range from 340.1 MPa (OHFZ, current study) to 0.4 MPa (Gole Larghe fault zone, Di Toro et al. (2005b)). A change of gradient is seen in this plot (note the logarithmic axes), essentially mirroring that seen in Fig. 6.3, so that at higher displacements, $\bar{\tau}$ drops off more rapidly.

Within the scatter of the data, trends of individual datasets can be picked out from Fig. 6.3. This is partly due to the restricted displacement ranges of each dataset but also because there appears to be some variation between their trends. The Otago dataset, for example, has typically higher vein thicknesses at each displacement than some of the other datasets, whilst the Hatagawa pseudotachylytes occupy the smaller displacement (<0.04 m) and thickness range. This effect can be seen when individual datasets are displayed in Fig. 6.4. Data from

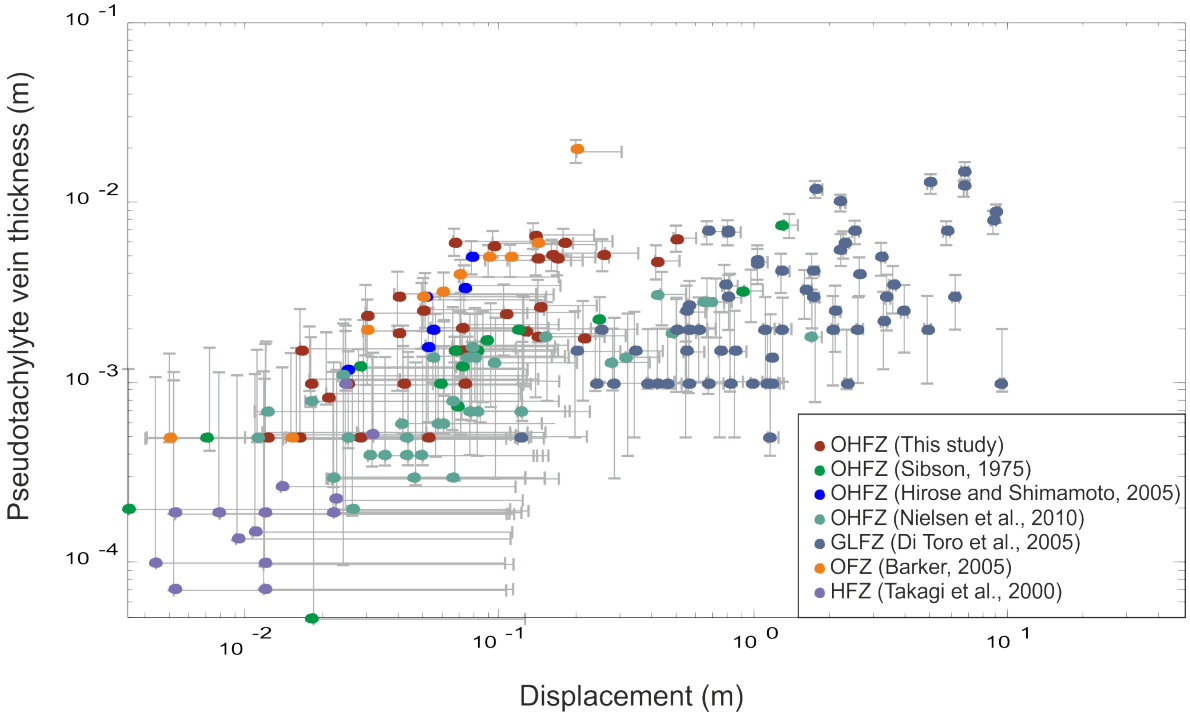

Figure 6.3: Thickness of pseudotachylyte fault veins plotted against the displacement seen across them. Error bars shown represent measurement inaccuracy (± 0.001 m) and true displacement uncertainty (+ 0.1 m).

all sources for the OHFZ are shown together in Fig. 6.4b. These data form a coherent trend with a well defined rate of change of $\bar{\tau}$ with displacement. The best fit power law for the OHFZ is $\bar{\tau} = 15.96$ d $^{-0.47}$ ($R^2 = 0.36$). For the Gole Large fault zone, the best fit power law is $\bar{\tau} = 9.16$ $d^{-0.54}$. The more negative exponent reflects the steeper trend seen in Fig. 6.4. For the Otago fault zone, displacements are not recorded >0.2 m. The weakening trend is flatter than the OHFZ and Gole Larghe, and has the best fit line $\bar{\tau} = 175.49$ $d^{-0.04}$. Although there is an obvious trend tracked out by the majority of the datapoints, two outliers can be seen. It is unclear what might cause the divergence of the outliers from the main trend, other than the field uncertainties covered in section 6.2.3. Overall, the Outer Hebrides, Gole Large and Hatagawa fault zones show power law exponents between -0.42 to -0.54, and the Otago normal faults show a different trend with an exponent of -0.14.

In Fig. 6.5, the calculations for average dynamic shear stress are plotted against displacement but demarcated by apparent slip sense (i.e. reverse, normal and strike slip). These

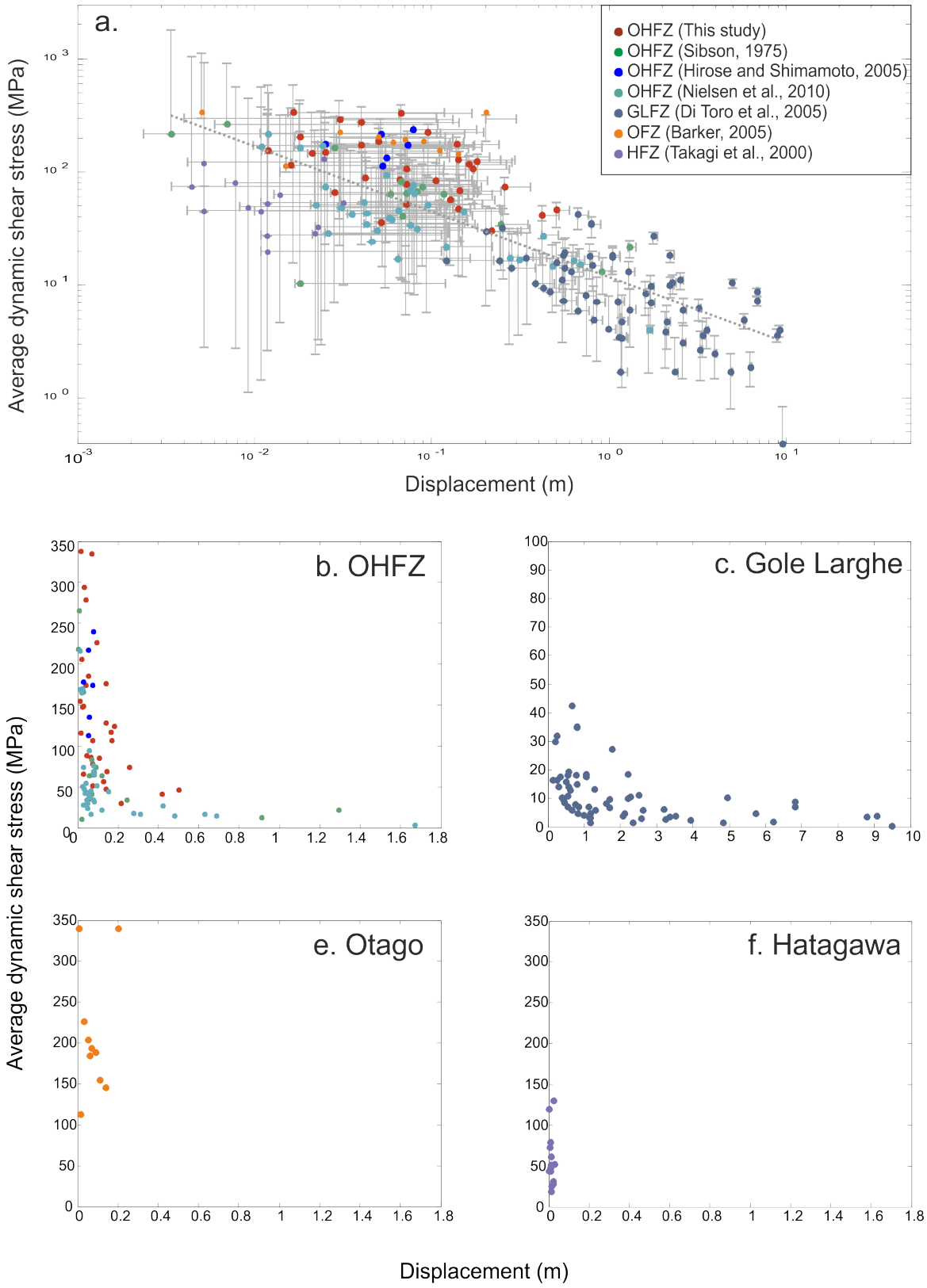

Figure 6.4: Average dynamic shear stress, $\bar{\tau}$, plotted against displacement for all datasets on a log-log graph (top) and for individual fault zones on linear axes (lower plots). Note the different axes used for the Gole Larghe plot. Error bars shown represent measurement inaccuracy ($\pm$ 0.001 m) and true displacement uncertainty (+ 0.1 m).

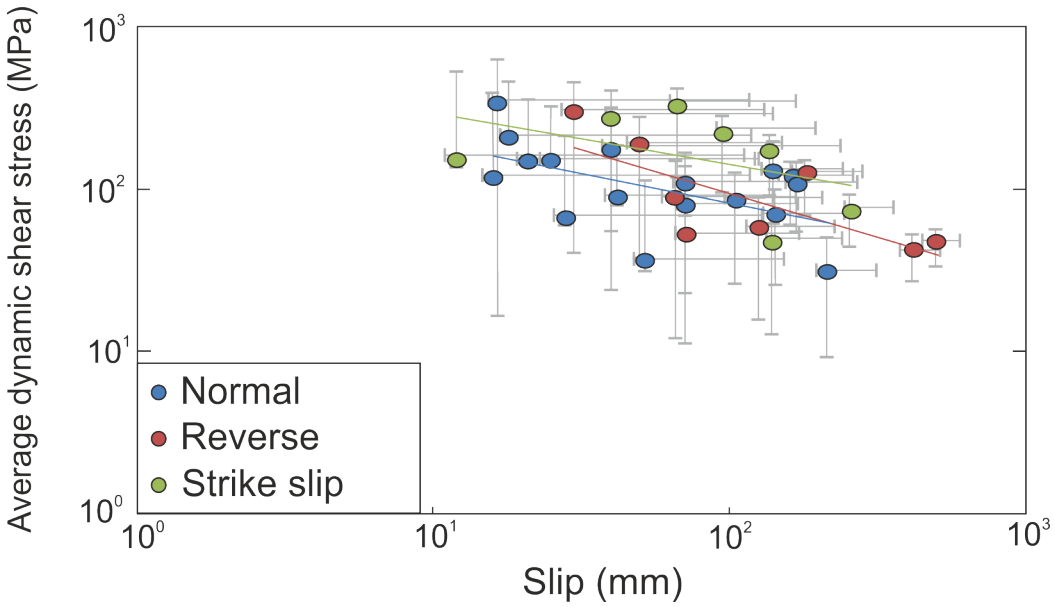

Figure 6.5: Average dynamic shear stress, $\bar{\tau}$, plotted against displacement for data from the OHFZ collected during this study, delineated by apparent sense of slip. Error bars shown represent measurement inaccuracy ($\pm$ 0.001 m) and true displacement uncertainty (+ 0.1 m).

data are from observations collected during this study from the OHFZ. Power-law best fit lines are also plotted. To test if there is statistical variance between the slip senses, one-way analysis of variance (ANOVA) tests were undertaken between the groups (Table 6.3) These are not normal distributions, which is an assumption of this test, but if the fault groups were separated by statistically different values at equivalent displacements, the means of the three groups should vary to reflect this and would be picked up by the test. However, no statistically significant differences are shown between the means of the three groups.

Table 6.3: Results of single factor ANOVA tests between $\bar{\tau}$ values for different fault types. The value 'F' must be greater than the value of 'F critical' for the results to be statistically different.

Fault types compared	F	F-critical
Thrust and normal	0.0636	4.2597
Thrust and strike slip	2.4071	4.6001
Normal and strike slip	3.0473	4.3010

Table 6.4: Differential and shear stresses needed to fail a 25° fault at 5 km and 10 km depth

Failure type	Differential stress (MPa)		Shear stress (MPa)	
	5 km	10 km	5 km	10 km
$\tau = 0.6\sigma_n + 50$	430	710	175	270
$\tau = 0.85\sigma_n$	455	965	180	965
$\tau = 0.6\sigma_n$	267	567	110	220

6.3.2 Yield stress

Each dataset in Fig. 6.4 shows how $\bar{\tau}$ approaches a maximum near the lowest observations of displacement. If the displacement is near zero (defined here as $\leq$ 0.02 m), the value of the maximum $\bar{\tau}$ at that displacement is considered to approximate τ_{yield} (section 6.2.5). The maximum average dynamic shear stress on the Gole Larghe fault zone occurs at 42.4 MPa, but this is not at the minimum displacement nor is the displacement $\leq$ 0.02 m. However, this value is still used for τ_{yield} as other datapoints suggest that $\bar{\tau}$ does indeed increase towards this value. Values of $\bar{\tau}$ are rounded upwards, to account for an increase as d decreases further towards zero. The values estimated for τ_{yield} are therefore, for the OHFZ, 300 MPa; for the Gole Larghe fault zone, 45 MPa; for the Otago normal fault zone, 350 MPa and for the Hatagawa fault zone, 125 MPa. The two highest $\bar{\tau}$ values for the OHFZ are 337.9 and 334.8 MPa , but the approximation to τ_{yield} is considered to be around 300 MPa because values at lower displacements from other OHFZ datasets (Sibson (1975) particularly), and the best fit power law, converge towards zero displacement at lower values than the outliers.

The following Mohr-Coulomb model (Fig. 6.6) is used to consider the stress state needed to achieve the yield shear stress of 300 MPa on OHFZ faults. Under lithostatic conditions, the stress state at both 5 km and 10 km depth lies below failure (Fig. 6.6a). To fail the rock, the differential stress is increased but σ_3 is kept pinned to the lithostatic stress (e.g Fig. 6.6b). The necessary differential stress and resultant shear stress for each failure mode is presented in Table. 6.4.

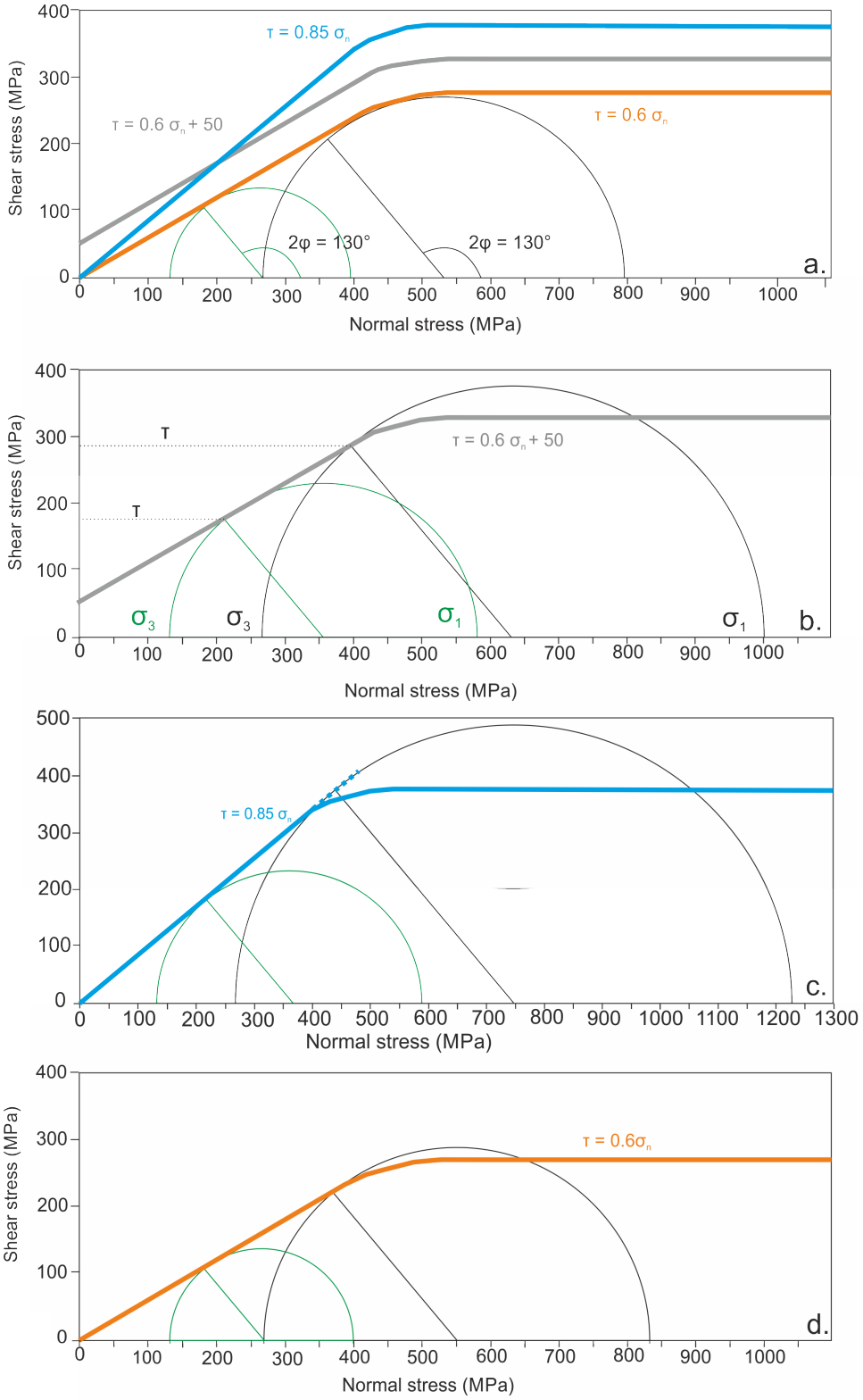

Figure 6.6: Mohrs circles representing constraints on the fault shear strength within the range 5-10 km (green circle = 5 km, black circle = 10 km) under the conditions of failure of : a. lithostatic stress state; b. $\tau = 0.6\sigma_n + 50$; c. $\tau = 0.85\sigma_n$; d.$\tau = 0.6\sigma_n$.

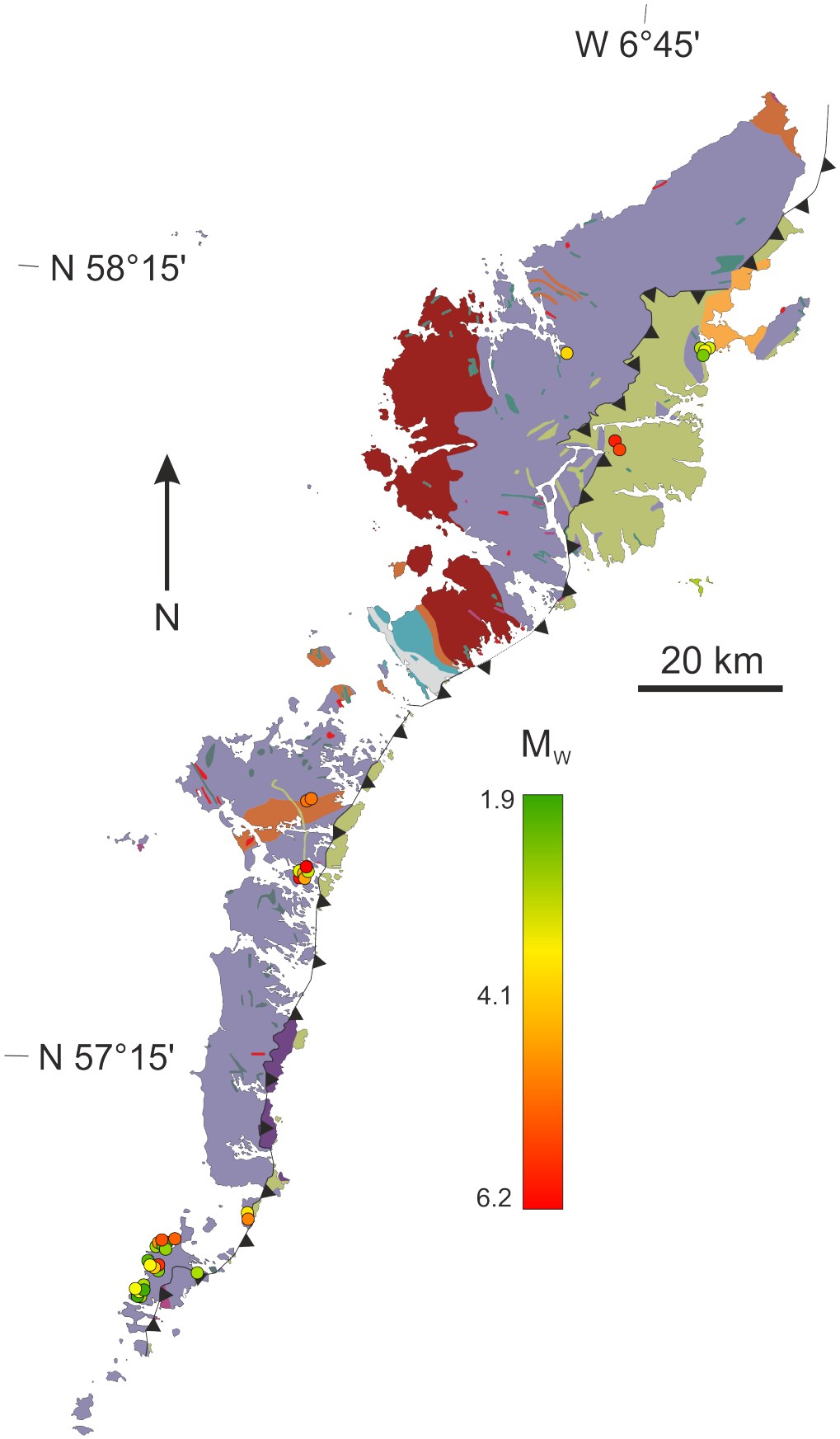

Figure 6.7: Moment magnitudes, M_W, plotted by location across the OHFZ from data collected during this study. Points are slightly offset from their location to allow visibility where many readings have been taken over a small area. For lithological key to basemap (geological map data ©NERC 2015) see Fig. 2.7.

6.3.3 Seismic moment and magnitudes

The range of seismic moments calculated for all datasets is 9.26 x 10^{11} to 2.40 x 10^{20} Nm. The range within the OHFZ is 9.26 x 10^{11} to 3.92 x 10^{18} Nm or 1.91 - 6.32 M_W. Moment magnitudes from the OHFZ data collected during this study are shown plotted by location on a geological basemap shown in Fig. 6.7. Larger earthquakes ($\sim$ 6 M_W) occur along the entire strike of the OHFZ, from Barra in the south to mid-Lewis in the north. Although several mid to large (to 4.88 M_W) magnitudes are seen west of the main fault trace (e.g. western Barra), clusters of larger magnitude events are found on Grimsay and Lewis close to the main faults. However, the high number of small events recorded in western Barra, for example, could be influenced by the greater number of measurements taken here.

6.3.4 Stress drops

Static stress drops ($\Delta\tau_s$, Fig. 6.1) range from 1.41 -14.36 MPa for all fault zones and 1.46 - 8.77 MPa for the OHFZ (Fig. 6.8). They increase as a power law against seismic moment. The relationship is $\Delta\tau_s = 0.05\ {M_0}^{0.12}$, where $R^2 = 1$ as both seismic moment and static stress drop are controlled by the displacement, so produce an artificially perfect relationship when plotted against each other. These static stress drops are within the range of seismic moment and stress drops covered by the data of Abercrombie and Rice (2005) and Baltay et al. (2011). However, the literature stress drop data are highly scattered and show limited overall increase in stress drop with moment, except at larger seismic moments, whilst the stress drop values calculated increase throughout the range (Fig. 6.8).

Dynamic stress drops (Fig. 6.1) range from 5.20 MPa - 591.99 MPa for all fault zones and 11.51 MPa - 591.99 MPa for the OHFZ (Fig. 6.8). The method of calculation produces negative values if $\bar{\tau} > \tau_{yield}$ (see section 6.3.2) - these are ignored as an artifact of the method and are not plotted. Values for $\Delta\tau_d$ are almost entirely greater than those of $\Delta\tau_s$ and the literature static stress values of Abercrombie and Rice (2005) and Baltay et al. (2011). The fault zone datasets are differentiated by the different values of τ_{yield} assigned in section 6.3.2,

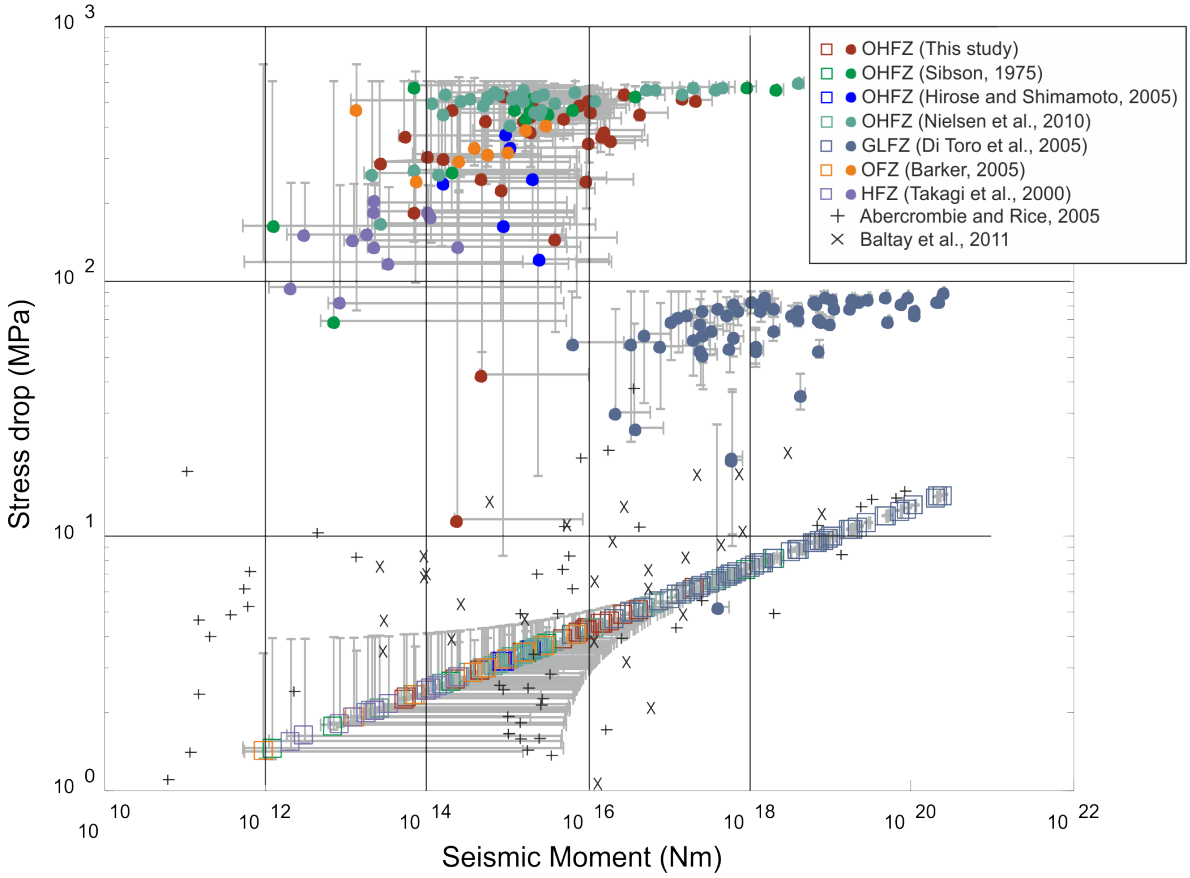

Figure 6.8: Static stress drops (open squares) and dynamic stress drops (closed circles) plotted against seismic moment for pseudotachylyte faults form all datasets. Also shown are literature values of seismically derived static stress drops from Abercrombie and Rice (2005) and Baltay et al. (2011). Error bars shown represent measurement inaccuracy (± 0.001 m) and true displacement uncertainty (+ 0.1 m).

so that the significantly lower yield strength given to the Gole Larghe fault Zone (45 MPa) causes the lower cluster of values shown by this dataset. Many of the fault zone datasets are best fit by a logarithmic distribution which shows an increase of some extent of $\Delta\tau_d$ with the seismic moment. The multiplying factor of the logarithm is between 22.9 - 31.1 for the OHFZ datasets and the Otago normal fault zone, compared to 3.9 for the Gole Larghe and 5.4 for the Hatagawa fault zone. These lower factors represent a flatter trend - i.e. a lower rate of increase of dynamic stress drop with seismic moment. However, the flatter trend seen in the Gole Larghe dataset, for example, may again represent the general pattern at higher displacements, rather than be a characteristic of the individual fault zone, as many of the other datasets flatten as moment increases (Fig. 6.8).

6.4 Discussion

Initially, the approach used for this analysis is considered, along with the limits on comparing field data with that obtained from experimental or seismological results. This is followed by a discussion on how the spread of the data for average dynamic shear stress may relate to coseismic weakening behaviour, and whether differing trends between the different fault zones can be explained. The results for static and dynamic stress drops are compared and implications for models of stress drop and magnitude relations discussed. Finally, the strength of fault zones are considered along with a discussion on the strength of the OHFZ and distribution of seismic magnitudes based on the OHFZ pseudotachylyte analysis above.

6.4.1 Critical assessment of approach

The data sources utilised for the various fault zones analysed in this chapter provide a range of slip senses (normal, strike-slip, thrust) and, to some extent, lithologies. However, apart from the Otago normal fault zone, all the fault zones are effectively hosted in granitoid-type rocks, meaning that the thermal and physical parameters input into Equation 6.3 are similar. Even for the Otago fault zone, which consists of quartz-albite-muscovite-chlorite schists, the latent heat of melting was approximated to that used for the Gole Larghe fault zone (Di Toro

et al. (2005b)) as a more appropriate value has not been quoted in the Otago faults literature. Additionally, the number of fault zones for which pseudotachylyte fault vein thickness and displacement observations are published are limited, so that studies comparing, for example, the differing behaviours of different slip modes, or different depths of faulting, are not yet viable until more data become available from other locations.

For the calculation of seismic moment and static shear stress, the provision or estimation of fault area is crucial, as these observations are unavailable, it is substituted using the scaling method outlined in section 6.2.5, where the global relationship of seismic moment (M_0) to slip area (A) was approximated as $A = M_0^{0.5868}$. Areas calculated in this way range from 1.36 x 10^4 to 1.18 x 10^9 m^2, more easily visualised in terms of the radius derived using the circular fault model - the radii range from 65.98 to 19402.23 m. For the OHFZ, the calculated radii range from 71.21 to 5801.53 m. These radii are much larger than any observed length of a pseudotachylyte bearing fault in the OHFZ. A common scaling law used in the literature is $M_0 \approx A^{1.5}$ (e.g. Kanamori and Brodsky (2004)), although it is only applied to earthquakes >6 M_W. This relationship yields fault radii for the OHFZ ranging from 0.01 - 127.16 m, much closer to values indicated by field observations. However, the static stress drops then calculated with these fault radii become unreasonably large (400.30 - 8871.72 MPa). In comparison, using the radii from the scaling law used in the analysis, static stress drops for the OHFZ lie between 1.46-8.77 MPa, within the typical range reported by seismology of 0.1-10 MPa (Kanamori and Brodsky (2004)). The large number of data used here to derive the area scaling law - 662 individual points (Fig. 6.2) - and the large range of seismic moment covered, suggests that the scaling relationship Area = 0.001 $M_0^{0.57}$ derived in this work is a valid relationship between rupture area and moment for small to moderate magnitude earthquakes.

6.4.2 Spatial averaging and comparison with seismological results

The influence of asperities on fault strength (Scholz (2002)) indicates that strength and stress drop should be heterogeneous across a single fault, which must be considered at all scales of investigation. Fault weakening models vary somewhat between those that consider the energy

budget of a point on a fault and those that look at the energy over a given area (e.g. Fig. 6.1). At the field scale, the analysis in this chapter seems best represented by area-averaged models, since the observed pseudotachylyte is generated from distributed slip along the fault it is found on. Values for $\bar{\tau}$ therefore average both slip distribution and slip period across the fault, or at least the section of the fault that contains the melt patch. The pseudotachylyte may not in fact extend over the entire length of the fault, which may partly contribute to why fault areas estimated via the moment scaling law are proportionally larger than the length of pseudotachylyte veins actually observed.

Faults are inherently heterogeneous due to natural roughness, varying material properties along the fault plane and slip strengthening or weakening processes along previously ruptured sections (Niemeijer et al. (2012)). Such variation may present itself as a series of smaller pseudotachylyte patches along a much larger scale fault plane, as melting is considered to preferentially occur at strong, high-friction asperities and/or in regions with high stress release. This interpretation leads to a common difficulty in relating field and seismological data. Seismological observations present magnitude and stress drops as averages for an entire fault, or even faults, as instantaneous multi-fault rupture is easily missed during initial seismograph analysis (Nissen et al. (2016)). Meanwhile, field observations represent point data along a fault, relative to the seismological scale. Even though the spatial distribution of slip and stress drop may be mapped using inversion of seismic data, these models have spatial resolutions an order of magnitude greater than that of, for example, a pseudotachylyte bearing slip patch (Bouchon (1997)). Thus, field data provides uniquely available information at the smaller, heterogeneous, but still fault-wide scale (Kirkpatrick et al. (2012)). The values presented here for shear strength and stress drops are likely to represent the stronger, asperity bearing parts of the faults they occur on, and therefore should be considered as maximum values relative to averages inclusive of the weaker or lower-slip parts of the fault.

6.4.3 Melt related weakening

The trend of increasing pseudotachylyte fault vein thickness with increasing displacement (Fig. 6.3) has been observed in Sibson (1975) and Hirose and Shimamoto (2005) using some of the datasets utilised here. Hirose and Shimamoto (2005) observed a different trend between their data and that of Sibson (1975), suggesting that different phases of pseudotachylyte generation (Fig. 3.13a) and different locations along the fault might cause different rates of pseudotachylyte development. However, within the spread of the data presented in this chapter, the datasets of Sibson (1975) and Hirose and Shimamoto (2005) both fall within the overall scatter (Fig. 6.3), even though the individual trends of the two datasets in question are noticeably different. Much of the scatter at this level of analysis (and also that propagated into later analysis) could be due to the uncertainties inherent in field observations (see section 6.2.3, Di Toro et al. (2005b)). It is possibly unjustified, therefore, to attribute such variations to differing processes of pseudotachylyte generation with certainty. However, variations would be expected to arise linked to the susceptibility of the mineralogy to melting, coseismic temperature evolution and the geometry of the fault, which should all influence how rapidly melt is generated and when a steady state slip is reached.

Plots of the average dynamic shear strength ($\bar{\tau}$), show progressive coseismic weakening as fault displacement increases (Fig. 6.4). The trend is remarkably consistent between datasets from different fault zones; scatter is created as much by variation within individual datasets as by differences between them. Whatever variations in depth of faulting, movement sense, lithology or other potential controls may exist between these fault zones, they are not observable here. The Otago normal fault zone, however, does appear to have a lower fall-off in shear strength with displacement relative to the other fault zones. The Otago fault zone is hosted by quartz - albite - chlorite - mica schists, which provide the only major textural and mineralogical difference in lithology across these datasets. The availability of minerals that preferentially melt, including amphibole and micas, might influence how rapidly melt is produced and weakening evolves, yet the presence of mechanically weak, low melting temperature minerals such as mica (Spray (2010)) in these schists suggests that this should not be

a limitation to weakening. Additionally, there are a number of physical parameters including slip rate, normal stress and the frictional coefficient that could restrict the change in temperature experienced along the fault (Sibson (1975)), which in turn could slow the rate of melt production. It is difficult to isolate the cause for this variation with the available information. In contrast, the Hatagawa fault zone has a known control that should influence its results - the mylonitisation of the pseudotachylyte veins, which could add some increment of displacement and possibly alter the thickness of the vein. In the simplest case, maintaining thickness whilst adding displacement, the ratio $\frac{t}{d}$ should be lower than expected, and the resulting $\bar{\tau}$ value may be underestimated too. Hatagawa values do sit at the lower side of the trend in Fig. 6.4, but in Fig. 6.3 continue the main trend nicely towards the lowest displacements. Hence, the magnitude of the effect of the mylonitisation on the input displacement and thickness is difficult to constrain.

The average dynamic shear stress, $\bar{\tau}$, is used here at a range of different displacements to approximate a typical weakening trend during progressive coseismic slip on a single hypothetical fault. There are some limitations to this approach. The shear strength or frictional behaviour observed during experiments at seismic slip speeds is simplified (as from the second frictional peak) in Fig. 6.1. One obvious difference to the results in Fig. 6.4 is that the late coseismic strengthening represented in Fig. 6.1 is lacking in the pseudotachylyte derived results. This is simply due to the irreversibly of melt production, so that pseudotachylyte production must always increase with slip and can never show a reduction in thickness that would be required to produce this late strengthening in the analysis. Thus, τ_{min} derived from $\bar{\tau}$ results will always occur at the end of slip at the highest displacements. In addition, the values of $\bar{\tau}$, as the average dynamic shear stress, are always higher than the real dynamic shear stress of a fault at an equivalent displacements.

6.4.4 Slip weakening distance

Although the trend in average dynamic shear stress versus displacement (Fig. 6.4) follows a power law for much of its length, at lower displacements there is less change in shear stress

and the values deviate from the trend. This change is also visible in the displacement versus thickness plot in Fig. 6.3. Sibson (1975) derived a power law relationship between pseudotachylyte thickness and fault displacement, but did not observe the change of rate that is presented here. This is likely to be a consequence of a limited dataset - the exponents of the trendlines derived by Sibson (1975) and derived here are similar, but observations with higher displacements have been collected in this study, extending the range to include the change in trend.

As this change originates from the primary field data, the divergence seen in Fig. 6.4 is likely to reflect a real, physical change in behaviour on pseudotachylyte faults. Hirose and Shimamoto (2005) showed that samples deformed in high velocity rotary shear experiments show increasing thickness of the cooled melt with increasing displacements. For experimental samples, thicknesses increase after the second frictional peak before reaching a steady state, where the change in thickness becomes limited at higher displacements, coinciding approximately with the onset of steady state friction (Hirose and Shimamoto (2005)). Such behaviour indicates that the reduced increase in melt thickness at higher displacements may be a function of the decreasing frictional heat production. Heat input is modelled to decrease with increasing displacement as a power law, which in turn is due to the increasing melt thickness reducing frictional contact between fault walls (Sibson (1975)). This influence is likely represented in the data here, and the feedback on fault weakening is shown in the change of rate at higher displacements that is observed in both Fig. 6.3 and Fig. 6.4.

This change in behaviour can be termed the slip weakening distance (D_c), a characteristic displacement over which a fault weakens during seismic slip (Ohnaka and Shen (1999), Hirose and Shimamoto (2005)). Locating the onset of steady state thickness in the relationship between pseudotachylyte thickness and fault displacement (Fig. 6.3) as suggested by Hirose and Shimamoto (2005) provides a slip-weakening distance of approximately 0.1 m for the OHFZ. This is an order of magnitude lower than the 1 m concluded by Hirose and Shimamoto (2005) for OHFZ pseudotachylytes. Given the relatively few data available to Hirose and Shimamoto (2005), 0.1 m is considered more reliable. The break in slope in the GLFZ is less clear but ap-

pears to occur between 1-3 m. These displacements are very similar to the location of breaks in slope on the shear stress versus displacement graph (Fig. 6.4). In the Otago fault zone, pseudotachylytes do not record the transition to steady-state thickness, which may occur at higher displacement than the field observations record. These two values cover the range of seismological estimates for slip-weakening distance, usually 0.1 - 1.0 m (Fukuyama et al. (2003), Mikumo et al. (2003), Mikumo and Yagi (2003)), which supports the conclusion of Hirose and Shimamoto (2005) that frictional melting is one dynamic weakening mechanism that influences the slip-weakening distance. Field based calculations of the slip weakening distance are important as comparisons with seismological derived values due to the sensitivity of those to the slip velocity model applied (Tinti et al. (2009)).

Dynamic stress drops, derived from the dynamic shear stress, also show this sharp change in trend as displacement progresses (Fig. 6.8), since here the calculation of seismic moment is mainly controlled by the displacement. The seismic moment at the point of change is equivalent to $\sim$ M_w 4.5 for the OHFZ and $\sim$ M_w 6.5 for the Gole Larghe fault zone. Earthquakes lower than these respective critical magnitudes show increasing dynamic stress drops with displacement and moment magnitude, whereas larger events have fairly constant stress drops. Hence, the slip weakening distance is critical to define whether dynamic stress drops should scale with earthquake magnitude, being equivalent to the critical magnitude. Faults with displacements $<D_c$ experience the scaling stress drop, and those with displacements $>D_c$ reach a constant stress drop value - the implication is that there is a maximum dynamic stress drop that can occur. This may be a complete stress drop; unfortunately, the calculated values for dynamic stress drop here are not considered reliable as they are often much larger than the calculated yield strengths, and hence offer little indication as to what the maximum stress drop might be.

The order of magnitude difference in D_c between the OHFZ and the Gole Larghe implies a different characteristic fault geometry, because D_c is thought to be proportional to the characteristic length scale of asperities on the fault plane (Matsu'ura et al. (1992), Ohnaka and Shen (1999)). Slip weakening distance is also sensitive to the width of the deformation zone,

the slip rate, transport capabilities for fluids and melts and, under certain conditions, temperature and normal stress (Ohnaka (1992), Noda and Shimamoto (2005)). In some models (e.g. 6.9b, Mikumo et al. (2003)) D_c increases with earthquake size. In the data here, based on multiple earthquakes, the Gole Larghe has a larger D_c than the OHFZ and also exhibits earthquakes of larger magnitudes than the range observed in the OHFZ (Fig. 6.8), although there is much overlap. Failure of intact rock has a higher D_c than slip on existing faults, if all else is equivalent (Ohnaka (2003)). Therefore other physical factors must overcome this - possibly the Gole Larghe has a larger length scale of characteristic roughness.

Overall, the slip model in Fig. 6.9 that is best supported by the data here is a combination of models c. and d. The proposed combination is shown in Fig. 6.9e, where the stress drop increases non-linearly with displacement until some characteristic distance, whereupon the behaviour alters and stress drops become constant. Further variation may be possible at higher magnitudes than are present in the data.

6.4.5 Stress drops

The static stress drop is shown to increase with seismic moment in Fig. 6.8. Whilst the perfect power law relationship shown is an artefact of the dependency of the value on the displacement from which many other parameters for it are derived, the derivation appropriates widely used relationships and assumptions. Other workers report an increase in stress drop with magnitude - for example, Mayeda and Walter (1996) suggest that $\Delta\tau_s \propto M_0^{0.25}$, whereas the results presented here have a similar relationship of $\Delta\tau_s \propto M_0^{0.12}$. Calculations of absolute stress drops on pseudotachylyte bearing faults have been made at 21 - 51 MPa (Kirkpatrick et al. (2012)) and 90 - 250 MPa (Griffith et al. (2009b)), which are larger than any static stresses calculated here but extend to the order of magnitude of the highest dynamic stress drops for this data. In addition, seismological studies, whilst often confined to stress drops >10 MPa (Kanamori and Brodsky (2004)), can report large ranges, for example 4 - 120 MPa for magnitude 1.8 - 2.1 M_w events on the San Andreas fault (Abercrombie (2014)). Additionally, the published static stress drops plotted on Fig. 6.8, which were chosen to cover a

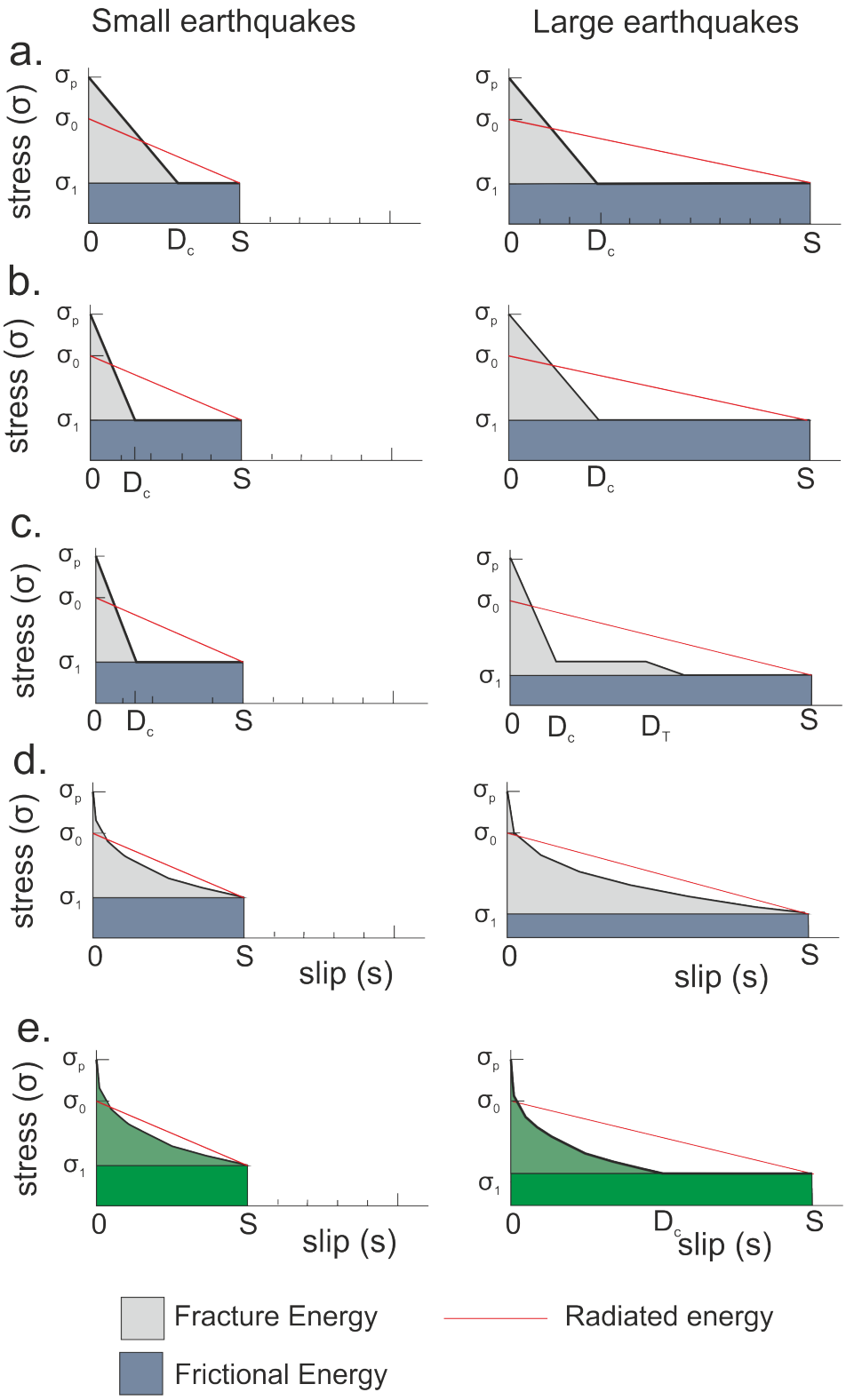

Figure 6.9: Four models of stress drop and fracture energy behaviour between large and small earthquakes from Abercrombie and Rice (2005) with model refined by this study. σ_P is yield stress, σ_0 initial stress, $\sigma 1$ final stress, D_c slip weakening distance and S final displacement: **a**. both stress drop ($\sigma_0 - \sigma_1$) and the fracture energy (light grey shading) are constant; **b**. stress drop is constant but fracture energy increases with earthquake size; **c**. stress drop changes after a certain threshold in displacement and/or magnitude; **d**. stress drop progressively increases with increasing earthquake size; **e**. model that best fits data.

similar range of seismic moments as calculated for the datasets here, cover a similar range to the static stress drops calculated within this work. Therefore, whilst the increase with earthquake size plotted in Fig. 6.8 might be artificial, the range of values produced are believed to be representative.

From Equation 6.11, the dynamic stress drop is proportional to $\bar{\tau}$ since for any given fault zone the value of τ_{yield} is kept constant. Therefore as $\bar{\tau}$ decreases with displacement, $\Delta\tau_d$ increases. In theory, pseudotachylyte should be a better recorder of the dynamic, rather than the static, stress drop given the approach highlighted in this chapter, as the static stress cannot be directly obtained from any properties of the pseudotachylyte, only the fault displacement. However, the maximum value for $\Delta\tau_d$ at 592 MPa is higher than most seismological studies report and too high for the predicted yield stress of the rock. If $\Delta\tau_d > \tau_{yield}$, the value for τ_{min} becomes negative. This highlights two uncertainties with the approach. The first is the definition of $\bar{\tau}$ itself. Beeler (2006) state that $\bar{\tau} = \frac{\tau_i - \tau_{min}}{2}$. However, in this case, the earliest onset of pseudotachylyte production is linked to the start of slip, so that low displacement $\bar{\tau}$ values are taken to relate rather to τ_{yield}. Therefore, the relationship of Beeler (2006) is modified to $\bar{\tau} = \frac{\tau_{yield} - \tau_{min}}{2}$. This leads to the second uncertainty, as whilst $\Delta\tau_d = \tau_i - \tau_{min}$, it is necessary here to assume that $\tau_{yield} \approx \tau_i$. However, the strength excess between τ_i and τ_{yield}, which is produced by the stress field of the approaching rupture tip, can be as much as 50 MPa (Mikumo and Miyatake (1993)), so the difference may not be insignificant. In general, considering that the calculations both of τ_{yield} and $\Delta\tau_d$ are based on these assumptions, it is difficult to allow $\Delta\tau_d$ to be greater than τ_{yield}. This may be because the definition of $\bar{\tau}$ versus what is actually calculated here using Equation 6.4 for $\bar{\tau}$ here might be overly simplistic.

6.4.6 Yield strength of fault zones

Despite the differing rate of change of weakening with slip in the Otago normal fault zone to the other datasets (Fig. 6.4), the yield stress indicated is very similar to that of the OHFZ, at 300-350 MPa. This suggests that the initial static strength of the rock is not necessarily an influence on how rapidly the fault weakens during slip. A weaker yield stress is recognised

for the Hatagawa fault zone (125 MPa), and even more so for the Gole Larghe (45 MPa). An analysis in Di Toro et al. (2005b) suggests that pseudotachylyte forming in cataclasite show that the faults in the cataclasite is weaker than faults in coherent rock. If observations for the Gole Larghe at the lowest displacements were made predominantly on pseudotachylyte faults in pre-existent cataclasite, it may explain why the extrapolated τ_{yield} is so much lower compared to the other fault zones. The Hatagawa fault zone has experienced shearing after pseudotachylyte generation. By adding further displacement (and possible thickness changes) to the pseudotachylytes, the indicated τ_{yield} value could become invalid because the ratio of vein thickness and displacement used in the calculation is altered after the initial brittle faulting. The apparently cyclical generation of cataclasite with pseudotachylyte, and mylonites, has led Takagi et al. (2000) to suggest that development of these fault rocks occurred at the brittle-ductile transition, where crustal strength is expected to reach a maximum before decaying due to the crystal-plastic flow law. However, the Hatagawa fault zone is postulated to be a major tectonic boundary between the Abukuma and South Kitakami belts (Takagi et al. (2000)), hence it is possible that a shear zone had already developed when the pseudotachylyte was produced. For example, Tomita et al. (2002) suggested that widespread mylonitisation preceded much of the brittle faulting. In this case, the shear strength of the faults would again be expected to be less than fault zones forming in intact rock, which is corroborated by the data, as the brittle yield shear strength is calculated to be $\sim$ 120 MPa (Fig. 6.4f). Comparing the Gole Larghe and Hatagawa results, brittle faults reactivating mylonites are stronger than brittle faults reactivating an existing brittle cataclasic fault.

The use of the Mohrs circle analysis is designed to provide a constraint on the estimates of τ_{yield} for the OHFZ. To cause failure in the models of section 6.3.2, the differential stress is increased above lithostatic values. This is considered valid, as in an active tectonic environment the relationship between σ_1 and σ_3 may deviate from the approximation in Eq. 6.5 which is more appropriate for sedimentary basins lacking horizontal strains (Cobbold et al. (2013)). Additionally, effective stress cannot be invoked if the assumption of a dry fault is upheld. The chosen angle of failure plane, 25°, is not always the optimum dip (Fig. 6.6) but this is not considered problematic as the value is based in the modern day geographical

reference frame, and tilting since the time of pseudotachylyte generation is uncertain.

At 5 km, the resolved shear stress at failure under any of the modelled failure conditions is significantly less than the yield stress for the OHFZ calculated in section 6.3.2 (Table 6.4). This implies that the depth of pseudotachylyte faulting in the OHFZ was >5 km. At 10 km, the predicted yield stress can be approached using the upper frictional strength of frictional sliding, where $\tau = 0.85\sigma_n$, at high differential stresses of 965 MPa (Table 6.4). Differential stress of this scale can be supported by granites at 10 km lithostatic pressure, but in intact rock (Byerlee (1978)). In contrast, the frictional sliding law needs a pre-existent failure surface. Additionally, in this model, brittle failure occurs at high normal stresses above the predicted brittle-ductile transition (Fig. 6.6c). In this case, a depth slightly less than 10 km might fail under more plausible conditions. Alternatively, the Mohr-Coulomb behaviour facilitates failure at 10 km under an applied shear stress of 270 MPa (Fig. 6.6d). Differential strength is still high (Table 6.4) but, as faulting is now modelled in intact rock, is plausible (Byerlee (1978)). Evidence from field and microstructural observations show that often, pseudotachylyte bearing faults did not form along previous slip planes in the OHFZ (section 4.3.1.2), which supports the use of Mohr-Coulomb failure over frictional sliding laws.

Taking the value of τ_{yield} for the OHFZ as having good certainty due to general agreement from several datasets, this is compared with discussion of fault strength in the literature. A study by Behr and Platt (2014) concluded that brittle faults rarely have strengths above 52 MPa regardless of their depth. This value, whilst applicable to $\tau_{yield} = 45$ MPa in the Gole Larghe fault zone, is an order of magnitude too low for the Otago normal faults and OHFZ. This may be due to the sample of faults in Behr and Platt (2014), which uses major, high-displacement faults. Faults typically tend to increasingly localise further phases of slip-weakening during their evolution (Perrin et al. (2016)), for example through weakening processes such as grain size reduction, or mechanical or chemical weakening of fault cores. Such behaviour is somewhat dependent on the balance between structural damage and healing, but it is generally accepted that the largest faults are often the most mature (Manighetti et al. (2007)). In contrast, the yield strength of small, low-displacement faults, and especially

of intact rock faulted for the first time, could be expected to be much higher. Experimental values of shear strength at normal stresses equivalent to $\sim$ 10 km (a maximum depth for unmylonitised OHFZ pseudotachylytes), are reported as 200-250 MPa (Byerlee (1978)). Additionally, residual stresses supported by the San Andreas have been observed as reaching 300 MPa (Chen et al. (2015)), despite it being supposedly weak. For the OHFZ, Sibson (1975) initially estimated a strength of 160 MPa, whilst Fettes et al. (1992) suggest 370-425 MPa, and favoured the lower value. Results presented here for the shear strength of OHFZ faults suggest that this latter study of Fettes et al. (1992) is more reliable and that the original calculation of Sibson (1975) was underestimated, in line with the differing depth estimates of OHFZ pseudotachylyte faulting proposed in Sibson (1975) relative to deeper values concluded here (section 4.4.1.2).

6.4.7 Fault zone structure

As shown in Fig. 6.7, the distribution of earthquakes between 1.9 - 6.2 M_W are not necessarily confined to what may be considered the main fault zone of the OHFZ in the east of the islands. It has long been observed that pseudotachylyte veins in general are well spread across the Isles (Sibson (1975), Butler et al. (1995), Imber (1998)). The question may be asked, therefore, as to why seismic activity is so dispersed across relatively small-displacement faults in the foreland of the OHFZ, rather than localised onto the main fault, which might be expected to be weaker and to fail at lower applied stresses below the yield strength of the outlying faults.

According to many fault growth models covering scales from laboratory samples to globally important fault zones (e.g. Scholz and Cowie (1990), Lockner et al. (1991), Gupta et al. (1998)), immature faults begin with restricted segment lengths, linkage and connectivity of slip, with slip events spread between many segments, and only as the fault zone matures does localisation of slip favour one set of progressively growing and linking segments (Gupta et al. (1998), Hardacre and Cowie (2003)). In the field and under the microscope, OHFZ pseudotachylytes can occasionally be seen cutting or perhaps re-using cataclasites (Fig. 4.6), suggesting that for at least one phase of pseudotachylyte generation, pre-existent faults were

present - although not necessarily in the preferred orientation. Many other pseudotachylytes appear to cut through clean rock, at least at the field scale. This is often true for pseudotachylyte outwith the main faults. In contrast, at many sites within the fault zone proper, large volumes of pseudotachylyte are identified in the crush zones (Fig. 2.3) where cataclasites and pseudotachylytes are repeatedly generated. One explanation, therefore, is that initially pseudotachylyte is generated via slip events on many small faults early on in the development of the brittle phase of the OHFZ. At this stage, the shear strength of these small new faults is high, around 300 MPa (section 6.3.2). Subsequently, pseudotachylyte continued to form on the major fault(s) during later episodes, creating the extensive vein networks seen in the crush zones, as displacement became localised to large slip episodes on these main faults.

A spatially varying distribution of pseudotachylyte veins involving a variety of fault slip senses could alternatively be produced during a relatively short time period (months to years) and involve perhaps only a few distinct episodes of seismicity. Near-concurrent seismicity on major and outlying faults could be explained by a sequence of mainshock slip on the main fault, followed by aftershocks distributed around smaller fault strands. Mechanisms such as Coulomb stress transfer, the change of the magnitude of stress due to an earthquake on another fault, (Freed (2004)), can act to increase the distribution of aftershocks onto surrounding faults, rather than along the same fault as the main shock (Stein (1999)). This mechanism can be an important controlling influence on the distribution of aftershocks, as well as much later earthquakes occurring up to years later, particularly in more diffuse fault zones lacking major localised structures (Verdecchia and Carena (2016)). Therefore, this model may apply in conjunction with timing much of the pseudotachylyte on the OHFZ to an early stage of its development.

A third option is that the scattered, small pseudotachylyte bearing faults are actually an expression of an expanded, complex fault zone. It is likely that some occurrences, such the number of occurrences of pseudotachylyte along the west coast of South Uist and Barra, form additional strands of the OHFZ as sometimes included in maps (e.g. Fettes et al. (1981)). The number of pseudotachylyte bearing faults in these areas make this interpretation fairly

certain. However, individual pseudotachylyte veins elsewhere could mark patches of high displacement across a larger connected structure not yet recognised. In general, slip distribution is often observed to be patchy along seismogenic faults (Bouchon (1997)) and it has already been noted that pseudotachylyte is more likely to form along asperities. The pseudotachylyte faults could therefore be small sections of larger faults, separated by low displacement sections between them making identification of the fault difficult. The difficulty associated with finding offset markers, and the restricted exposure, might suggest that this might be feasible in the OHFZ. However, other indicators of a significant fault strand, such as the development of cataclasite, or surrounding damage, would be expected, and this is not observed on the scale approaching the length of the faults either in the mapped trace of the OHFZ on the east or even the possible fault tracing through the west coast of Barra. This reasoning is therefore thought unlikely without further field evidence.

6.5 Chapter conclusions

The field-based datasets featured here provide an interesting and important link between laboratory and seismological scales of investigation into coseismic slip behaviour. As highlighted with the initial presentation of the method in Di Toro et al. (2005b), there are a number of uncertainties, of which many derive from the field observations. Despite this, when several datasets are collated as they are here, they produce a coherent trend. This suggests that the method is robust and therefore useful in examining the behaviour of different fault zones. At present there is insufficient data available to isolate the controls on differing behaviours identified, but this remains an approach that should be considered further as more observations are published. At present, the conclusions of this study are:

- Despite the differences in slip sense, lithology and depth between the selected fault zones, their respective trends of reduction in shear strength during coseismic slip are similar. However, the Otago normal faults show a more rapid fall of strength with displacement than the other fault zones. This does not seem to be related to either the normal sense of slip or to the initial strength of the faults.

- Both the OHFZ and the Otago normal fault zone had seismicity occurring on strong faults with brittle yield strengths at 300 - 350 MPa. In the case of the OHFZ, these values likely represent activity across an immature fault zone with rupturing of previously intact rock, in contrast to the Gole Larghe which is known to have lower yield shear strength due to the pre-existent clataclasic faults.

- In the Outer Hebrides Fault Zone, moment magnitudes between M_W 1.9-6.2 are recorded by pseudotachylytes. There is no systematic distribution of magnitudes between fault strands, but larger events may be seen to occur in the vicinity of the more major fault segments.

- This field based technique may provide comparable results with maxima for magnitudes and stress drops reported from seismological studies.

- There is a marked change in trend in the fall of dynamic shear stress with displacement which appears to be linked to reduced pseudotachylyte production and vein thickening at $\sim$ 0.1 m displacement. This is interpreted to result from reduced frictional heat production due to lessened fault wall contact, leading to the inference that the fault weakening distance is also 0.1 m. This characteristic distance is larger in the Gole Larghe Fault Zone, where it appears to be in the range of 1 m.

- Dynamic shear stress decreases progressively with slip until the fault weakening distance. In the OHFZ the dynamic stress drop therefore increases with slip up to a threshold displacement $\sim$ 0.1 m. This increase is non-linear with displacement and seismic moment between the magnitudes of 1.9 -4.5 M_W. At higher magnitudes the dynamic stress drop changes very little.

- Values calculated for dynamic stress drops become unfeasibly high for the OHFZ at higher displacements. This implies that the derivation $\Delta\tau_d = 2(\tau_{yield} - \bar{\tau})$ may be oversimplified.

Chapter 7

Discussion and synthesis

7.1 Introduction

This chapter summarises and discusses the findings presented in the preceding results (chapters 3-6). The aims of the chapter are to discuss:

- the use and applicability of quantitative data derived from pseudotachylytes;
- the proposed model for the evolution of seismicity and fault development along the OHFZ, incorporating:
  - the evidence of fault reactivation on the OHFZ and the timing of pseudotachylyte - generating seismic activity;
  - constraints on the depth of pseudotachylyte - generating seismicity, and on the temperature, strength and stresses that characterised the seismic environment of the OHFZ;
  - the controls on spatial heterogeneity of seismic activity on the OHFZ;
- the applicability of the OHFZ model to generic fault zone and seismicity models;
- the applicability of the OHFZ model to orogenic models.

7.2 Use and applicability of pseudotachylyte to constrain earthquake parameters

This section considers the use of pseudotachylyte to quantify parameters related to ancient earthquakes and discusses some of the approaches used in this work.

7.2.1 Preservation of primary crystallisation

Derivation of environmental constraints on seismicity and pseudotachylyte generation (e.g. pressure, ΔT, ambient temperature, melt temperature) from the compositions and microstructures of pseudotachylyte veins often relies on the preservation of primary crystallisation assemblages and textures. Although pseudotachylytes are often described in the field as glassy, most micrographs show them to be at least partially crystallised (e.g. Fig. 4.3). However, uncertainty remains because crystal morphologies produced by quench crystallisation and those produced by devitrification are very similar (compare Lofgren (1971), Lofgren (1974)). The identification of timing of crystallisation is therefore important for the interpretation of what temperature and pressure calculations relate to. This section discusses the crystallisation preserved in OHFZ pseudotachylytes and the consequent meaning of melt temperature and thermobarometry results.

It seems that in many cases that primary crystallisation does not develop until flow of the pseudotachylyte has ceased (section 7.3.2.1, Fig. 7.1). Flow textures, preferred crystal orientations and clast flow indicators are not present in the majority of pseudotachylytes either in the OHFZ or elsewhere, although there are plenty of individual examples. Hence, crystallisation is not complete until after slip has ceased. For a slip duration of 0.3 s, melt is predicted to exist for 1 s (Caggianelli et al. (2005), Fig. 7.1). The growth rate of pseudotachylyte matrix crystals is in the region of 0.5 μms^{-1} for an undercooling of 300°C (Petrík et al. (2003)). As Petrík et al. (2003) report that haematite crystals in their study grew to 2-8 μm, 4-16 seconds would be required for the duration of crystallisation. Within this time period, the melt temperature could drop to 500°C, based on the models of Caggianelli et al.

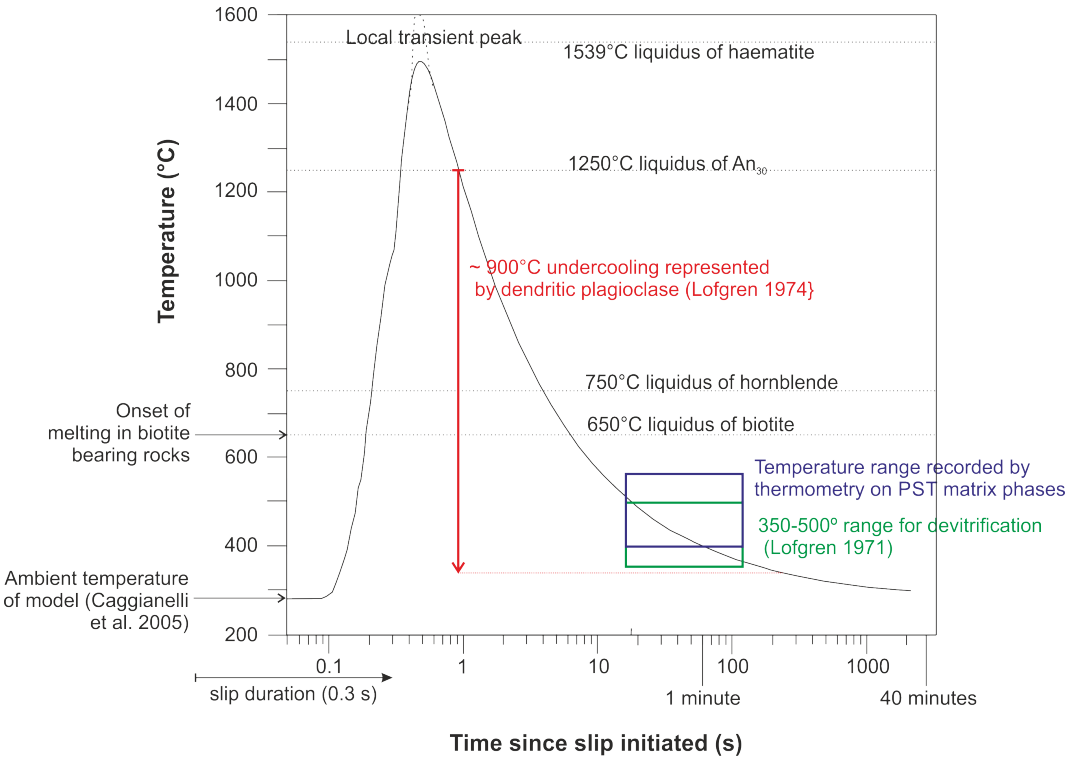

Figure 7.1: Cooling model for timing of crystallisation of pseudotachylytes. Cooling curve is taken from the model of Caggianelli et al. (2005), using a slip duration of 0.3 s, displacement of 20 mm and a point beginning 1 mm away from the fault plane. Mineral melting temperatures are taken from Spray (2010) and Lide (2004).

(2005) (Fig. 7.1). This, and the undercooling observations of Lofgren (1974), indicate that rapid cooling may lead to primary crystallisation representing temperatures some hundreds of degrees cooler than when crystal nucleation began (Fig. 7.1). For devitrification, Lofgren (1971) found that rhyolitic glass devitrified between 350 - 500 °C over six days or more at 200-350 MPa pressure. On cooling to ambient temperatures, Caledonian OHFZ pseudotachylytes might be expected to devitrify along the cooling path. Divitrification may be only partial, occurring where interstitial glass was present. For example, in Figs. 4.3 and 4.4, the interstitial matrix between plagioclase laths and the body of the spherulite, respectively, have an intergrown exsolution texture on the ≤ 1 μ m scale. This may have developed during devitrification of a mixed glass, whilst the larger scale microstructures in both these samples are arguably primary (section 7.3.2.1).

The use of thermobarometry on pseudotachylytes is one technique used in this work

(section 4.3.5) that is dependent on interpretation of the timing of crystallisation. Most thermobarometric analyses on pseudotachylytes have been undertaken either on altered or re-deformed, mylonitised pseudotachylytes to provide minimum temperatures and pressures (White (1996a), Ueda et al. (2008), Leib et al. (2016)), or are semi-quantitative estimates based on the matrix assemblage (Austrheim and Boundy (1994), Toyoshima (1990), Camacho et al. (1995), Nestola et al. (2010), Altenberger et al. (2011)). Alternatively, thermodynamic modelling software may be used to predict a liquidus temperature (Di Toro and Pennacchioni (2004)). Both these assemblage crystallisation and liquidus temperatures are used to give a minimum temperature for the melt. These are likely to best approximate the melt temperature when the indicator mineral used is a high temperature metastable phase, such as the dmisteinbergite (hexagonal anorthite) in a Gole Larghe pseudotachylyte (Nestola et al. (2010)). Many resultant temperatures are >1000°C, which is reasonable based on other melt temperature indicators for pseudotachylytes, but may potentially be significantly cooler than the actual figure (e.g. 1400°C, Di Toro et al. (2005b)).

Amphibole-plagioclase thermobarometry undertaken on OHFZ pseudotachylytes (section 4.3.5) produce temperatures that most likely represent immediate devitrification of the interstitial matrix during the latest stages of cooling to ambient temperature (section 4.3.6). The technique requires analysis of adjacent amphibole and plagioclase crystals (assumed to be in equilibrium), so that primary structures such as the plagioclase lath phenocrysts were not sampled. In general, the meaning of temperatures and pressures recorded by crystallisation in pseudotachylytes should be carefully considered.

7.2.2 Magnitudes and stress drops

As discussed in Chapter 6, commonly used scaling relationships from seismology can be used to calculate seismic moments and stress drops from field measurements on pseudotachylyte veins. Many of these calculations depend on the displacement along the fault (section 6.2.5). As noted in section 6.4.2, pseudotachylyte - bearing patches along a fault are likely to be formed at regions of higher stress drop, perhaps over asperities, and so pseudotachylyte de-

rived values for stress drop and moment will be local maxima, higher than the average values derived from seismic data. Static stress drops calculated here from pseudotachylyte - bearing fault displacements remain comparable to those resolved from seismic corner frequencies over the same magnitude range (Fig. 6.8), whilst the dynamic stress drops may be an order of magnitude larger. An uncertainty in the static stress calculation results from the need to oversimplify the rupture shape as a circle, or sometimes a rectangle, a geometrical model which is also a major source of unrealistic values in corner frequency processing (Wang et al. (2015)). Rupture shape and size, with variation of slip and stress drop across a fault, can be shown by seismic inversion models (e.g. Bouchon (1997)), but the resolution is not comparable to the scale of pseudotachylyte faults which may be 10-20 m at most. More recently, fault slip models have improved in detail, and can also be produced from geodetic data, with the increasing global coverage of GPS and InSAR datasets (e.g. Tong et al. (2010)). Thus, mapped variations in shear stress change (which can be an increase, e.g. Luttrell et al. (2011)) across a fault allow comparison of the maximum stress change with values derived here from pseudotachylytes on similarly sized faults. For example, the M_w 6.9 2010 Yushu earthquake records a maximum stress drop of 8.3 MPa, compared to a fault-wide average of 2 MPa (Wen et al. (2013)). For an earthquake of this moment, the relationship derived in this study for static stress drop and seismic moment ($\Delta\tau_s = 0.05\ {M_0}^{0.12}$, Fig. 6.8) results in a stress drop of 10.8 MPa, larger than the maximum recorded by Wen et al. (2013). However, the error in the fault slip models, which are sensitive to the choice of smoothing, is of the order of some few MPa and so covers the difference (Wang et al. (2015)). The relationship between maximum static stress drop and seismic magnitude shown in Fig. 6.8 is hence thought to be an applicable approximation to many fault zones, despite the high interdependency in the derivation.

7.3 Forming a model of seismic slip on the Outer Hebrides Fault Zone

This section discusses the results of this study in the context of the evolution of the Outer Hebrides Fault Zone, drawing on evidence from throughout the thesis - in particular the likely timing of the various phases of slip identified, the depth and temperature of seismicity, and the changing strength and behavior of OHFZ faults.

7.3.1 Tectonic significance of pseudotachylyte in the Outer Hebrides Fault Zone

7.3.1.1 Impact vs tectonic generation of pseudotachylyte

Pseudotachylyte, defined as a frictional melt, can be generated not only during coseismic slip along tectonic faults (e.g. Sibson (1975)) but also during meteorite impacts. The question as to whether any of the OHFZ pseudotachylytes are related to impact processes arises from the proposed evidence for an impact ejecta layer in the $\sim$ 1180 Ma Stac Fada member of the Torridon supergroup on the adjacent mainland (Amor et al. (2008), Reddy et al. (2015)). This date notably coincides with some of the $^{40}Ar/^{39}Ar$ dates for OHFZ pseudotachylytes obtained by Sherlock et al. (2009). However, pseudotachylyte occurrences in the Western Isles are clearly linked to fault movement on the OHFZ and associated fault strands (e.g. Sibson (1975), Imber (1998), current work) and have so far fitted well into the proposed history for movement on the OHFZ (e.g. Butler et al. (1995), Imber et al. (2002), Osinski et al. (2001)).

7.3.1.2 Applicability of observations from the Outer Hebrides Fault Zone to global fault zones

Despite being held as a classic fault zone for the study of tectonic pseudotachylyte following the work of Sibson (1975), the Outer Hebrides Fault Zone is not necessarily considered a typical fault zone amongst the many ancient and active faults recognised globally today, whether

pseudotachylyte is present or not. This is mainly due to the large volume of pseudotachylyte observed across the OHFZ. Individual, high-melt volume pseudotachylyte structures such as the breccias and injection-vein networks seen in the OHFZ (e.g. Figs. 3.1b-d, 3.2a,d) are not unusual in themselves, being reported in several other exhumed fault zones (e.g. Grocott (1981), Camacho et al. (1995), Bjørnerud and Magloughlin (2004)). The overall prevalence of pseudotachylyte across the Outer Hebrides can also be attributed to three factors: the activity of different structures under different kinematic regimes through time, in several cases producing pseudotachylyte; the later differential uplift of small fault blocks between late, steep faults dissection the Outer Hebrides (e.g. Fettes et al. (1992), Butler (1995)) juxtaposing pseudotachylyte faults that were not initially adjacent; and the over-simplified portrayal of the OHFZ as a single, or localised, fault zone in the east of the Western Isles, when in common with many similar fault zones it should be expected to consist of several parallel and oblique linking segments (e.g. Moine Thrust Zone, Freeman et al. (1998), Northern Italy Cheloni et al. (2016)). The arguments of Kirkpatrick et al. (2009)) as to whether pseudotachylytes are rarely preserved, generated or reported also come into play here, as many (although not all) of the OHFZ pseudotachylytes are well preserved and not completely overprinted by fluid-assisted alteration or by later deformation.

However, some characteristics must make the OHFZ repeatedly susceptible to producing pseudotachylyte across several episodic periods of earthquake activity. A major contributer is likely to be the strength of the fault zone, influenced by mineralogy, structure and fluids. The resistant quartz-plagioclase dominant composition of much of the Lewisian Gneiss unit in the Western Isles exhibit high levels of frictional behaviour in comparison to lithologies richer in the mechanically and thermally weaker amphibole and plagioclase (section 5.3.3). These lithologies are also expected to exhibit higher levels of friction than rocks rich in phylosillicates (Wallis et al. (2015)), common in fault rocks due to reactions facilitated by fluid influx. The apparent lack of free fluids in the OHFZ until late in the Caledonian Orogen (Imber et al. (1997)) has therefore maintained dry, constant mineralogies capable of producing the frictional heat necessary for coseismic frictional melting in the OHFZ. This is in contrast to many major fault zones observed around the world, for example the Alpine Fault Zone, New Zealand, where

pseudotachylyte is limited temporally to a $\sim$ 20 Ma time period of seismic activity (Warr et al. (2003)), and spatially to anhydrous parts of the fault complex (Toy et al. (2011)). In addition, limited early localisation to a single major fault segment (Sibson (1975)) allows the preservation of high shear strengths on the scale of the fault zone. Hence, the mineralogical and structural development of the OHFZ was ideal for facilitating pseudotachylyte to be generated over several tectonic episodes, but this should not be expected on typical major faults.

7.3.2 Evolution of OHFZ seismic activity in time

7.3.2.1 Timing of seismicity

This work has focused on the brittle pseudotachylytes preserved in the OHFZ, and the behaviour and timing of the earliest, resheared phase of pseudotachylyte seen in the Lewis mylonites are only discussed in passing. These are taken to be pre-Caledonian after Butler et al. (1995), Imber et al. (2001) and Osinski et al. (2001) and are discussed in detail by Sibson (1980) and White (1996a).

The suggestion that the majority of the pseudotachylytes in the OHFZ relate to the Caledonian orogeny is based on the established order of fault movement (Butler et al. (1995), Imber et al. (2002), Osinski et al. (2001), Szulc et al. (2008)) along with consideration of the absolute dates available from argon-argon dating directly on the pseudotachylytes (Kelley et al. (1994), Sherlock et al. (2009)). These dates include 430$\pm$6 Ma from Grimsay (Kelley et al. (1994)), 1300-1200 Ma in Barra and South Uist, and 700 Ma in Barra, South Uist and North Uist (Sherlock et al. (2009)). The Grimsay date fits well with the Caledonian thrusting hypothesis for the top-to-NW or top-to-SE faulting observed in Grimsay (section 3.3.3). The 1300-1200 Ma dates may correlate with Grenvillian orogenic or post-orogenic activity (Sherlock et al. (2008)) which is linked to pseudotachylyte faulting on the Scottish mainland (Sherlock et al. (2008)) and is also the proposed timing for initiation of ductile thrusting on the northern OHFZ (Imber et al. (2002), Williams and Foden (2011)). These dates support the reasoning that undeformed pseudotachylytes may exist in the Southern section equivalent in age to

the sheared pseudotachylytes observed in Lewis related to the OHFZ's early activity Sibson (1980), Imber et al. (2002)). The $^{40}Ar/^{39}Ar$ technique is vulnerable to 'technical difficulties' (Sherlock et al. (2009)), due to external argon contamination of the pseudotachylyte matrix and thermal resetting postdating pseudotachylyte formation (Sherlock et al. (2009)). Some of the dates produced (e.g. 700 Ma) are difficult to related to known regional deformational events, unless farfield effects of tectonic episodes are invoked. Therefore, the association of most undeformed pseudotachylyte in the OHFZ with Caledonian tectonics stands.

7.3.2.2 Environmental conditions of earthquake slip

The depth range of pseudotachylyte generation in the OHFZ, and hence seismicity, was not previously well constrained. The early phase mylonitised pseudotachylytes of the northern section are deep, high grade features formed at depths of 13 - 18 km (Fettes et al. (1992) and White (1996a)). The Caledonian pseudotachylytes are generally considered to have been produced at depths of 5 - 10 km (Sibson and Toy (2006)). Results of the current study have provided better constraints on the environment of seismicity, using evidence for pressure, ambient temperature and melt temperature conditions gathered throughout this work. Improving understanding of these conditions should improve both the general understanding of the evolution of seismicity and deformation behaviour of the OHFZ. Additionally, it facilitates more accurate onward analyses that use, for example, coseismic temperature increase as an input parameter, as many estimations of the seismic energy budget from pseudotachylytes do (e.g. O'Hara (2001), Di Toro et al. (2005b), Chapter 6 in this work).

7.3.2.2.1 Depth of pseudotachylyte generation in the OHFZ A significant proportion of pseudotachylyte veins studied were generated during seismicity on faults around $\sim$ 10 km depth or greater, at the higher end of the range initially suggested by Sibson (1975). This value is obtained from calculations of the typical yield strength of small pseudotachylyte bearing faults (section 6.3.2). Assuming a typical geotherm of 25-30°C km^{-1}, it is in agreement with the range for minimum ambient temperature given by:

1. greenschist facies alteration assemblages in pseudotachylyte veins (section 4.3.4.3 provide a minimum temperature, assuming no later burial: minimum T =$\sim$ 250 - 300°C);

2. published temperatures for the deformation of phyllonites that overprint pseudotachylytes (Szulc et al. (2008), T =230$\pm$20°C and Osinski et al. (2001), T =370$\pm$20°C) ;

3. the magnitude of undercooling estimated from plagioclase quench morphologies (section 4.3.2, T = 230-350°C);

4. the range of plagioclase-amphibole thermometry which represent maximum ambient conditions (400 - 550°C) and some barometry values (400-600 MPa) though these are not well constrained (section 4.3.5).

In addition, mechanical models based on the predicted yield shear strength of OHFZ pseudotachylyte - bearing faults suggest that the depth of faulting was $\sim$ 10 km or above, in order to reach the necessary mean and differential stresses needed to fail the rock (section 6.3.2). The compatibility of these various results suggests that many of the pseudotachylytes were generated at a similar depth range in the crust despite the varying kinematic phases they may represent (section 3.7.4.3). However, these techniques for depth estimation may not be able to resolve the changes in depth that could be expected with discrete periods of compression (i.e. burial of the footwall) before extension (i.e. uplift).

In summary, the brittle thrusting phase is considered to have had a depth range of 10 - 13 km based on the evidence presented here (sections 4.4.1.2, 6.4.6) and the ambient temperature values for later deformation of 370$\pm$20°C (Osinski et al. (2001)) with a possibly elevated geotherm range of 25-30°C km^{-1}. Later deformation phases (strike slip and extension) may have been shallower; reduced temperatures are recorded by the phyllonites and extensional detachments (Osinski et al. (2001), Szulc et al. (2008)). Alternatively, seismic faulting may have remained active at similar depths whilst these later deformation mechanisms became active at shallower levels on the fault.

7.3.2.2.2 Temperature of pseudotachylyte melts in the OHFZ Previous melt temperature estimates for the OHFZ pseudotachylytes have been suggested to be 1100-1200°C (Sibson (1975)) and >1000°C (Maddock (1983)). The objective in this work was to collect available evidence to constrain these values, as the melt temperature is used again in this study to both constrain ambient temperature values (sections 4.3.2) and to calculate energy budgets and stress drops (Chapter 6). Peak melt temperature for a typical OHFZ pseudotachylyte is 1230-1350°C, as defined from melting temperatures of the melted phases, with support from the undercooling results (section 4.3.2) when based on the minimum ambient temperature for later deformation phases (Szulc et al. (2008)). Because the same set of minerals are melted or partially melted in OHFZ pseudotachylytes as in many crystalline hosted pseudotachylytes worldwide, the peak melt temperature is much the same as reported elsewhere (Camacho et al. (1995), Di Toro and Pennacchioni (2004), Nestola et al. (2010), Altenberger et al. (2011)). Although this 1230-1350°C range is reported as the 'peak' values, the melt must locally and transiently reach higher temperatures, as discussed in section 4.4.1.1.

7.3.3 Kinematic evolution of pseudotachylyte faults in the OHFZ

As concluded in Chapter 3, multiple phases of slip have been identified from cross-cutting relationships. These may show different fault orientations and slip senses (e.g. Figs. 3.13a, 3.25a). From observations of bulk datasets sourced from various orientation data (e.g. sections 3.3, 3.5, 3.6.1 and 3.6.2), it is apparent that there are discrete periods of differing slip senses. Oblique reverse faulting and strike-slip on oblique faults may well be concurrent, but an extensional set of faults is thought to be a separate kinematic phase. This is because, firstly, extensional pseudotachylyte - bearing faults are seen to cut other pseudotachylyte veins (e.g. Fig. 3.25a, in agreement with MacInnes et al. (2000)) and secondly, because the dip-slip tendency of the extensional faults is dissimilar to the varyingly oblique slip of the reverse faults of the same orientation, suggesting that thrusting and normal faulting were not synchronous. This extensional phase is thought to be late relative to other pseudotachylyte generations, based on the field evidence stated above (section 3.7.6). A left lateral strike-slip

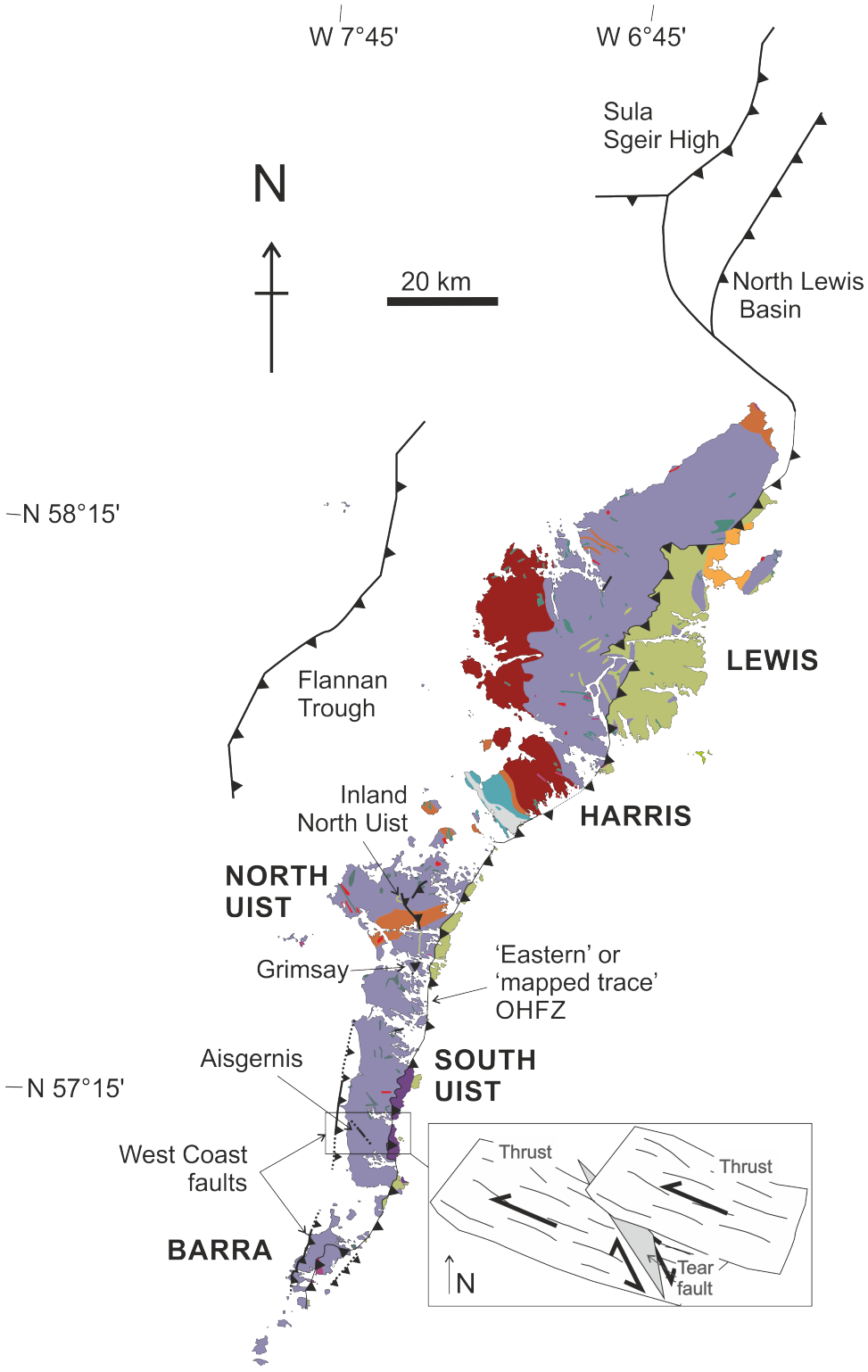

Figure 7.2: Map of fault strands suggested to have originated as brittle thrusts, including offshore strands after Brewer and Smythe (1986) later reactivated into extensional basin bounding faults. Inset is suggested model to explain apparent linking structures such as Aisgernis faults.

phase is also distinguished in this work from the oblique reverse pseudotachylytes. This may be part of a transitional evolution, but is considered to post-date the main oblique reverse phase because of noted localisation onto the major OHFZ fault structures (section 3.7.6). Localisation onto the main fault segments is proposed to occur with progressive slip and fault evolution, in line with published models (e.g. Cowie (1998)), and fits a gradual transition to increasingly oblique plate convergence and strike- slip faulting as a feature of the Caledonian regional history (Dewey and Strachan (2003)). The broad order of kinematic phases on SE, E or NE dipping faults is therefore: 1) oblique reverse; 2) left-lateral strike slip; 3) extension. Less optimally orientated faults may differ from these phases.

7.3.3.1 Fault zone structure and control on location of seismic activity

The distribution of pseudotachylyte across the fault zone may reflect a heterogeneous occurrence of seismicity. Changes in fault zone structure can be traced in the distribution of pseudotachylyte bearing faults. Displacement between the OHFZ trace in South Uist and that in Barra is usually explained by an E-W orientated lateral-ramp style structure (Fig. 7.2, MacInnes et al. (2000)) linking the Barra segment, and the suggestion of the 'main' trace continuing offshore to the east (Sibson (1977b), Butler (1995)) or with a right lateral strike slip offset between Eriskay and Barra (Butler (1995)). This jog apparently consists of a single major fault, which contains pseudotachylyte (MacInnes et al. (2000), also this study [73067 801845]). A similar structure may be observed in a set of steep, NW-SE trending pseudotachylyte breccia bodies and paired shear zones near Aisgernis, South Uist (Fig. 3.1c, [75692 823056]), a region that lacks other deformation normally associated with significant brittle faulting. The slip sense is often left lateral, usually top-to-NW strike slip. Two N-S trending faults that offset a metasedimentary band by ∼200 m are mapped across this locality (Fettes et al. (1981)). However, it is instead suggested that these pseudotachylyte faults represent a linking ramp (Fig. 7.2) between the mapped OHFZ in the east and the fault zone represented by abundant pseudotachylyte at the west coast headland of Àird a' Mhuile ([71125 829655]). The mapped N-S faults are later structures, as seen in smaller scale right lateral N-S offsets cutting the pseudotachylyte features. This seismogenic linkage fault, and others like it, will

provide some of the orientations termed 'misaligned' (Fig. 3.22) relative to the dip of the main fault zone.

The number of pseudotachylyte bearing faults concentrated at Àird a' Mhuile, South Uist, and at western Barra localities such as Àird Ghrèin, Allathasdal beach and Bàgh Halaman (e.g. Fig. 2.3a) suggest that one or more fault zones pass through these localities, probably parallel to the mapped trace of the OHFZ in the east (Fig. 7.2). A thrust trace is sometimes mapped onto southwest Barra (e.g. Fettes et al. (1981)), as the easterly dipping planar indents termed 'topographic thrusts' (e.g. Sibson (1977b)) picked out in the slopes of Beinn Tangabhal [6384 79913] there are similar to those noted in the mapped OHFZ by Sibson (1977b) and Butler (1995). In South Uist, the northwestern most headland of Àird a' Mhachair also contains pseudotachylyte veining, although mainly injections veins are exposed, on its northeast shore [7475 84591]. It is not certain whether a singe fault zone might extend from Àird a' Mhachair through to Àird a' Mhuile and even beyond to Barra, as there is little exposure on the sandy western shores.

Furthermore, thrust faults have been inferred to form inverted bounding faults for some of the small basins on the Hebridean platform lying offshore to the west of the Western Isles, where the Lewisian gneiss forms a hard substrate seabed (e.g. West Lewis Basin, Hitchen et al. (1995)). As another example, already included on BGS mapping (Fettes et al. (1981)), the Druim Reallasger pseudotachylyte locality [8613 86662] (Fig. 2.3) is part of another fault zone strand that joins outcrops of pseudotachylyte faulting across inland North Uist (Fig. 7.2). Therefore, the OHFZ, in its earlier history at least, should be envisaged not as a single plane of discontinuity but as one of a series of parallel fault zones accommodating movement (section 6.4.7), with smaller, but still seismic, faults scattered between the more major fault zones (Fig. 7.2). This is a common model for continental thrust fault zones, in contrast to the more continuous single fault planes of subduction zones (e.g. Lin et al. (2011), Cheloni et al. (2016)). During progressive slip associated with the Caledonian orogeny, it is proposed that the intense damage (e.g. crush zones) and influx of fluids along the mapped OHFZ trace led to major localisation, leading to the development of a more obvious fault zone along its

current trace.

7.3.3.2 Strength of faults in the Outer Hebrides Fault Zone

Pseudotachylyte bearing faults in the OHFZ appear to not in general reactivate existing faults, although there are exceptions (Fig. 4.6). More commonly, they cut across and rework other fault rocks. In the field, there are cases where the pseudotachylyte fault forms entirely within cataclased and fragmented rock, as is often the case in the crush zones. It has also been shown that many pseudotachylyte faults are not completely parallel to foliation (section 3.4.1). An individual fault, although it may cut weakened material, is not expected to be an inherently weak plane prior to the pseudotachylyte generating episode. Static shear strengths of pseudotachylyte bearing faults in the OHFZ are relatively high, around 300 MPa (section 6.3.2). These small, strong faults fit well within a proposed model where one or more phases of pseudotachylyte generation take place on small, scattered faults across an initially immature fault zone (section 6.4.7), a setting initially envisaged by Sibson (1975) but supported by critical evidence here. Within the brittle regime, the presence of a solidified pseudotachylyte vein along a fault serves to weld the fault plane, making it unlikely that the plane can be reactivated, unless fluid ingress and alteration are present. This effect may well be seen in local fault zone structures such as the Aisgernis tear fault, South Uist (Fig. 7.2), which might be expected to frequently slip (Lin et al. (2011)). However, instead of a localised, reactivated single fault or fault zone, a set of parallel pseudotachylyte -breccia bearing faults occur within more or less intact gneiss, so that each breccia represents a single-slip event.

The NE dipping orientation of many pseudotachylyte faults in the OHFZ (Fig. 3.3) is oblique to the dominant compressional and extensional slip directions, as well as to the main trend of the OHFZ. This arrangement may contribute to the high strength of the pseudotachylyte faults in general, as higher shear stresses are required to produce slip with increasing angle of misalignment, all other factors (e.g. frictional coefficient) being constant (Hill and Thatcher (1992)). Pseudotachylyte faults in the Western Isles show slip vectors misaligned relative to dip slip movement; modal angles of misalignment are 15° and 65-80°, the latter probably

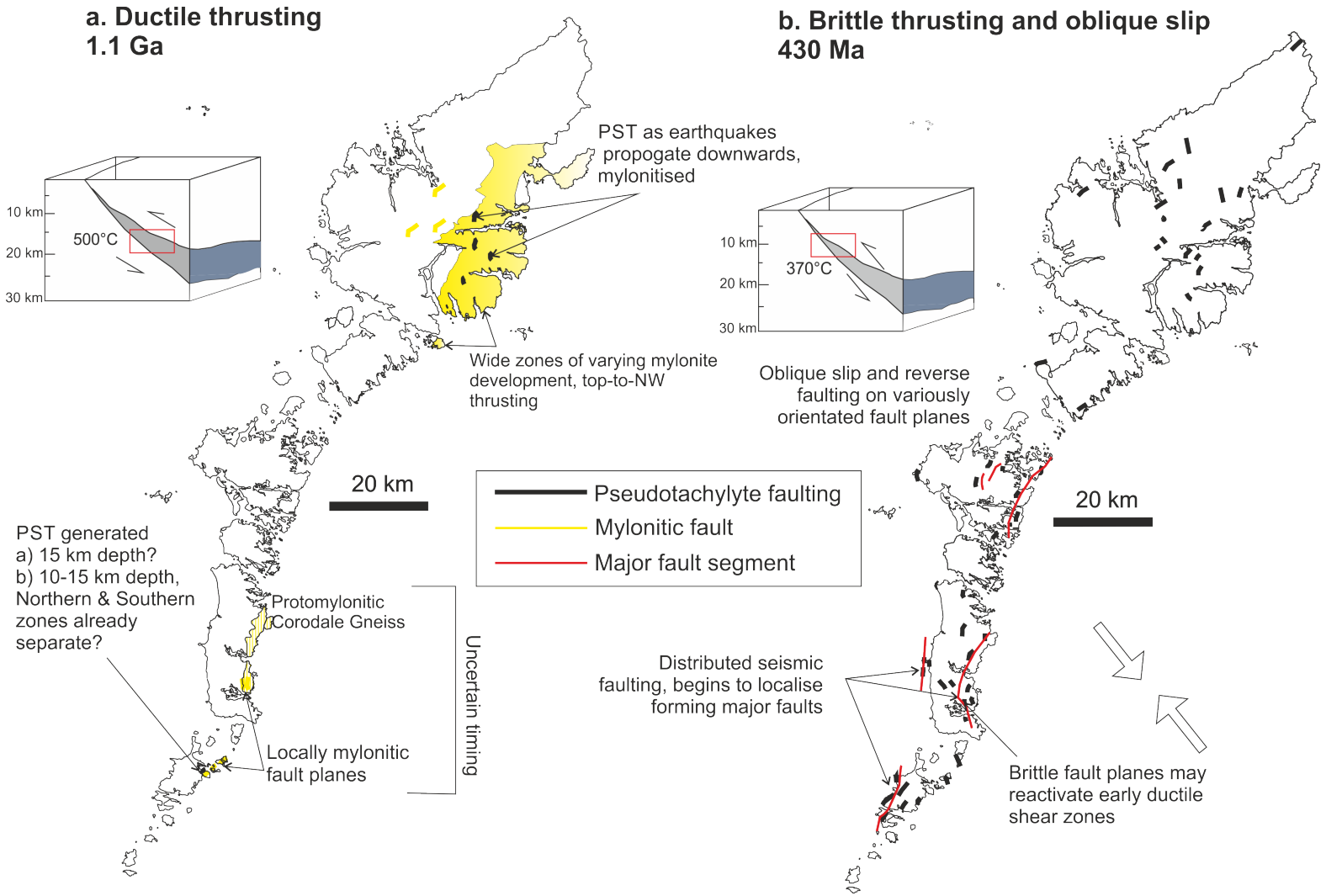

Figure 7.3: Seismic slip evolution of the OHFZ, part 1: a. early ductile top-to-NW thrusting in wide mylonite zones in Northern section of fault zone, and possibly on discrete mylonite bands on southern section. Transient brittle seismicity recorded; b. Initiation of Caledonian brittle top-to-NW thrusting begins as scattered seismicity on small faults, over time localises onto main fault zones. Oblique convergence reflected in some oblique slip faults.

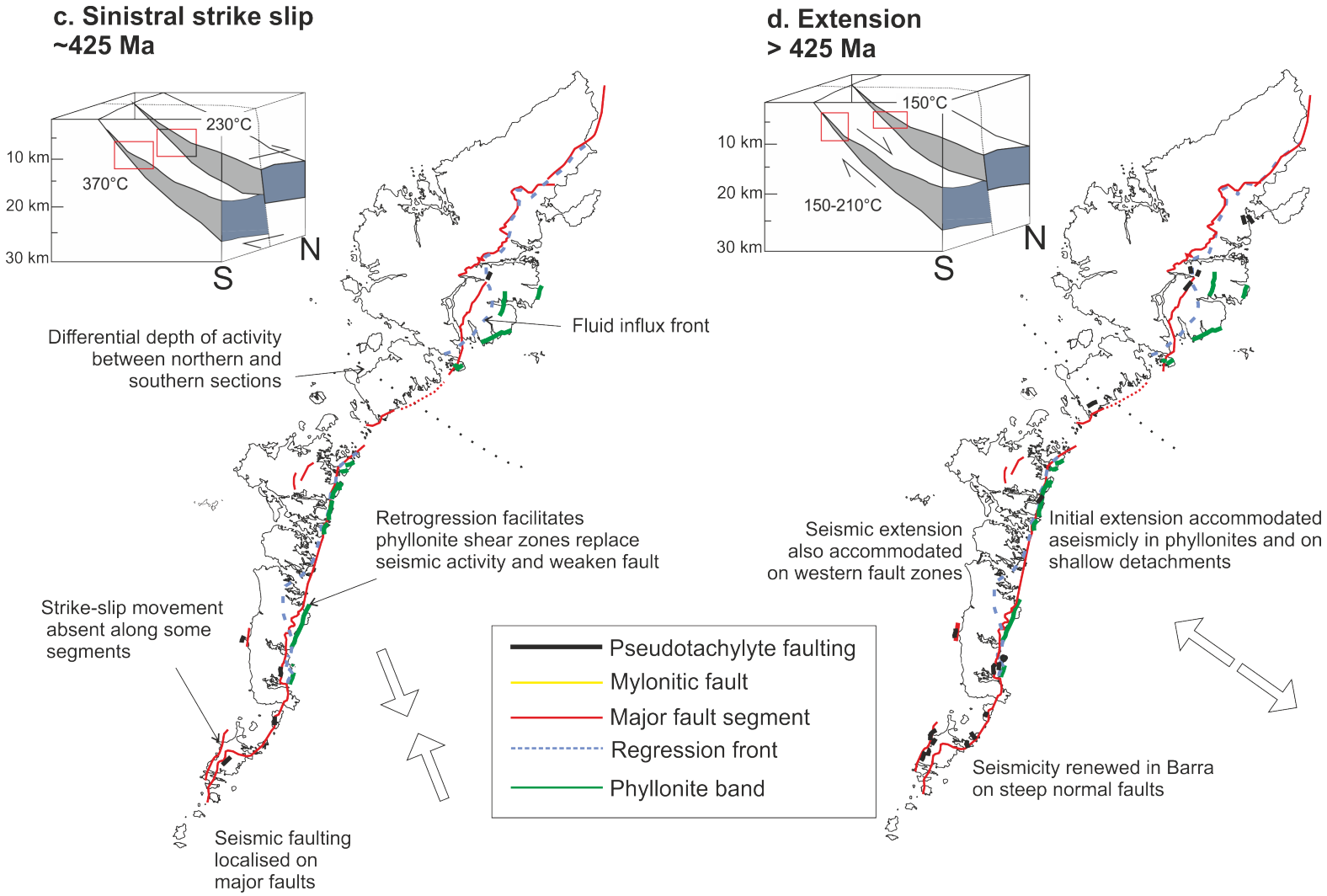

Figure 7.4: Seismic slip evolution of the OHFZ, part 2: c. Increasing obliquity of convergence favours left lateral strike-slip, initially as seismic reactivation on established fault segments. Influx of fluids and resultant greenschist facies regression allows phyllonite belts to form, weakening the fault zone, and seismicity ceases; d. extension of the orogen accommodated in the OHFZ by several mechanisms, including ductile deformation of phyllonites, detachment faulting, and seismic slip either at depth or on fault segments lacking phyllonites. Location of phyllonites and regression front from Imber (1998).

better regarded as representing 10-25° divergence from pure strike slip movement (Fig. 3.22). In general, the angle of misalignment is small. Slip on misaligned faults is usually considered in terms of reactivation of existing faults (Sibson (1985), Hill and Thatcher (1992)), whereas it is argued here to occur in new faulting in intact rock. In fact, the NE-dipping faults which seem to be most misaligned relative to the main OHFZ tend to show strike slip movement directed NW or SE, and could therefore be small scale tear or lateral ramp faults similar to the larger structures envisaged in NE Barra and South Uist at Aisgernis (Fig. 7.2). In addition, some may represent oblique slip, related to Caledonian oblique convergence at the regional scale (e.g. Holdsworth and Strachan (1991)).

Over time, the strength of a fault zone will generally weaken (Fig. 7.5) due to mechanical and mineralogical processes (Holdsworth (2004)). Fluid influx is one driver of such weakening (Imber et al. (1997)), and might be expected to prohibit pseudotachylyte generation if the frictional strength of the fault is low, or if aseismic fluid-assisted deformation mechanisms are favoured over seismic slip. A late Caledonian (Butler et al. (1995)) greenschist-facies regression zone on the eastern seaboard has a mappable front that flirts with the trace of the OHFZ (Fig. 7.4, Imber (1998)). Combined with fluid inclusion thermometry values from phyllonites at different regions along the strike of the OHFZ (Szulc et al. (2008)), this suggests that the regressive fluid influx, along with the development of phyllonites, was very variable along the OHFZ. Dry, high frictional faulting on adjacent fault segments would be possible if the stress could increase sufficiently. However, the phyllonites, where present, would be expected to be weaker (Imber (1998), Wallis et al. (2015)) so that some spatial stress heterogeneity would be required. On the segments with no phyllonite development, such as on Barra, brittle, seismic faulting could (and is observed to, MacInnes et al. (2000)) have continued into the strike slip and extensional phases (7.5c). Alternatively, the pseudotachylytes may have formed at slightly deeper levels during the same phase of faulting, where the fault zone was stronger.

7.3.3.3 Summary of OHFZ slip evolution

This section (7.3) has drawn on evidence from throughout the thesis to constrain and modify a model of pseudotachylyte generation and seismic evolution along the OHFZ. This model is presented in Figs. 7.3 and 7.4. To summerise these main lines of evidence, discussed in more detail above:

- the depth of pseudotachylyte faulting is generally 10-13 km, based on ambient temperatures of 230-400 °C from alteration assemblages, thermobarometry, quench textures and geomechanical models (sections 4.4.1.2,6.4.6) ;
- reverse, strike-slip and extensional kinimatics can be identified in OHFZ pseudotachylytes, with the dominant slip direction NW-SE. These can be interpreted as separate kinematic phases, with oblique reverse slip tranisitioning to strike slip dominant movement, and tie in with the published models of Caledonian OHFZ development (sections 3.7.4.3, 3.7.6);
- there remains little evidence that lithology exerted a major control on the location of pseudotachylyte along the OHFZ. Instead, the structure of the fault zone and the location of seismic activity may have done so (section 5.4.6;
- Pseudotachylyte in the OHFZ was often generated along small, high shear strength, high friction faults, suggesting that early in its development, and locally in later stages, the OHFZ remained a strong fault zone with frictional deformation mechanisms (section 6.4.6);
- Pseudotachylyte , and seismicity, was at least initially scattered on many linking and parallel fault segments across the OHFZ (section 6.4.7).

A revised model for the evolution of the OHFZ, tying in results from the literature with observations from this work, is outlined here (and see Figs. 7.3 and 7.4):

1. *NW directed ductile thrusting* initiates the OHFZ as a shear zone. Pseudotachylyte is intermittently produced and resheared, probably due to transient increases in strain rate from seismogenic activity nucleating at shallower crustal levels (Fig. 7.3a, Fig. 7.5a).

Timing: Grenvillian, ∼1100 Ma (Sherlock et al. (2009), Imber et al. (2002)) or earliest Caledonian at >450 Ma (MacInnes et al. (2000)). Depth:13-18 km (Fettes et al. (1992), White (1996a)); ambient temperature: 500±30°C (Szulc et al. (2008)).

2. *NW directed brittle thrusting* across entirety of OHFZ region, developing several parallel fault zone segments and on scattered faults, or small localised fault zones (e.g. Grimsay) in between. Seismic activity on reverse faults and on linkage structures (strike slip ramps and tears) produces pseudotachylyte with NW (or SE, in case of back thrusts) directed slip indicators (Fig. 7.3b, Fig. 7.5b). Localised extensional faulting, and dilational structures (e.g. pseudotachylyte breccias) may occur to accommodate space problems during fault block movements. Timing: Caledonian, ∼ 430 Ma (Kelley et al. (1994)). Depth: ∼ 10 km; ambient temperature: >230±20°C (Szulc et al. (2008)), >370±20°C (Osinski et al. (2001)).

3. *Left lateral strike slip* begins to dominate, possibly the cumulation of increasingly oblique collision. Initially, slip remains dry and brittle; top-to-NE slip observed on pseudotachylyte - generating seismic faults, including in the west coast fault zone, but not everywhere (e.g. NW Barra). Fluid influx into the OHFZ in the Uists, Harris and Lewis across fluid-present greenschist facies phyllonites/mylonites leads to localisation of deformation along this weakening fault strand, frictional-viscous flow type processes may prevail in phyllonites (Imber et al. (2001), Wallis et al. (2015)) and inhibit pseudotachylyte -producing seismicity along segments of the OHFZ (Fig. 7.4c, Fig. 7.5c). Timing: Late Caledonian. Depth: ∼10 km, ambient temperature of phyllonites 230±20°C (Szulc et al. (2008)) - 370±20°C (Osinski et al. (2001)).

4. *SE and NW directed extension* possibly related to relaxation and orogenic collapse (Coward (1983)). Initiates as low angle detachments and reactivation of phyllonite, progresses to steeper normal faults (Butler et al. (1995), MacInnes et al. (2000)). These steep faults may contain pseudotachylyte (MacInnes et al. (2000)), indicating seismicity during the extensional phase. However, seismicity may only have occurred in areas where the fluid influx was not present so that development of phyllonite was limited (e.g. Barra) (Fig. 7.4d, Fig. 7.5d). Timing: Later Caledonian (Imber et al. (2002), MacInnes et al.

(2000)). Ambient temperature of phylloinites and detachments: 150±20°C - 210±20°C (Szulc et al. (2008), Osinski et al. (2001)).

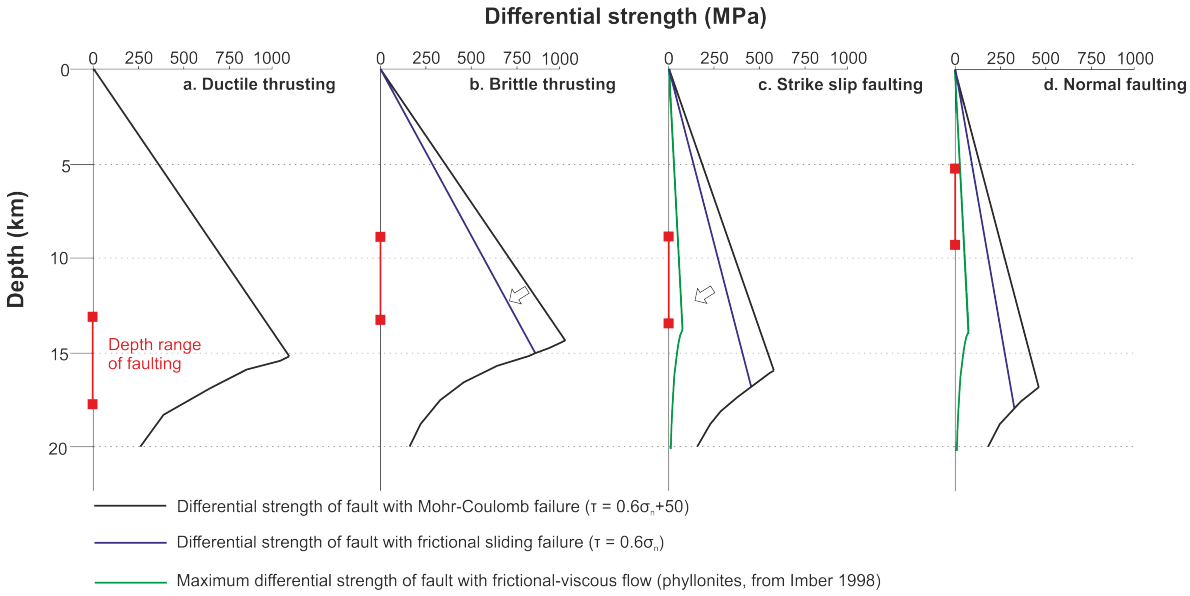

Figure 7.5: Model of strength evolution during faulting episodes on the OHFZ: a. Early ductile thrusting, $\sim$ 1.1 Ga, depth range from Fettes et al. (1992) and White (1996a); b. Caledonian brittle thrusting, initially forming from intact rock with localisation onto large faults with time, depth estimate from Osinski et al. (2001) and results from this study; c. Left-lateral strike slip faulting, later Caledonian, initially brittle seismogenic faulting but strength rapidly reduces with fluid infiltration and phyllonite formation, which then dominates fault movement, depth estimates encompass both Northern and Southern zones (Osinski et al. (2001), Szulc et al. (2008)); d. Late Caledonian extension, differing deformation mechanisms found on different fault segments, seismogenic slip seen on phyllonite-free segments and possibly at deeper crustal levels. Depth estimates encompass both Northern and Southern zones (Osinski et al. (2001), Szulc et al. (2008)). Fault strength is shown in differential stress. Phyllonite frictional-viscous flow for the OHFZ is taken from Imber (1998), and elsewhere dry quartz flow law at $10^{-15}s^{-1}$ (Jackson (2002)).

7.4 Application to fault zone models

7.4.1 Fault zone style of the OHFZ

The OHFZ was a large crustal fault, cutting down to near the Moho (Smythe et al. (1982)). It appears to have initiated primarily as a reverse fault in the ductile regime (Imber et al. (2002)) and to have reactivated predominantly as a thrust during the Caledonian orogeny (e.g. Sibson (1975), Imber et al. (2002), Szulc et al. (2008)). At the level of present day

exhumation, it cuts basement rock of the Laurentian continent, the Lewisian gneisses. This style of deformation is typical of 'thick-skinned' faulting. The location of the OHFZ will have been initially determined during its initiation in the Grenvillian (Imber et al. (2002)). The early, ductile shear zones are seen to form a loci for reactivation in the later brittle slip phase (Osinski et al. (2001)), so that the main structural trend of reactivated faults in the OHFZ is expected to be dependent on the unknown kinematic and stress fields of the initiation phase.

As a brittle fault zone, the parallel thrust segments, linkage structures and diffuse network of smaller faults are similar to continental thrust systems, as might be found today in Algeria (Lin et al. (2011)), Southern Californian thrust zones (e.g. Dickinson (2002)) or the Northern Appenine thrust belt (Cheloni et al. (2016)). The main contrast with plate boundary faults, particularly subduction zones, is the continuity of the main fault (Lin et al. (2011)). Although the OHFZ for some of its history has been part of a major collisional plate boundary, its position within the resultant orogen (Fig. 2.6), combined with the depth of faulting into regionally homogeneous, strong crust makes the continental fault style a good model.

7.4.2 Development of fault zones through time: strain localisation and strength evolution

The current, exhumed state of the OHFZ, as with all ancient fault zones, is a combined record of activity along the fault at different stages in time. Unlike sedimentary basins or even fold-and-thrust belts, it is not easy to track the development of fault structures, or of trends such as strain localisation, without high temporal and spatial resolution dating, which is not available for the OHFZ. Instead, general models of fault zone evolution are compared with the changes in seismic slip direction and location understood from the evidence provided by pseudotachylytes and collected in this work.

7.4.2.1 Fault growth and strain localisation

The scattered distribution of small pseudotachylyte faults around the Western Isles is attributed to early seismicity around an immature, diffuse fault zone (section 6.4.7), in agreement with Sibson (1975). With time, fault zones are expected to evolve via strain localisation, or the preferential slip and growth of larger faults, whilst smaller faults tend to become inactive (Nicol et al. (1997)). As a fault zone matures, it is therefore expected that slip transitions from a set of diffuse faults, through to a power-law distribution of fault sizes, and finally to localise on a few major structures (e.g. Gupta et al. (1998), Walsh et al. (2003), Hardacre and Cowie (2003)). Although most field studies and numerical models are based on normal faults, the same models should apply to reverse and strike slip systems (e.g. Davis et al. (2005)). In the OHFZ, the major localised structure is the mapped trace of the OHFZ in the east of the islands. Fault rocks such as the intensely fractured cataclasite-pseudotachylyte crush zones indicate repeated slip along some sections of the faults here, and whilst the now almost-continuous traceable strike for $\sim$ 200 km along the island chain suggests growth and linkage of the dominant structure relative to the extent of any local strands (Fig. 7.3 and 7.4). Therefore, considering the long-lived seismicity through varying slip modes portrayed by the pseudotachylytes, it is proposed that whilst early seismicity was indeed diffuse, as the Caledonian orogeny progressed, localisation onto the more discrete fault strands followed and led to repeating slip events on some strands of the mapped OHFZ (e.g. South Uist, section 5.4.6). By the time left-lateral strike slip became dominant, the mapped trace of the OHFZ, and the phyllonite zones that formed in its hangingwall, were the preferred loci for seismic and aseismic slip (Fig. 7.4).

Mechanisms for such localisation of slip along one or more large faults include the stress interactions between faults as they start to overlap and link (Gupta et al. (1998)), seismicity feedback mechanisms through Coulomb stress transfer between nearby, well orientated faults (Cowie (1998)), and progressive weakening of the fault plane so that it may slip under lower applied stress (Holdsworth (2004)). In the OHFZ, it is possible that all these have featured at some point in time. Weakening of the basal plane of the eastern OHFZ (Fig. 7.2) is partly

evidenced by the large damage zone of fracturing and fragmentation. Elsewhere, small faults may have been healed by the presence of pseudotachylyte and inhibited further slip on the same plane. Additionally, some segments of the mapped OHFZ have suffered the influx of fluids, resulting in the development of phyllonite fault zones, although these do not spatially extend westwards to the major basal fault plane (Butler et al. (1995)).

As slip localisation occurs, the distribution of fault sizes changes from a power-law to a non-power-law distribution, often with more large faults than expected (Scholz and Cowie (1990)). Because the size of the fault is proportional to earthquake magnitude (Scholz (2002)), a power-law distribution of fault sizes should equate to the Gutenberg-Richter distribution of earthquake magnitude (Walsh et al. (2003)). As the fault size distribution moves away from the power-law distribution towards strain-localised larger faults, so the distribution of earthquake magnitudes begins to approach the characteristic earthquake model, where earthquakes of similar magnitude repeat at regular time intervals along the same stretch of fault (Wesnousky (1994)). On the OHFZ, the population of pseudotachylyte bearing faults sampled for shear strength, stress drop and seismic moment (Chapter 6) display a Gutenberg-Richter distribution of $\log(N) = a - b(M_w)$, where N is the number of earthquakes greater than the given moment magnitude, and a and b are constants (Fig. 7.6). The constant b for the distribution of OHFZ and Gole Larghe earthquakes (Fig.7.6) is similar to the typical value found for small faults, 0.66 (Scholz (1997)). Although these earthquakes may have large time gaps between them, the power-law distribution should be maintained over several episodes of seismicity, providing the constants a and b remain consistent over time. Hence, it is implied by the frequency-magnitude relationship of the OHFZ (Fig. 7.6) that localisation onto large faults did not progress sufficiently for a characteristic style of seismicity to evolve. The repetition of pseudotachylyte generation along some sections of the mapped OHFZ (e.g. the crush zone on the basal fault at Bealach an Easain, South Uist, section 5.4.6), suggests that repetition of seismic slip did occur preferentially along some segments of the main fault. Unfortunately, the rather chaotic nature of pseudotachylyte veining in the crush zone at this site precludes measurements of displacement and hence estimates of magnitude, so that it remains unclear if the earthquakes were of similar size as would be expected if the characteristic earthquake

model was applicable.

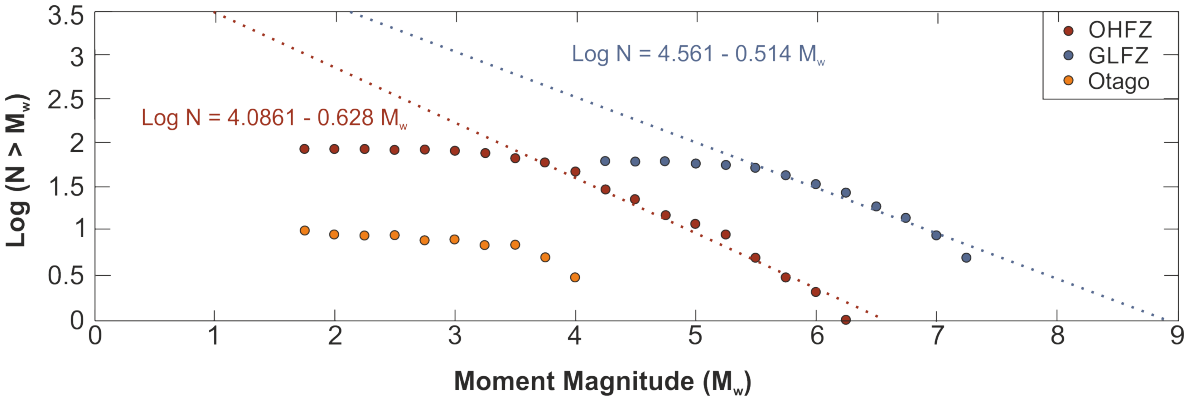

Figure 7.6: Cumulative frequencies of magnitudes calculated in section 6.3.3 for the OHFZ, the Gole Larghe Fault Zone (GLFZ) and the Otago normal faults. The data from the OHFZ and GLFZ are shown to satisfy the relationship Log(N) = a - b M_w, where N is the number of earthquakes greater than the magnitude. The data in the linear section of the Otago set are considered too few to draw meaningful conclusions.

7.4.2.2 Strength of the crust

The OHFZ pseudotachylytes discussed here are representative of behaviour near the base of the brittle crust, at around 10-13 km (section 6.4.6). The strength of the brittle upper crust increases with depth in accordance to the Mohr-Coulomb criterium (e.g. Burov and Watts (2006)). At the brittle-ductile transition zone, typically around 10 -15 km (Sibson (1977a)), the onset of crystal-plastic behaviour in minerals reduces the strength of the crust, following a flow law (Burov and Watts (2006), Hirth et al. (2001)). Pseudotachylytes on the OHFZ therefore reveal seismogenic behaviour from the base of the near the strongest part of the crust, where the brittle yield strength of the rock will be at its highest in dry rock (Fig. 7.5).

Fault zone strength models emphasise the weakness of the fault core relative to the intact surrounding rock (e.g. Holdsworth (2004)). Weakness is promoted by a number of factors, including: focused fluid flow (Johnson and McEvilly (1995)); weak fault rocks produced during previous slip episodes (Collettini et al. (2009)); reaction productions driven by fluids and deformation (Wintsch et al. (1995)); and mechanical weakening of the fault walls through damage (Faulkner et al. (2006)). These models are compatible with the concept of fault lo-

calisation by providing mechanisms by which the fault core may fail at a lower stress than the surrounding wallrock and also any adjacent stronger faults, even if the weak fault is misorientated relative to the principal stress directions (Faulkner et al. (2006)). This behaviour characterises the mature phase of many continental faults, such as the San Andreas (Chester et al. (1993)), Karakorum (Wallis et al. (2013)), or the southern Alpine Fault (Barth et al. (2013)). Behr and Platt (2014) suggest that the peak shear strength for many brittle faults is $\sim$ 50 MPa, because of the widespread occurrence of some mechanism of weakening in the brittle regime. However this analysis, which includes in its dataset the maximum shear strength of 48 MPa recorded from pseudotachylytes in the Gole Larghe fault zone (Di Toro et al. (2005b), see Fig. 6.4), indicates peak strengths far below the yield shear strength estimates for seismogenic faults on the OHFZ, the Otago normal faults and the Hatagawa fault zone (300 MPa, 350 MPa and 125 MPa respectively, Fig. 6.4). The study of Behr and Platt (2014) takes data predominantly from major fault zones, both active and ancient, that are well-developed and mature, and hence are weak compared to immature fault zones. This is an important distinction because immature fault zones display a more scattered distribution of seismicity that is difficult to predict, as shown by the location and magnitudes of sesimicity indicted by pseudotachylyte in the OHFZ. Modelling of seismic activity in similar fault zones needs accurate strength estimates. Behr and Platt (2014) do infer that weakening mechanisms may be discontinuous with depth, and that an increase in fault strength may therefore occur near the brittle-ductile transition, allowing earthquake nucleation below weak, creeping faults. This behavior may apply to segments of the OHFZ during later, fluid-present strike slip and extensional detachment activity (Table 7.3.3.3), allowing left-lateral strike slip seismicity, recorded in some pseudotachylytes (section 3.7.4.3), to occur under a segment of fault weakened by phyllonitisation (Fig. 7.5).

In summary, fault strength models need to account for the evolution and maturity of fault zones with time if they are to be generally applied to fault zones worldwide (Fig. 7.5). The OHFZ records the development of various faulting mechanisms through time, including the strong, dispersed early seismicity recorded by many of the pseudotachylytes, through to weak phyllonite zone development and eventual localisation on the main OHFZ plane.

7.4.3 Fault zones within multiple lithologies

Micro-scale frictional behavior of faults between two lithologies has been shown in this study (section 5.3.1.1) to differ to the behaviour of faults contained entirely within one rock type, so that multi-lithology behaviour is not a simple average of the two individual behaviours of the two rock types. This is partly due to the evolution of the slip zone geometry (i.e. the roughness of the fault wall, section 5.3.1.4) and, during slip on pseudotachylyte producing faults, to the viscosity and clast content of the melt produced (section 5.3.2.1). These factors are dominantly controlled by the mineralogy of the wall rock lithologies - both the fraction of minerals present, and their orientation and distribution within the rock. Roughness is shown to be dominated by grain-size wavelengths (Figs. 5.7, 5.9) and therefore is difficult to upscale to the field and above. Such observations support the findings of Brodsky et al. (2016) that roughness has a scale dependence.

The main OHFZ strands where lithological contrast exists, between the Corodale pyroxene gneiss and the quartzofeldspathic gneiss in South Uist, is the location of repeated slip (section 7.4.2.1), creating a prominent crush zone near the basal fault consisting of cataclasite, pseudotachylyte and fragmented rock. Similar crush zones exist elsewhere (e.g. North Uist) but lack equivalent volumes of pseudotachylyte. Seismic activity, or the feasibility of frictional melting, might be concentrated along the South Uist segment because of the lithological contrast around the fault zone. Seismic slip along boundaries between contrasting materials, or bi-material interfaces, are known to exhibit different behaviour to those in homogeneous rock. Bi-material interfaces are more likely to produce uni-directional ruptures (McGuire et al. (2002)) and to experience supershear rupture velocities (velocities >shear wave speed) in one direction (e.g. Xia et al. (2005), Shi and Ben-Zion (2006), Langer et al. (2012)) because of asymmetry in elastic properties between the wallrock along the fault. Felsic gneisses and pyroxene granulites analogous the the Lewisian quartzofeldspathic and Corodale gneisses differ in P-wave velocity by around 10-15%, with a pyroxene granulite gneiss at 0.4 GPa and 300°C exhibiting an average P-wave velocity of 6.9 km s^{-1} (Kanao and Ishikawa (2004)). Ex-

periments on analogue materials have shown bi-material rupture characteristics with a ∼3% difference in P-wave velocity (Xia et al. (2005)), so it is possible that such behaviour might be observed in this section of the OHFZ with the Corodale gneiss. The configuration of the faster Corodale gneiss in the hangingwall, assuming a simple reverse movement, means that preferred rupture propagation, faster slip velocities and rupture propagation speeds would be found on propagation in the down-dip (SE) direction, as would larger strength drops and a lesser number of aftershocks (Rubin and Ampuero (2007), Ma and Beroza (2008)). In addition, in the case of dominant rupture propagation downdip to the SE, the tensile damage may be overwhelmingly found in the higher wavespeed fault wall (Rubin and Ampuero (2007)), in this case the Corodale gneiss. There is, in fact, more faulting and fracturing observed in the Corodale hangingwall relative to the quartzofeldspathic footwall, which would support this model, similar to the observations on faults in California and Turkey (Dor et al. (2006) .

7.5 The Outer Hebrides Fault Zone and orogenic models

7.5.1 The OHFZ as an orogenic fault

The Caledonian slip episodes on the OHFZ occured not in isolation, but as part of the wider orogen recorded on the Scottish mainland and across the extent of the Caledonides in Scandinavia, Greenland and North America (Fig. 7.7). The OHFZ forms a basement fault in the foreland to the retro wedge of the orogen (Fig. 7.7, Streule et al. (2010)). Unlike, for example, the Himalayan orogen, the Caledonian had a number of thrusts such as the OHFZ in the retro-wedge as well as in the pro-wedge, which is best developed in Scandinavia. Streule et al. (2010) attribute this difference to the availability of pre-existent fault structures for reactivation, of which the OHFZ represents one example.

Without good records of overall displacement it is difficult to evaluate the significance of movement on the OHFZ relative to other major structures, both across the entire orogen and also within the section of the Laurentian margin that NW Scotland occupied (Fig. 7.7), somewhat on the outskirts of the orogen (Streule et al. (2010)). The Caledonian Moine thrust zone in mainland NW Scotland is thought to have taken up to 100 km of reverse movement (Butler

(2010)) and the Great Glen Fault around 200 km of left lateral strike slip offset (Dewey and Strachan (2003)), as examples of the major regional faults in this region (Fig. 7.7). However, these were not necessarily active together (Streule et al. (2010)). In contrast, brittle displacement on the OHFZ is estimated at 2-8 km (Coward (1969), Francis and Sibson (1973)) although there are unconstrained assumptions associated with both studies (outlined in section 2.2.3). Recently, based on the recognition of the pre-Caledonian history of the OHFZ (e.g. Imber et al. (2002), Sherlock et al. (2009)), it has been suggested that the Caledonian movement on the fault was fairly insignificant in the context of the orogen (Streule et al. (2010)). However, the pseudotachylyte along the OHFZ is evidence that Caledonian seismicity of the fault was frequent and occasionally sizable, indicating magnitudes up to M_w 6.2 (Fig 6.8). The OHFZ appears to have been the major fault accommodating brittle basement shortening preserved within the Scottish Caledonides (Fig. 7.7). Hence, whilst the absolute displacement may have been relatively low when compared to the Moine and thrusts in the pro-wedge (Fig. 7.7), it would nevertheless have been significant in the context of accommodating convergence.

7.5.2 Collisional history recorded in OHFZ pseudotachylytes

7.5.2.1 Oblique convergence and strain partitioning

Most collisional plate boundaries worldwide involve a component of oblique convergence, rather than true orogen-normal slip. Examples of major active plate boundaries known to have oblique slip include the Alpine Fault, NZ (e.g. Norris and Cooper (2001)), the Nankai subduction zone (e.g. Martin et al. (2010)), the San Andreas (e.g. Avé Lallemant (1997)), the Philippines trough (e.g. Pinet and Cobbold (1992)), the Sumatran Arc (e.g. McCaffrey (1991)) and the Himalaya (e.g. Jouanne et al. (1999)). Evidence for oblique convergence is also present in parts of ancient collision zones, including the European Alps (e.g. Prosser (1998)) and the Caledonides (e.g. Holdsworth and Strachan (1991)). As Jones et al. (2005) state, "relative motion that is oblique to the plate margins is an inevitable consequence of plate kinematics on a sphere", so that in any collisional zone it seems reasonable to assume that some aspect of oblique slip is present.

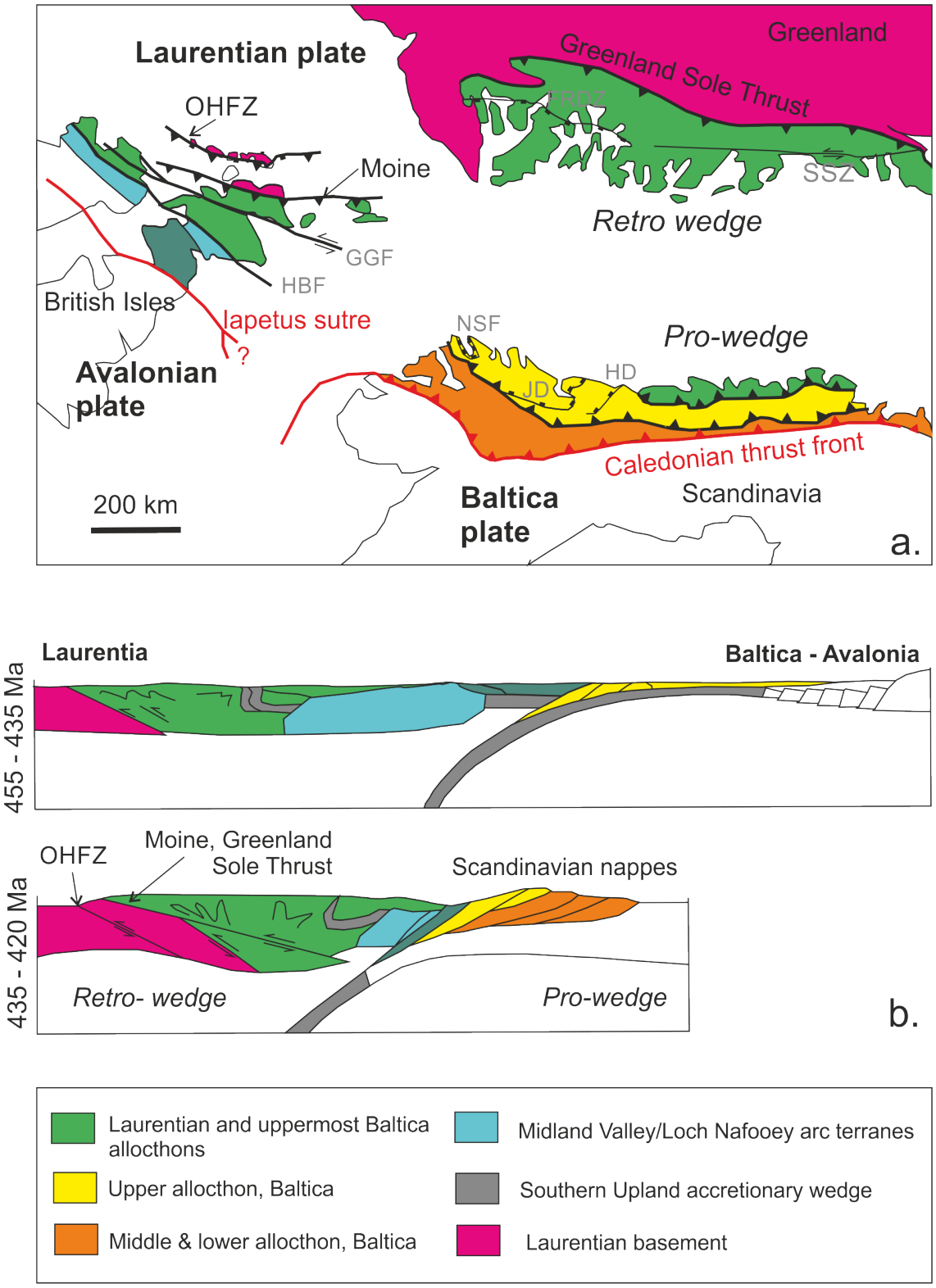

Figure 7.7: Caledonian plate configuration highlighting location and role of OHFZ, modified after Streule et al. (2010). a. Pre-Atlantic plate configuration, showing location of major thrusts, in doubly verging pro-wedge and retro-wedge geometry, and also major strike slip faults and extensional detachments. GGF = Great Glen Fault, HBF = Highland Boundary Fault, SSZ = Storstrommen Shear Zone, FRDZ = Fjord Region Detachment Zone, NSD = Nordfjord-Sognn Detachment, JD = Jotn Detachment, KD = Kollstraumen Detachment; b. schematic cross sections showing Scandian phase of Caledonian orogen (455-420 Ma), the last phase of which triggers movement on the OHFZ in the Laurentian basement.

The mechanics of uptake of oblique slip across collisional zones varies, both across different fault zones and in time and space across an individual fault zone. Strain partitioning is often present to some extent. In subduction zones, a large-displacement strike-slip fault may sit behind the subduction megathrust, so that strike slip and dip slip movement occur on different planes. Examples include the Median Tectonic Line behind the Nankai trough (Kubota and Takeshita (2008)), the Phillipines Fault behind the Phillipines Trough (Pinet and Cobbold (1992)), and the Great Sumatran Fault and the Mentawai Fault behind the Sumatran trough (Tikoff and Teyssier (1994)). The partitioning of slip between megathrusts and associated strike slip components is controlled by the changing obliquity of relative plate movement, which may change along strike. Complete strain partitioning in this style is likely easier to produce if pre-existent weak structures around the edges of the oblique fault zone are susceptible to reactivation as a strike slip fault (e.g. Jones and Tanner (1995)). Conversely, an absence of such structures may lead to other distributions of strain partitioning. For example, the Clarence Fault, New Zealand, which forms part of the Malborough fault system between the Alpine Fault and the Hikurangi subduction zone, is a transpressive fault exhibiting strike-slip displacement at its surface trace (Nicol and Van Dissen (2002)). Despite topographic uplift in the hangingwall, no large displacement reverse faults are observed at the surface to accommodate the compressional component; rather, it is argued (Nicol and Van Dissen (2002)) that oblique convergence is taken up by oblique slip at depth on the Clarence fault, with partitioning occurring at shallower levels between small, distributed reverse slip faults in the hanging wall and strike slip on the main fault. Thus, partitioning is variable with changing depth along a single major fault. In contrast to this scenario, Holdsworth and Strachan (1991) concluded that mid-crustal partitioning with separate strike slip and reverse faults can still occur at amphibolite facies depths, as observed in an exhumed Caledonide fault zone in NE Greenland.

The changing relative movement vectors of plate movement can lead to temporal changes in slip rate and slip direction across a collisional fault zone. In the Italian Alps, the North Giudicarie Line, part of the Insubric Line, shows overprinting along the same fault section

from ductile oblique reverse/dextral strike slip movement into brittle, sightly transpressive left lateral strike slip (Prosser (1998)). Both these movement phases are localised to the North Giudicarie Line along its northern section; however, further south left-lateral slip along the fault has been much less because the movement has instead been accommodated by smaller, diffusely scattered faults (Prosser (1998)).

The Outer Hebrides Fault Zone can be considered to be part of the uptake of an oblique slip vector, based on the common occurrence of oblique slip recognised in global fault zones. Indeed the Caledonian orogeny, during which most phases of pseudotachylyte production have been concluded to belong to have formed (section 7.3.3.3), is widely thought to involve oblique left lateral convergence throughout the phases of collision (Dewey and Strachan (2003)). This global scale collision vector is consistent with the left-lateral oblique thrusting and left-lateral strike slip fault movements recorded in the OHFZ pseudotachylytes (sections 4.6, 4.7), and with the wider kinematics of the Caledonian OHFZ proposed elsewhere (Imber et al. (2002), MacInnes et al. (2000)). Structures recording this oblique Caledonian collision are present as strain partitioning faults in Greenland (e.g. Holdsworth and Strachan (1991)) and as major sinistral strike slip faults, including the Great Glen Fault, Scotland (Dewey and Strachan (2003)).

Left lateral obliquity is consistent with the slip directions of pseudotachylyte bearing faults in the Western Isles, which record dominantly reverse, oblique reverse-left lateral and left lateral strike slip movement, as well as extension (sections 3.6.1, 3.7.4). OHFZ fault movement in the Caledonian is thought to have progressed from reverse thrusting into strike slip movement towards the late stages of the Caledonian orogney (Butler et al. (1995), Imber et al. (1997)). Although the pseudotachylytes are not dated with sufficient resolution to test whether the strike slip and reverse slip seismicity were distinct in time, the distribution of the variously slipping faults provide some clues. NE-dipping faults, which may have significant elements of either left or right lateral strike slip, are considered to develop as tear faults concurrent with the thrust system (section 7.3.3.2, Fig. 7.2). Additional left-lateral strike slip faults plot dominantly along the mapped trace of the OHFZ in contrast to the reverse and reverse-oblique

slip pseudotachylyte faults that are observed along the trace of the OHFZ, along parallel fault segments and also in scattered off-fault locations (Fig. 7.3, 7.4). Considering pseudotachylyte faults only, this distinction suggests that purely sinistral strike slip may have developed along the trace of the OHFZ, which would need to be an already localised, relatively weak structure. However, continued convergence may have been taken up by continuing reverse or reverse-dominated oblique slip dispersed away from the OHFZ trace in the east; this model is similar to the Clarence Fault (Nicol and Van Dissen (2002)) and contributes to the idea that where slip partitioning occurs, the strike slip component tends to favour large, weak, pre-existing structures (Jones and Tanner (1995)). The switch to strike-slip motion along the OHFZ trace requires a change in convergence angle to increasingly orogen-parallel movement, which is inferred to have occurred in the Caledonian at around 425 Ma (Dewey and Strachan (2003)). This post- dates (or is synchronous within error) a thrust pseudotachylyte in the OHFZ dated at 430±6 Ma (Kelley et al. (1994)). Brittle, seismogenic strike-slip and continued thrusting was superceded along some segments of the OHFZ by the development of strike-slip phyllonites facilitated by fluid influx (Butler et al. (1995)). Despite apparent localisation of seismogenic strike-slip pseudotachylytes along the OHFZ trace, the phyllonitisation occurred in the hangingwall adjacent to the brittle OHFZ, presumably controlled by the limit to fluid influx. Frictional-viscous flow is one deformation mechanism that could be triggered in phyllonites (Imber et al. (2001), Wallis et al. (2015)) and provides a weaker slip mechanism than frictional fault slip (Fig. 7.5), making concurrent seismicity on stronger faults difficult to explain. Slip partitioning in the OHFZ is hence envisaged to have progressively developed through the Caledonian convergence.

7.5.2.2 Other controls on the distribution of orogenic seismicity

The distribution of seismic activity within an active orogen is not purely influenced by the static, farfield stresses of convergence, but also by the dynamic changes invoked by the occurrence of an earthquake on a component fault (Harris (1998)). These effects may include aftershock distribution and/or Coulomb stress transfer. Coulomb stress changes are caused by the coseismic failure of an adjacent fault, the postseismic stress changes along an adjacent

fault, or by stress changes caused by the passage of seismic waves, although this latter tends to be a very transient change (Freed (2004)). Changes in the static stress field can influence the spatial distribution of aftershocks following a main shock, and can trigger events that occur years later (Freed (2004)). Whilst Coulomb stress changes are most commonly used to explain failure on faults within the same fault zone, they may also directly or indirectly trigger seismicity thousands of kilometres away (Hill et al. (1993)). Local Coulomb stress change triggered events are particularly relevant to diffuse, continental-style fault zones with complex fault zone structure, several fault segments and less predictable seismicity with lower strain rates (Cheloni et al. (2016), Verdecchia and Carena (2016)). In contrast, high-slip fault zones, often at plate boundaries, tend to have shorter repeat times and possibly more characteristic earthquakes (Verdecchia and Carena (2016)). The fault segments identified in addition to the mapped trace of the OHFZ (i.e. the one or more faults on the west coast of Barra and South Uist, and the strand suggested to lie east of Barra (Fig. 7.2) are separated by <5 km distance perpendicular to the fault dips. Although the spatial area influenced by Coulomb stress changes depends on the mainshock magnitude and fault geometry, this distance is within that expected to be affected by earthquakes of moment magnitude ∼6 M_W to the extent that simultaneous slip can be triggered within this distance, and greater (Hicks and Rietbrock (2015)).

Coulomb failure stress changes are typically small, in the region of <0.5 MPa (Stein (1999)). Nevertheless, Coulomb stress increases may account for a large proportion of recorded ruptures in a given time period along a given stretch of fault zone (Verdecchia and Carena (2016)), indicating that many faults exist in a near-critically stressed state (Townend and Zoback (2000)). Given that many OHFZ faults have been shown to be strong (section 6.3.2), that the stress needed to fail them (∼ 300 MPa) is higher than the lithostatic stress at a depth of 10 km (section 6.3.2), and yet the applied shear stress is high enough that the strongest faults do fail, it seems likely during tectonic activity that many OHFZ faults were near-critically stressed. The effect of Coulomb stress changes include the increase of shear stress in regions away from the fault, as well as at the fault tips, which is considered to cause aftershocks to form on off-fault failure planes (Das and Scholz (1981)), rather than on the

mainshock fault. These aftershocks may not be on the same orientation of fault or in the same slip mode as the mainshock, so that a suite of normal, strike slip and reverse failures may form in a single seismic episode (Dempsey et al. (2014)). If calculated moment magnitudes on the OHFZ are mapped out (Fig. 6.7, section 6.3.3), a spectrum of magnitudes is observed in which the largest events (up to M_W 6.3) are spatially surrounded by smaller magnitude failures across the range. This behaviour suggests that a local suite of pseudotachylytes could feasibly represent a set of aftershocks to a larger mainshock, forming a complex set of orientated faults and slip patterns due to the pattern of Coulomb stress transfer. Again, a series of aftershocks is expected to show the Gutenberg-Richter distribution, which the OHFZ pseudotachylytes do in fact show (Fig. 7.6).

This argument for control of seismic feedback mechanisms on distribution of seismicity contradicts the earlier discussion on orogen-scale changes in plate convergence and stress fields (section 7.5.2), which mainly relies on temporal changes to produce faults of differing slip senses and orientations. It is likely that the explanation for the OHFZ's scattered and complex array of seismic, pseudotachylyte generating faults inevitably lies somewhere in between, the two models. In other words, the OHFZ represents a mix of long-term tectonic forcing and relatively short term developments driven by bouts of seismic activity, especially as the fault zone developed and more fault surfaces were formed and available for interaction and reactivation.

Chapter 8

Conclusions and Further Work

8.1 Conclusions

- Pseudotachylyte bearing faults in the OHFZ are variously oriented and often display some component of oblique slip. However, three main slip senses can be classified - reverse (top-to-NW), left lateral strike slip (top-to-NE) and extensional (top-down-to-SE). These are in agreement with slip indicators from other fault rocks across the OHFZ. The oblique slip of many faults and the transition from thrusting to strike slip are consistent with models of oblique convergence.

- Techniques that constrain the slip vector of pseudotachylyte faults, either from field measurements using off-fault tensile cracks, or from analysis such as AMS, are useful for reconstructing the slip history of fault zones and can be used to recreate focal mechanisms for ancient fault zones.

- Cataclasite can be produced synchronously with pseudotachylyte melt. The coupled thermal and mechanical processes that operate during seismic slip vary in dominance through the slip period as well as spatialy across the vein, so that measurements based on relative clast and melt fractions can be very variable within a single pseudotachylyte vein.

- Seismic faulting, producing pseudotachylyte, took place at 10 km depth or greater during Caledonian thrusting and may have shallowed slightly during later movement. Earlier

(probably Grenvillian), deeper pseudotachylyte generation is also recorded in the OHFZ.

- The OHFZ was a seismogenic fault over several periods of reactivation. Initially this was due to immaturity during the early stages of thrusting, when the shear strength of the faults was 300 MPa and above. Later, the variable development of weakening mechanisms such as fluid presence and phyllonitisation between fault segments meant that later normal movement was still locally seismic and produce pseudotachylyte along several fault segments, even whilst the fault zone as a whole was weak.

- The weakening behavior, and stress drop, during slip is influenced by the composition of the wall rocks - firstly because the composition and viscosity of the melt produced influences the shear strength of the fault during slip, and secondly because the mineralogy and fabric of the rock influences the geometry of the slip zone margins, the evolution of asperities and the contact area across the slipping fault.

- When two different lithologies are juxtaposed, as in many large thrust faults, the composition of the melt will be dominated by minerals that preferentially melt. The fault walls will therefore evolve differently to each other dependent on the relative thermal and mechanical strengths of their mineralogies. However, the development in roughness of a fault wall is changed by the type of lithology in the opposing wall.

- Static stress drops derived from pseudotachylyte field measurements are within the range recorded by seismic observations for similarly sized earthquakes. In the OHFZ, pseudotachylytes record earthquakes from magnitudes of 1.9-6.2 M_w and static stress drops of between 1.46-8.77 MPa. The range of dynamic stress drops is much larger, 5.2-592.0 MPa. These values likely reflect localised maxima on the fault plane distribution, but some uncertainty remains from the assumptions and errors introduced in the field and in the scaling relationships used to calculate these values.

- Dynamic stress drops increase with progressive displacement (and hence moment magnitude) until a threshold value, the slip-weakening distance. In the OHFZ, this occurs at $\sim$ 0.1m, but is seen to vary for other fault zones.

8.2 Future Work

8.2.1 Slip direction

Three dimensional measurements of fault slip are valuable for reconstructing slip histories and assessing the reactivation of different fault segments, but are often difficult to obtain in the field. This thesis has presented three techniques that can produce three-dimensional results; two models of injection vein formation, and the technique of Anisotropy of Magnetic Susceptibility (AMS). So far, AMS has only been conducted on one sample from the OHFZ (Ferré et al. (2016), section 3.6.2.3). However, recent improvements in the application of AMS to pseudotachylytes makes such analysis relatively quick and reliable (Ferré et al. (2016)). AMS could therefore be applied much more widely to pseudotachylyte bearing faults within the OHFZ in order to support the results gained from the existing data. In addition, AMS could be used to study the flow of the pseudotachylyte within the fault plane. Such a study could refine understanding of how injection veins are supplied with melt from the generation plane, and whether this supports injection fractures being produced at the propagating rupture tip (Griffith et al. (2009b), Ngo et al. (2012)), a test of the model that field derived slip vectors are provided from in the current study.

8.2.2 Thermobarometry

Greater constraints could be provided to test the validity of temperatures and pressures produced by amphibole-plagioclase geothermometry. Firstly, applying the technique to more pseudotachylyte samples would allow better constraint on the range of valid values for temperature and pressure, as consistency would be expected between some samples. Secondly, minimum temperatures could be gained from analysing the composition of the alteration assemblages. The best candidate would be chlorite thermometry, as it commonly occurs as alteration of the vein matrix, or in fractures cutting through the pseudotachylyte veins. A number of chlorite thermometry calibrations exist (e.g. Kranidiotis and MacLean (1987), Cathelineau (1988), Zang and Fyfe (1995)) and the choice would be dependent on the com-

position of the chlorite (Klein and Koppe (2000)).

8.2.3 Controls on roughness during slip

In common with previous studies on experimental sample roughness (Hirose and Shimamoto (2003), Nielsen et al. (2010b)), the analysis here (section 5.3.1.4) relies on two dimensional sectioning. Field analysis of roughness, meanwhile, may utilise three dimensional techniques such as LiDAR on exposed fault planes (e.g. Brodsky et al. (2011), Bistacchi et al. (2011)) and analyse the directional anisotropy of fault roughness (Lee and Bruhn (1996)). Applying an equivalent three dimensional approach to experimental slip surfaces would allow interpretation of variance of roughness with displacement and slip velocity (if they vary across the sample, as in rotary shear experiments) as well as with the fabric of the rock. Micro-X-ray computed technology (micro-CT scanning) would be appropriate for this scale and has been used to image and analyse slip surfaces down to resolutions of $\sim$36 μm (Resor et al. (2013)).

The fabric of the wallrock may have an effect on the roughness of the slip surface, as indicated by the use of cleavage planes as planes of weakness for removing material (e.g. Fig. 5.8d). The crystal orientation will control the relative orientation of the cleavage to the slip direction, and hence the resolved shear stress, which may contribute to the mechanical wear resolved onto cleavage planes rather than other features in the wall rock. The use of EBSD (electron backscatter diffraction) to analyse three dimensional orientation of wallrock minerals relative to the slip surface would provide constraints on how much the orientation, and preferred orientation of minerals across the entire sample, contributed to the significance of the cleavage-scale of roughness. This concept could be extended by further experiments on rock samples with various strength of fabrics or mineral alignments, and with those fabrics cut in various orientations relative to the slip surface, in order to investigate the sample-wide effects of crystal preferred orientations on the geometry of the fault surface and hence on the slip behaviour during faulting.

Mylonite, as a rock type with strong fabric that could be used for such an experimen-

tal investigation, is a pseudotachylyte hosting lithology in the OHFZ. However, a strongly deformed rock would open another line of investigation, that of the impact of pre-existent damage on the slip behaviour. Such a study would probably have to focus on ductile deformation, or healed fractures, if using rotary shear apparatus due to the need for competent samples. At temperatures above 500°C, dislocations could influence the nucleation of cracks, whilst deformation lamellae and kink bands could provide stress concentrations at lower temperatures (Kranz (1983)). At high coseismic fault plane temperatures, a number of crystalline deformation structures could promote brittle damage and alter the geometry of the slip plane, as well as reduce the overall strength of the rock, but the effect of these features on frictional melting has not been widely studied experimentally.

8.2.4 Strength of pseudotachylyte bearing fault zones

Pseudotachylyte -bearing fault zones are proposed to be strong (Sibson (1975)), yet may also form fault zones with pre-existent fault rocks and damage (e.g. Di Toro et al. (2005b)). In Chapter 6 of this thesis, a comparison of the pre- and coseismic strengths of different fault zones was undertaken, but currently the relevant data are only available from a few fault zones worldwide. It would therefore be useful to extend the range of field data from pseudotachylyte bearing fault zones at various depths and in differing lithologies, to better constrain how the initial strength of the fault zone may control the coseismic slip behavior, and to determine whether weaker faults commonly produce frictional melts.

Appendix A

Appendix: Characteristics of pseudotachylyte samples used in compositional analysis

Table A.1: Sampling location and fault characteristics (where applicable) of pseudotachylyte samples used for qualitative and quantitative compositional analysis

Sample #	**Latitude**	**Longitude**	**Location**	**Pseudotachylyte type**	**Moment sense**	**Fault type**	**Indicator**
B7	56.9916	-7.3853	Bruairnis, Barra	Fault vein	Uncertain	Uncertain	
B10	56.9773	-7.4742	Heabhal, Barra	Fault vein	Top-to-NW	Reverse	Preferred clast orientation, sigmoidal clast shape
SU2	57.2403	-7.4506	Aird a Mhuile, South Uist	Fault vein	Top-to-W	Reverse	AMS, S-C shears in cataclasic margin
SU3	57.2392	-7.4523	Aird a Mhuile, South Uist	Breccia	Top-to-SW (?)	Reverse (?)	Cataclasite in wall (presumed to predate PST)
SU4	57.1833	-7.3697	Aisgernis, South Uist	Breccia	Top-to-NE	Reverse	Preferred clast orientation
SU9	57.1652	-7.2827	Bealach an Easain, South Uist	Injection veins	NA	NA	
NU15	57.5486	-7.1680	Burabhal, North Uist	Injection veins	NA	NA	
G1	57.4867	-7.2377	Grimsay	Fault vein	Top-to-NW followed by top-to-SE	Reverse followed by normal	Offset across veins
HA10	57.7600	-6.9670	Beinn na h-Aire, South Harris	Injection veins from breccia	NA	NA	
SH9	58.0599	-6.5761	Ceann Shiphoirt , Lewis	Fault vein	Uncertain	Uncertain	

Table A.2: Microstructural and compositional characteristics of pseudotachylyte samples used for qualitative and quantitative compositional analysis. Key to mineral abbreviations: Qtz = quartz, plag = plagioclase, Kspar = potassium feldspar, hbl = hornblende, act = actinolite, bt = biotite, ep = epidote, chl = chlorite, pump = pumpellyite, px = pyroxene, py = pyrope, ti = titanite, ap = apatite, FeO = undifferentiated iron oxide.

Sample #	**PST features/texture**	**PST composition**	**Host composition**
B7	Spherulitic in part, granular elsewhere	Plag - hbl - FeO	Plag - qtz - K spar - bt - epidote gneiss
B10		Plag - hbl - bt	Plag - qtz - K spar - hbl - bt gneiss
SU2	Well developed microlites and very fine intersititial crystallisation	Plag - hbl - bt - FeO	Plag - qtz - K spar - hbl - bt - ti gneiss
SU3	Breccia matrix, high clast content (cataclasite) in sections	Plag - hbl - FeO - ep - pump	Plag - qtz - bt - K spar - hbl - chl gneiss
SU4	Well developed microlites	Plag - hbl - bt - FeO	Plag - qtz - K spar - bt - zir gneiss
SU9	Clast rich in part, patchy alteration of PST matrix	Plag - chl - ep	Plag - qtz - hbl - bt - Kspar - zir - ap - chl gneiss
NU15	Clast content variable	Plag - hbl	Plag - qtz - bt - px - ep gneiss
G1	Spherulitic in part	Plg - hbl- FeO	Plag - qtz -K spar - hbl - bt gneiss
HA10	Epidote-actinolite alteration of PST	Plag - py - ep - act	Plag - hbl - qtz - chl - ep - ti anorthosite
SH9		Plag - hbl - FeO	Mylonitic felsic gneiss, pre-existent cataclasite

Bibliography

Abercrombie, R. E. (2014). Stress drops of repeating earthquakes on the San Andreas Fault at Parkfield. *Geophysical Research Letters*, 41(24):8784–8791.

Abercrombie, R. E. and Rice, J. R. (2005). Can observations of earthquake scaling constrain slip weakening? *Geophysical Journal International*, 162(2):406–424.

Aki, K. (1972). Earthquake mechanism. *Tectonophysics*, 13(14):423–446.

Allen, J. L. (2005). A multi-kilometer pseudotachylyte system as an exhumed record of earthquake rupture geometry at hypocentral depths (Colorado, USA). *Tectonophysics*, 402(14):37–54.

Allen, J. L., O'Hara, K. D., and Moecher, D. P. (2002). Structural geometry and thermal history of pseudotachylyte from the Homestake shear zone, Sawatch Range, Colorado. *Field Guides*, 3:17–32.

Altenberger, U., Prosser, G., Ruggiero, M., and Günter, C. (2011). Microstructure and petrology of a Calabrian garnet-bearing pseudotachylyte a link to lower-crustal seismicity. *Geological Society, London, Special Publications*, 359(1):153–168.

Amor, K., Hesselbo, S. P., Porcelli, D., Thackrey, S., and Parnell, J. (2008). A Precambrian proximal ejecta blanket from Scotland. *Geology*, 36(4):303–306.

Andersen, T. B. and Austrheim, H. (2006). Fossil earthquakes recorded by pseudotachylytes in mantle peridotite from the Alpine subduction complex of Corsica. *Earth and Planetary Science Letters*, 242(12):58–72.

Anderson, E. M. (1942). *The dynamics of faulting.* Oliver and Boyd, London.

Anderson, J. L. and Smith, D. R. (1995). The effects of temperature and fO2 on the Al-in-hornblende barometer. *American Mineralogist*, 80(5-6):549–559.

Austrheim, H. and Andersen, T. B. (2004). Pseudotachylytes from Corsica: fossil earthquakes from a subduction complex. *Terra Nova*, 16(4):193–197.

Austrheim, H. and Boundy, T. M. (1994). Pseudotachylytes Generated During Seismic Faulting and Eclogitization of the Deep Crust. *Science*, 265(5168):82–83.

Avé Lallemant, H. G. (1997). Transpression, displacement partitioning, and exhumation in the eastern Caribbean / South American plate boundary zone. *Tectonics*, 16(2):272–289.

Avouac, J.-P. and Tapponnier, P. (1993). Kinematic model of active deformation in central Asia. *Geophysical Research Letters*, 20(10):895–898.

Baba, S. (2002). Tectono-metamorphic Events in the North Atlantic Region in the Palaeoproterozoic from the View Point of High-grade Metamorphic Rocks in the Lewisian Complex, South Harris, NW Scotland. *Gondwana Research*, 5(4):757–770.

Bagdassarov, N. and Dingwell, D. (1992). A rheological investigation of vesicular rhyolite. *Journal of Volcanology and Geothermal Research*, 50(3):307–322.

Baltay, A., Ide, S., Prieto, G., and Beroza, G. (2011). Variability in earthquake stress drop and apparent stress. *Geophysical Research Letters*, 38(6):L06303.

Barker, S. L. L. (2005). Pseudotachylyte-generating faults in Central Otago, New Zealand. *Tectonophysics*, 397(34):211–223.

Barth, N. C., Boulton, C., Carpenter, B. M., Batt, G. E., and Toy, V. G. (2013). Slip localization on the southern Alpine Fault, New Zealand. *Tectonics*, 32(3):620–640.

Beacom, L. E., Holdsworth, R. E., McCaffrey, K. J. W., and Anderson, T. B. (2001). A quantitative study of the influence of pre-existing compositional and fabric heterogeneities upon fracture-zone development during basement reactivation. In Holdsworth, R. E., Strachan, R. A., Magloughlin, J. F., and Knipe, R. J., editors, *Nature and Tectonic Significance of Fault Zone Weakening*, volume 186, pages 195–211. Geological Soc Publishing House, Bath.

Beeler, N. M. (2006). Inferring Earthquake Source Properties from Laboratory Observations and the Scope of Lab Contributions to Source Physics. In *Earthquakes: Radiated Energy and the Physics of Faulting*, pages 99–119. American Geophysical Union.

Behr, W. M. and Platt, J. P. (2014). Brittle faults are weak, yet the ductile middle crust is strong: Implications for lithospheric mechanics. *Geophysical Research Letters*, 41(22):2014GL061349.

Ben-Zion, Y. and Andrews, D. J. (1998). Properties and implications of dynamic rupture along a material interface. *Bulletin of the Seismological Society of America*, 88(4):1085–1094.

Benn, K. (1994). Overprinting of magnetic fabrics in granites by small strains: numerical modelling. *Tectonophysics*, 233(3):153–162.

Berg, S. S. and Skar, T. (2005). Controls on damage zone asymmetry of a normal fault zone: outcrop analyses of a segment of the Moab fault, SE Utah. *Journal of Structural Geology*, 27(10):1803–1822.

Best, M. G. (2009). *Igneous and Metamorphic Petrology*. Blackwell Publishing Ltd, 2nd edition.

Bestmann, M., Pennacchioni, G., Frank, G., Göken, M., and de Wall, H. (2011). Pseudotachylyte in muscovite-bearing quartzite: Coseismic friction-induced melting and plastic deformation of quartz. *Journal of Structural Geology*, 33(2):169–186.

Bird, A. F., Thirlwall, M. F., Strachan, R. A., and Manning, C. J. (2013). LuHf and SmNd dating of metamorphic garnet: evidence for multiple accretion events during the Caledonian orogeny in Scotland. *Journal of the Geological Society*, 170(2):301–317.

Bistacchi, A., Griffith, W., Smith, S., Di Toro, G., Jones, R., and Nielsen, S. (2011). Fault Roughness at Seismogenic Depths from LIDAR and Photogrammetric Analysis. *Pure and Applied Geophysics*, 168(12):2345–2363.

Bjørnerud, M. (2010). Rethinking conditions necessary for pseudotachylyte formation: Observations from the Otago schists, South Island, New Zealand. *Tectonophysics*, 490(1-2):69–80.

Bjørnerud, M. and Magloughlin, J. F. (2004). Pressure-related feedback processes in the generation of pseudotachylytes. *Journal of Structural Geology*, 26(12):2317–2323.

Blenkinsop, T. (1991). Cataclasis and processes of particle size reduction. *Pure and Applied Geophysics*, 136(1):59–86.

Blundy, J. D. and Holland, T. J. B. (1990). Calcic amphibole equilibria and a new amphibole-plagioclase geothermometer. *Contributions to Mineralogy and Petrology*, 104(2):208–224.

Borok, V. K. (1959). On estimation of the displacement in an earthquake source and of source dimensions. *Annals of Geophysics*, 12(2):205–214.

Borradaile, G. J. and Henry, B. (1997). Tectonic applications of magnetic susceptibility and its anisotropy. *Earth-Science Reviews*, 42(1):49–93.

Bouchon, M. (1997). The state of stress on some faults of the San Andreas System as inferred from near-field strong motion data. *Journal of Geophysical Research: Solid Earth*, 102(B6):11731–11744.

Bouillin, J.-P., Bouchez, J.-L., Lespinasse, P., and Pecher, A. (1993). Granite emplacement in an extensional setting: an AMS study of the magmatic structures of Monte Capanne (Elba, Italy). *Earth and Planetary Science Letters*, 118(1):263–279.

Breeding, C. M. and Ague, J. J. (2002). Slab-derived fluids and quartz-vein formation in an accretionary prism, Otago Schist, New Zealand. *Geology*, 30(6):499–502.

Brewer, J. A., Matthews, D. H., Warner, M. R., Hall, J., Smythe, D. K., and Whittington, R. J. (1983). BIRPS deep seismic reflection studies of the British Caledonides. *Nature*, 305(5931):206–210.

Brewer, J. A. and Smythe, D. K. (1986). Deep structure of the foreland to the Caledonian Orogen, NW Scotland: Results of the Birps Winch Profile. *Tectonics*, 5(2):171–194.

Britton, T. B., Jiang, J., Guo, Y., Vilalta-Clemente, A., Wallis, D., Hansen, L. N., Winkelmann, A., and Wilkinson, A. J. (2016). Tutorial: Crystal orientations and EBSD Or which way is up? *Materials Characterization*, 117:113–126.

Brodsky, E. E., Gilchrist, J. J., Sagy, A., and Collettini, C. (2011). Faults smooth gradually as a function of slip. *Earth and Planetary Science Letters*, 302(1-2):185–193.

Brodsky, E. E. and Kanamori, H. (2001). Elastohydrodynamic lubrication of faults. *Journal of Geophysical Research: Solid Earth*, 106(B8):16357–16374.

Brodsky, E. E., Kirkpatrick, J. D., and Candela, T. (2016). Constraints from fault roughness on the scale-dependent strength of rocks. *Geology*, 44(1):19–22.

Burov, E. and Watts, A. (2006). The long-term strength of the continental lithosphere: "jelly sandwich" or "creme brulee"? *GSA Today*, 16(1):4.

Butler, C. A. (1995). *Basement fault reactivation: The kinematic evolution of the Outer Hebrides Fault Zone, Scotland.* PhD thesis, Durham University.

Butler, C. A., Holdsworth, R. E., and Strachan, R. A. (1995). Evidence for Caledonian sinistral strike-slip motion and associated fault zone weakening, Outer Hebrides Fault Zone, NW Scotland. *Journal of the Geological Society*, 152(5):743–746.

Butler, R. W. H. (2010). The role of thrust tectonic models in understanding structural evolution in NW Scotland. *Geological Society, London, Special Publications*, 335(1):293–320.

Byerlee, J. (1978). Friction of rocks. *Pure and Applied Geophysics*, 116(4-5):615–626.

Caggianelli, A., de Lorenzo, S., and Prosser, G. (2005). Modelling the heat pulses generated on a fault plane during coseismic slip: Inferences from the pseudotachylites of the Copanello cliffs (Calabria, Italy). *Tectonophysics*, 405(14):99–119.

Camacho, A., Vernon, R., and Fitz Gerald, J. (1995). Large volumes of anhydrous pseudotachylyte in the Woodroffe Thrust, eastern Musgrave Ranges, Australia. *Journal of Structural Geology*, 17(3):371–383.

Cardozo, N. and Allmendinger, R. W. (2013). Spherical projections with OSXStereonet. *Computers & Geosciences*, 51:193–205.

Cathelineau, M. (1988). Cation site occupancy in chlorites and illites as a function of temperature. *Clay Minerals*, 23(4):471 LP – 485.

Cheloni, D., Giuliani, R., D'Agostino, N., Mattone, M., Bonano, M., Fornaro, G., Lanari, R., Reale, D., and Atzori, S. (2016). New insights into fault activation and stress transfer between en echelon thrusts: The 2012 Emilia, Northern Italy, earthquake sequence. *Journal of Geophysical Research: Solid Earth*, 121(6):4742–4766.

Chen, K., Kunz, M., Tamura, N., and Wenk, H.-R. (2015). Residual stress preserved in quartz from the San Andreas Fault Observatory at Depth. *Geology*, 43(3):219–222.

Chester, F. M., Evans, J. P., and Biegel, R. L. (1993). Internal structure and weakening mechanisms of the San Andreas Fault. *Journal of Geophysical Research: Solid Earth*, 98(B1):771–786.

Chester, J. S., Chester, F. M., and Kronenberg, A. K. (2005). Fracture surface energy of the Punchbowl fault, San Andreas system. *Nature*, 437(7055):133–136.

Cirrincione, R., Fazio, E., Ortolano, G., Pezzino, A., and Punturo, R. (2012). Fault-related rocks: Deciphering the structural-metamorphic evolution of an accretionary wedge in a collisional belt, NE Sicily. *International Geology Review*, 54(8):940–956.

Clemente, C. S., Amorós, E. B., and Crespo, M. G. (2007). Dike intrusion under shear stress: Effects on magnetic and vesicle fabrics in dikes from rift zones of Tenerife (Canary Islands). *Journal of Structural Geology*, 29(12):1931–1942.

Cliff, R. A. and Rex, D. C. (1989). Short Paper: Evidence for a Grenville' event in the Lewisian of the northern Outer Hebrides. *Journal of the Geological Society*, 146(6):921–924.

Cliff, R. A., Rex, D. C., and Guise, P. G. (1998). Geochronological studies of Proterozoic crustal evolution in the northern Outer Hebrides. *Precambrian Research*, 91(34):401–418.

Cobbold, P. R., Zanella, A., Rodrigues, N., and Løseth, H. (2013). Bedding-parallel fibrous veins (beef and cone-in-cone): Worldwide occurrence and possible significance in terms of fluid overpressure, hydrocarbon generation and mineralization. *Marine and Petroleum Geology*, 43:1–20.

Collettini, C., Niemeijer, A., Viti, C., and Marone, C. (2009). Fault zone fabric and fault weakness. *Nature*, 462(7275):907–910.

Cowan, D. S. (1999). Do faults preserve a record of seismic slip? A field geologist's opinion. *Journal of Structural Geology*, 21(8-9):995–1001.

Coward, M. P. (1969). *The structural and metamorphic geology of South Uist, Outer Hebrides*. PhD thesis, University of London.

Coward, M. P. (1972). The Eastern Gneisses of South Uist. *Scottish Journal of Geology*, 8(1):1–12.

Coward, M. P. (1983). The thrust and shear zones of the Moine thrust zone and the NW Scottish Caledonides. *Journal of the Geological Society*, 140(5):795–811.

Coward, M. P., Francis, P. W., Graham, R. H., and Watson, J. (1970). Large-scale Laxfordian structures of the outer hebrides in relation to those of the Scottish mainland. *Tectonophysics*, 10(4):425–435.

Cowie, P. A. (1998). A healingreloading feedback control on the growth rate of seismogenic faults. *Journal of Structural Geology*, 20(8):1075–1087.

Cowie, P. A. and Scholz, C. H. (1992). Growth of faults by accumulation of seismic slip. *Journal of Geophysical Research: Solid Earth*, 97(B7):11085–11095.

Craddock, J. P. and Magloughlin, J. F. (2005). Calcite strains, kinematic indicators, and magnetic flow fabric of a proterozoic pseudotachylyte swarm, Minnesota River valley, USA. *Tectonophysics*, 402(1-4):153–168.

Dalguer, L. A., Irikura, K., and Riera, J. D. (2003). Simulation of tensile crack generation by three-dimensional dynamic shear rupture propagation during an earthquake. *Journal of Geophysical Research: Solid Earth*, 108(B3):2144.

Das, S. and Scholz, C. H. (1981). Off-fault aftershock clusters caused by shear stress increase? *Bulletin of the Seismological Society of America*, 71(5):1669–1675.

Davies, F., Lisle, R., and Watson, J. (1975). The tectonic evolution of the Lewisian complex in northern Lewis, Outer Hebrides. *Proceedings of the Geologists' Association*, 86(1):45–IN2.

Davis, K., Burbank, D. W., Fisher, D., Wallace, S., and Nobes, D. (2005). Thrust-fault growth and segment linkage in the active Ostler fault zone, New Zealand. *Journal of Structural Geology*, 27(8):1528–1546.

De Paola, N., Hirose, T., Mitchell, T., Di Toro, G., Viti, C., and Shimamoto, T. (2010). Fault lubrication and earthquake propagation in thermally unstable rocks. *Geology*, 39(1):35–38.

De Paola, N., Holdsworth, R. E., Viti, C., Collettini, C., and Bullock, R. (2015). Can grain size sensitive flow lubricate faults during the initial stages of earthquake propagation? *Earth and Planetary Science Letters*, 431:48–58.

Deer, W., Howie, R., and Zussman, J. (1992). *An Introduction to the Rock Forming Minerals*. Prentice Hall, 2nd edition.

Del Gaudio, P., Di Toro, G., Han, R., Hirose, T., Nielsen, S., Shimamoto, T., and Cavallo, A. (2009). Frictional melting of peridotite and seismic slip. *Journal of Geophysical Research: Solid Earth*, 114(B6):n/a–n/a.

Dempsey, E. D., Holdsworth, R. E., Imber, J., Bistacchi, A., and Di Toro, G. (2014). A geological explanation for intraplate earthquake clustering complexity: The zeolite-bearing fault/fracture networks in the Adamello Massif (Southern Italian Alps). *Journal of Structural Geology*, 66(0):58–74.

Dewey, J. F. and Strachan, R. A. (2003). Changing SilurianDevonian relative plate motion in the Caledonides: sinistral transpression to sinistral transtension. *Journal of the Geological Society*, 160(2):219–229.

Di Toro, G., Goldsby, D. L., and Tullis, T. E. (2004). Friction falls towards zero in quartz rock as slip velocity approaches seismic rates. *Nature*, 427(6973):436–439.

Di Toro, G., Hirose, T., Nielsen, S., Pennacchioni, G., and Shimamoto, T. (2006a). Natural and Experimental Evidence of Melt Lubrication of Faults During Earthquakes. *Science*, 311(5761):647–649.

Di Toro, G., Hirose, T., Nielsen, S., and Shimamoto, T. (2006b). Relating high-velocity rock-friction experiments to coseismic slip in the presence of melts. In *Earthquakes: Radiated Energy and the Physics of Faulting*, volume 170, pages 121–134. AGU, Washington, DC.

Di Toro, G., Nielsen, S., and Pennacchioni, G. (2005a). Earthquake rupture dynamics frozen in exhumed ancient faults. *Nature*, 436(7053):1009–1012.

Di Toro, G. and Pennacchioni, G. (2004). Superheated friction-induced melts in zoned pseudotachylytes within the Adamello tonalites (Italian Southern Alps). *Journal of Structural Geology*, 26(10):1783–1801.

Di Toro, G. and Pennacchioni, G. (2005). Fault plane processes and mesoscopic structure of a strong-type seismogenic fault in tonalites (Adamello batholith, Southern Alps). *Tectonophysics*, 402(14):55–80.

Di Toro, G., Pennacchioni, G., and Teza, G. (2005b). Can pseudotachylytes be used to infer earthquake source parameters? An example of limitations in the study of exhumed faults. *Tectonophysics*, 402(14):3–20.

Dickinson, W. R. (2002). Reappraisal of hypothetical Franciscan thrust wedging at Coalinga: Implications for tectonic relations along the Great Valley flank of the California Coast Ranges. *Tectonics*, 21(5):3–14.

Dor, O., Rockwell, T. K., and Ben-Zion, Y. (2006). Geological Observations of Damage Asymmetry in the Structure of the San Jacinto, San Andreas and Punchbowl Faults in Southern California: A Possible Indicator for Preferred Rupture Propagation Direction. *pure and applied geophysics*, 163(2):301–349.

Droop, G. T. R., Fernandes, L. A. D., and Shaw, S. (1999). Laxfordian metamorphic conditions of the Palaeoproterozoic Loch Maree Group, Lewisian Complex, NW Scotland. *Scottish Journal of Geology*, 35(1):31–50.

Earle, M. M., Jankowski, E. J., and Vann, I. R. (1989). Structural and stratigraphic evolution of the Faeroe-Shetland Channel and Northern Rockall Trough: Chapter 30: European-

African Margins. In *M 46: Extensional Tectonics and Stratigraphy of the North Atlantic Margins*, chapter 30, pages 461–469. American Association of Petroeum Geology, Tulsa.

Fabbri, O., Lin, A. M., and Tokushige, H. (2000). Coeval formation of cataclasite and pseudotachylyte in a Miocene forearc granodiorite, southern Kyushu, Japan. *Journal of Structural Geology*, 22(8):1015–1025.

Faulkner, D. R., Mitchell, T. M., Healy, D., and Heap, M. J. (2006). Slip on 'weak' faults by the rotation of regional stress in the fracture damage zone. *Nature*, 444(7121):922–925.

Ferré, E. C., Chou, Y.-M., Kuo, R. L., Yeh, E.-C., Leibovitz, N. R., Meado, A. L., Campbell, L., and Geissman, J. W. (2016). Deciphering viscous flow of frictional melts with the mini-AMS method. *Journal of Structural Geology*, 90:15–26.

Ferré, E. C., Geissman, J. W., Chauvet, A., Vauchez, A., and Zechmeister, M. S. (2015). Focal mechanism of prehistoric earthquakes deduced from pseudotachylyte fabric. *Geology*, 43(6):531–534.

Ferré, E. C., Geissman, J. W., Demory, F., Gattacceca, J., Zechmeister, M. S., and Hill, M. J. (2014). Coseismic magnetization of fault pseudotachylytes: 1. Thermal demagnetization experiments. *Journal of Geophysical Research: Solid Earth*, 119(8):2014JB011168.

Ferry, J. M. and Spear, F. S. (1978). Experimental calibration of the partitioning of Fe and Mg between biotite and garnet. *Contributions to Mineralogy and Petrology*, 66(2):113–117.

Fettes, D. J. and Mendum, J. R. (1987). The evolution of the Lewisian complex in the Outer Hebrides. *Geological Society, London, Special Publications*, 27(1):27–44.

Fettes, D. J., Mendum, J. R., Smith, D. I., and Watson, J. (1981). 1:100 000 geological sheets (Solid): Lewis and Harris, Uist and Barra. Technical report, British Geological Survey, London.

Fettes, D. J., Mendum, J. R., Smith, D. I., and Watson, J. V. (1992). *Geology of the Outer Hebrides: memoir for 1:100 000 geological sheets, Lewis and Harris, Uist and Barra*. HMSO, London.

Flodin, E. A. and Aydin, A. (2004). Evolution of a strike-slip fault network, Valley of Fire State Park, southern Nevada. *Geological Society of America Bulletin*, 116(1-2):42–59.

Fossen, H. (2016). *Structural Geology*. Cambridge University Press, Cambridge, UK, 2nd edition.

Francis, P. and Sibson, R. (1973). The Outer Hebrides Thrust. In Park, R. G. and Tarney, J., editors, *The Early Precambrian of Scotland and Related Rocks of Greenland*, pages 95–104. University of Keele, Keele, 1st edition.

Francis, P. W., Moorbath, S., and Welke, H. J. (1971). Isotopic age data from Scourian intrusive rocks on the Isle of Barra, Outer Hebrides, north-west Scotland. *Geological Magazine*, 108(01):13–21.

Freed, A. M. (2004). Earthquake triggering by static, dynamic, and postseismic stress transfer. *Annual Review of Earth and Planetary Sciences*, 33(1):335–367.

Freeman, S. R., Butler, R. W. H., Cliff, R. A., and Rex, D. C. (1998). Direct dating of mylonite evolution: a multi-disciplinary geochronological study from the Moine Thrust Zone, NW Scotland. *Journal of the Geological Society*, 155(5):745–758.

Friend, C. and Kinny, P. (2001). A reappraisal of the Lewisian Gneiss Complex: geochronological evidence for its tectonic assembly from disparate terranes in the Proterozoic. *Contributions to Mineralogy and Petrology*, 142(2):198–218.

Fuhrmann, M. L. and Lindsley, D. H. (1988). Ternary feldspar modelling and thermometry. *American Mineralogist*, 73:201–216.

Fukuyama, E., Mikumo, T., and Olsen, K. B. (2003). Estimation of the Critical Slip-Weakening Distance: Theoretical Background. *Bulletin of the Seismological Society of America*, 93(4):1835–1840.

Gapais, D., Cobbold, P. R., Bourgeois, O., Rouby, D., and de Urreiztieta, M. (2000). Tectonic significance of fault-slip data. *Journal of Structural Geology*, 22(7):881–888.

Garza, R. S. M., Geissman, J., Wawrzyniec, T., Weber, B., López Martínez, M., and Aranda-Gómez, J. (2009). An integrated magnetic and geological study of cataclasite- dominated pseudotachylytes in the Chiapas Massif, Mexico: A snapshot of stress orientation following slip. *Geophysical Journal International*, 177(3):891–912.

Gibowicz, S. J., Young, R. P., Talebi, S., and Rawlence, D. J. (1991). Source parameters of seismic events at the Underground Research Laboratory in Manitoba, Canada: Scaling relations for events with moment magnitude smaller than 2. *Bulletin of the Seismological Society of America*, 81(4):1157–1182.

Goodenough, K. M., Millar, I., Strachan, R. A., Krabbendam, M., and Evans, J. A. (2011). Timing of regional deformation and development of the Moine Thrust Zone in the Scottish Caledonides: constraints from the UPb geochronology of alkaline intrusions. *Journal of the Geological Society*, 168(1):99–114.

Griffith, A. A. (1924). The theory of rupture. In Biezeno, C. B. and Burgers, J. M., editors, *Proceedings of the Institute of the International Congress of Applied Mechanics*, pages 54–63, Delft. Tech. Boekhandel en Drukkerij J Walter Jr.

Griffith, W. A., Di Toro, G., Pennacchioni, G., Pollard, D. D., and Nielsen, S. (2009a). Static stress drop associated with brittle slip events on exhumed faults. *Journal of Geophysical Research: Solid Earth*, 114(B2):B02402.

Griffith, W. A., Mitchell, T. M., Renner, J., and Di Toro, G. (2012). Coseismic damage and softening of fault rocks at seismogenic depths. *Earth and Planetary Science Letters*, 353354(0):219–230.

Griffith, W. A., Rosakis, A., Pollard, D. D., and Ko, C. W. (2009b). Dynamic rupture experiments elucidate tensile crack development during propagating earthquake ruptures. *Geology*, 37(9):795–798.

Grocott, J. (1981). Fracture geometry of pseudotachylyte generation zones: a study of shear fractures formed during seismic events. *Journal of Structural Geology*, 3(2):169–178.

Grohmann, C. and Campanha, G. (2010). OpenStereo: opensource, cross-platform software for structural geology analysis. In *AGU Fall Meeting*.

Gupta, S., Cowie, P. A., Dawers, N. H., and Underhill, J. R. (1998). A mechanism to explain rift-basin subsidence and stratigraphic patterns through fault-array evolution. *Geology*, 26(7):595–598.

Han, R., Hirose, T., Shimamoto, T., Lee, Y., and Ando, J.-i. (2011). Granular nanoparticles lubricate faults during seismic slip. *Geology*, 39(6):599–602.

Han, R., Shimamoto, T., Hirose, T., Ree, J. H., and Ando, J. I. (2007). Geophysics: Ultralow friction of carbonate faults caused by thermal decomposition. *Science*, 316(5826):878–881.

Hardacre, K. M. and Cowie, P. A. (2003). Variability in fault size scaling due to rock strength heterogeneity: a finite element investigation. *Journal of Structural Geology*, 25(10):1735–1750.

Harris, R. A. (1998). Introduction to Special Section: Stress Triggers, Stress Shadows, and Implications for Seismic Hazard. *Journal of Geophysical Research: Solid Earth*, 103(B10):24347–24358.

Heaton, T. H. and Hartzell, S. H. (1987). Earthquake Hazards on the Cascadia Subduction Zone. *Science*, 236(4798):162–168.

Helz, R. T. (1979). Alkali exchange between hornblende and melt: a temperature-sensitive reaction. *American Mineralogist*, 64:935–965.

Hesselbo, S. P., Oates, M. J., and Jenkyns, H. C. (1998). The lower Lias Group of the Hebrides Basin. *Scottish Journal of Geology*, 34(1):23–60.

Heyes, A. J. (1978). *A metamorphic, structural and geochemical study of the South Harris Anorthosite, Outer Hebrides*. PhD thesis, University of London.

Hicks, S. P. and Rietbrock, A. (2015). Seismic slip on an upper-plate normal fault during a large subduction megathrust rupture. *Nature Geosci*, 8(12):955–960.

Hill, D. P., Reasenberg, P. A., Michael, A., Arabaz, W. J., Beroza, G., Brumbaugh, D., Brune, J. N., Castro, R., Davis, S., DePolo, D., Ellsworth, W. L., Gomberg, J., Harmsen, S., House, L., Jackson, S. M., Johnston, M. J. S., Jones, L., Keller, R., Malone, S., Munguia, L., Nava, S., Pechmann, J. C., Sanford, A., Simpson, R. W., Smith, R. B., Stark, M., Stickney, M., Vidal, A., Walter, S., Wong, V., and Zollweg, J. (1993). Seismicity Remotely Triggered by the Magnitude 7.3 Landers, California, Earthquake. *Science*, 260(5114):1617–1623.

Hill, D. P. and Thatcher, W. (1992). An energy constraint for frictional slip on misoriented faults. *Bulletin of the Seismological Society of America*, 82(2):883–897.

Hirose, T. (2005). Growth of molten zone as a mechanism of slip weakening of simulated faults in gabbro during frictional melting. *Journal of Geophysical Research*, 110(B5):B05202.

Hirose, T. and Shimamoto, T. (2003). Fractal dimension of molten surfaces as a possible parameter to infer the slip-weakening distance of faults from natural pseudotachylytes. *Journal of Structural Geology*, 25(10):1569–1574.

Hirose, T. and Shimamoto, T. (2005). Slip-Weakening Distance of Faults during Frictional Melting as Inferred from Experimental and Natural Pseudotachylytes. *Bulletin of the Seismological Society of America*, 95(5):1666–1673.

Hirth, G., Teyssier, C., and Dunlap, J. W. (2001). An evaluation of quartzite flow laws based on comparisons between experimentally and naturally deformed rocks. *International Journal of Earth Sciences*, 90(1):77–87.

Hirth, G. and Tullis, J. (1992). Dislocation creep regimes in quartz aggregates. *Journal of Structural Geology*, 14(2):145–159.

Hisada, E. (2004). Clast-size analysis of impact-generated pseudotachylite from Vredefort Dome, South Africa. *Journal of Structural Geology*, 26(8):1419–1424.

Hitchen, K., Stoker, M. S., Evans, D., and Beddoe-Stephens, B. (1995). Permo-Triassic sedimentary and volcanic rocks in basins to the north and west of Scotland. *Geological Society, London, Special Publications*, 91(1):87–102.

Hobbs, B. E., Ord, A., and Teyssier, C. (1986). Earthquakes in the ductile regime? *Pure and Applied Geophysics*, 124(1):309–336.

Hodson, T. O., Powell, R. D., Brachfeld, S. A., Tulaczyk, S., and Scherer, R. P. (2016). Physical processes in Subglacial Lake Whillans, West Antarctica: Inferences from sediment cores. *Earth and Planetary Science Letters*, 444:56–63.

Hoek, J. D. (1991). A classification of dyke-fracture geometry with examples from Precambrian dyke swarms in the Vestfold Hills, Antarctica. *Geologische Rundschau*, 80(2):233–248.

Holdsworth, R. E. (2004). Weak Faults–Rotten Cores. *Science*, 303(5655):181–182.

Holdsworth, R. E. and Strachan, R. A. (1991). Interlinked system of ductile strike slip and thrusting formed by Caledonian sinistral transpression in northeastern Greenland. *Geology*, 19(5):510–513.

Holland, T. and Blundy, J. (1994). Non-ideal interactions in calcic amphiboles and their bearing on amphibole-plagioclase thermometry. *Contributions to Mineralogy and Petrology*, 116(4):433–447.

Holland, T. J. B. and Powell, R. (1990). An enlarged and updated internally consistent thermodynamic dataset with uncertainties and correlations: the system K2ONa2OCaOMgOMnOFeOFe2O3Al2O3TiO2SiO2CH2O2. *Journal of Metamorphic Geology*, 8(1):89–124.

Imanishi, K. and Ellsworth, W. L. (2006). Source Scaling Relationships of Microearthquakes at Parkfield, CA, Determined Using the SAFOD Pilot Hole Seismic Array. In *Earthquakes: Radiated Energy and the Physics of Faulting*, pages 81–90. American Geophysical Union.

Imber, J. (1998). *Deformation and fluid-rock interaction along the reactivated Outer Hebrides Fault Zone, Scotland.* PhD thesis, Durham University.

Imber, J., Holdsworth, R. E., Butler, C. A., and Lloyd, G. E. (1997). Fault-zone weakening processes along the reactivated Outer Hebrides Fault Zone, Scotland. *Journal of the Geological Society*, 154(1):105–109.

Imber, J., Holdsworth, R. E., Butler, C. A., and Strachan, R. A. (2001). A reappraisal of the Sibson-Scholz fault zone model: The nature of the frictional to viscous (brittle-ductile) transition along a long-lived, crustal-scale fault, Outer Hebrides, Scotland. *Tectonics*, 20(5):601–624.

Imber, J., Strachan, R. A., Holdsworth, R. E., and Butler, C. A. (2002). The initiation and early tectonic significance of the Outer Hebrides Fault Zone, Scotland. *Geological Magazine*, 139(06):609–619.

Jackson, J. (2002). Strength of the continental lithosphere: time to abandon the jelly sandwich? *GSA Today*, 12(9):4–9.

Jaeger, J. and Cook, N. (1979). *Fundamentals of Rock Mechanics*. Chapman & Hall, London, 3rd edition.

Jaeger, J. C. (1959). The frictional properties of joints in rock. *Geofisica pura e applicata*, 43(1):148–158.

Janssen, C., Wirth, R., Lin, A., and Dresen, G. (2013). TEM microstructural analysis in a fault gouge sample of the Nojima Fault Zone, Japan. *Tectonophysics*, 583(0):101–104.

Jehu, T. J. and Craig, R. M. (1923). Geology of the Outer Hebrides. Part I - The Barra Isles. *Transactions of the Royal Society of Edinburgh*, 53(2):419–441.

Jehu, T. J. and Craig, R. M. (1927). Geology of the Outer Hebrides. Part IV - South Harris. *Transactions of the Royal Society of Edinburgh*, 55:457 – 488.

Jelinek, V. (1981). Characterization of the magnetic fabric of rocks. *Tectonophysics*, 79(3):T63–T67.

Johnson, M. C. and Rutherford, M. J. (1989). Experimental calibration of the aluminum-in-hornblende geobarometer with application to Long Valley caldera (California) volcanic rocks. *Geology*, 17(9):837–841.

Johnson, P. A. and McEvilly, T. V. (1995). Parkfield seismicity: Fluid-driven? *Journal of Geophysical Research: Solid Earth*, 100(B7):12937–12950.

Jones, P. B. (1996). Triangle zone geometry, terminology and kinematics. *Bulletin of Canadian Petroleum Geology*, 44(2):139–152.

Jones, R. R., Holdsworth, R. E., McCaffrey, K. J. W., Clegg, P., and Tavarnelli, E. (2005). Scale dependence, strain compatibility and heterogeneity of three-dimensional deformation during mountain building: a discussion. *Journal of Structural Geology*, 27(7):1190–1204.

Jones, R. R. and Tanner, P. W. G. (1995). Strain partitioning in transpression zones. *Journal of Structural Geology*, 17(6):793–802.

Jordan, T. E., Isacks, B. L., Allmendinger, R. W., Brewer, J. O. N. A., Ramos, V. A., and Ando, C. J. (1983). Andean tectonics related to geometry of subducted Nazca plate. *Geological Society of America Bulletin*, 94(3):341–361.

Jouanne, F., Mugnier, J. L., Pandey, M. R., Gamond, J. F., Le Fort, P., Serrurier, L., Vigny, C., and Avouac, J. P. (1999). Oblique convergence in the Himalayas of western Nepal deduced from preliminary results of GPS measurements. *Geophysical Research Letters*, 26(13):1933–1936.

Kanamori, H. and Anderson, D. L. (1975). Theoretical basis of some empirical relations in seismology. *Bulletin of the Seismological Society of America*, 65(5):1073–1095.

Kanamori, H., Anderson, D. L., and Heaton, T. H. (1998). Frictional Melting During the Rupture of the 1994 Bolivian Earthquake. *Science*, 279(5352):839–842.

Kanamori, H. and Brodsky, E. (2004). The physics of earthquakes. *Reports on Progress in Physics*, 67(8):1429.

Kanao, M. and Ishikawa, M. (2004). Origins of the lower crustal reflectivity in the Lützow-Holm Complex, Enderby Land, East Antarctica. *Earth, Planets and Space*, 56(2):151–162.

Kelley, S. P., Reddy, S. M., and Maddock, R. (1994). Laser-probe 40Ar/39Ar investigation of a pseudotachylyte and its host rock from the Outer Isles thrust, Scotland. *Geology*, 22(5):443–446.

Kirkpatrick, J. D., Dobson, K. J., Mark, D. F., Shipton, Z. K., Brodsky, E. E., and Stuart, F. M. (2012). The depth of pseudotachylyte formation from detailed thermochronology and constraints on coseismic stress drop variability. *J. Geophys. Res.*, 117(B6):B06406.

Kirkpatrick, J. D. and Shipton, Z. K. (2009). Geologic evidence for multiple slip weakening mechanisms during seismic slip in crystalline rock. *J. Geophys. Res.*, 114(B12):B12401.

Kirkpatrick, J. D., Shipton, Z. K., and Persano, C. (2009). Pseudotachylytes: Rarely Generated, Rarely Preserved, or Rarely Reported? *Bulletin of the Seismological Society of America*, 99(1):382–388.

Kitano, T., Kataoka, T., and Shirota, T. (1981). An empirical equation of the relative viscosity of polymer melts filled with various inorganic fillers. *Rheologica Acta*, 20(2):207–209.

Klein, E. and Koppe, J. (2000). Chlorite geothermometry and physicochemical conditions of gold mineralization in the Paleaoproterzic Caxias deposit, So Luís craton, northern Brazil. *Geochimica Brasiliensis*, 14(2):219–232.

Kohn, M. and Spear, F. S. (1989). Empirical calibration of geobarometers for the assemblage garnet + hornnblende + plagioclase + quartz. *American Mineralogist*, 74(1-2):77–84.

Kranidiotis, P. and MacLean, W. H. (1987). Systematics of chlorite alteration at the Phelps Dodge massive sulfide deposit, Matagami, Quebec. *Economic Geology*, 82(7):1898–1911.

Kranz, R. L. (1983). Microcracks in rocks: A review. *Tectonophysics*, 100(1-3):449–480.

Kubota, Y. and Takeshita, T. (2008). Paleocene large-scale normal faulting along the Median Tectonic Line, western Shikoku, Japan. *Island Arc*, 17(1):129–151.

Lachenbruch, A. H. (1980). Frictional Heating, Fluid Pressure, and the Resistance to Fault Motion. *J. Geophys. Res.*, 85(B11):6097–6112.

Langer, S., Olsen-Kettle, L., and Weatherley, D. (2012). Identification of supershear transition mechanisms due to material contrast at bimaterial faults. *Geophysical Journal International*, 190(2):1169–1180.

Lavallée, Y., Hirose, T., Kendrick, J. E., Hess, K.-U., and Dingwell, D. B. (2015). Fault rheology beyond frictional melting. *Proceedings of the National Academy of Sciences*, 112(30):9276–9280.

Lee, J.-J. and Bruhn, R. L. (1996). Structural anisotropy of normal fault surfaces. *Journal of Structural Geology*, 18(8):1043–1059.

Leib, S. E., Moecher, D. P., Steltenpohl, M. G., and Andresen, A. (2016). Thermobarometry of metamorphosed pseudotachylyte and associated mylonite: Constraints on dynamic Co-seismic rupture depth attending Caledonian extension, North Norway. *Tectonophysics*, 682:85–95.

Lide, D. (2004). *CRC handbook of chemistry and physics: a ready-reference book of chemical and physical data*. CRC Press, Boca Raton, Florida, 85th edition.

Lin, A. (1996). Injection veins of crushing-originated pseudotachylyte and fault gouge formed during seismic faulting. *Engineering Geology*, 43(23):213–224.

Lin, A. (1999). Roundness of clasts in pseudotachylytes and cataclastic rocks as an indicator of frictional melting. *Journal of Structural Geology*, 21(5):473–478.

Lin, A. and Nishikawa, M. (2011). Riedel shear structures in the co-seismic surface rupture zone produced by the 2001 Mw 7.8 Kunlun earthquake, northern Tibetan Plateau. *Journal of Structural Geology*, 33(9):1302–1311.

Lin, A. M. (2008). Seismic slip in the lower crust inferred from granulite-related pseudotachylyte in the Woodroffe thrust, central Australia. *Pure and Applied Geophysics*, 165(2):215–233.

Lin, A. M., Chen, A. L., Liau, C. F., Lee, C. T., Lin, C. C., Lin, P. S., Wen, S. C., and Ouchi, T. (2001). Frictional fusion due to coseismic landsliding during the 1999 Chi-Chi (Taiwan) M-L 7.3 earthquake. *Geophysical Research Letters*, 28(20):4011–4014.

Lin, A. M. and Shimamoto, T. (1998). Selective melting processes as inferred from experimentally generated pseudotachylytes. *Journal of Asian Earth Sciences*, 16(5-6):533–545.

Lin, J., Stein, R. S., Meghraoui, M., Toda, S., Ayadi, A., Dorbath, C., and Belabbes, S. (2011). Stress transfer among en echelon and opposing thrusts and tear faults: Triggering caused by the 2003 M w = 6.9 Zemmouri, Algeria, earthquake. *Journal of Geophysical Research*, 116(B3):B03305.

Lin, Y. Y., Ma, K. F., and Oye, V. (2012). Observation and scaling of microearthquakes from the Taiwan Chelungpu-fault borehole seismometers. *Geophysical Journal International*, 190(1):665–676.

Lloyd, G. E. (1987). Atomic number and crystallographic contrast images with the SEM: A review of backscattered electron techniques. *Mineralogical Magazine*, 51(359):3 – 19.

Lockner, D. A., Byerlee, J. D., Kuksenko, V., Ponomarev, A., and Sidorin, A. (1991). Quasi-static fault growth and shear fracture energy in granite. *Nature*, 350(6313):39–42.

Lockner, D. A. and Okubo, P. G. (1983). Measurements of frictional heating in granite. *Journal of Geophysical Research: Solid Earth*, 88(B5):4313–4320.

Lofgren, G. (1971). Experimentally Produced Devitrification Textures in Natural Rhyolitic Glass. *Geological Society of America Bulletin*, 82(1):111–124.

Lofgren, G. (1974). An experimental study of plagioclase crystal morphology; isothermal crystallization. *American Journal of Science*, 274(3):243–273.

Lund, M. G. and Austrheim, H. (2003). High-pressure metamorphism and deep-crustal seismicity: evidence from contemporaneous formation of pseudotachylytes and eclogite facies coronas. *Tectonophysics*, 372(1-2):59–83.

Luttrell, K. M., Tong, X., Sandwell, D. T., Brooks, B. A., and Bevis, M. G. (2011). Estimates of stress drop and crustal tectonic stress from the 27 February 2010 Maule, Chile, earthquake: Implications for fault strength. *Journal of Geophysical Research: Solid Earth*, 116(B11):B11401.

Ma, S. and Beroza, G. C. (2008). Rupture Dynamics on a Bimaterial Interface for Dipping Faults. *Bulletin of the Seismological Society of America*, 98(4):1642–1658.

Macaudière, J. and Brown, W. L. (1982). Transcrystalline shear fracturing and pseudotachylite generation in a meta-anorthosite (Harris, Scotland). *Journal of Structural Geology*, 4(4):395–406.

Macaudière, J., Brown, W. L., and Ohnenstetter, D. (1985). Microcrystalline textures resulting from rapid crystallization in a pseudotachylite melt in a meta-anorthosite. *Contributions to Mineralogy and Petrology*, 89(1):39–51.

MacInnes, E. A., Alsop, G. I., and Oliver, G. J. H. (2000). Contrasting modes of reactivation in the Outer Hebrides Fault Zone, northern Barra, Scotland. *Journal of the Geological Society*, 157(5):1009–1017.

Maddock, R. H. (1983). Melt origin of fault-generated pseudotachylytes demonstrated by textures. *Geology*, 11(2):105–108.

Maddock, R. H. (1992). Effects of lithology, cataclasis and melting on the composition of fault-generated pseudotachylytes in Lewisian gneiss, Scotland. *Tectonophysics*, 204(3-4):261–278.

Maddock, R. H., Grocott, J., and Van Nes, M. (1987). Vesicles, amygdales and similar structures in fault-generated pseudotachylytes. *Lithos*, 20(5):419–432.

Magee, C., O'Driscoll, B., Petronis, M. S., and Stevenson, C. T. E. (2016). Three-dimensional magma flow dynamics within subvolcanic sheet intrusions. *Geosphere*, 12(3):842–866.

Magloughlin, J. F. and Spray, J. G. (1992). Frictional melting processes and products in geological materials: introduction and discussion. *Tectonophysics*, 204(34):197–204.

Mahapatro, S. N., Tripathy, A. K., Nanda, J. K., and Roy, A. (2009). Coexisting ultramylonite and pseudotachylyte from the eastern segment of the Mahanadi shear zone, Eastern Ghats Mobile Belt. *Journal of the Geological Society of India*, 74(6):679–689.

Manighetti, I., Campillo, M., Bouley, S., and Cotton, F. (2007). Earthquake scaling, fault segmentation, and structural maturity. *Earth and Planetary Science Letters*, 253(3-4):429–438.

Mardia, K. (1975). Statistics of Directional Data. *Journal of the Royal Statistical Society*, 37(3):349–393.

Marrett, R. and Allmendinger, R. W. (1990). Kinematic analysis of fault-slip data. *Journal of Structural Geology*, 12(8):973–986.

Martin, K. M., Gulick, S. P. S., Bangs, N. L. B., Moore, G. F., Ashi, J., Park, J.-O., Kuramoto, S., and Taira, A. (2010). Possible strain partitioning structure between the Kumano fore-arc basin and the slope of the Nankai Trough accretionary prism. *Geochemistry, Geophysics, Geosystems*, 11(5):Q0AD02.

Masch, L., Wenk, H. R., and Preuss, E. (1985). Electron microscopy study of hyalomylonite-sevidence for frictional melting in landslides. *Tectonophysics*, 115(12):131–160.

Mason, A. J. and Brewer, T. S. (2004). Mafic dyke remnants in the Lewisian Complex of the Outer Hebrides, NW scotland: a geochemical record of continental break-up and re-assembly. *Precambrian Research*, 133(12):121–141.

Mason, A. J., Parrish, R. R., and Brewer, T. S. (2004). UPb geochronology of Lewisian orthogneisses in the Outer Hebrides, Scotland: implications for the tectonic setting and correlation of the South Harris Complex. *Journal of the Geological Society*, 161(1):45–54.

Matsu'ura, M., Kataoka, H., and Shibazaki, B. (1992). Slip-dependent friction law and nucleation processes in earthquake rupture. *Tectonophysics*, 211(1):135–148.

Mayeda, K. and Walter, W. R. (1996). Moment, energy, stress drop, and source spectra of western United States earthquakes from regional coda envelopes. *Journal of Geophysical Research: Solid Earth*, 101(B5):11195–11208.

McCaffrey, R. (1991). Slip vectors and stretching of the Sumatran fore arc. *Geology*, 19(9):881–884.

McGuire, J. J., Zhao, L., and Jordan, T. H. (2002). Predominance of Unilateral Rupture for a Global Catalog of Large Earthquakes. *Bulletin of the Seismological Society of America*, 92(8):3309–3317.

McKenzie, D. and Brune, J. N. (1972). Melting on Fault Planes During Large Earthquakes. *Geophysical Journal of the Royal Astronomical Society*, 29(1):65–78.

Melosh, B. L., Rowe, C. D., Smit, L., Groenewald, C., Lambert, C. W., and Macey, P. (2014). Snap, Crackle, Pop: Dilational fault breccias record seismic slip below the brittleplastic transition. *Earth and Planetary Science Letters*, 403(0):432–445.

Melosh, H. J. (1996). Dynamical weakening of faults by acoustic fluidization. *Nature*, 379(6566):601–606.

Metzner, A. B. (1985). Rheology of Suspensions in Polymeric Liquids. *Journal of Rheology*, 29(6).

Mikumo, T. and Miyatake, T. (1993). Dynamic Rupture Processes on a Dipping Fault, and Estimates of Stress Drop and Strength Excess from the Results of Waveform Inversion. *Geophysical Journal International*, 112(3):481–496.

Mikumo, T., Olsen, K. B., Fukuyama, E., and Yagi, Y. (2003). Stress-Breakdown Time and Slip-Weakening Distance Inferred from Slip-Velocity Functions on Earthquake Faults. *Bulletin of the Seismological Society of America*, 93(1):264–282.

Mikumo, T. and Yagi, Y. (2003). Slip-weakening distance in dynamic rupture of in-slab normal-faulting earthquakes. *Geophysical Journal International*, 155(2):443–455.

Molnar, P. and Tapponnier, P. (1978). Active tectonics of Tibet. *Journal of Geophysical Research: Solid Earth*, 83(B11):5361–5375.

Moorbath, S., Powell, J., and Taylor, P. (1975). Isotopic evidence for the age and origin of the grey gneiss complex of the southern Outer Hebrides, Scotland. *Journal of the Geological Society*, 131(2):213–222.

Moore, D. E. and Lockner, D. A. (1995). The role of microcracking in shear-fracture propagation in granite. *Journal of Structural Geology*, 17(1):95–114.

Myers, J. S. (1971). The Late Laxfordian granite-migmatite complex of western Harris, Outer Hebrides. *Scottish Journal of Geology*, 7(3):254–284.

Nadeau, R. M. and Johnson, L. R. (1998). Seismological studies at Parkfield VI: Moment release rates and estimates of source parameters for small repeating earthquakes. *Bulletin of the Seismological Society of America*, 88(3):790–814.

Nakamura, N., Hirose, T., and Borradaile, G. J. (2002). Laboratory verification of submicron magnetite production in pseudotachylytes: relevance for paleointensity studies. *Earth and Planetary Science Letters*, 201(1):13–18.

Nestola, F., Mittempergher, S., Toro, G. D., Zorzi, F., and Pedron, D. (2010). Evidence of dmisteinbergite (hexagonal form of CaAl2Si 2O8) in pseudotachylyte: A tool to constrain the thermal history of a seismic event. *American Mineralogist*, 95(2-3):405–409.

Ngo, D., Huang, Y., Rosakis, A., Griffith, W. A., and Pollard, D. (2012). Off-fault tensile cracks: A link between geological fault observations, lab experiments, and dynamic rupture models. *Journal of Geophysical Research: Solid Earth*, 117(B1):B01307.

Nicol, A. and Van Dissen, R. (2002). Up-dip partitioning of displacement components on the oblique-slip Clarence Fault, New Zealand. *Journal of Structural Geology*, 24(9):1521–1535.

Nicol, A., Walsh, J. J., Watterson, J., and Underhill, J. R. (1997). Displacement rates of normal faults. *Nature*, 390(6656):157–159.

Nielsen, S., Di Toro, G., Hirose, T., and Shimamoto, T. (2008). Frictional melt and seismic slip. *Journal of Geophysical Research: Solid Earth*, 113(B1):n/a–n/a.

Nielsen, S., Mosca, P., Giberti, G., Di Toro, G., Hirose, T., and Shimamoto, T. (2010a). On the transient behavior of frictional melt during seismic slip. *Journal of Geophysical Research*, 115(B10):B10301.

Nielsen, S., Toro, G. D., and Griffith, W. A. (2010b). Friction and roughness of a melting rock surface. *Geophysical Journal International*, 182(1):299–310.

Niemeijer, A., Di Toro, G., Griffith, W. A., Bistacchi, A., Smith, S. A. F., and Nielsen, S. (2012). Inferring earthquake physics and chemistry using an integrated field and laboratory approach. *Journal of Structural Geology*, 39(0):2–36.

Nissen, E., Elliott, J. R., Sloan, R. A., Craig, T. J., Funning, G. J., Hutko, A., Parsons, B. E., and Wright, T. J. (2016). Limitations of rupture forecasting exposed by instantaneously triggered earthquake doublet. *Nature Geosci*, 9(4):330–336.

Noda, H. and Shimamoto, T. (2005). Thermal Pressurization and Slip-Weakening Distance of a Fault: An Example of the Hanaore Fault, Southwest Japan. *Bulletin of the Seismological Society of America*, 95(4):1224–1233.

Norris, R. J. and Cooper, A. F. (2001). Late Quaternary slip rates and slip partitioning on the Alpine Fault, New Zealand. *Journal of Structural Geology*, 23(23):507–520.

O'Hara, K. D. (2001). A pseudotachylyte geothermometer. *Journal of Structural Geology*, 23(9):1345–1357.

Ohnaka, M. (1992). Earthquake source nucleation: A physical model for short-term precursors. *Tectonophysics*, 211(1):149–178.

Ohnaka, M. (2003). A constitutive scaling law and a unified comprehension for frictional slip failure, shear fracture of intact rock, and earthquake rupture. *Journal of Geophysical Research: Solid Earth*, 108(B2):2080.

Ohnaka, M. and Shen, L.-f. (1999). Scaling of the shear rupture process from nucleation to dynamic propagation: Implications of geometric irregularity of the rupturing surfaces. *Journal of Geophysical Research: Solid Earth*, 104(B1):817–844.

Osinski, G. R., I, A. G., and Oliver, G. J. H. (2001). Extensional tectonics of the Outer Hebrides Fault Zone, South Uist, northwest Scotland. *Geological Magazine*, 138(3):325–344.

Otsuki, K., Monzawa, N., and Nagase, T. (2003). Fluidization and melting of fault gouge during seismic slip: Identification in the Nojima fault zone and implications for focal earthquake mechanisms. *Journal of Geophysical Research: Solid Earth*, 108(B4):2192.

Parsons, A. J., Law, R. D., Lloyd, G. E., Phillips, R. J., and Searle, M. P. (2016). Thermokinematic evolution of the Annapurna-Dhaulagiri Himalaya, central Nepal: The Composite Orogenic System. *Geochemistry, Geophysics, Geosystems*, 17(4):1511–1539.

Pec, M., Stünitz, H., Heilbronner, R., Drury, M., and de Capitani, C. (2012). Origin of pseudotachylites in slow creep experiments. *Earth and Planetary Science Letters*, 355356(0):299–310.

Peng, S. and Johnson, A. M. (1972). Crack growth and faulting in cylindrical specimens of chelmsford granite. *International Journal of Rock Mechanics and Mining Sciences & Geomechanics Abstracts*, 9(1):37–86.

Perrin, C., Manighetti, I., Ampuero, J.-P., Cappa, F., and Gaudemer, Y. (2016). Location of largest earthquake slip and fast rupture controlled by along-strike change in fault structural maturity due to fault growth. *Journal of Geophysical Research: Solid Earth*, 121(5):3666–3685.

Petit, J. P. (1987). Criteria for the sense of movement on fault surfaces in brittle rocks. *Journal of Structural Geology*, 9(5):597–608.

Petrík, I., Nabelek, P. I., Janák, M., and Plašienka, D. (2003). Conditions of Formation and Crystallization Kinetics of Highly Oxidized Pseudotachylytes from the High Tatras (Slovakia). *Journal of Petrology*, 44(5):901–927.

Petzold, A. and Hinz, W. (1976). *Silikatchemie*. VEB, Leipzig.

Philpotts, A. R. and Miller, J. A. (1963). A Pre-Cambrian Glass from St. Alexis-des-Monts, Quebec. *Geological Magazine*, 100(04):337–344.

Pinet, N. and Cobbold, P. R. (1992). Experimental insights into the partitioning of motion within zones of oblique subduction. *Tectonophysics*, 206(3):371–388.

Piper, J. D. A. and Poppleton, T. J. (1989). Palaeomagnetic dating of pseudotachylyte formation in the Lewisian complex. *Scottish Journal of Geology*, 24(3):263–272.

Poliakov, A. N. B., Dmowska, R., and Rice, J. R. (2002). Dynamic shear rupture interactions with fault bends and off-axis secondary faulting. *Journal of Geophysical Research: Solid Earth*, 107(B11):2295.

Pollard, D. D. and Aydin, A. (1984). Propagation and linkage of oceanic ridge segments. *Journal of Geophysical Research: Solid Earth*, 89(B12):10017–10028.

Pollard, D. D., Segall, P., and Delaney, P. T. (1982). Formation and interpretation of dilatant echelon cracks. *Geological Society of America Bulletin*, 93(12):1291–1303.

Power, W. L., Tullis, T. E., and Weeks, J. D. (1988). Roughness and wear during brittle faulting. *Journal of Geophysical Research*, 93(B12):15268.

Price, N. A., Johnson, S. E., Gerbi, C. C., and West, D. P. (2012). Identifying deformed pseudotachylyte and its influence on the strength and evolution of a crustal shear zone at the base of the seismogenic zone. *Tectonophysics*, 518:63–83.

Prosser, G. (1998). Strike-slip movements and thrusting along a transpressive fault zone: The North Giudicarie line (Insubric line, northern Italy). *Tectonics*, 17(6):921–937.

Ravna, E. K. (2000). Distribution of Fe2+ and Mg between coexisting garnet and hornblende in synthetic and natural systems: an empirical calibration of the garnethornblende FeMg geothermometer. *Lithos*, 53(34):265–277.

Ray, S. K. (1999). Transformation of cataclastically deformed rocks to pseudotachylyte by pervasion of frictional melt: inferences from clast-size analysis. *Tectonophysics*, 301(34):283–304.

Ray, S. K. (2004). Meltclast interaction and power-law size distribution of clasts in pseudotachylytes. *Journal of Structural Geology*, 26(10):1831–1843.

Reddy, S. M., Johnson, T. E., Fischer, S., Rickard, W. D. A., and Taylor, R. J. M. (2015). Precambrian reidite discovered in shocked zircon from the Stac Fada impactite, Scotland. *Geology*, 43(10):899–902.

Rees, A. I. (1965). The use of anisotropy of magnetic susceptibility in the estimation of sedimentary fabric. *Sedimentology*, 4(4):257–271.

Reimold, W. U. (1995). Pseudotachylite in impact structures generation by friction melting and shock brecciation?: A review and discussion. *Earth-Science Reviews*, 39(3):247–265.

Resor, P., Shervais, K., Resor Katherine, P., and Shervais (2013). Imaging the 3D geometry of pseudotachylyte-bearing faults. *EGU General Assembly*.

Rice, J. R. (2006). Heating and weakening of faults during earthquake slip. *Journal of Geophysical Research: Solid Earth*, 111(B5):n/a–n/a.

Rino, S., Kon, Y., Sato, W., Maruyama, S., Santosh, M., and Zhao, D. (2008). The Grenvillian and Pan-African orogens: World's largest orogenies through geologic time, and their implications on the origin of superplume. *Gondwana Research*, 14(12):51–72.

Roberts, A. M. and Holdsworth, R. E. (1999). Linking onshore and offshore structures: Mesozoic extension in the Scottish Highlands. *Journal of the Geological Society*, 156(6):1061–1064.

Roberts, D. G. (1989). Basin inversion in and around the British Isles. *Geological Society, London, Special Publications*, 44(1):131–150.

Robie, R. A. and Waldbaum, D. (1968). Thermodynamic properties of minerals and related substances at 298.15K (25.0C) and one atmosphere (1.1013 bars) pressure and at higher temperatures. Technical report, USGS.

Rochette, P., Jackson, M., and Aubourg, C. (1992). Rock magnetism and the interpretation of anisotropy of magnetic susceptibility. *Reviews of Geophysics*, 30(3):209–226.

Rowe, C. D. and Griffith, W. A. (2015). Do faults preserve a record of seismic slip: A second opinion. *Journal of Structural Geology*, 78:1–26.

Rowe, C. D., Kirkpatrick, J. D., and Brodsky, E. E. (2012). Fault rock injections record paleo-earthquakes. *Earth and Planetary Science Letters*, 335336(0):154–166.

Rowe, C. D., Moore, J. C., Meneghini, F., and McKeirnan, A. W. (2005). Large-scale pseudotachylytes and fluidized cataclasites from an ancient subduction thrust fault. *Geology*, 33(12):937–940.

Rubin, A. M. and Ampuero, J.-P. (2007). Aftershock asymmetry on a bimaterial interface. *Journal of Geophysical Research: Solid Earth*, 112(B5):n/a–n/a.

Sammis, C., King, G., and Biegel, R. (1987). The kinematics of gouge deformation. *pure and applied geophysics*, 125(5):777–812.

Sanders, I. S. and Johnston, J. D. (1989). The Torridonian Stac Fada Member: an extrusion of fluidised peperite? *Earth and Environmental Science Transactions of the Royal Society of Edinburgh*, 80(01):1–4.

Savage, H. M., Polissar, P. J., Sheppard, R., Rowe, C. D., and Brodsky, E. E. (2014). Biomarkers heat up during earthquakes: New evidence of seismic slip in the rock record. *Geology*, 42(2):99–102.

Schmid, S. M. and Kissling, E. (2000). The arc of the western Alps in the light of geophysical data on deep crustal structure. *Tectonics*, 19(1):62–85.

Schmidt, M. W. (1992). Amphibole composition in tonalite as a function of pressure: an experimental calibration of the Al-in-hornblende barometer. *Contributions to Mineralogy and Petrology*, 110(2):304–310.

Schneider, C. A., Rasband, W. S., and Eliceiri, K. W. (2012). NIH Image to ImageJ: 25 years of image analysis. *Nature Methods*, 9(7):671–675.

Scholz, C. H. (1987). Wear and gouge formation in brittle faulting. *Geology*, 15(6):493.

Scholz, C. H. (1988). The brittle-plastic transition and the depth of seismic faulting. *Geologische Rundschau*, 77(1):319–328.

Scholz, C. H. (1997). Size distributions for large and small earthquakes. *Bulletin of the Seismological Society of America*, 87(4):1074 LP – 1077.

Scholz, C. H. (2002). *The mechanics of earthquakes and faulting*. Cambridge University Press, Cambridge, UK, 2nd edition.

Scholz, C. H. and Cowie, P. A. (1990). Determination of total strain from faulting using slip measurements. *Nature*, 346(6287):837–839.

Schön, J. (1983). *Petrophysik*. Ferdinand Enke, Stuttgart.

Scott, R. G. and Spray, J. G. (1999). Applications of Magnetic Anisotropies to Fabric Studies of Rocks and SedimentsMagnetic fabric constraints on friction melt flow regimes and ore emplacement direction within the South Range Breccia Belt, Sudbury Impact Structure. *Tectonophysics*, 307(1):163–189.

Segall, P. and Pollard, D. D. (1980). Mechanics of discontinuous faults. *Journal of Geophysical Research: Solid Earth*, 85(B8):4337–4350.

Sen, S. K. (1959). Potassium Content of Natural Plagioclases and the Origin of Antiperthites. *The Journal of Geology*, 67(5):479–495.

Seward, D. and Sibson, R. H. (1985). Fission-track age for a pseudotachylite from the Alpine Fault Zone, New Zealand. *New Zealand Journal of Geology and Geophysics*, 28(3):553–557.

Shaw, H. R. (1972). Viscosities of magmatic silicate liquids; an empirical method of prediction. *American Journal of Science*, 272(9):870–893.

Sherlock, S. C., Jones, K. A., and Park, R. (2008). Grenville-age pseudotachylite in the Lewisian: laserprobe 40Ar/39Ar ages from the Gairloch region of Scotland (UK). *Journal of the Geological Society*, 165(1):73–83.

Sherlock, S. C., Strachan, R. A., and Jones, K. A. (2009). High spatial resolution 40Ar/39Ar dating of pseudotachylites: geochronological evidence for multiple phases of faulting within basement gneisses of the Outer Hebrides (UK). *Journal of the Geological Society*, 166(6):1049–1059.

Shi, Z. and Ben-Zion, Y. (2006). Dynamic rupture on a bimaterial interface governed by slip-weakening friction. *Geophysical Journal International*, 165(2):469–484.

Shimamoto, T. and Nagahama, H. (1992). An argument against the crush origin of pseudotachylytes based on the analysis of clast-size distribution. *Journal of Structural Geology*, 14(89):999–1006.

Sibson, R. (1986). Brecciation processes in fault zones: Inferences from earthquake rupturing. *Pure and Applied Geophysics*, 124(1-2):159–175.

Sibson, R. H. (1975). Generation of peseudotachylyte by ancient seismic faulting. *Geophysical Journal of the Royal Astronomical Society*, 43(3):775–&.

Sibson, R. H. (1977a). Fault rocks and fault mechanisms. *Journal of the Geological Society*, 133(3):191–213.

Sibson, R. H. (1977b). *The Outer Hebrides Thrust: Its structure, mechanism and deformation environment*. PhD thesis, University of London.

Sibson, R. H. (1980). Transient discontinuities in ductile shear zones. *Journal of Structural Geology*, 2(12):165–171.

Sibson, R. H. (1983). Continental fault structure and the shallow earthquake source. *Journal of the Geological Society*, 140(5):741–767.

Sibson, R. H. (1985). A note on fault reactivation. *Journal of Structural Geology*, 7(6):751–754.

Sibson, R. H. and Toy, V. G. (2006). The habitat of fault-generated pseudotachylyte: Presence vs. absence of friction-melt. In *Earthquakes: Radiated Energy and the Physics of Faulting*, volume 170, pages 153–166. AGU, Washington, DC.

Smythe, D. K., Dobinson, A., McQuillin, R., Brewer, J. A., Matthews, D. H., Blundell, D. J., and Kelk, B. (1982). Deep structure of the Scottish Caledonides revealed by the MOIST reflection profile. *Nature*, 299(5881):338–340.

Soper, N. J., Ryan, P. D., and Dewey, J. F. (1999). Age of the Grampian orogeny in Scotland and Ireland. *Journal of the Geological Society*, 156(6):1231–1236.

Spray, J. G. (1987). Artificial generation of pseudotachylyte using friction welding apparatus: simulation of melting on a fault plane. *Journal of Structural Geology*, 9(1):49–60.

Spray, J. G. (1988). Generation and crystallization of an amphibolite shear melt: an investigation using radial friction welding apparatus. *Contributions to Mineralogy and Petrology*, 99(4):464–475.

Spray, J. G. (1993). Viscosity determinations of some frictionally generated silicate melts: implications for fault zone rheology at high strain rates. *Journal of Geophysical Research*, 98(B5):8053–8068.

Spray, J. G. (2010). Frictional Melting Processes in Planetary Materials: From Hypervelocity Impact to Earthquakes. *Annual Review of Earth and Planetary Sciences*, 38(1):221–254.

Steel, R. J. and Wilson, A. C. (1975). Sedimentation and tectonism (?Permo-Triassic) on the margin of the North Minch Basin, Lewis. *Journal of the Geological Society*, 131(2):183–200.

Stein, A. M. (1988). Basement controls upon basin development in the Caledonian foreland, NW Scotland. *Basin Research*, 1(2):107–119.

Stein, A. M. and Blundell, D. J. (1990). Geological inheritance and crystal dynamics of the northwest Scottish continental shelf. *Tectonophysics*, 173(14):455–467.

Stein, R. S. (1999). The role of stress transfer in earthquake occurrence. *Nature*, 402(6762):605–609.

Stewart, A. (2002). *The later Proterozoic Torridonian rocks of Scotland; their sedimentology, geochemistry and origin*. Geologial Society of London, Bath.

Stoker, M. S., Hitchen, K., and Graham, C. C. (1993). *United Kingdom offshore regional report: the geology of the Hebrides and West Shetland Shelves and adjacent deep-water areas*. HMSO, London.

Streule, M. J., Strachan, R. A., Searle, M. P., and Law, R. D. (2010). Comparing Tibet-Himalayan and Caledonian crustal architecture, evolution and mountain building processes. *Geological Society, London, Special Publications*, 335(1):207–232.

Suggate, R. and Grindley, G. (1972). Geological Map of New Zealand, 1:1 000 000 scale. Technical report, New Zealand Geological Survey.

Swanson, M. T. (1988). Pseudotachylyte-bearing strike-slip duplex structures in the Fort Foster Brittle Zone, S. Maine. *Journal of Structural Geology*, 10(8):813–828.

Szulc, A. G., Alsop, G. I., and Oliver, G. J. H. (2008). Kinematic and thermal constraints on the reactivation of the Outer Hebrides Fault Zone, NW Scotland. *Geological Magazine*, 145(05):623–636.

Takagi, H., Goto, K., and Shigematsu, N. (2000). Ultramylonite bands derived from cataclasite and pseudotachylyte in granites, northeast Japan. *Journal of Structural Geology*, 22(9):1325–1339.

Tanner, P. W. G. and Evans, J. A. (2003). Late Precambrian UPb titanite age for peak regional metamorphism and deformation (Knoydartian orogeny) in the western Moine, Scotland. *Journal of the Geological Society*, 160(4):555–564.

Thompson, L. M. and Spray, J. G. (1992). Pseudotachylytic rock distribution and genesis within the Sudbury impact structure. *Geological Society of America Special Papers*, 293:275–288.

Tikoff, B. and Teyssier, C. (1994). Structures and Tectonics at Different Lithospheric Levels Strain modeling of displacement-field partitioning in transpressional orogens. *Journal of Structural Geology*, 16(11):1575–1588.

Tinti, E., Cocco, M., Fukuyama, E., and Piatanesi, A. (2009). Dependence of slip weakening distance (Dc) on final slip during dynamic rupture of earthquakes. *Geophysical Journal International*, 177(3):1205–1220.

Tomita, T., Ohtani, T., Shigematsu, N., Tanaka, H., Fujimoto, K., Kobayashi, Y., Miyashita, Y., and Omura, K. (2002). Development of the Hatagawa Fault Zone clarified by geological and geochronological studies. *Earth, Planets and Space*, 54(11):1095–1102.

Tong, X., Sandwell, D., Luttrell, K., Brooks, B., Bevis, M., Shimada, M., Foster, J., Smalley, R., Parra, H., Báez Soto, J. C., Blanco, M., Kendrick, E., Genrich, J., and Caccamise, D. J. (2010). The 2010 Maule, Chile earthquake: Downdip rupture limit revealed by space geodesy. *Geophysical Research Letters*, 37(24):L24311.

Torvela, T. and Ehlers, C. (2010). Microstructures associated with the Sottunga-Jurmo shear

zone and their implications for the 1.83-1.79 Ga tectonic development of SW Finland. *Bulletin of the Geological Society of Finland*, 82:5–29.

Townend, J. and Zoback, M. D. (2000). How faulting keeps the crust strong. *Geology*, 28(5):399–402.

Toy, V. G., Ritchie, S., and Sibson, R. H. (2011). Diverse habitats of pseudotachylytes in the Alpine Fault Zone and relationships to current seismicity. *Geological Society, London, Special Publications*, 359(1):115–133.

Toyoshima, T. (1990). Pseudotachylite from the Main Zone of the Hidaka metamorphic belt, Hokkaido, northern Japan. *Journal of Metamorphic Geology*, 8(5):507–523.

Tsutsumi, A. and Shimamoto, T. (1997). High-velocity frictional properties of gabbro. *Geophysical Research Letters*, 24(6):699–702.

Tullis, J. and Yund, R. A. (1991). Diffusion creep in feldspar aggregates: experimental evidence. *Journal of Structural Geology*, 13(9):987–1000.

Turnbull, M. J. M., Whitehouse, M. J., and Moorbath, S. (1996). New isotopic age determinations for the Torridonian, NW Scotland. *Journal of the Geological Society*, 153(6):955–964.

Twiss, R. J. and Unruh, J. R. (1998). Analysis of fault slip inversions: Do they constrain stress or strain rate? *Journal of Geophysical Research: Solid Earth*, 103(B6):12205–12222.

Ueda, T., Obata, M., Di Toro, G., Kanagawa, K., and Ozawa, K. (2008). Mantle earthquakes frozen in mylonitized ultramafic pseudotachylytes of spinel-lherzolite facies. *Geology*, 36(8):607–610.

Ujiie, K., Yamaguchi, H., Sakaguchi, A., and Toh, S. (2007). Pseudotachylytes in an ancient accretionary complex and implications for melt lubrication during subduction zone earthquakes. *Journal of Structural Geology*, 29(4):599–613.

van Breemen, O., Aftalion, M., and Pidgeon, R. T. (1971). The age of the granitic injection complex of Harris, Outer Hebrides. *Scottish Journal of Geology*, 7(2):139–152.

Verdecchia, A. and Carena, S. (2016). Coulomb stress evolution in a diffuse plate boundary: 1400years of earthquakes in eastern California and western Nevada, USA. *Tectonics*, pages n/a–n/a.

Vermilye, J. M. and Scholz, C. H. (1998). The process zone: A microstructural view of fault growth. *Journal of Geophysical Research: Solid Earth*, 103(B6):12223–12237.

Viganò, A., Tumiati, S., Recchia, S., Martin, S., Marelli, M., and Rigon, R. (2011). Carbonate pseudotachylytes: evidence for seismic faulting along carbonate faults. *Terra Nova*, 23(3):187–194.

Violay, M., Nielsen, S., Gibert, B., Spagnuolo, E., Cavallo, A., Azais, P., Vinciguerra, S., and Di Toro, G. (2014). Effect of water on the frictional behavior of cohesive rocks during earthquakes. *Geology*, 42(1):27–30.

Wallis, D., Lloyd, G. E., Phillips, R. J., Parsons, A. J., and Walshaw, R. D. (2015). Low effective fault strength due to frictional-viscous flow in phyllonites, Karakoram Fault Zone, NW India. *Journal of Structural Geology*, 77(0):45–61.

Wallis, D., Phillips, R. J., and Lloyd, G. E. (2013). Fault weakening across the frictional-viscous transition zone, Karakoram Fault Zone, NW Himalaya. *Tectonics*, 32(5):1227–1246.

Walsh, J. J., Childs, C., Imber, J., Manzocchi, T., Watterson, J., and Nell, P. A. R. (2003). Strain localisation and population changes during fault system growth within the Inner Moray Firth, Northern North Sea. *Journal of Structural Geology*, 25(2):307–315.

Wang, L., Zöller, G., and Hainzl, S. (2015). Joint Determination of Slip and Stress Drop in a Bayesian Inversion Approach: A Case Study for the 2010 M8.8 Maule Earthquake. *Pure and Applied Geophysics*, 172(2):375–388.

Wang, W. and Scholz, C. H. (1994). Wear processes during frictional sliding of rock: A theoretical and experimental study. *Journal of Geophysical Research: Solid Earth*, 99(B4):6789–6799.

Warr, L., van der Pluijm, B., Schleicher, A., and Anonymous (2010). The importance of the

pseudotachylyte clast-matrix ratio in determining the mechanism, age and crustal depth of episodic coseismic faulting. *Geophysical Research Abstracts*, 12:EGU2010–8588.

Warr, L. N., van der Pluijm, B. A., Peacor, D. R., and Hall, C. M. (2003). Frictional melt pulses during a 1.1 Ma earthquake along the Alpine Fault, New Zealand. *Earth and Planetary Science Letters*, 209(12):39–52.

Watson, J. (1977). The Outer Hebrides: a geological perspective. *Proceedings of the Geologists' Association*, 88:1–14.

Wells, D. L. and Coppersmith, K. J. (1994). New empirical relationships among magnitude, rupture length, rupture width, rupture area, and surface displacement. *Bulletin of the Seismological Society of America*, 84(4):974–1002,A1–A4,B1–B11,C1–C49.

Wen, Y., Xu, C., Liu, Y., Jiang, G., and He, P. (2013). Coseismic slip in the 2010 Yushu earthquake (China), constrained by wide-swath and strip-map InSAR. *Natural Hazards and Earth System Sciences*, 13(1):35–44.

Wenk, H. and Bulakh, A. (2004). *Minerals*. Cambridge University Press, Cambridge, UK, 1st edition.

Wenk, H. and Weiss, L. (1982). Al-rich calcic pyroxene in pseudotachylite: An indicator of high pressure and high temperature? *Tectonophysics*, 84(2-4):329–341.

Wesnousky, S. G. (1994). The Gutenberg-Richter or characteristic earthquake distribution, which is it? *Bulletin of the Seismological Society of America*, 84(6):1940–1959.

White, J. C. (1996a). Transient discontinuities revisited: pseudotachylyte, plastic instability and the influence of low pore fluid pressure on deformation processes in the mid-crust. *Journal of Structural Geology*, 18(12):1471–1486.

White, J. C. (1996b). Transient discontinuities revisited: pseudotachylyte, plastic instability and the influence of low pore fluid pressure on deformation processes in the mid-crust. *Journal of Structural Geology*, 18(12):1471–1486.

White, J. C. and Williams, P. F. (1987). Special session: Rocks, minerals, and materials science Session. *Canadian Journal of Earth Sciences*, 24(3):505.

White, S. H. and Glasser, J. (1987). The Outer Hebrides Fault Zone: evidence for normal movements. *Geological Society, London, Special Publications*, 27(1):175–183.

Whitehouse, M. J. (1993). Age of the Corodale Gneisses, South Uist. *Scottish Journal of Geology*, 29(1):1–7.

Whitehouse, M. J., Bridgwater, D., and Park, R. G. (1997). Detrital zircon ages from the Loch Maree Group, Lewisian Complex, NW Scotland: confirmation of a Palaeoproterozoic LaurentiaFennoscandia connection. *Terra Nova*, 9(5-6):260–263.

Williams, G. E. and Foden, J. (2011). A unifying model for the Torridon Group (early Neoproterozoic), NW Scotland: Product of post-Grenvillian extensional collapse. *Earth-Science Reviews*, 108(12):34–49.

Wilshire, H. G. (1971). Pseudotachylite from the Vredefort Ring, South Africa. *The Journal of Geology*, 79(2):195–206.

Wilson, R. W., Holdsworth, R. E., Wild, L. E., Mccaffrey, K. J. W., England, R. W., Imber, J., and Strachan, R. A. (2010). Basement-influenced rifting and basin development: a reappraisal of post-Caledonian faulting patterns from the North Coast Transfer Zone, Scotland. *Geological Society, London, Special Publications*, 335(1):795–826.

Wintsch, R. P., Christoffersen, R., and Kronenberg, A. K. (1995). Fluid-rock reaction weakening of fault zones. *Journal of Geophysical Research: Solid Earth*, 100(B7):13021–13032.

Wirth, R. (2009). Focused Ion Beam (FIB) combined with SEM and TEM: Advanced analytical tools for studies of chemical composition, microstructure and crystal structure in geomaterials on a nanometre scale. *Chemical Geology*, 261(34):217–229.

Witty, G. J. (1975). *The geochemistry of the roneval anorthosite, South Harris, Scotland.* PhD thesis, University of London.

Xia, K., Rosakis, A. J., Kanamori, H., and Rice, J. R. (2005). Laboratory Earthquakes Along Inhomogeneous Faults: Directionality and Supershear. *Science*, 308(5722):681–684.

Yin, A. and Harrison, T. M. (2000). Geologic Evolution of the Himalayan-Tibetan Orogen. *Annual Review of Earth and Planetary Sciences*, 28(1):211–280.

Zang, W. and Fyfe, W. S. (1995). Chloritization of the hydrothermally altered bedrock at the Igarapé Bahia gold deposit, Carajás, Brazil. *Mineralium Deposita*, 30(1):30–38.